**REPUBLIC OF TÜRKİYE**

**YILDIZ TECHNICAL UNIVERSITY**

**GRADUATE SCHOOL OF SCIENCE AND ENGINEERING**

# INVESTIGATION OF CRYSTALLIZATION EFFECT ON SURFACE TENSION OF NANOPARTICLE EMBEDDED BOROSILICATE GLASS-CERAMIC COATINGS

**NURULLAH ÇÖPOĞLU**

DOCTOR OF PHILOSOPHY THESIS

Department of Metallurgical and Materials Engineering

Program of Material

Supervisor

Assoc. Prof. Dr. Buğra ÇİÇEK

July, 2024

**REPUBLIC OF TÜRKİYE**

**YILDIZ TECHNICAL UNIVERSITY**

**GRADUATE SCHOOL OF SCIENCE AND ENGINEERING**

# INVESTIGATION OF CRYSTALLIZATION EFFECT ON SURFACE TENSION OF NANOPARTICLE EMBEDDED BOROSILICATE GLASS-CERAMIC COATINGS

A thesis submitted by Nurullah ÇÖPOĞLU in partial fulfillment of the requirements for the degree of **DOCTOR OF PHILOSOPHY** is approved by the committee on 22.07.2024 in Department of Metallurgical and Materials Engineering, Program of Material.

Prof. Dr. Buğra ÇİÇEK
Yıldız Technical University
Supervisor

**Approved By the Examining Committee**

Assoc. Prof. Dr. Buğra ÇİÇEK, Supervisor
Yildiz Technical University _____

Assoc. Prof. Dr. Metin GENÇTEN, Member
Yildiz Technical University _____

Prof. Dr. Suat YILMAZ, Member
Istanbul University - Cerrahpasa _____

Assoc. Prof. Dr. Bilge COŞKUNER FİLİZ, Member
Yildiz Technical University _____

Assoc. Prof. Dr. Ergün KELEŞOĞLU, Member
Turkish-German University _____

I hereby declare that I have obtained the required legal permissions during data collection and exploitation procedures, that I have made the in-text citations and cited the references properly, that I haven't falsified and/or fabricated research data and results of the study and that I have abided by the principles of the scientific research and ethics during my Thesis Study under the title of "Investigation of Crystallization Effect on Surface Tension of Nanoparticle Embedded Borosilicate Glass-Ceramic" supervised by my supervisor, Assoc. Prof. Dr. Buğra ÇİÇEK. In the case of a discovery of false statement, I am to acknowledge any legal consequence.

Nurullah ÇÖPOĞLU

Signature

*Dedicated to my family*

*and my beloved nieces*

# ACKNOWLEDGEMENTS

This PhD thesis would not have been possible without the support and guidance of many individuals who contributed their time, expertise, and encouragement throughout this journey. First and foremost, I would like to express my deepest gratitude to my advisor, Assoc. Prof. Dr. Buğra ÇİÇEK. His insightful guidance, valuable feedback, and unwavering support have been crucial in shaping this research. His mentorship has been an inspiration and a source of motivation throughout my doctoral studies.

I am also deeply grateful to Dr. Oguz Karaahmet for his expert guidance and invaluable support for my thesis. His dedication and knowledge significantly contributed to the progress of this work. Special thanks to Yasin Bozkurt Yilmaz, Ph.D. Candidate, Sinan Daloglu, M.Sc., Abdi Soylu, M.Sc., Emre Toy, M.Sc., and Kumru Karaman, M.Sc., for their assistance with measurements, and various other essential tasks. Their technical expertise and collaborative spirit were instrumental in overcoming many challenges encountered during this research.

I would also like to acknowledge the support of my friends who have been a constant source of encouragement and joy. Atty. Gulfikar Kotan and Dr. Ingrid Berenice Sánchez Carrillo have been invaluable companions throughout this journey. Their friendship and moral support have been indispensable.

I would like to extend my heartfelt thanks to my sister, Hilal, for her unwavering support, encouragement, and understanding throughout the course of this thesis.

Finally, I extend my deepest appreciation to my family and friends who have stood by me with unwavering support and encouragement. Their love and understanding have been my foundation throughout this journey. This thesis is dedicated to all those who have been part of this incredible journey.

Nurullah ÇÖPOĞLU

# TABLE OF CONTENTS

**LIST OF SYMBOLS** vii
**LIST OF ABBREVIATIONS** x
**LIST OF FIGURES** xi
**LIST OF TABLES** xvi
**ABSTRACT** xvii
**ÖZET** xix
**1 INTRODUCTION** 1
1.1 Background and Motivation ..... 1
1.2 Objectives of the Study ..... 3
1.3 Research Hypotheses ..... 4
1.4 Scope and Limitations ..... 6
**2 GLASS-CERAMIC COATINGS** 8
2.1 Composition of Glass-Ceramic Coatings ..... 8
2.2 Properties of Glass-Ceramic Coatings ..... 11
2.2.1 Mechanical Properties ..... 11
2.2.2 Thermal Properties ..... 13
2.2.3 Chemical Durability ..... 13
2.2.4 Optical Properties ..... 14
2.2.5 Surface Properties ..... 15
2.3 Crystallization Process and Kinetics ..... 16
2.3.1 Nucleation ..... 16
2.3.2 Growth ..... 17
2.4 Applications of Glass-Ceramic Coatings ..... 19
2.4.1 Protective Coatings ..... 19
2.4.2 Thermal Barrier Coatings ..... 20
2.4.3 Biomedical Implants ..... 21
2.4.4 Optoelectronics ..... 21
2.5 Phosphate-Containing Lithium Zinc Borosilicate Glass-Ceramics ..... 22
2.5.1 Crystallization Process ..... 24
2.5.2 Properties ..... 25
2.5.3 Adhesion to Steel Substrates ..... 26
2.6 Role of Nano-CuO and Nano-ZnO in Glass-Ceramic Systems ..... 27

2.6.1 Sintering and Densification ..... 27
2.6.2 Microstructure and Crystallization ..... 29
2.6.3 Phase Transformation ..... 30
2.6.4 Role of CuO and ZnO in Specific Systems ..... 32
**3 CRYSTALLIZATION KINETICS 34**
3.1 Johnson-Mehl-Avrami-Kolmogorov (JMAK) Theory ..... 34
3.2 Ozawa Theory ..... 38
3.3 Augis-Bennett Method ..... 39
3.4 Kissinger Method ..... 40
3.5 Flynn-Wall-Ozawa (FWO) Method ..... 40
3.6 Friedman Method ..... 41
3.7 Avrami-Erofeev Model ..... 42
**4 SURFACE TENSION 44**
4.1 Definition and Measurement ..... 44
4.2 Surface Tension in Glass-Ceramics ..... 46
4.3 Influence of Surface Tension on Coating Performance ..... 48
4.4 Previous Studies on Nano-Additives in Glass-Ceramics ..... 50
**5 EXPERIMENTAL DETAILS 53**
5.1 Materials ..... 53
5.1.1 Composition of Glass-Ceramic Coatings ..... 53
5.1.2 Characteristics of Nano-CuO and Nano-ZnO ..... 54
5.2 Sample Preparation ..... 55
5.3 Experimental Techniques ..... 56
5.4 X-Ray Fluorescence (XRF) Analysis ..... 56
5.5 Hot Stage Microscope Analysis ..... 56
5.6 Differential Thermal Analysis (DTA) ..... 57
5.7 X-ray Diffraction (XRD) Analysis ..... 57
5.8 Scanning Electron Microscopy (SEM) ..... 57
5.9 Optical Microscopy ..... 58
5.10 3D Surface Analysis ..... 58
5.11 Viscosity Measurements ..... 59
5.12 Contact Angle Measurements ..... 59
**6 RESULTS AND DISCUSSION 61**
6.1 Chemical Composition ..... 61
6.2 Thermal Analyses ..... 63

6.2.1 Hot Stage Microscopy ..... 63
6.2.2 Dilatometer ..... 65
6.2.3 Viscosity Measurements ..... 66
6.2.4 Differential Thermal Analysis (DTA) ..... 68
6.3 Kinetic Calculations ..... 70
6.4 Structural Analyses ..... 73
6.4.1 XRD Analyses ..... 73
6.5 Morphology Analyses ..... 81
6.5.1 Scanning Electron Microscopy (SEM) Analyses ..... 81
6.6 Surface Characterization ..... 100
6.6.1 Optical Microscopy ..... 100
6.6.2 Surface Topography Analysis ..... 106
6.6.3 Surface Roughness Analysis ..... 113
6.7 Contact Angle Analysis ..... 117
6.7.1 Nano CuO Addition ..... 117
6.7.2 Nano-ZnO Addition ..... 119
**7 COMPREHENSIVE ANALYSIS ..... 122**
7.1 Impact of Nano-CuO and Nano-ZnO on Surface Attributes ..... 122
7.2 Influence on Surface Tension and Hydrophilicity ..... 124
7.3 Correlation Between Crystallization and Surface Properties ..... 126
7.4 Comparison with Existing Literature ..... 128
**8 CONCLUSION 136**
**REFERENCES 141**
**PUBLICATIONS FROM THE THESIS 174**

# LIST OF SYMBOLS

| | |
|---|---|
| $T$ | Absolute Temperature |
| $E_a$ | Activation Energy |
| Å | Ångström |
| Ra | Arithmetic Average Roughness |
| n | Avrami Exponent |
| °C | Centigrade Degree |
| $C_1$ | Constant |
| $T_c$ | Crystallization Onset Temperature |
| E | Energy |
| F | Force |
| $\phi$s | Fraction of Liquid-Solid Area |
| X(t) | Fraction of Material Crystallized at Time t |
| A | Frequency Factor |
| R | Gas Constant |
| $T_g$ | Glass Transition Temperature |
| β | Heating Rate |
| i | Index of Conversion |
| j | Index of the Curve |
| J | Joule |
| $K_\alpha$ | K-alpha |
| K | Kelvin |
| kJ | Kilojoule |
| kV | Kilovolt |
| L | Length |
| $\alpha_L$ | Linear Coefficient of Thermal Expansion |
| Rz | Maximum Height of Roughness Profile |
| μm | Micrometer |
| mg | Miligrams |
| mA | Milliampere |
| nm | Nanometre |
| m | Ozawa Exponent |
| $T_p$ | Peak Crystallization Temperature |

| | |
|---|---|
| $\pi$ | pi |
| $\pm$ | Plus-Minus |
| A | Pre-Exponential Factor |
| r | Radial Rate |
| k | Rate Constant |
| Rq | Root Mean Square Roughness |
| $r_f$ | Roughness Parameter |
| $T_s$ | Softening Temperature |
| $\gamma$ | Surface Tension |
| $\gamma$LV | Surface Tensions of the Liquid-Vapor |
| $\gamma$SL | Surface Tensions of the Solid-Liquid |
| $\gamma$SV | Surface Tensions of the Solid-Vapor |
| T | Temperature |
| $K_T$ | Temperature-dependent Rate Constant |
| B | VFT Constant |
| $\eta$ | Viscosity |
| $T_0$ | Vogel Temperature |
| V | Volume |
| $\alpha_V$ | Volumetric Coefficient of Thermal Expansion |
| wt.% | Weight Percent |
| $\theta_Y$ | Young Contact Angle |

# LIST OF ABBREVIATIONS

| | |
|---|---|
| 3D | 3-Dimensional |
| BSE | Backscattered Electron |
| CTE | Coefficient of Thermal Expansion |
| CVD | Chemical Vapor Deposition |
| DSC | Differential Scanning Calorimetry |
| DTA | Differential Thermal Analysis |
| EDS | Energy Dispersive X-ray |
| EN | European Norm |
| FWO | Flynn-Wall-Ozawa |
| GCC | Glass-ceramic coating |
| HSM | Hot Stage Microscope |
| JMAK | Johnson-Mehl-Avrami-Kolmogorov |
| LAS | Lithium-Aluminosilicate |
| LMZBS | Lithium Magnesium Zinc Borosilicate |
| LZBS | Lithium Zinc Borosilicate |
| NBO | Non-Bridging Oxygen |
| SE | Secondary Electron |
| SEM | Scanning Electron Microscopy |
| SOEC | Solid Oxide Electrolysis Cell |
| SOFC | Solid Oxide Fuel Cell |
| TEM | Transmission Electron Microscopy |
| TG | Thermogravimetry |
| TTT | Time–Temperature-Transformation |
| UV | Ultraviolet |
| VFT | Vogel-Fulcher-Tammann |
| XRD | X-ray Diffraction |
| XRF | X-Ray Fluorescence |

# LIST OF FIGURES

**Figure 2.1** The arrow indicates the direction of the crack; several toughening mechanisms are recognizable, such as pull-out of the grains (A), bridging (B), crack deflection (C) ..... 12

**Figure 2.2** (A) Representative XRD spectra for the 154540 GAP-Se glass following nucleation at 190°C, with furnace HT at temperatures shown for 30 min. (B) Measured refractive index ($\lambda$ = 4.515 μm) versus growth temperature for various nucleation temperatures. (C) Measured (experimental) refractive index values obtained as a function of HT temperature, as compared to calculated refractive index based on volume fraction of crystal phase formed from XRD spectra ..... 14

**Figure 2.3** Measurement of the contact angle of a three-phase system ..... 15

**Figure 2.4** Evolution of the microstructure from glass to glass–ceramic through volume crystallisation from a bulk glass or sinter-crystallisation.. 16

**Figure 2.5** This schematic model illustrates the strategy for controlling the crystallization habit of glass. Graph a) shows the classical curves of the temperature-dependent nucleation and growth rate. Graphs b) and c) demonstrate how reshaping the crystallization rate curves by suppressing or enhancing the nucleation rate can lead to microcrystallization (b) or nanocrystallization (c), respectively.... 18

**Figure 2.6** (a) Transmission Electron Microscopy (TEM) bright-field micrographs display crystallites with sizes in the range of 5-10 nm. (b) The transmission spectra illustrate the characteristics of the $MgAl_2O_4$ spinel precursor glass (top) and the glass-ceramic nanocomposites (bottom) ..... 22

**Figure 2.7** Crystal structures of $Li_2ZnSiO_4$ polymorphs: (a) monoclinic (space group $P2_1/n$) and (b) orthorhombic (space group $Pmn2_1$) ..... 25

**Figure 4.1** Illustration of the sessile drop method ..... 45

**Figure 4.2** Illustration of Wilhelmy plate method ..... 45

**Figure 4.3** Illustration of capillary rise in a vertical plate ..... 46

**Figure 4.4** Schematic illustration of the pendant drop procedure. (a) pendant drop for surface tension measurements, (b) and (c) spreading dynamics ..... 46

**Figure 4.5** (a) Young's equation (b) Wenzel State (c) Cassie–Baxter State (d) Hydrophobic Surface (Contact angle > 90°) (e) Hydrophobic Surface (Contact angle < 90°) ..... 48

**Figure 6.1** Hot-stage microscopy analysis results of the precursor LZBS sample: sintering, softening, sphere, half-sphere, and melting temperatures. ..... 63

**Figure 6.2** Optical dilatometer analysis result of the LZBS sample up to 600 °C showing glass transition ($T_g$) and dilatometric softening ($T_{peak}$) points. ..... 65

**Figure 6.3** Viscosity versus temperature for the precursor LZBS sample. The lines are plotted according to the VFT equation determined from HSM and DIL analyses. ..... 67

**Figure 6.4** DTA analysis performed on the glass-ceramic coatings using different heating rates of 5, 10, 15, and 20 °C/min. ..... 69

**Figure 6.5** The Kissinger plot of the studied LZBS sample ..... 72

**Figure 6.6** XRD results of the studied LZBS samples crystallized a) at 750, 800 and 850 °C, with nano-copper oxide additions of 0.5, 1.0, 2.5, and 5.0 wt. % ..... 76

**Figure 6.7** XRD results of the studied LZBS samples crystallized at 750, 800 and 850 °C, with nano-copper oxide additions at ranges between 2θ: 20° – 28° ..... 77

**Figure 6.8** XRD results of the studied LZBS samples crystallized with nano-copper oxide additions at ranges between 2θ: 30° – 37°, a) at 750 °C, b) at 800 °C, and c) at 850 °C. ..... 77

**Figure 6.9** XRD results of the studied LZBS samples crystallized with nano-zinc oxide additions of 0.5, 1.0, 2.5, and 5.0 wt. at 750 °C ..... 78

**Figure 6.10** XRD results of the studied LZBS samples crystallized with nano-zinc oxide additions of 0.5, 1.0, 2.5, and 5.0 wt. at 800 °C ..... 79

**Figure 6.11** XRD results of the studied LZBS samples crystallized with nano-zinc oxide additions of 0.5, 1.0, 2.5, and 5.0 wt. at 850 °C ..... 80

**Figure 6.12** SEM images of the studied LZBS reference samples without additions a) at 750 °C, b) at 800 °C, and c) at 850 °C ..... 82

**Figure 6.13** SEM image (left) and EDS analyses of the defined parts (right) of the LZBS_REF sample at 750 °C ..... 82

**Figure 6.14** SEM image (left) and EDS analyses of the defined parts (right) of the LZBS_REF sample at 800 °C ..... 83

**Figure 6.15** SEM image (left) and EDS analyses of the defined parts (right) of the LZBS_REF sample at 850 °C ..... 83

**Figure 6.16** SEM images of the studied LZBS reference samples with 0.5 wt. % nano-CuO addition a) at 800 °C, and b) at 850 °C ..... 83

**Figure 6.17** SEM image (left) and EDS analyses of the defined parts (right) of the LZBS_05_CuO sample at 800 °C ..... 84

**Figure 6.18** SEM image (left) and EDS analyses of the defined parts (right) of the LZBS_05_CuO sample at 850 °C ..... 84

**Figure 6.19** SEM images of the studied LZBS reference samples with 1.0 wt. % nano-CuO addition a) at 750 °C, b) at 800 °C, and c) at 850 °C ... 85

**Figure 6.20** SEM image (left) and EDS analyses of the defined parts (right) of the LZBS_10_CuO sample at 750 °C ..... 85

**Figure 6.21** SEM image (left) and EDS analyses of the defined parts (right) of the LZBS_10_CuO sample at 800 °C ..... 86

**Figure 6.22** SEM image (left) and EDS analyses of the defined parts (right) of the LZBS_10_CuO sample at 850 °C ..... 86

**Figure 6.23** SEM images of the studied samples with 2.5 wt. % nano-CuO addition and crystallized a) at 750 °C, b) at 800 °C, and c) at 850 °C ..... 87

**Figure 6.24** SEM image (left) and EDS analyses of the defined parts (right) of the LZBS_25_CuO sample at 750 °C ..... 87

**Figure 6.25** SEM image (left) and EDS analyses of the defined parts (right) of the LZBS_25_CuO sample at 800 °C ..... 88

**Figure 6.26** SEM image (left) and EDS analyses of the defined parts (right) of the LZBS_25_CuO sample at 850 °C ..... 88

**Figure 6.27** SEM images of the studied LZBS reference samples with 2.5 wt. % nano-CuO addition a) at 750 °C, b) at 800 °C, and c) at 850 °C ... 89

**Figure 6.28** SEM image (left) and EDS analyses of the defined parts (right) of the LZBS_50_CuO sample at 750 °C ..... 89

**Figure 6.29** SEM image (left) and EDS analyses of the defined parts (right) of the LZBS_50_CuO sample at 800 °C ..... 90

**Figure 6.30** SEM image (left) and EDS analyses of the defined parts (right) of the LZBS_50_CuO sample at 850 °C ..... 90

**Figure 6.31** SEM images of the studied LZBS samples crystallized at 750 °C with addition of a) 0.5 wt.%, b) 1.0 wt.%, c) 2.5 wt.%, and d) a) 5.0 wt.% nano-ZnO ..... 93

**Figure 6.32** SEM image (left) and EDS analyses of the defined parts (right) of the LZBS_05_ZnO sample at 750 °C ..... 94

**Figure 6.33** SEM image (left) and EDS analyses of the defined parts (right) of the LZBS_10_ZnO sample at 750 °C ..... 94

**Figure 6.34** SEM image (left) and EDS analyses of the defined parts (right) of the LZBS_25_ZnO sample at 750 °C ..... 94

**Figure 6.35** SEM image (left) and EDS analyses of the defined parts (right) of the LZBS_50_ZnO sample at 750 °C ..... 95

**Figure 6.36** SEM images of the studied LZBS samples crystallized at 800 °C with addition of a) 0.5 wt.%, b) 1.0 wt.%, c) 2.5 wt.%, and d) a) 5.0 wt.% nano-ZnO ..... 95

**Figure 6.37** SEM image (left) and EDS analyses of the defined parts (right) of the LZBS_05_ZnO sample at 800 °C ..... 96

**Figure 6.38** SEM image (left) and EDS analyses of the defined parts (right) of the LZBS_10_ZnO sample at 800 °C ..... 96

**Figure 6.39** SEM image (left) and EDS analyses of the defined parts (right) of the LZBS_25_ZnO sample at 800 °C ..... 96

**Figure 6.40** SEM image (left) and EDS analyses of the defined parts (right) of the LZBS_50_ZnO sample at 800 °C ..... 97

**Figure 6.41** SEM images of the studied LZBS samples crystallized at 850 °C with addition of a) 0.5 wt.%, b) 1.0 wt.%, c) 2.5 wt.%, and d) a) 5.0 wt.% nano-ZnO ..... 98

**Figure 6.42** SEM image (left) and EDS analyses of the defined parts (right) of the LZBS_05_ZnO sample at 850 °C ..... 98

**Figure 6.43** SEM image (left) and EDS analyses of the defined parts (right) of the LZBS_10_ZnO sample at 850 °C ..... 99

**Figure 6.44** SEM image (left) and EDS analyses of the defined parts (right) of the LZBS_25_ZnO sample at 850 °C ..... 99

**Figure 6.45** SEM image (left) and EDS analyses of the defined parts (right) of the LZBS_50_ZnO sample at 850 °C ..... 99

**Figure 6.46** Optical microscopy images of the studied LZBS reference samples without additions a) at 750 °C, b) at 800 °C, and c) at 850 °C ... 101

**Figure 6.47** Optical microscopy images of the studied LZBS samples crystallized at 750 °C with the addition of a)1.0 wt.%, b) 2.5 wt.%, and c) 5.0 wt.% nano-CuO ..... 101

**Figure 6.48** Optical microscopy images of the studied LZBS samples crystallized at 800 °C with addition of a) 0.5 wt.%, b) 1.0 wt.%, c) 2.5 wt.%, and d) a) 5.0 wt.% nano-CuO ..... 102

**Figure 6.49** Optical microscopy images of the studied LZBS samples crystallized at 850 °C with addition of a) 0.5 wt.%, b) 1.0 wt.%, c) 2.5 wt.%, and d) a) 5.0 wt.% nano-CuO ..... 102

**Figure 6.50** Optical microscopy images of the studied LZBS samples crystallized at 750 °C with addition of a) 0.5 wt.%, b) 1.0 wt.%, c) 2.5 wt.%, and d) a) 5.0 wt.% nano-CuO ..... 105

**Figure 6.51** Optical microscopy images of the studied LZBS samples crystallized at 800 °C with addition of a) 0.5 wt.%, b) 1.0 wt.%, c) 2.5 wt.%, and d) a) 5.0 wt.% nano-CuO ..... 105

**Figure 6.52** Optical microscopy images of the studied LZBS samples crystallized at 850 °C with addition of a) 0.5 wt.%, b) 1.0 wt.%, c) 2.5 wt.%, and d) a) 5.0 wt.% nano-CuO ..... 106

**Figure 6.53** 3D surface topography images of the studied LZBS reference samples without additions a) at 750 °C, b) at 800 °C, and c) at 850 °C..... 107

**Figure 6.54** 3D surface topography images of the studied LZBS samples crystallized at 750 °C with the addition of a) 1.0 wt.%, b) 2.5 wt.%, and c) 5.0 wt.% nano-CuO ..... 108

**Figure 6.55** 3D surface topography images of the studied LZBS samples crystallized at 800 °C with the addition of a) 0.5 wt.%, b)1.0 wt.%, c) 2.5 wt.%, and d) 5.0 wt.% nano-CuO ..... 108

**Figure 6.56** 3D surface topography images of the studied LZBS samples crystallized at 850 °C with the addition of a) 0.5 wt.%, b)1.0 wt.%, c) 2.5 wt.%, and d) 5.0 wt.% nano-CuO .....109

**Figure 6.57** 3D surface topography images of the studied LZBS samples crystallized at 750 °C with the addition of a) 0.5 wt.%, b)1.0 wt.%, c) 2.5 wt.%, and d) 5.0 wt.% nano-ZnO .....110

**Figure 6.58** 3D surface topography images of the studied LZBS samples crystallized at 800 °C with the addition of a) 0.5 wt.%, b)1.0 wt.%, c) 2.5 wt.%, and d) 5.0 wt.% nano-ZnO .....111

**Figure 6.59** 3D surface topography images of the studied LZBS samples crystallized at 850 °C with the addition of a) 0.5 wt.%, b)1.0 wt.%, c) 2.5 wt.%, and d) 5.0 wt.% nano-ZnO .....111

# LIST OF TABLES


**Table 2.1** Functions of different oxide constituents in glass-ceramic sealants 9

**Table 5.1** The codes and contents of the samples with nano-CuO .....54

**Table 5.2** The codes and contents of the samples with nano-ZnO.....55

**Table 6.1** Chemical composition of the studied system.....61

**Table 6.2** Kinetic Parameters derived from the Kissinger Equation.....72

**Table 6.3** Surface roughness amplitude parameters of the nano-CuO incorporated samples.....113

**Table 6.4** Surface roughness amplitude parameters of the nano-ZnO incorporated samples.....115

**Table 6.5** Optical tensiometer analysis results of the nano-CuO incorporated samples.....117

**Table 6.6** Approximate surface tension calculation results of the the nano-CuO incorporated samples.....118

**Table 6.8** Optical tensiometer analysis results of the nano-ZnO incorporated samples.....120

**Table 6.9** Approximate surface tension calculation results of the nano-ZnO incorporated samples.....120

# ABSTRACT

## Investigation of Crystallization Effect on Surface Tension of Nanoparticle Embedded Borosilicate Glass-Ceramic Coatings

Nurullah ÇÖPOĞLU

Department of Metallurgical and Materials Engineering

Doctor of Philosophy Thesis

Supervisor: Assoc. Prof. Dr. Buğra ÇİÇEK

Glass-ceramic coatings, integrating the advantageous properties of glasses and ceramics, play a pivotal role in various industrial applications owing to their superior mechanical strength, thermal stability, chemical durability, and optical characteristics. This research delves into phosphate-containing lithium zinc borosilicate (LZBS) glass-ceramic coatings, specifically enhanced with nano-CuO and nano-ZnO. The primary objective of this study is to investigate the kinetics of the LZSB systems and subsequently influence of nano-CuO and nano-ZnO on the surface characteristics of the LZBS glass-ceramic coatings. Key methods employed include differential thermal analysis (DTA) to determine thermal properties, X-ray diffraction (XRD) for phase identification, scanning electron microscopy (SEM) for microstructural analysis, and contact angle measurements for assessing surface hydrophilicity and tension. The glass-ceramic coating was formulated with a base composition of $Li_2O$-ZnO-$B_2O_3$-$SiO_2$, modified with $P_2O_5$, NiO, and CoO. The glass-ceramic precursor was melted at 1400°C, quenched, and then dried to produce fine glass particles. Nano-CuO (38 nm) and nano-ZnO (30-50 nm) were added in varying concentrations (0.5 to 5.0 wt.%) to study their influence on the coating properties. Hot-stage microscopy revealed the thermal transformation stages of LZBS precursor glass, with sintering starting at 681°C, softening at 722°C, liquid phase transition at 748°C, sphere deformation at 773°C, and complete melting at

782°C. VFT analysis showed viscosity parameters: A = 4122.09, B = 5262.74, and $T_0$ = 691.12. The Kissinger equation determined an activation energy ($E_a$) of 11,362 kJ/mol and a pre-exponential factor (ln(A)) of 7.19, indicating a significant energy barrier for crystallization. X-ray diffraction (XRD) analysis revealed that glass-ceramic coatings with nano-CuO exhibit distinct phase compositions ($SiO_2$, $Li_2ZnSiO_4$, $Li_3PO_4$), with $Li_3PO_4$ intensity increasing at higher temperatures (750°C to 850°C) and up to 2.5 wt% nano-CuO. Nano-ZnO-doped coatings showed enhanced crystallization and phase stability of $Li_2ZnSiO_4$ and $Li_3PO_4$ at varying temperatures (750°C, 800°C, 850°C) and concentrations (0.5, 1.0, 2.5, 5.0 wt%). Optical microscopy confirmed increasing grain size with temperature, with fine-grained structures at 750°C, coarser structures at 800°C, and irregular grains at 850°C. The incorporation of nano-CuO and nano-ZnO significantly enhances ceramic surface wettability, with 0.5 wt% nano-CuO reducing contact angles from 67.04° ± 2.53 to 18.42° ± 2.38 at 750°C, and 0.5 wt% nano-ZnO lowering them to 42.11° ± 2.26, thereby increasing surface tension to 286.62 mN/m for nano-CuO and 257.50 mN/m for nano-ZnO at 850°C. This thesis provides a comprehensive understanding of the sequential multi-stage thermal transformation of LZBS precursor glass, from sintering initiation to complete melting.

**Keywords:** Glass-ceramic coating, lithium zinc borosilicate, crystallization, nano-CuO, nano-ZnO, contact angle

# ÖZET

## Nanopartikül İçeren Borosilikat Cam Seramik Kaplamalarının Yüzey Gerilimi Üzerindeki Kristalleşme Etkisinin İncelenmesi

Nurullah ÇÖPOĞLU

Metalurji ve Malzeme Mühendisliği Anabilim Dalı
Doktora Tezi

Danışman: Doç. Dr. Buğra ÇİÇEK

Cam ve seramiğin avantajlı özelliklerini birleştiren cam-seramik kaplamalar, üstün mekanik mukavemet, termal kararlılık, kimyasal dayanıklılık ve optik özellikleri sayesinde çeşitli endüstriyel uygulamalarda önemli bir rol oynamaktadır. Bu araştırma, özellikle nano-CuO ve nano-ZnO ile güçlendirilmiş fosfat içeren lityum çinko borosilikat (LZBS) cam-seramik kaplamaları incelemektedir. Çalışmanın ana amacı, LZSB cam-seramiklerinin kristalizasyon kinetiğini arastırmak ve sonrasında nano-CuO ve nano-ZnO katkılarının bu cam-seramik kaplamaların yüzey özellikleri üzerindeki etkisini araştırmaktır. Kullanılan temel yöntemler arasında termal özellikleri belirlemek için diferansiyel termal analiz (DTA), faz tanımlaması için X-ışını difraksiyonu (XRD), mikroyapısal analiz için taramalı elektron mikroskobu (SEM) ve yüzey hidrofiliği ve gerilimini değerlendirmek için temas açısı ölçümleri bulunmaktadır. Cam-seramik kaplama, $P_2O_5$, NiO ve CoO ile modifiye edilmiş $Li_2O$-ZnO-$B_2O_3$-$SiO_2$ baz bileşimi ile formüle edilmiştir. Cam-seramik öncüsü 1400°C'de eritilmiş, soğutulmuş ve ardından ince cam parçacıkları üretmek için kurutulmuştur. Kaplama özelliklerini incelemek için çeşitli konsantrasyonlarda (0.5 ila 5.0 wt.%) nano-CuO (38 nm) ve nano-ZnO (30-50 nm) eklenmiştir. Isı mikroskobu, LZBS öncül camının termal dönüşüm aşamalarını ortaya koymuştur: sinterleme 681°C'de başlamış, yumuşama 722°C'de, sıvı faz geçişi 748°C'de, küre deformasyonu 773°C'de ve tam erime 782°C'de gerçekleşmiştir. VFT analizi viskozite parametrelerini göstermiştir: A = 4122.09, B

= 5262.74 ve T0 = 691.12. Kissinger denklemi, kristalizasyon için önemli bir enerji bariyerine işaret eden 11,362 kJ/mol aktivasyon enerjisi ($E_a$) ve 7.19 doğal logaritma (ln(A)) ön-eksponensiyel faktörünü belirlemiştir. X-ışını difraksiyonu (XRD) analizi, nano-CuO içeren cam-seramik kaplamaların belirgin faz kompozisyonları ($SiO_2$, $Li_2ZnSiO_4$, $Li_3PO_4$) sergilediğini, $Li_3PO_4$ yoğunluğunun daha yüksek sıcaklıklarda (750°C'den 850°C'ye) ve %2.5 nano-CuO'ya kadar arttığını ortaya koymuştur. Nano-ZnO ile katkılanmış kaplamalar, çeşitli sıcaklıklar (750°C, 800°C, 850°C) ve konsantrasyonlarda (0.5, 1.0, 2.5, 5.0 wt%) $Li_2ZnSiO_4$ ve $Li_3PO_4$'ün kristalizasyonunu ve faz kararlılığını artırmıştır. Optik mikroskop, sıcaklıkla artan tane boyutunu doğrulamış, 750°C'de ince taneli yapılar, 800°C'de daha kaba yapılar ve 850°C'de düzensiz taneler gözlemlenmiştir. Nano-CuO ve nano-ZnO ilavesi, cam-seramik yüzeylerin ıslanabilirliğini önemli ölçüde artırmaktadır; %0.5 nano-CuO, temas açılarını 750°C'de 67.04° ± 2.53'ten 18.42° ± 2.38'e düşürürken, %0.5 nano-ZnO temas açısını 42.11° ± 2.26'ya indirmekte ve yüzey gerilimini 850°C'de nano-CuO için 286.62 mN/m'ye, nano-ZnO için ise 257.50 mN/m'ye yükseltmektedir. Bu tez, LZBS öncül camının sinterleme başlangıcından tam ergimeye kadar olan ardışık çok aşamalı termal dönüşümünün kapsamlı bir şekilde anlaşılmasını sağlamaktadır.

**Anahtar Kelimeler:** Cam-seramik kaplama, lityum çinko borosilikat, kristalizasyon, nano-CuO, nano-ZnO, temas açısı

# 1
# INTRODUCTION

## 1.1 Background and Motivation

Glass-ceramic coatings represent a technologically significant class of materials that synergistically employ the advantageous attributes of glasses and ceramics when applied to steel substrates [1-3]. These multifunctional coatings are engineered through a meticulously controlled crystallization process, wherein a glassy precursor transforms a semi-crystalline structure upon the substrate [4, 5]. Characterized by their robust mechanical strength [5], superior thermal stability [4], pronounced chemical durability[6], and visually appealing optical properties [7], glass-ceramic coatings find pivotal applications across diverse sectors, including but not limited to protective coatings, biomedical implants, electronic components, and optical instruments [8, 9].

Within the spectrum of glass-ceramic systems, phosphate-containing lithium zinc borosilicate glasses are of particular interest [10, 11]. This subset of glasses distinguishes itself through a unique amalgamation of attributes, including exceptional chemical durability—a crucial trait for resisting corrosive environments — and thermal resilience that withstands elevated temperatures without notable deterioration [12, 13]. Furthermore, these transparent glasses can be effectively doped with luminescent elements, rendering them highly suitable for photonics applications[14, 15].

The impetus for advancing the properties of phosphate-containing lithium zinc borosilicate glass-ceramic coatings is driven by the escalating demands of cutting-edge technological applications [13, 16]. A strategic avenue to enhance these properties involves the integration of nanoparticles [17, 18]. Owing to their immense surface-to-volume ratio and distinctive physicochemical characteristics, nanoparticles can profoundly modify the mechanical and functional traits of the base material. Notably, nanoparticles are observed to bolster the performance of glass-ceramic coatings significantly[16, 19, 20].

Nano-CuO is distinguished for its remarkable thermal conductivity, inherent antibacterial properties, and catalytic efficiency [21 - 23]. Its inclusion in glass-ceramic coatings can enhance thermal management features, facilitating more efficient heat dissipation—a critical factor in numerous application scenarios [24]. Additionally, nano-CuO can influence the crystallization dynamics within the coatings, encouraging the development of preferred crystalline phases that improve mechanical robustness [25, 26].

Conversely, nano-ZnO stands out due to its robust UV absorption capacity, antibacterial prowess, and piezoelectric properties [27 - 29]. The integration of nano-ZnO into glass-ceramic coatings can elevate their optical performance by providing effective UV shielding, an advantageous feature for protective coatings in outdoor settings [30 - 32]. Moreover, nano-ZnO can modify the crystallization kinetics and augment surface characteristics such as roughness and hydrophilicity, which are vital for tailored wettability in specific applications [33, 34].

The crystallization behavior within these materials is a critical determinant of their final properties. Controlled crystallization can result in the emergence of specific crystalline phases that present desired mechanical and thermal characteristics upon the coatings. However, the introduction of nanoparticles leads to complexity by generating additional nucleation sites and altering the energetic thresholds required for crystal growth. A thorough comprehension of how nano-CuO and nano-ZnO affect these crystallization kinetics is paramount for optimizing the fabrication processes of glass-ceramic coatings [25, 33, 35 - 37].

Surface characteristics, encompassing aspects like roughness, texture, and hydrophilicity, are fundamental in defining the operational efficacy of glass-ceramic coatings [38, 39]. For instance, surface roughness can significantly influence cellular adhesion and proliferation in biomedical contexts [40]. In protective coatings, surface texture contributes to wear and corrosion resistance [41]. The integration of nanoparticles such as nano-CuO and nano-ZnO can substantially transform these surface parameters [42]. Nano-CuO, for instance, can refine inter-crystal spacing and enhance surface texture, thus reducing roughness [43]. Conversely, nano-ZnO can boost surface hydrophilicity, thereby enhancing

the coating's wettability—an essential trait for applications demanding high water spreadability [44].

Surface tension is another critical factor influenced by nanoparticle addition, impacting the wetting behaviors crucial for a range of applications from liquid coatings to biomedical implants [45]. By altering the surface energy, nano-CuO and nano-ZnO modify the contact angles and surface tension, offering insights that could guide the design of coatings with modified surface properties tailored for specific applications [46, 47].

This study endeavors to conduct an exhaustive investigation into the effects of nano-CuO and nano-ZnO on the surface attributes, surface tension, and overall surface properties of phosphate-containing lithium zinc borosilicate glass-ceramic coatings in different crystallization temperatures. Utilizing a comprehensive suite of analytical techniques, including thermal analysis, structural characterization, and surface attribute assessments, this research aims to elucidate the nuanced roles of nanoparticles in tailoring the attributes of glass-ceramic coatings. The anticipated outcomes of this study are poised to substantially contribute to the development of advanced glass-ceramic coatings, thereby enhancing their performance across a numerous of industrial applications.

## 1.2 Objectives of the Study

The objectives of this study are meticulously designed to address key aspects of the interaction between nanoparticles and glass-ceramic coatings. These objectives focus on understanding the fundamental changes induced by nano-CuO and nano-ZnO additions in phosphate-containing lithium zinc borosilicate glass-ceramic systems. The comprehensive nature of these objectives reflects the multi-faceted approach required to advance the field of glass-ceramic materials.

The primary objective of this study is to investigate the crystallization kinetics parameters of phosphate-containing lithium zinc borosilicate glass-ceramic coatings. Crystallization represents a crucial phase transformation that dictates the microstructure and, consequently, the macroscopic properties of glass-ceramics. Given the paucity of studies in the existing literature, this investigation will be conducted with exceptional focus and rigor. Differential thermal analysis (DTA)

will be employed to ascertain the glass transition temperature (Tg), the crystallization onset temperature (Tc), and the overall crystallization behavior. Additionally, the Johnson-Mehl-Avrami-Kolmogorov (JMAK) model will be utilized to determine the activation energy (Ea) of the reaction kinetics.

The second objective aims to analyze how the addition of nano-CuO and nano-ZnO affects the surface attributes of the glass-ceramic coatings. Surface attributes, including topograph, roughness, texture, are crucial for the performance of coatings in various applications, such as corrosion resistance, wear resistance, and biomedical compatibility. Surface roughness and texture will be examined using automated digital microscope. Additionally, 3D surface profilometry will be employed to provide a detailed analysis of the surface topography.

The third objective focuses on measuring and evaluating the hydrophilicity and surface tension of the glass-ceramic coatings, both with and without the addition of nano-CuO and nano-ZnO. Surface tension influences the wetting behavior, adhesion, and overall surface energy, which are critical for coating applications. Surface tension will be measured using the pendant drop method, where the shape of a droplet is analyzed to determine the surface tension. Contact angle goniometry will also be used to correlate surface tension with wettability.

The fourth objective is to establish a clear correlation between the increase in crystallization temperature and the resultant surface properties when nano-CuO and nano-ZnO are added to the glass-ceramic coatings. This correlation is essential for optimizing the material properties for specific applications. This will involve a comparative analysis of the data obtained from thermal analysis, structural characterization, and surface property evaluations.

In summary, these objectives are designed to provide a holistic understanding of the effects of nano-CuO and nano-ZnO additions on phosphate-containing lithium zinc borosilicate glass-ceramic coatings. By systematically investigating the crystallization process, surface properties, and their interrelationships, this study aims to advance the material science of glass-ceramics and open new avenues for their application in high-performance environments.

## 1.3 Research Hypotheses

This research focuses on investigating the crystallization kinetics of phosphate-containing lithium zinc borosilicate glass-ceramic coatings. The study specifically examines the impact of different crystallization temperatures on this system, including the influence of nano-CuO and nano-ZnO additions. The research is based on the following hypotheses:

The primary hypothesis posits that the crystallization kinetics of phosphate-containing lithium zinc borosilicate glass-ceramic coatings can be accurately characterized. This involves determining key kinetic parameters, such as the activation energy for crystallization, and understanding the nucleation and growth mechanisms of the crystalline phases. It is hypothesized that the activation energy for crystallization can be quantified, providing insights into the energy barriers involved in the crystallization process. This parameter is crucial for predicting how the system behaves under different thermal conditions.

The second hypothesis asserts that the addition of nano-CuO and nano-ZnO will influence the crystallization properties of the glass-ceramic coatings. These nanoparticles are expected to act as nucleation sites, thereby modifying the crystallization behavior. It is hypothesized that the presence of nano-CuO and nano-ZnO will lower the activation energy required for crystallization. This reduction is anticipated because nanoparticles can facilitate nucleation by providing additional sites for crystal formation.

The third hypothesis focuses on the formation of specific crystalline phases in the presence of nano-CuO and nano-ZnO at different crystallization temperatures. The emergence and stabilization of these phases are critical for the final properties of the glass-ceramic coatings. It is hypothesized that nano-CuO and nano-ZnO will promote the formation of specific crystalline phases such as $Li_2ZnSiO_4$ and $Li_3PO_4$. The presence of these nanoparticles is expected to enhance the nucleation of these phases, resulting in improved mechanical and thermal properties of the coatings. By testing these hypotheses, the study aims to provide a comprehensive understanding of the crystallization kinetics of phosphate-containing lithium zinc borosilicate glass-ceramic coatings, including the impact of nano-CuO and nano-ZnO additions. The findings will contribute to the optimization of the crystallization process, enhancing the material properties for various studies and applications.

## 1.4 Scope and Limitations

This thesis is dedicated to the comprehensive investigation of phosphate-containing lithium zinc borosilicate glass-ceramic coatings, with a particular focus on the addition of nano-CuO and nano-ZnO. The primary aim is to elucidate the effect of nanoparticles and the resultant properties of these coatings when subjected to different crystallization temperatures.

The study involves the synthesis of glass-ceramic coatings incorporating varying concentrations of nano-CuO and nano-ZnO. Ensuring homogeneous dispersion of nanoparticles within the glass matrix is crucial for accurately assessing their impact on the crystallization process. Differential thermal analysis (DTA) will be employed to determine critical thermal properties such as the glass transition temperature (Tg), and peak crystallization temperature (Tp). These analyses are essential for understanding the thermal stability of the glass-ceramic system and the influence of nanoparticles on crystallization behavior at increasing crystallization temperatures.

Structural characterization will be conducted using X-ray diffraction (XRD) to identify and quantify the crystalline phases formed during the crystallization process. Scanning electron microscopy (SEM) will provide detailed images of the microstructure, allowing for the evaluation of the morphology and distribution of crystalline phases induced by the nanoparticles. Evaluating surface properties, such as roughness, texture, and hydrophilicity, will be crucial for optimizing the coatings for specific applications. Techniques including SEM, surface topography, and contact angle measurements will be used to provide a comprehensive evaluation of these properties. Additionally, surface tension will be measured using methods such as the pendant drop technique and contact angle goniometry to explore its relationship with nanoparticle addition. Lower surface tension can enhance the applicability of the coatings by improving their wettability and adhesion properties.

The study is limited by the specific composition of the glass-ceramic matrix used. The research focuses on phosphate-containing lithium zinc borosilicate glass, and the findings may not be directly applicable to other glass compositions with different chemical formulations. Furthermore, only nano-CuO and nano-ZnO are investigated in this study. The effects observed with these nanoparticles may differ

from those of other types of nanoparticles, which might possess different physical and chemical characteristics.

Results are specific to the experimental conditions and methods employed in this study. Variations in experimental parameters, such as annealing temperatures, crystallization temperatures, heating rates, and environmental conditions, might lead to different outcomes. The research is conducted on a laboratory scale, which may not fully replicate the conditions encountered in industrial applications. Scaling up the process for industrial use could introduce additional variables and challenges that are beyond the scope of this study.

The accuracy and precision of the measurement techniques used, such as DTA, XRD, SEM, surface topography, and contact angle measurements, may have inherent limitations. These limitations can affect the reproducibility and generalizability of the results. By delineating these scope and limitations, this thesis provides a clear framework for understanding the crystallization kinetics and surface properties of phosphate-containing lithium zinc borosilicate glass-ceramic coatings with nanoparticle additions. The insights gained from this research will contribute significantly to the field of materials science, offering potential pathways for the development of advanced glass-ceramic coatings with tailored properties for a variety of industrial applications.

# 2
# GLASS-CERAMIC COATINGS

## 2.1 Composition of Glass-Ceramic Coatings

Glass-ceramic coatings are sophisticated materials synthesized through a controlled crystallization process, converting a parent glass into a partially crystalline material. The composition of these coatings is critical, as it dictates the distribution and properties of the resulting crystalline phases and the residual glass matrix [48, 49]. The primary components of glass-ceramic coatings include network formers, network modifiers, and intermediate oxides, each contributing to the final material properties through specific mechanisms [50, 51]. Table 2.1 shows the functions of different oxide constituents in glass-ceramic sealants.

Network formers are the fundamental building blocks of the glass matrix, creating a continuous three-dimensional network through strong covalent bonds. Common network formers include silicon dioxide ($SiO_2$), boron trioxide ($B_2O_3$), and phosphorous pentoxide ($P_2O_5$) [48]. $SiO_2$ is the most prevalent network former in many glass-ceramic systems due to its ability to form a robust tetrahedral network of $SiO_4$ units linked by shared oxygen atoms. This structure provides high chemical durability and thermal stability [52]. The rigidity and high bond dissociation energy of Si-O bonds contribute to a high melting point and low thermal expansion coefficient, which enhances the thermal stability and resistance to thermal shock in glass-ceramic coatings [53].

Boron trioxide ($B_2O_3$) is often used to create borosilicate glasses, which are known for their low thermal expansion and high resistance to thermal shock. The borate network can exist in both trigonal ($BO_3$) and tetrahedral ($BO_4$) configurations, depending on the presence of modifiers and the glass composition. The flexibility of the borate network allows for easier processing and lower melting temperatures, while still maintaining good chemical durability and mechanical strength [53]. Phosphorous pentoxide ($P_2O_5$) forms a phosphate network with $PO_4$ tetrahedra, which can provide high ionic conductivity and unique optical properties. Phosphate glasses are less rigid than silicate glasses due to the weaker P-O bonds compared to

Si-O bonds. This results in higher thermal expansion coefficients and lower melting points, which can be advantageous for specific applications such as solid electrolytes and optical devices [54, 55]. Network modifiers are introduced to disrupt the continuous network of the network formers, creating non-bridging oxygens (NBOs) that alter the physical and chemical properties of the glass-ceramic. Common network modifiers include alkali oxides (e.g., $Na_2O$, $K_2O$) and alkaline earth oxides (e.g., CaO, MgO).

**Table 2.1** Functions of different oxide constituents in glass-ceramic sealants [56]

| **Glass constituent** | **Oxide** | **Function** |
|---|---|---|
| Network former | $SiO_2$, $B_2O_3$ | Form glass network<br>Determine Tg and Ts<br>Determine thermal expansion coefficient<br>Determine adhesion/wetting with other SOFC/SOEC components |
| Network modifier | $Li_2O$, $Na_2O$, $K_2O$ | Maintain charge neutrality<br>Create non-bridging oxygen species |
| | BaO, SrO, CaO, MgO | Modify glass properties such as Tg, Ts, and thermal expansion coefficient |
| Intermediate | $Al_2O_3$, $Ga_2O_3$ | Hinder devitrification<br>Modify glass viscosity |
| Additive | $La_2O_3$, $Nd_2O_3$, $Y_2O_3$ | Modify glass viscosity<br>Increase thermal expansion coefficient |
| | ZnO, PbO | Improve glass flowability |
| | NiO, CuO, CoO, MnO $Cr_2O_3$, $V_2O_5$ | Improve seal glass adhesion to other cell components |
| | $TiO_2$, $ZrO_2$ | Induce devitrification |

Alkali oxides ($Na_2O$, $K_2O$, etc.) disrupt the network structure by breaking Si-O-Si or B-O-B bonds and creating NBOs. This disruption lowers the melting temperature and increases the ionic mobility, enhancing properties like ionic conductivity. The

presence of NBOs weakens the overall network, making the glass-ceramic more pliable and easier to process at lower temperatures [57, 58].

Alkaline earth oxides (CaO, MgO, etc.) can act as both network modifiers and intermediate oxides, depending on their concentration and the overall composition of the glass. They can introduce additional cross-links within the glass structure, increasing the connectivity of the network. This enhances the mechanical properties, such as hardness and strength, by reinforcing the glass matrix and making it more resistant to deformation and wear. Additionally, these oxides can improve chemical durability by stabilizing the network against attack from corrosive agents [59, 60].

Intermediate oxides, such as aluminum oxide ($Al_2O_3$), play a versatile role in glass-ceramic coatings. They can function both as network formers and modifiers, depending on the surrounding chemical environment. $Al_2O_3$ can enhance the structural integrity of the glass network by acting as a network former and increasing the viscosity of the glass melt. This increased viscosity aids in controlling the crystallization process, ensuring a uniform distribution of crystalline phases [61]. $Al_2O_3$ can enter the glass network as $AlO_4$ tetrahedra, contributing to network connectivity and improving mechanical properties such as hardness and toughness. The presence of $Al_2O_3$ also enhances chemical durability by reducing the solubility of the glass in aqueous and acidic environments [62, 63].

The precise composition of glass-ceramic coatings is meticulously designed to achieve specific thermal, mechanical, and chemical properties. By manipulating the proportions of network formers, modifiers, and intermediate oxides, the properties of the glass-ceramic can be tailored to meet particular application requirements [64, 65].

The incorporation of $SiO_2$ and $B_2O_3$ helps achieve low thermal expansion and high resistance to thermal shock. The strong Si-O bonds provide a high melting point and low coefficient of thermal expansion (CTE), while the flexibility of the borate network allows for absorption of thermal stress without cracking [66, 67].

The addition of $Al_2O_3$ and alkaline earth oxides such as CaO and MgO enhances the mechanical properties by increasing the cross-link density of the glass network.

This reinforcement improves the hardness and fracture toughness of the glass-ceramic, making it more resistant to mechanical wear and impact [68].

The presence of $SiO_2$, $P_2O_5$, and CaO enhances the chemical resistance of the glass-ceramic. $SiO_2$ provides a stable network that is resistant to acid and base attack, while $P_2O_5$ and CaO contribute to the formation of chemically stable crystalline phases during the heat treatment process. This ensures that the coatings can withstand prolonged exposure to corrosive environments without significant degradation [69, 70].

The optical characteristics of glass-ceramic coatings can be tailored by adjusting the composition to include oxides that affect light transmission and refractive index. For instance, the inclusion of $P_2O_5$ can improve optical clarity and provide specific refractive properties that are useful in optical devices [71].

In summary, the composition of glass-ceramic coatings is a critical factor that determines their overall performance. By carefully selecting and balancing the various network formers, modifiers, and intermediate oxides, the properties of the glass-ceramic can be optimized for a wide range of applications. The controlled crystallization process, guided by this precise composition, enables the development of advanced glass-ceramic coatings with tailored properties that meet the stringent demands of industrial applications.

## 2.2 Properties of Glass-Ceramic Coatings

The unique properties of glass-ceramic coatings stem from their dual-phase structure, which comprises both amorphous and crystalline phases. This combination leverages the advantages of both glasses and ceramics, resulting in a material with superior performance characteristics that are unattainable with either phase alone. The primary properties of glass-ceramic coatings include mechanical strength, thermal stability, chemical durability, optical clarity, and tailored surface characteristics. These properties are deeply rooted in the materials science, chemistry, and physics underlying the formation and structure of glass-ceramics.

### 2.2.1 Mechanical Properties

Glass-ceramic coatings are renowned for their exceptional mechanical properties, including high hardness, strength, and fracture toughness. These properties arise

from the controlled crystallization process that forms fine, interlocking crystalline phases within the amorphous glass matrix. The crystalline phases, typically more rigid and harder than the amorphous phase, serve to reinforce the glass network [72, 73].

The hardness of glass-ceramic coatings is significantly enhanced by the presence of crystalline phases such as spinels, garnets, and other complex oxides. These phases disrupt the amorphous network, creating regions of high stiffness that resist indentation and abrasion. Hardness is quantitatively measured using techniques such as Vickers or Knoop hardness tests, which assess the material's resistance to localized plastic deformation [74, 75].

The interlocking nature of crystalline phases within the glass matrix contributes to the material's overall strength and toughness. The crystalline inclusions act as barriers to crack propagation, increasing the energy required for cracks to advance. This mechanism, known as crack bridging or crack deflection, enhances the fracture toughness of the material, making it more resilient to mechanical stress and impact. The flexural strength and fracture toughness are often evaluated through three-point bending tests and fracture mechanics analyses [76].

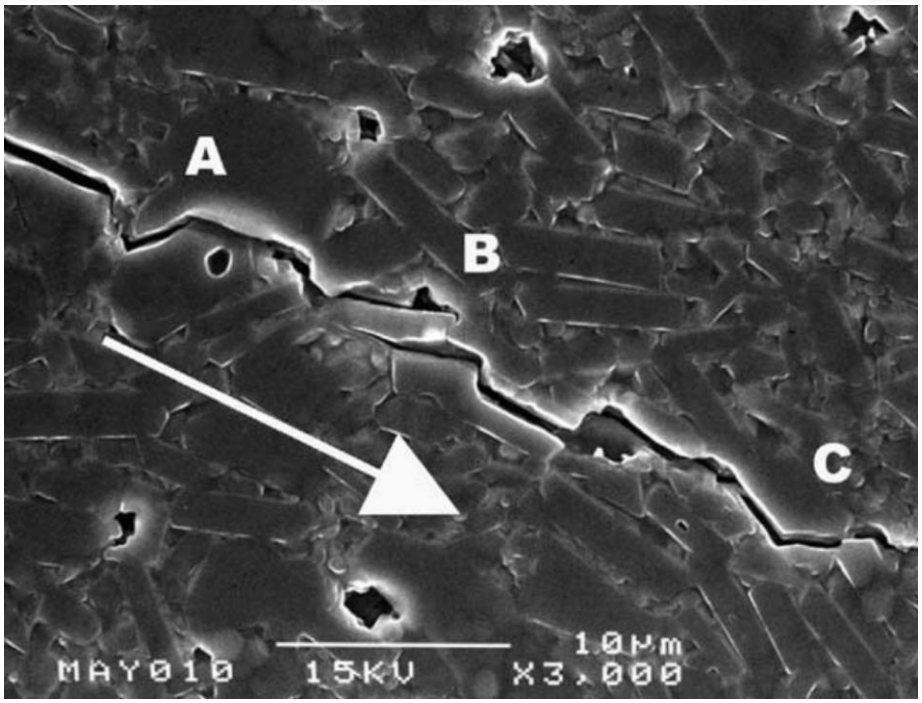



**Figure 2.1** The arrow indicates the direction of the crack; several toughening mechanisms are recognizable, such as pull-out of the grains (A), bridging (B), crack deflection (C) [76].

### 2.2.2 Thermal Properties

Glass-ceramic coatings exhibit outstanding thermal properties, including low thermal expansion, high thermal conductivity, and excellent resistance to thermal shock. These attributes are crucial for applications involving extreme temperature variations. The low thermal expansion coefficient (CTE) of glass-ceramics is primarily due to the crystalline phases, which often have lower CTEs compared to the amorphous glass matrix. Materials such as β-quartz and β-eucryptite exhibit negative or near-zero thermal expansion, counteracting the expansion of the glass matrix and minimizing overall dimensional changes with temperature fluctuations. The CTE is measured using dilatometry, which tracks the dimensional changes of a material as it is heated or cooled [76].

High thermal conductivity in glass-ceramic coatings ensures efficient heat dissipation, which is vital for thermal barrier coatings in aerospace and industrial applications. The crystalline phases, which have well-ordered atomic structures, facilitate phonon transport, thereby enhancing thermal conductivity. This property is assessed using techniques such as laser flash analysis or steady-state heat flow methods [75]. The combination of low CTE and high thermal conductivity grants glass-ceramic coatings excellent resistance to thermal shock. They can endure rapid temperature changes without cracking or spalling, making them suitable for environments where materials are subjected to sudden heating or cooling [77].

### 2.2.3 Chemical Durability

The chemical durability of glass-ceramic coatings is a result of their dense and inert crystalline phases, which protect against chemical attack. This makes them ideal for use in corrosive environments, such as chemical processing plants and biomedical implants. The crystalline phases in glass-ceramics, such as aluminosilicates and phosphates, are chemically stable and resist dissolution or reaction with acids, bases, and other corrosive agents. This property is critical for maintaining the integrity of coatings in harsh environments. Chemical durability is typically assessed through immersion tests in various chemical solutions, followed by measurements of weight loss and surface analysis using techniques like X-ray photoelectron spectroscopy (XPS) [78, 79]. The incorporation of chemically stable phases ensures long-term durability, reducing maintenance and replacement costs.

The glass matrix itself can also contribute to chemical durability by forming a passivating layer that inhibits further attack [80].

### 2.2.4 Optical Properties

Certain glass-ceramic coatings can be engineered to possess desirable optical properties, such as transparency, refractive index control, and light transmission. These properties are essential for optoelectronic applications, including lenses, optical fibers, and display technologies. The transparency of glass-ceramics depends on the size and distribution of crystalline phases. When the crystalline phases are smaller than the wavelength of visible light (typically less than 400 nm), the material can remain transparent. This is achieved through careful control of the crystallization process to ensure the formation of nanocrystalline phases. The optical clarity is assessed using spectrophotometry to measure the transmission and absorption of light through the material [81, 82]. Figure 2.2 shows the XRD phase formation, the observed effective refractive index change, and its direct association with the crystallization process in the glass-ceramic formation process.

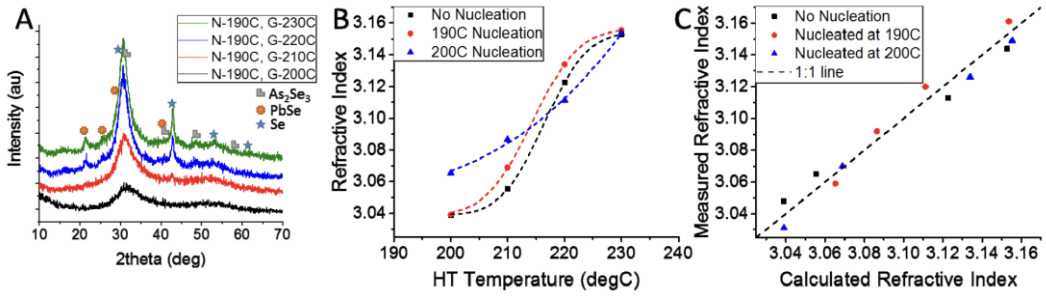



**Figure 2.2** (A) Representative XRD spectra for the 154540 GAP-Se glass following nucleation at 190°C, with furnace HT at temperatures shown for 30 min. (B) Measured refractive index (λ = 4.515 μm) versus growth temperature for various nucleation temperatures. (C) Measured (experimental) refractive index values obtained as a function of HT temperature, as compared to calculated refractive index based on volume fraction of crystal phase formed from XRD spectra [82]

The refractive index of glass-ceramics can be tailored by adjusting the composition and crystallization process. The presence of high-refractive-index phases, such as titanates or niobates, can enhance the refractive index, making these materials suitable for high-performance optical applications. Ellipsometry and refractometry

are used to measure the refractive index and its uniformity across the coating [83 - 85].

### 2.2.5 Surface Properties

The surface properties of glass-ceramic coatings, including roughness, texture, and wettability, are critical for their functional performance. These properties can be precisely controlled through the crystallization process to meet specific application requirements. The surface roughness and texture of glass-ceramic coatings are influenced by the size and distribution of crystalline phases on the surface. Smoother surfaces reduce friction and wear, making them suitable for applications such as sliding bearings or biomedical implants. Conversely, textured surfaces can enhance adhesion or increase surface area for catalytic applications. Surface roughness is quantitatively measured using profilometry or atomic force microscopy (AFM), which provide detailed topographical maps of the surface [86, 87].

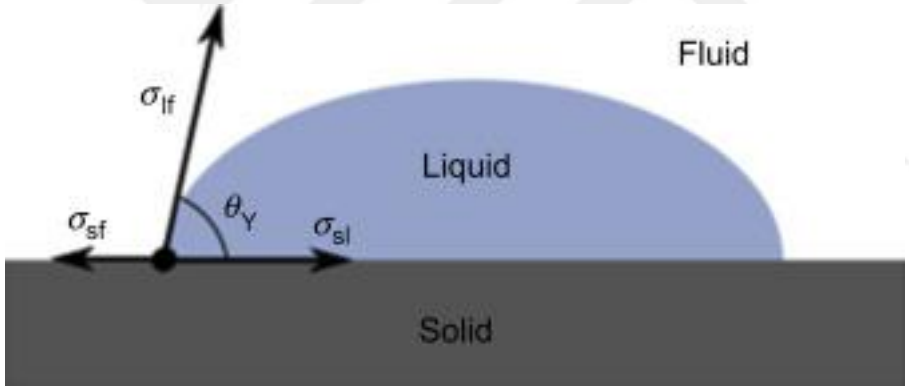



**Figure 2.3** Measurement of the contact angle of a three-phase system [88]

The wettability of glass-ceramic surfaces, characterized by the contact angle of a liquid droplet on the surface, is influenced by surface chemistry and roughness. Hydrophilic surfaces, with low contact angles, improve the spreadability of liquids, which is beneficial for coatings in biomedical or self-cleaning applications. Wettability is measured using contact angle goniometry, which quantifies the angle formed between a liquid droplet and the solid surface [89, 90]. Figure 2.3 shows the contact angle measurement basics.

In conclusion, the dual-phase structure of glass-ceramic coatings, comprising both amorphous and crystalline phases, imparts a unique combination of mechanical,

thermal, chemical, optical, and surface properties. These properties are finely tuned through the controlled crystallization process, enabling the development of advanced materials that meet the rigorous demands of various industrial applications. By leveraging the principles of materials science, chemistry, and physics, researchers can design glass-ceramic coatings with tailored properties for optimal performance in specific environments [91, 92].

## 2.3 Crystallization Process and Kinetics

The controlled crystallization process is fundamental to the development of glass-ceramic coatings, as it determines the formation and distribution of crystalline phases within the amorphous glass matrix. This process is typically divided into two main stages: nucleation and growth. Understanding and controlling these stages are essential for optimizing the properties of glass-ceramic coatings.

### 2.3.1 Nucleation

Nucleation is the initial stage of crystallization, where small, stable clusters of atoms or molecules, known as nuclei, form within the amorphous glass matrix. Figure 2.4 shows the crystallization processes of glass-ceramics.

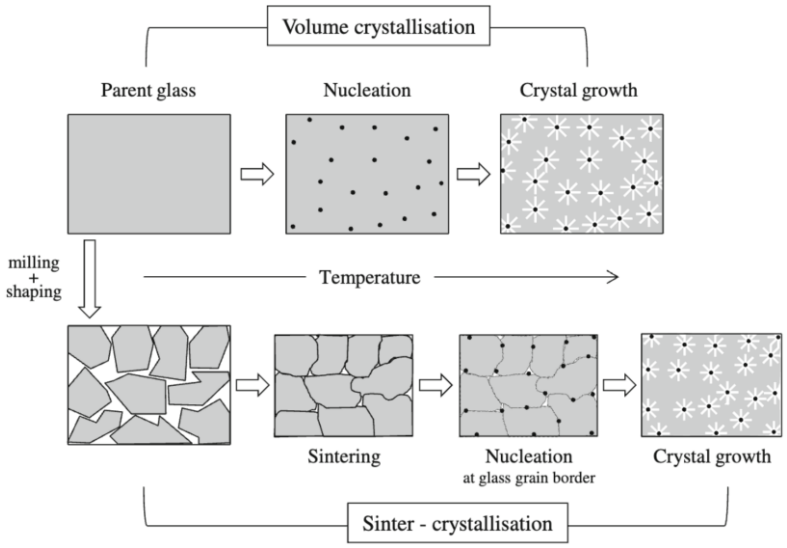



**Figure 2.4** Evolution of the microstructure from glass to glass–ceramic through volume crystallisation from a bulk glass or sinter-crystallisation [93]

The rate of nucleation is a critical factor in determining the final microstructure of the glass-ceramic and is influenced by several parameters. The chemical

composition of the glass plays a crucial role in nucleation. Certain components, such as $P_2O_5$ and $B_2O_3$, can enhance nucleation by lowering the activation energy required for nucleation to occur. This is because these components can act as nucleating agents or create conditions conducive to nucleation. The presence of specific ions or molecular groups in the glass can also promote nucleation by providing sites where nucleation can preferentially occur [92, 94].

The addition of nucleating agents, such as $TiO_2$, $ZrO_2$, or nano-particles, can significantly increase the nucleation rate. These agents act as heterogeneous nucleation sites, lowering the energy barrier for nucleation and facilitating the formation of nuclei. The effectiveness of these nucleating agents depends on their size, distribution, and chemical compatibility with the glass matrix [95, 96].

The temperature and duration of the heat treatment are critical parameters that influence nucleation. Typically, nucleation occurs at a temperature below the glass transition temperature ($T_g$) but above the fictive temperature of the glass. The nucleation rate follows an Arrhenius-type behavior, where an increase in temperature can exponentially increase the rate up to a certain point. Controlled heating and cooling rates are employed to maximize the nucleation rate while preventing premature growth of the nuclei [97, 98].

Efficient nucleation is essential for achieving a fine and uniform distribution of crystalline phases within the glass matrix. A high nucleation rate results in a large number of small, evenly distributed nuclei, which are necessary for developing a microstructure that enhances the mechanical and thermal properties of the glass-ceramic coating [99].

### 2.3.2 Growth

Following nucleation, the nuclei grow into larger crystalline phases during the subsequent heat treatment. The growth rate of these nuclei is influenced by the thermal profile and the mobility of ions within the glass matrix. The growth stage typically occurs at temperatures higher than the nucleation temperature. The thermal profile, including the maximum temperature reached and the duration of the heat treatment, determines the growth rate of the crystalline phases. Higher temperatures generally increase the atomic mobility, allowing ions to migrate more freely and contribute to crystal growth. However, excessively high temperatures

can lead to unwanted coarsening of the crystalline phases, which can negatively affect the properties of the glass-ceramic [100, 101].

The mobility of ions within the glass matrix is a function of temperature and the viscosity of the glass. As the temperature increases, the viscosity decreases, enhancing the diffusion of ions necessary for crystal growth. The presence of certain network modifiers, such as alkali and alkaline earth oxides, can further reduce the viscosity and facilitate ion mobility. This ion migration is crucial for the incorporation of atoms into the growing crystalline lattice, leading to the expansion of the crystalline phases [102, 103]. Figure 2.5 illustrates microceramics and nanoceramics from nucleus during growth.

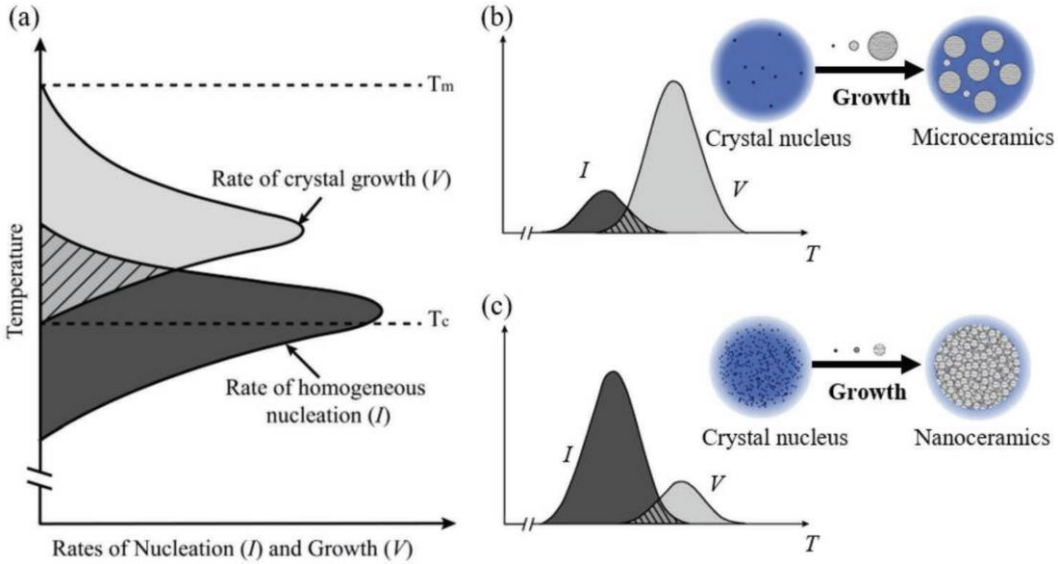



**Figure 2.5** This schematic model illustrates the strategy for controlling the crystallization habit of glass. Graph a) shows the classical curves of the temperature-dependent nucleation and growth rate. Graphs b) and c) demonstrate how reshaping the crystallization rate curves by suppressing or enhancing the nucleation rate can lead to microcrystallization (b) or nanocrystallization (c), respectively [104].

The type and amount of crystalline phases formed during growth are determined by the glass composition and the thermal treatment parameters. Phases such as silicates, phosphates, or other complex oxides can form depending on the specific components in the glass. The crystallization kinetics must be carefully controlled to ensure the desired phases are produced in the right proportions and distribution

[105, 106]. Controlling the growth process is crucial to ensuring the desired microstructure of the glass-ceramic coating. A well-controlled crystallization process results in coatings with enhanced mechanical strength, thermal stability, and chemical resistance. This is because the size, shape, and distribution of the crystalline phases within the amorphous matrix significantly influence these properties. For example, fine, evenly distributed crystalline phases can act as reinforcement within the glass matrix, improving hardness and fracture toughness. Similarly, a well-defined crystalline structure can enhance thermal conductivity and reduce thermal expansion, leading to better thermal stability [107, 108].

## 2.4 Applications of Glass-Ceramic Coatings

Given their unique combination of properties, glass-ceramic coatings find applications in a wide range of industrial fields. Their ability to combine high mechanical strength, thermal stability, chemical durability, and tailored surface characteristics makes them indispensable in several critical areas.

### 2.4.1 Protective Coatings

Glass-ceramic coatings are extensively used as protective barriers for steel and cast iron substrates, which are commonly employed in environments that are prone to corrosion, wear, and thermal degradation. The high mechanical strength of glass-ceramics, derived from their interlocking crystalline phases, provides exceptional resistance to abrasion and mechanical damage. Additionally, the chemical durability of these coatings, ensured by their dense and inert crystalline structure, protects the underlying metal from corrosive agents [109].

The crystalline phases in glass-ceramic coatings, such as aluminosilicates and phosphates, form a chemically stable barrier that resists penetration by corrosive substances. This is due to the low solubility and high chemical stability of these phases, which are less likely to react with aggressive chemicals compared to amorphous glass. For example, the formation of a dense crystalline aluminosilicate phase can effectively block the diffusion of corrosive species, thereby enhancing the coating's resistance to chemical attack. This makes these coatings ideal for use in chemical processing equipment, where exposure to acids, bases, and other corrosive chemicals is common [110, 111].

The hardness of glass-ceramic coatings provides excellent wear resistance, protecting metal substrates from mechanical erosion and extending the service life of components in industrial machinery and tools. The interlocking crystalline phases act as a reinforcement within the amorphous matrix, distributing applied stresses more evenly and reducing the likelihood of mechanical failure. This property is particularly important in applications where the coatings are subjected to high friction and wear, such as in cutting tools, bearings, and engine components [112, 113].

### 2.4.2 Thermal Barrier Coatings

In aerospace and industrial gas turbine engines, glass-ceramic coatings serve as thermal barriers. These coatings are designed to protect underlying components from the extreme temperatures encountered during operation. The low thermal conductivity of glass-ceramics limits heat transfer, while their high thermal stability ensures that they remain effective even at elevated temperatures [114, 115].

The crystalline phases with low thermal expansion coefficients help to maintain dimensional stability under thermal cycling, preventing thermal stresses and potential failure of the coating. Materials such as β-quartz and β-eucryptite have very low or even negative thermal expansion coefficients, which can counteract the expansion of the glass matrix and minimize overall dimensional changes. This property is crucial for components such as turbine blades and combustors, which are subjected to rapid temperature changes. The low thermal conductivity of these phases also reduces the rate of heat transfer to the substrate, providing effective thermal insulation [116, 117].

By protecting the metal substrate from high temperatures, glass-ceramic thermal barrier coatings enable the use of higher operating temperatures, which can improve the efficiency and performance of gas turbines and other thermal systems. Higher operating temperatures typically result in more efficient combustion and energy conversion, reducing fuel consumption and emissions. The ability to maintain structural integrity at these elevated temperatures is a key advantage of glass-ceramic coatings [118, 119].

### 2.4.3 Biomedical Implants

The biocompatibility and chemical resistance of glass-ceramic coatings make them suitable for biomedical applications. These coatings are used to coat implants and prosthetics, enhancing their integration with biological tissues and providing a durable, non-reactive surface that resists degradation in bodily fluids [120, 121]. Glass-ceramics can be engineered to possess surface properties that promote cellular adhesion and proliferation, improving the integration of implants with bone and other tissues. This is achieved through surface texturing and modification of the chemical composition to mimic the natural environment of cells. For example, the incorporation of bioactive glass-ceramic phases such as hydroxyapatite can enhance osteointegration by providing a surface that supports bone cell attachment and growth. The surface chemistry and topography play crucial roles in mediating the interactions between the implant and surrounding tissues [122, 123].

The stable crystalline phases in glass-ceramic coatings protect biomedical implants from corrosion and wear in the harsh environment of the human body. This ensures long-term functionality and reduces the risk of implant failure. The low solubility and high chemical stability of the crystalline phases minimize the release of potentially harmful ions into the body, making these coatings safe for long-term use. Additionally, the resistance to biofouling and microbial colonization is an important factor in preventing infections and ensuring the longevity of the implants [124, 125].

### 2.4.4 Optoelectronics

Glass-ceramic coatings with tailored optical properties are used in various optoelectronic devices. Their ability to control light transmission and refractive index makes them suitable for applications in lenses, optical fibers, and display technologies [126].

The transparency of glass-ceramics can be maintained by ensuring that the crystalline phases are smaller than the wavelength of visible light. This allows for high optical clarity, essential for lenses and other optical components. The crystallization process must be carefully controlled to produce nanocrystalline phases that do not scatter visible light, thereby maintaining transparency. Techniques such as sol-gel processing and controlled heat treatment are often

employed to achieve the desired microstructure [127, 128]. Figure 2.6 illustrates the alteration in transparency of spinel glass-ceramics subsequent to the crystallization process.

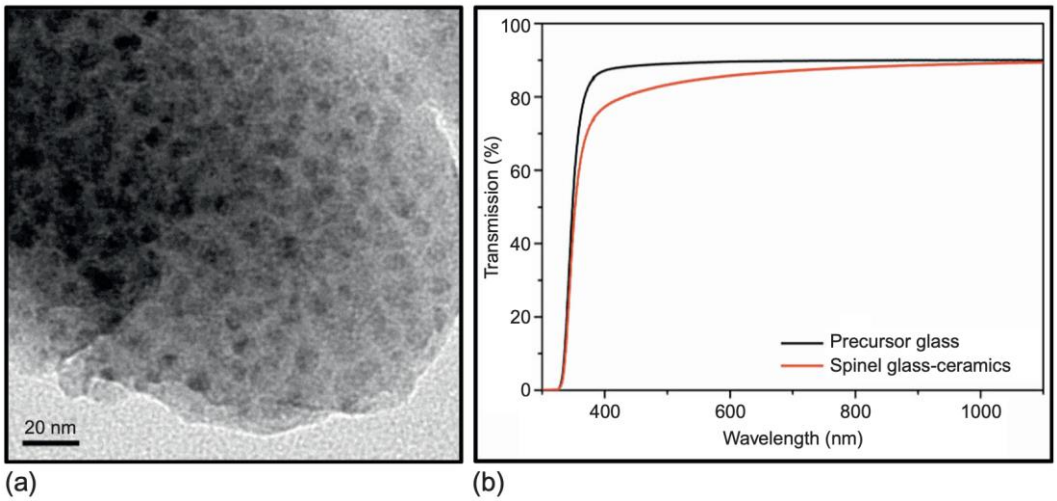



**Figure 2.6** (a) Transmission Electron Microscopy (TEM) bright-field micrographs display crystallites with sizes in the range of 5-10 nm. (b) The transmission spectra illustrate the characteristics of the $MgAl_2O_4$ spinel precursor glass (top) and the glass-ceramic nanocomposites (bottom) [127, 128]

By adjusting the composition and crystallization process, the refractive index of glass-ceramics can be finely tuned. This property is critical for applications in optical fibers, where precise control of light propagation is required, and in display technologies, where specific refractive indices can enhance image quality and brightness. The inclusion of high-refractive-index materials in the glass matrix can significantly alter the optical properties, making glass-ceramic coatings highly versatile for a range of optoelectronic applications [129].

## 2.5 Phosphate-Containing Lithium Zinc Borosilicate Glass-Ceramics

Phosphate-containing lithium zinc borosilicate glass-ceramics represent a specialized subclass within the broader category of glass-ceramic materials. These compositions leverage the synergistic properties of phosphate, lithium, zinc, and borosilicate components to produce materials with exceptional thermal, mechanical, and chemical characteristics. Understanding the role of each component in the matrix and how they interact during the crystallization process is

critical for optimizing the performance of these advanced materials, especially when applied as coatings on steel surfaces. The adhesion of these coatings to steel substrates is a key factor in their effectiveness, influencing their durability and performance in various applications [130, 131].

Phosphorous pentoxide ($P_2O_5$) acts as a network former, creating a phosphate network within the glass matrix. The inclusion of phosphate groups can lead to the formation of unique crystalline phases such as $Li_3PO_4$ and $Zn_3(PO_4)_2$ during heat treatment. These phases contribute to the high ionic conductivity and specific optical properties of the glass-ceramics. The formation of these crystalline phases is facilitated by the high mobility of phosphate ions, which can easily migrate and reorganize during the crystallization process [132, 133].

Silicon dioxide ($SiO_2$) forms the backbone of the glass network, providing structural integrity and enhancing chemical durability. The strong Si-O bonds contribute to the material's high thermal stability and resistance to thermal shock. In combination with $P_2O_5$, $SiO_2$ helps to create a robust, interconnected network that supports the formation of crystalline phases during the controlled crystallization process. The presence of $SiO_2$ ensures that the glass matrix remains stable and resistant to chemical attack, even under harsh conditions [134].

Boron trioxide ($B_2O_3$) acts both as a network former and a modifier, reducing the melting temperature of the glass and enhancing its thermal shock resistance. The presence of boron in the glass matrix allows for the formation of $BO_3$ and $BO_4$ units, which can adapt their coordination depending on the overall composition and thermal history of the glass. This flexibility improves the glass's ability to accommodate different crystalline phases. $B_2O_3$ also lowers the viscosity of the glass melt, facilitating easier processing and formation of a uniform coating [135].

Lithium oxide ($Li_2O$) is a critical component for inducing crystallization and forming lithium-based crystalline phases such as $Li_2ZnSiO_4$ and $Li_3PO_4$. Lithium ions are highly mobile, which can enhance the ionic conductivity of the glass-ceramic. Moreover, the small ionic radius of lithium allows it to easily fit into various crystal lattices, facilitating the formation of stable crystalline phases. The presence of lithium also reduces the overall thermal expansion coefficient, improving the thermal compatibility of the coating with steel substrates [136, 137].

Zinc oxide (ZnO) serves as a network modifier that influences the crystallization behavior and enhances the mechanical properties of the glass-ceramic. The incorporation of ZnO can lead to the formation of zinc-containing crystalline phases, which can further reinforce the glass matrix. Zinc oxide also improves the optical properties by increasing the refractive index and enhancing the glass-ceramic's transparency. The role of ZnO in promoting crystallization and improving mechanical strength is particularly important for applications requiring durable and high-performance coatings [138, 139].

### 2.5.1 Crystallization Process

The crystallization process in phosphate-containing lithium zinc borosilicate glass-ceramics involves a series of carefully controlled thermal treatments designed to promote the formation of specific crystalline phases that enhance the material's properties.

Initial nucleation occurs within the amorphous glass matrix when the temperature is raised to just below the glass transition temperature ($T_g$). The presence of $P_2O_5$ and $B_2O_3$ lowers the activation energy for nucleation, allowing for the formation of nuclei at lower temperatures. The addition of $Li_2O$ and ZnO can further act as nucleating agents, increasing the number of nucleation sites and promoting the uniform distribution of crystalline phases. This stage is crucial for achieving a fine-grained microstructure, which is essential for optimizing mechanical and thermal properties [140, 141].

Once nucleation has occurred, the temperature is further increased to promote the growth of crystalline phases. The specific temperature and duration of this stage are tailored to optimize the size and distribution of the crystals. During this stage, phases such as $Li_2ZnSiO_4$, $Li_3PO_4$, and $Zn_3(PO_4)_2$ form and grow, contributing to the material's enhanced mechanical and thermal properties. Controlled growth ensures that the crystalline phases are fine and evenly distributed, preventing the formation of large, brittle crystals that could compromise the material's integrity [142 - 144]. Figure 2.7 demonstrates polymorphs of $Li_2ZnSiO_4$ cyrstal.

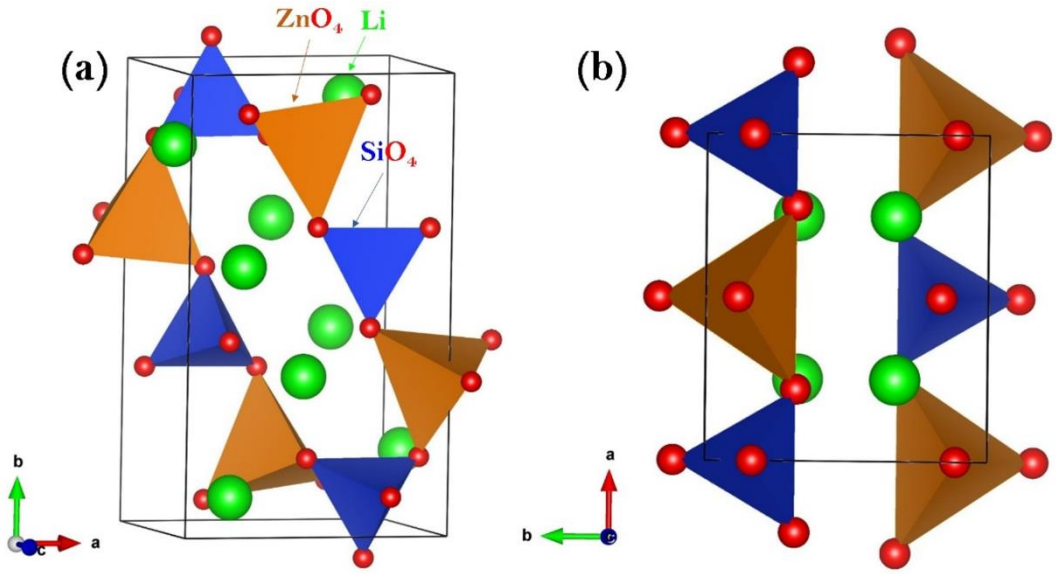



**Figure 2.7** Crystal structures of $Li_2ZnSiO_4$ polymorphs: (a) monoclinic (space group $P2_1/n$) and (b) orthorhombic (space group $Pmn2_1$).[145]

### 2.5.2 Properties

Lithium zinc borosilicate glass-ceramics exhibit a unique combination of properties due to their complex composition and controlled crystallization process. These properties make them particularly suitable for use as coatings on steel substrates, where adhesion and durability are critical. The presence of $SiO_2$ and specific lithium and zinc crystalline phases contribute to the material's high thermal stability and low thermal expansion coefficient. This makes these glass-ceramics suitable for applications requiring precise dimensional stability under thermal cycling conditions. The low thermal expansion ensures good thermal compatibility with steel substrates, minimizing the risk of delamination or cracking [146 - 148].

The incorporation of $P_2O_5$ and the formation of lithium phosphate phases ($Li_3PO_4$) enhance the ionic conductivity of the glass-ceramic. This property is particularly valuable in electrochemical applications, such as solid electrolytes in batteries and fuel cells. The high ionic mobility of lithium ions facilitates efficient ion transport, which is essential for the performance of these devices [149, 150].

The interlocking crystalline phases, such as $Li_2ZnSiO_4$, reinforce the glass matrix and improve its mechanical strength and fracture toughness. The controlled crystallization process ensures a fine microstructure that can withstand mechanical stresses and resist crack propagation. This is particularly important for coatings on

steel substrates, which are often subjected to mechanical loads and impact [149, 151].

The dense crystalline phases formed during the heat treatment provide excellent chemical durability, protecting the material from corrosion in harsh chemical environments. This property is essential for applications in chemical processing and biomedical implants, where resistance to chemical attack is critical. The strong chemical bonds in the crystalline phases make the material less susceptible to dissolution or degradation [152, 153].

The refractive index and transparency of the glass-ceramic can be tailored by adjusting the composition and crystallization process. The inclusion of ZnO enhances the refractive index, making these materials suitable for optical applications, including lenses and optical fibers. The ability to control the optical properties through composition and processing provides flexibility in designing materials for specific optical requirements [154 - 156].

### 2.5.3 Adhesion to Steel Substrates

The adhesion of lithium zinc borosilicate glass-ceramics to steel substrates is a critical factor that influences their performance and durability in practical applications. Several mechanisms contribute to the strong adhesion between the coating and the steel substrate. The formation of chemical bonds at the interface between the glass-ceramic and the steel substrate enhances adhesion. The presence of reactive species in the glass-ceramic, such as lithium and zinc ions, can interact with the steel surface, forming strong chemical bonds that anchor the coating to the substrate [157, 158].

The roughness of the steel substrate can provide mechanical interlocking, where the glass-ceramic infiltrates and conforms to the surface irregularities of the steel. This physical interlocking enhances the mechanical adhesion of the coating, providing resistance to delamination and peeling [159, 160].

The low thermal expansion coefficient of the glass-ceramic, matched with the thermal expansion of steel, minimizes thermal stresses at the interface during thermal cycling. This compatibility reduces the likelihood of cracking or delamination due to thermal expansion mismatch [157].

In summary, phosphate-containing lithium zinc borosilicate glass-ceramics are a versatile and advanced material class, offering a unique combination of thermal, mechanical, chemical, and optical properties. Through careful control of composition and crystallization processes, these materials can be tailored to meet the specific demands of a wide range of industrial applications. The strong adhesion to steel substrates further enhances their utility, making them ideal for protective coatings and other high-performance applications [161, 162].

## 2.6 Role of Nano-CuO and Nano-ZnO in Glass-Ceramic Systems

The integration of nanoparticles, specifically nano-CuO (copper oxide) and nano-ZnO (zinc oxide), into glass-ceramic systems significantly enhances their properties through unique physical and chemical mechanisms. The nanoscale dimensions of these particles lead to distinct behaviors that influence crystallization kinetics, mechanical strength, thermal stability, and surface properties.

### 2.6.1 Sintering and Densification

Sintering and densification are critical processes in the development of glass-ceramic systems, significantly influenced by the incorporation of nanomaterials such as nano-CuO and nano-ZnO. These processes determine the final properties of the ceramics, including their mechanical strength, electrical properties, and microstructural characteristics.

The addition of nano-CuO to glass-ceramic systems, such as ZnO-glass composites, facilitates liquid-phase sintering by lowering the melting point and increasing the diffusion rates. This occurs at temperatures above 850°C, leading to enhanced densification and the reduction of leakage currents. As a result, the material exhibits improved dielectric properties, such as higher breakdown electric fields and nonlinearity coefficients, which are crucial for electronic applications [163].

Nano-CuO acts as a sintering aid in various ceramic systems by promoting the formation of a transient liquid phase during sintering. For example, the addition of CuO to $Pb(Zr_{0.95}Ti_{0.05})_{0.98}Nb_{0.02}O_3$ ceramics significantly reduces the sintering temperature by over 200°C, enhancing the densification process. The optimized

composition exhibits a relative density of 96.7%, with excellent electric properties [164].

Nano-ZnO contributes to the formation of fine, homogeneous microstructures in glass-ceramic systems. The use of nano-ZnO in sintering processes results in smaller grain sizes and higher densities at lower temperatures compared to micro-sized ZnO powders. For instance, ZnO nanocrystals embedded in $SiO_2$ matrices show improved densification behavior and reduced grain growth, which enhances the material's mechanical and optical properties [165].

The introduction of nano-CuO and nano-ZnO in glass-ceramic systems influences phase formation and stability during sintering. For example, in $BaTi_4O_9$ ceramics with $BaO–ZnO–B_2O_3–SiO_2$ glass frit, the presence of ZnO enhances densification and phase stability under reducing atmospheres. This results in materials with optimized microstructures and superior dielectric properties [166].

The addition of nano-$TiO_2$ to alumina and zirconia-based ceramics controls grain growth and improves densification. The fine particle size of nano-$TiO_2$ promotes the formation of dense microstructures with smaller, more uniform grains. This enhances the mechanical strength and thermal stability of the ceramics [167].

Nano-ZnO exhibits unique sintering mechanisms that differ from those of micro-sized powders. For example, the sintering of nano-ZnO powders involves a combination of viscous flow and volume diffusion mechanisms, resulting in high-density materials with improved electrical properties. This is critical for applications requiring high-performance ceramic components [168].

In summary, the incorporation of nano-CuO and nano-ZnO significantly enhances the sintering and densification processes in glass-ceramic systems. These nanomaterials facilitate liquid-phase sintering, improve microstructural homogeneity, control grain growth, and influence phase formation, resulting in ceramics with superior mechanical, electrical, and optical properties.

### 2.6.2 Microstructure and Crystallization

Microstructure and crystallization play crucial roles in defining the physical properties and performance of glass-ceramic systems. The incorporation of nano-CuO and nano-ZnO significantly influences these aspects, contributing to improved mechanical, optical, and electrical properties.

The addition of nano-CuO to glass-ceramic systems can lower the crystallization temperature, promoting the formation of desired crystalline phases. For instance, in the $Li_2O$-ZnO-$B_2O_3$-$SiO_2$ (LZBS) glass system, CuO addition results in the formation of lithium zinc silicate as the primary crystalline phase at lower temperatures (550°C), while also reducing the volume fraction of less desirable quartz phase. This leads to improved thermal expansion properties and overall structural stability [169].

Nano-ZnO contributes significantly to the microstructural evolution of glass-ceramics. For example, in ZnO-glass ceramic films doped with various metal oxides, the presence of nano-ZnO facilitates the formation of uniform, fine-grained microstructures, which enhance the material's mechanical properties and electrical performance [170].

The crystallization mechanisms of nano-CuO and nano-ZnO in glass-ceramic systems often involve complex interactions between the nanomaterials and the glass matrix. In systems such as ZnO-$Al_2O_3$-$SiO_2$ (ZAS), the formation of Gahnite ($ZnAl_2O_4$) nanocrystals without the need for conventional nucleating agents leads to highly transparent and thermally stable glass-ceramics. This precise control over nucleation and crystallization enhances both optical and mechanical properties [171].

The incorporation of nano-ZnO and nano-CuO significantly improves the optical properties of glass-ceramics. In the case of transparent nanocrystalline glass-ceramics, the presence of ZnO and CuO enhances the photoluminescence properties by facilitating the formation of ZnO and $Zn_2SiO_4$ nanoparticles. These nanoparticles act as hosts for rare earth ions, improving energy transfer and increasing photoluminescence intensity [35].

Nano-CuO also plays a role in enhancing the magnetic properties of glass-ceramics. For instance, the gradual addition of CuO to ferromagnetic glass-ceramics in the $Fe_2O_3$-CaO-ZnO-$SiO_2$ system leads to the formation of nanometric magnetite crystals, improving the material's magnetic saturation and coercivity. This makes such materials suitable for applications requiring strong magnetic properties [172].

The presence of nano-ZnO in glass-ceramics enhances structural and thermal stability by promoting the formation of stable crystalline phases at lower temperatures. For example, in the fabrication of $TiO_2$ nano-crystallized glass, ZnO substitution enhances the stability of anatase phase, resulting in glass-ceramics with high transparency and improved thermal properties [173].

### 2.6.3 Phase Transformation

Phase transformation in glass-ceramics is a process whereby an initially amorphous glass is systematically converted into a crystalline or semi-crystalline material through controlled thermal treatment. This transformation encompasses the nucleation and subsequent growth of crystals within the glass matrix, resulting in the formation of distinct crystalline phases. Phase transformation is a critical process in the development of glass-ceramic systems, significantly influenced by the incorporation of nanoparticles. These nanomaterials facilitate the formation of various crystalline phases, which in turn affect the physical properties of the glass-ceramic materials.

The incorporation of nano-ZnO in glass-ceramic systems, such as the $K_2O$–ZnO–$Al_2O_3$–$SiO_2$ system, results in temperature-dependent phase transformations. At lower temperatures (680-800°C), ZnO nanocrystals form, while at higher temperatures (860-1000°C), β-$Zn_2SiO_4$ and α-$Zn_2SiO_4$ nanocrystals precipitate, with the material transitioning from transparent to opaque. The crystallization of potassium aluminosilicates at temperatures above 1000°C further alters the microstructure and optical properties of the material [174].

The addition of nano-ZnO to iron borate glass-ceramics modifies the crystallization behavior, facilitating the formation of single crystalline phases and structural units like $ZnO_6$. This controlled crystallization enhances the thermal and mechanical

stability of the material without forming secondary phases even at high additive concentrations [155].

Nano-ZnO plays a vital role in the microstructural evolution of calcium phosphosilicate glass-ceramics. With varying ZnO content, different crystalline phases such as calcium phosphate, hematite, and magnetite emerge during heat treatment. The presence of ZnO leads to the formation of nano-sized grains at lower temperatures (800°C), which grow larger with increased heat treatment temperature (1000°C), enhancing the material's structural integrity [175].

The preparation of highly crystallized transparent glass ceramics containing dual-phase $ZnGa_2O_4$ spinel and α-$Zn_2SiO_4$ willemite nanocrystals is achieved through controlled crystallization from a quaternary glass system. These dual-phase TGCs exhibit enhanced luminescence properties due to the presence of multiple crystalline environments, making them suitable for photonics and optoelectronics applications [176].

In nano zinc titanate ceramics, the phase transformation mechanism involves the coexistence of $ZnTiO_3$ and α-$Zn_2TiO_4$ phases at low temperatures (800°C) without the presence of $TiO_2$ (rutile). A new mechanism suggests the partial diffusion of $TiO_2$ in the ZnO lattice, forming $ZnTiO_3$, while $TiO_2$ acts as a catalyst for the transformation to α-$Zn_2TiO_4$, enhancing the material's structural properties [177].

The incorporation of nano-ZnO in the $SiO_2$–$Li_2O$–$P_2O_5$–$TiO_2$–CaO–ZnO–$Al_2O_3$ system results in the formation of lithium disilicate and lithium silicate phases, which enhance the mechanical properties of the glass-ceramics. This results in high crystallized fractions, improved hardness, and high flexural strength, making these materials suitable for various high-performance applications [178].

In summary, nano-CuO and nano-ZnO significantly influence the phase transformation processes in glass-ceramic systems. These nanomaterials facilitate controlled crystallization, enhance microstructural stability, and improve the mechanical and optical properties of the materials, making them suitable for advanced technological applications.

### 2.6.4 Role of CuO and ZnO in Specific Systems

In the $ZnO$-$Al_2O_3$-$SiO_2$ (ZAS) system, nano-ZnO plays a critical role in the crystallization and microstructure of the glass-ceramics. Transparent glass-ceramics in this system can be achieved without the use of traditional nucleating agents, through the formation of Gahnite ($ZnAl_2O_4$) nanocrystals. These nanocrystals enhance the optical properties and transparency of the glass-ceramics, making them suitable for optical applications [171].

In the fabrication of ZnO/CuO mixed metal oxide nanocomposites, nano-CuO enhances the photocatalytic degradation of organic pollutants. The hierarchical nanostructures of ZnO/CuO exhibit improved optical responses and decreased recombination rates of charge carriers, which are essential for effective photodegradation of contaminants such as methyl orange under UV light irradiation [179].

In the $TiO_2$-based glass-ceramics, substituting $Bi_2O_3$ with ZnO improves the formation of anatase phase, enhancing transparency and thermal properties. Nano-ZnO acts as both an intermediate and a network modifier, facilitating the precipitation of anatase nanocrystals and improving the overall performance of the glass-ceramics [173]. The synthesis of spike-shaped CuO/ZnO heterostructures using a two-step solution-system method significantly enhances photocatalytic properties. These nanostructures demonstrate superior photodegradation capabilities for organic pollutants like methyl orange, attributed to the formation of effective heterojunction systems and unique morphological characteristics [180].

In glass systems containing $TiO_2$ and ZnO, the inclusion of these nanocrystals provides enhanced photocatalytic activity and improved microhardness. These properties are critical for environmental applications, such as the degradation of humic acid, a major precursor of disinfection by-products in water treatment [181].

Nano-CuO significantly enhances the magnetic properties of ferromagnetic glass-ceramics in the $Fe_2O_3$-CaO-ZnO-$SiO_2$ system. The gradual addition of CuO facilitates the crystallization of magnetite nanocrystals, improving the material's magnetic saturation and coercivity, which are essential for various magnetic

applications [172]. The incorporation of $Eu^{3+}$ ions into $ZnO\text{-}Ga_2O_3\text{-}SiO_2$ glass-ceramics results in enhanced photoluminescence properties. The presence of $ZnGa_2O_4$ nanocrystals within the glass matrix significantly increases the emission intensity, making these materials suitable for photonic applications [182].

# 3
# CRYSTALLIZATION KINETICS

Crystallization kinetics refers to the study of the rates at which crystalline phases form and grow within an amorphous glass matrix. Understanding these kinetics is crucial for tailoring the properties of glass-ceramics to meet specific application requirements. Several theoretical models and experimental methods are used to describe and determine the kinetics of crystallization.

## 3.1 Johnson-Mehl-Avrami-Kolmogorov (JMAK) Theory

The Johnson-Mehl-Avrami-Kolmogorov (JMAK) theory provides a comprehensive framework for understanding the kinetics of phase transformations, including the crystallization process in glass-ceramics. The theory describes the fraction of material transformed from the amorphous to the crystalline state as a function of time and temperature, incorporating both nucleation and growth mechanisms [183 - 187]. The general form of the JMAK equation is [188]:

$$X(t) = 1 - \exp(-kt^n) \tag{3.1}$$

where, X(t) is the fraction of material crystallized at time t, k is the rate constant, and n is the Avrami exponent.

The derivation assumes that: i) nucleation occurs at a constant rate (I) per unit volume, ii) each nucleus grows at a constant radial rate r, resulting in spherical growth, and iii) until impingement occurs, particles grow independently.

The constant nucleation rate implies that nuclei appear continuously throughout the material. Given the isotropic growth assumption, a nucleus that appears at time t′ will grow to a radius r(t−t′) by time t.

The volume V of a sphere growing from a nucleus formed at time t′ and observed at time t is given by:

$$V(t, t') = \frac{4}{3}\pi[r(t - t')^3] \tag{3.2}$$

The probability that any point in the material has not been transformed by a particle nucleated at t′ is the complement of the volume fraction occupied by that particle. Assuming independence among nucleating particles, the cumulative probability that a point remains untransformed by all particles nucleated up to time t is an exponential function of the total transformed volume.

To find the total volume fraction transformed by time t, integrate the volume contributions from all particles nucleated from time 0 to t:

$$\text{Untransformed fraction} = \exp(-\int_0^t I.\frac{4}{3}\pi[t-t']^3 dt') \tag{3.3}$$

Assuming r is constant simplifies the integral:

$$= \exp(-I.\frac{4}{3}\pi r^3 \int_0^t (t-t')^3 dt') \tag{3.4}$$

$$= \exp(-I.\frac{4}{3}\pi r^3 \frac{t^4}{4}) \tag{3.5}$$

$$= \exp(-kt^4) \tag{3.6}$$

where k consolidates constants and reflects the nucleation and growth rates.

For different scenarios, n in $kt^n$ varies depending on the growth geometry and the kinetics of nucleation and growth, hence the generalized form:

$$X(t) = 1 - \exp(-kt^n) \tag{3.1}$$

This equation models the crystallization process by describing how the fraction of crystallized material evolves over time. The rate constant k and the Avrami exponent n are key parameters that encapsulate the effects of temperature and the specific mechanisms of nucleation and growth. The Avrami exponent n provides insights into the dimensionality of growth and the nature of nucleation mechanisms. It is a critical parameter that helps in understanding the crystallization kinetics and the geometry of the growing crystals [189, 190].

- n=1: Indicates one-dimensional growth, such as needle-like or rod-like crystals, with constant nucleation rate. This scenario is typical for fiber-like crystals forming in a matrix.

- n=2: Indicates two-dimensional growth, such as plate-like or disk-shaped crystals, with constant nucleation rate. This is often observed in thin film or layered crystal structures.
- n=3: Indicates three-dimensional growth, such as spherical or equiaxed crystals, with constant nucleation rate. This is common for bulk crystallization processes where crystals grow uniformly in all directions.
- Values of n between 1 and 4: These can represent different combinations of nucleation and growth mechanisms. In site-saturated nucleation, all nuclei form at the beginning of the process, and growth occurs without the formation of new nuclei. In continuous nucleation, nuclei form continuously throughout the crystallization process, leading to a more complex growth pattern [191 - 193].

The value of n is typically determined experimentally by fitting the JMAK equation to crystallization data obtained from techniques like DSC (Differential Scanning Calorimetry). The rate constant k in the JMAK equation is temperature-dependent and follows an Arrhenius-type relationship [193]:

$$k = k_0 \exp\left(-\frac{E_a}{RT}\right) \tag{3.7}$$

where, $k_0$ is the pre-exponential factor, $E_a$ is the activation energy for crystallization, R is the gas constant, and T is the absolute temperature.

The Arrhenius equation is based on the assumption that particles must overcome a certain energy barrier, known as the activation energy $E_a$, in order to react. The kinetic theory of gases provides insights into how molecular energies are distributed according to temperature, described by the Maxwell-Boltzmann distribution.

It is assumed that a reaction can only occur when particles collide with energy greater than or equal to the activation energy $E_a$. The proportion of particles with sufficient energy follows the Maxwell-Boltzmann distribution.

The fraction of molecules exceeding a certain energy barrier $E_a$ at temperature T is given by:

$$P(E \geq E_a) = \int_0^{\infty} \frac{e^{-e/k_b t}}{k_b t} dE \quad (3.8)$$

where $k_B$ is the Boltzmann constant, and E represents the energy.

The integral simplifies under the assumption that the energy distribution is sharply peaked, leading to:

$$P(E \geq E_a) \approx e^{-E_a/k_b t} \quad (3.9)$$

The rate constant k is proportional to the number of effective collisions per unit time, which in turn is proportional to the fraction of molecules with sufficient energy:

$$k = k_0 e^{-E_a/k_b t} \quad (3.10)$$

where $k_0$ is a pre-exponential factor that includes the frequency of collisions and the orientation factor.

By substituting $k_B$ with the universal gas constant R (where $R=N_A k_B$ , $N_A$ being Avogadro's number), the equation for k becomes:

$$k = k_0 \exp\left(-\frac{E_a}{RT}\right) \quad (3.7)$$

This relationship implies that the rate constant k increases with temperature, reflecting the increased mobility of atoms or ions at higher temperatures, which facilitates nucleation and growth processes [190 - 193].

To determine the parameters k and n, experimental techniques such as DSC or DTA (Differential Thermal Analysis) are used. These methods involve heating the glass-ceramic sample at controlled rates and recording the heat flow associated with the crystallization process. The data obtained are then fitted to the JMAK model to extract the rate constant and Avrami exponent [191, 193].

The JMAK theory provides a robust framework for analyzing and understanding the crystallization kinetics in glass-ceramics. By describing the fraction of material crystallized as a function of time and temperature, and by incorporating parameters

that capture the effects of nucleation and growth mechanisms, the JMAK equation enables to optimize the crystallization process and tailor the properties of glass-ceramic materials for a wide range of applications [194, 195].

## 3.2 Ozawa Theory

The Ozawa theory extends the JMAK model to non-isothermal conditions, making it suitable for analyzing crystallization processes under varying temperatures. This extension is particularly valuable for understanding crystallization kinetics during continuous heating or cooling processes, as it accounts for the effects of changing temperature on the transformation rate [196, 197]. The Ozawa equation modifies the JMAK framework to describe the crystallization fraction as a function of temperature under non-isothermal conditions. The general form of the Ozawa equation is [196]:

$$\ln\left[-\ln(1-X(T)\right] = m\ln(\beta) + \ln\left(K_T\right) \tag{3.11}$$

where, X(T) is the fraction crystallized at temperature T, β is the heating rate, m is the Ozawa exponent and $K_T$ is the temperature-dependent rate constant.

This equation relates the double logarithm of the uncrystallized fraction to the logarithm of the heating rate and a temperature-dependent term, providing a means to analyze the kinetics of crystallization under varying thermal conditions [196].

X(T) represents the fraction of the material that has crystallized at a given temperature T. This parameter is derived from experimental data, typically obtained through differential scanning calorimetry (DSC) or differential thermal analysis (DTA), by integrating the area under the exothermic peak corresponding to crystallization [198]. The heating rate β is the rate at which the temperature is increased during the experiment. Different heating rates affect the kinetics of the crystallization process, with faster heating rates generally leading to higher crystallization temperatures [199]. The Ozawa exponent m provides insights into the nature of the crystallization process. Similar to the Avrami exponent in the JMAK theory, m can indicate different growth geometries and nucleation mechanisms. However, m specifically adapts these insights to non-isothermal conditions [200]. The rate constant $K_T$ varies with temperature and encapsulates the

kinetics of the crystallization process. It is influenced by the activation energy for crystallization and the mobility of atoms or molecules within the material [201].

The primary advantage of the Ozawa theory is its applicability to non-isothermal conditions, which are more representative of real-world processing environments where temperatures are continuously changing [202]. The theory is flexible and can be applied to a wide range of materials and crystallization processes. It provides a more accurate description of kinetics compared to isothermal models, especially when dealing with varying heating or cooling rates [203]. By incorporating the heating rate into the analysis, the Ozawa theory allows for a more comprehensive understanding of the crystallization kinetics, including the identification of activation energies and growth mechanisms under dynamic thermal conditions [204].

The Ozawa theory provides an essential extension to the JMAK model by adapting it to non-isothermal conditions, thereby offering a robust framework for analyzing crystallization kinetics during continuous heating or cooling processes. The use of the Ozawa equation enables the determination of key kinetic parameters such as the Ozawa exponent and temperature-dependent rate constant, facilitating a deeper understanding of the crystallization behavior of glass-ceramics and other materials under practical processing conditions. This theoretical approach is crucial for optimizing thermal treatments and enhancing the properties of materials in various industrial applications [205].

## 3.3 Augis-Bennett Method

The Augis-Bennett method is a well-established approach for analyzing non-isothermal crystallization data, particularly focusing on the shape of the crystallization peak observed in differential scanning calorimetry (DSC) or differential thermal analysis (DTA) experiments. This method is useful for determining the activation energy for crystallization by analyzing the shift in peak temperature with different heating rates [206, 207]. The equation is given by:

$$\ln\frac{T_P}{\beta} = -\frac{E_a}{RT_P} + C_1 \tag{3.12}$$

where, $T_p$ is the peak temperature of crystallization, R is the gas constant, and β is the heating rate and $C_1$ is the constant [208]. By focusing on the shape of the crystallization peak, this method provides a more detailed understanding of the crystallization process [209]. It is suitable for analyzing crystallization under non-isothermal conditions, making it applicable to real-world thermal treatments[210].

## 3.4 Kissinger Method

The Kissinger method is a widely used technique for determining the activation energy for crystallization from non-isothermal data. This method analyzes the shift in peak temperatures with varying heating rates, providing a straightforward and reliable way to calculate the activation energy [211 - 213]. The Kissinger equation is expressed as:

$$\ln\left(\frac{\beta}{{T_p}^2}\right) = -\frac{E_a}{RT_p} + constant \tag{3.13}$$

where, β is the heating rate, $T_p$ is the peak temperature, $E_a$ is the activation energy for crystallization, and R is the gas constant [211, 212, 214].

The method is straightforward and does not require complex data manipulation, making it easy to apply [215]. It provides accurate determination of activation energy by considering the temperature dependence of the crystallization process [216].

Both the Augis-Bennett and Kissinger methods are valuable for analyzing non-isothermal crystallization kinetics. The Augis-Bennett method offers detailed insights through peak shape analysis, while the Kissinger method provides a straightforward approach to determine activation energy by analyzing the shift in peak temperatures with different heating rates.

Together, these methods enhance our understanding of the crystallization kinetics in glass-ceramics and other materials, enabling the optimization of thermal treatments and material properties for various industrial applications.

## 3.5 Flynn-Wall-Ozawa (FWO) Method

The Flynn-Wall-Ozawa (FWO) method is a widely used model-free approach to determine the activation energy for crystallization without assuming a specific reaction model. This method is particularly advantageous because it provides a straightforward way to analyze non-isothermal crystallization data obtained from differential scanning calorimetry (DSC) or differential thermal analysis (DTA) [217, 218].

The FWO model is expressed by the given equation [219]:

$$\log(\beta) = \log\left(\frac{AE_a}{Rg(a)}\right) - 2.314 - \frac{0.457E_a}{RT} \tag{3.14}$$

where A is the frequency factor ($s^{-1}$), $E_a$ (J/mol) is the activation energy of reaction, g(a) is an integral reaction model whose value depends on the reaction mechanism followed by the fuel, and R is the universal gas constant (8.314 J/mol K).

This equation relates the logarithm of the heating rate to the reciprocal of the absolute temperature, allowing for the determination of the activation energy from experimental data [220]. The FWO method does not require any assumption about the reaction mechanism, making it versatile and applicable to various materials and crystallization processes [221]. The method is straightforward, involving simple linear regression of experimental data [222]. It is suitable for analyzing non-isothermal crystallization data, which is more representative of practical processing conditions [223]. The Flynn-Wall-Ozawa (FWO) method provides a reliable and straightforward approach to determine the activation energy for crystallization under non-isothermal conditions. By plotting log(β) versus 1/T, the method allows for the extraction of activation energy without assuming a specific crystallization model. This makes the FWO method particularly useful for analyzing complex materials and processes, thereby enhancing our understanding of the crystallization kinetics in glass-ceramics and other materials.

## 3.6 Friedman Method

The Friedman method is a robust model-free approach for analyzing the kinetics of phase transformations, particularly crystallization in glass-ceramics. Unlike other methods that rely on specific reaction models, the Friedman method directly evaluates the rate of transformation as a function of temperature and time, providing

a flexible and accurate determination of activation energy without the need for prior assumptions about the reaction mechanism [224]. The Friedman method evaluates the rate of transformation (dα/dt) using the following equation:

$$ln\frac{d\alpha}{dt}\mathrm{I}_{ai} = \ln\left(A_i f\left(a_{i,j}\right)\right) - \frac{E_{ai}}{RT_{i,j}} \tag{3.15}$$

In the given expression, "i" represents the index of conversion, "j" represents the index of the curve, "$E_{ai}$" denotes the apparent activation energy at $\alpha_i$, and $f(\alpha_{i,j})$ is a function dependent on the reaction model assumed to be constant for a given reaction progress $\alpha_{i,j}$ for all curves j. Since f(α) is constant at each conversion degree αi, the dependence of the logarithm of the reaction rate on 1/T is linear, with the slope of $E_a/R$ and intercept A. [225]. This equation implies that by plotting ln(dtdX) versus $T_1$, one can determine the activation energy Ea from the slope of the linear fit, where the slope is equal to $-E_a/R$ [226].

The Friedman method does not assume any specific reaction mechanism, making it applicable to a wide range of materials and transformation processes [227]. This method directly uses experimental data on the rate of transformation, providing a more accurate representation of the kinetics involved [228]. The Friedman method is well-suited for analyzing non-isothermal data, reflecting realistic processing conditions. This method provides a powerful and flexible approach to determine the activation energy for crystallization in glass-ceramics. By directly analyzing the rate of transformation as a function of temperature and time, this method offers a model-free alternative that is both accurate and versatile. The ability to apply the Friedman method to non-isothermal data makes it particularly useful for real-world applications, where dynamic thermal conditions are common. This method enhances our understanding of the crystallization kinetics in glass-ceramics, aiding in the optimization of thermal treatments and the development of materials with tailored properties for various industrial applications [229].

## 3.7 Avrami-Erofeev Model

The Avrami-Erofeev model, an extension of the Johnson-Mehl-Avrami-Kolmogorov (JMAK) theory, is a widely used approach to describe solid-state transformations, including the crystallization process in glass-ceramics. This model

provides a comprehensive framework for analyzing the kinetics of phase transformations by accommodating various nucleation and growth scenarios. The general form of the Avrami-Erofeev equation is:

$$\alpha = 1 - \exp(-kt^n) \tag{3.16}$$

where, α is the fraction of material transformed at time t, k is the rate constant, t is the time, and n is the Avrami exponent. This equation describes how the fraction of material transformed (α) evolves over time (t) as a function of the rate constant (k) and the Avrami exponent (n) [230, 231].

The fraction transformed, α, represents the proportion of the material that has undergone the phase transformation at a given time. It ranges from 0 (no transformation) to 1 (complete transformation). The rate constant, k, incorporates the effects of temperature, nucleation rate, and growth rate [232]. The model accommodates various nucleation and growth scenarios, making it applicable to a wide range of materials and transformation processes [233]. By incorporating both nucleation and growth mechanisms, the model provides a detailed understanding of the kinetics of phase transformations [234]. The Avrami exponent n offers valuable insights into the dimensionality of the growth process and the nature of nucleation, aiding in the interpretation of experimental data.

The Avrami-Erofeev model provides a powerful and flexible framework for analyzing the kinetics of solid-state transformations, including crystallization in glass-ceramics. By accommodating various nucleation and growth scenarios, this model offers detailed insights into the mechanisms governing phase transformations. The ability to extract key parameters such as the rate constant and Avrami exponent, and to determine activation energy, makes the Avrami-Erofeev model an essential tool for researchers aiming to optimize the thermal treatment and properties of glass-ceramic materials [235].

# 4
# SURFACE TENSION

When it comes to coating performance and application—especially in glass-ceramics—surface tension is a crucial factor. It significantly impacts the wettability, adhesion, and overall quality of the coated surface. A thorough understanding of surface tension, its theoretical background, measurement techniques, and specific relevance to glass-ceramics is essential for optimizing coating properties [236 - 238].

## 4.1 Definition and Measurement

The force per unit length operating along a liquid's surface that causes it to contract is known as surface tension. The imbalance between the intermolecular forces at the liquid's surface and bulk causes this phenomenon. Surface tension affects how the coated surface and the surroundings interact in the context of glass-ceramic coatings [239]. Mathematically, surface tension (γ) is expressed as [240]:

$$\gamma = LF \tag{3.17}$$

where F is the force acting along the surface, and L is the length over which the force acts. Several techniques are employed to measure surface tension and related properties such as contact angle, which provides indirect information about surface tension [239].

- **Sessile Drop Method:** A droplet is placed on a solid substrate, and the contact angle formed between the droplet and the surface is measured. The surface tension can be inferred from the contact angle and the interfacial tensions between the liquid, solid, and air. This method is particularly useful for characterizing the wettability of coated surfaces [241]. Figure 4.1 shows the illustration of sessile drop method.

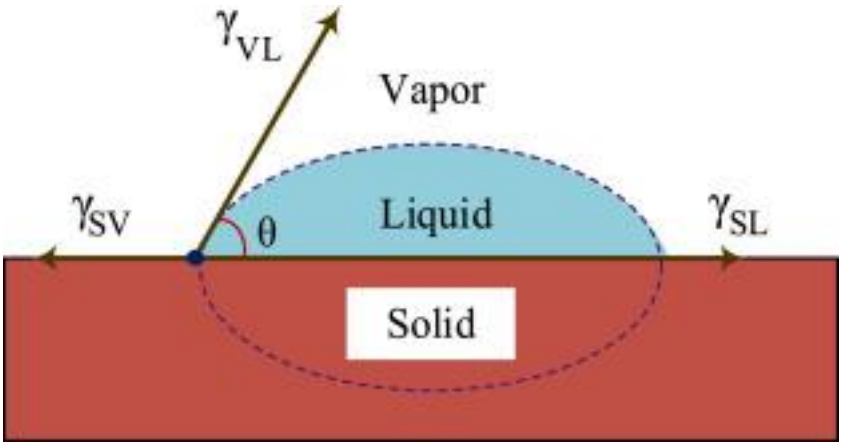



**Figure 4.1** Illustration of the sessile drop method [242].

- **Wilhelmy Plate Method:** A thin plate is partially immersed in the liquid, and the force exerted on the plate due to surface tension is measured. This force, combined with the perimeter of the plate, allows for the calculation of surface tension [243]. Figure 4.2 shows the illustration of Wilhelmy plate method.

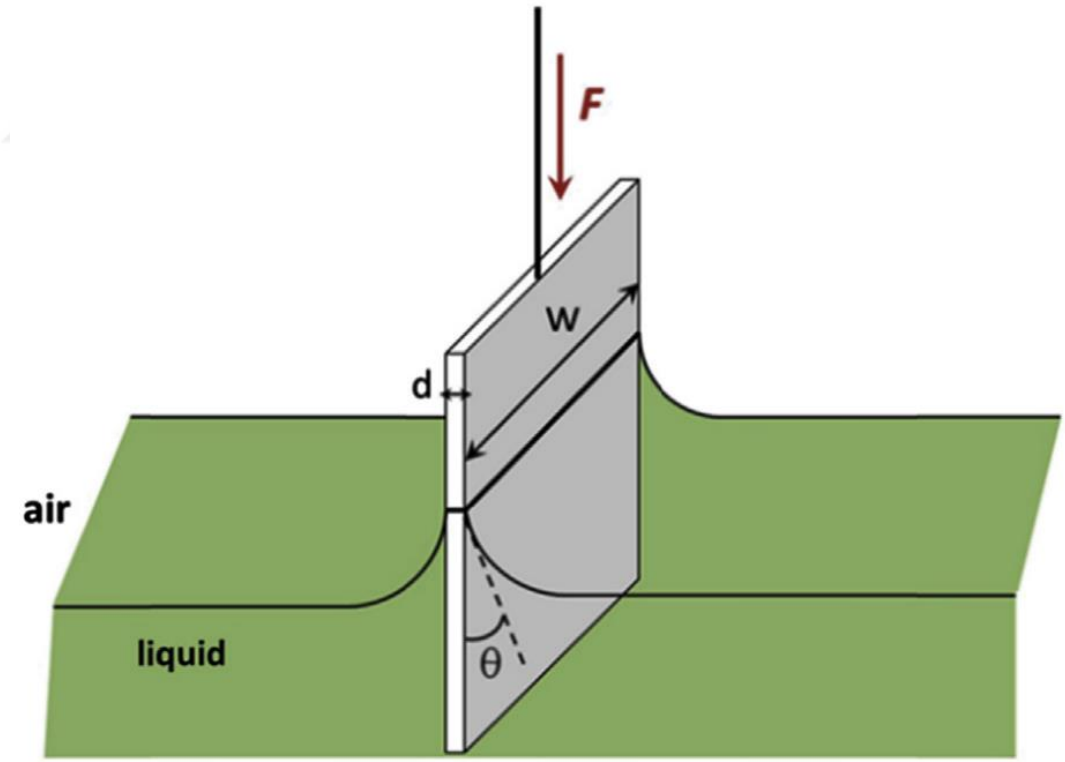



**Figure 4.2** Illustration of Wilhelmy plate method [244].

- **Capillary Rise Method:** Measures the height to which a liquid rises or falls in a capillary tube due to surface tension. The surface tension is related to

the height, the radius of the capillary, and the density of the liquid [245]. Figure 4.3 illustrates capillary rise method.

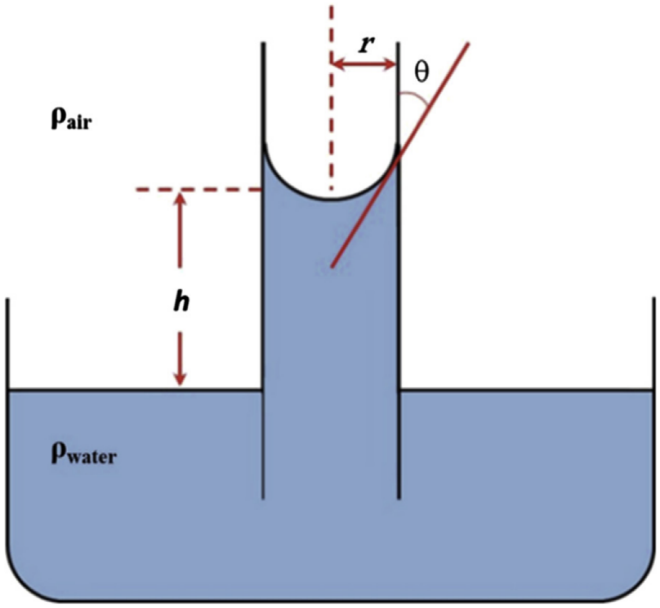



**Figure 4.3** Illustration of capillary rise in a vertical plate [244].

- **Pendant Drop Method:** Analyzes the shape of a droplet suspended from a needle. The surface tension is determined by fitting the droplet shape to the Young-Laplace equation, which describes the balance of forces acting on the droplet [246]. Figure 4.4 shows the illustration of pendant drop method.

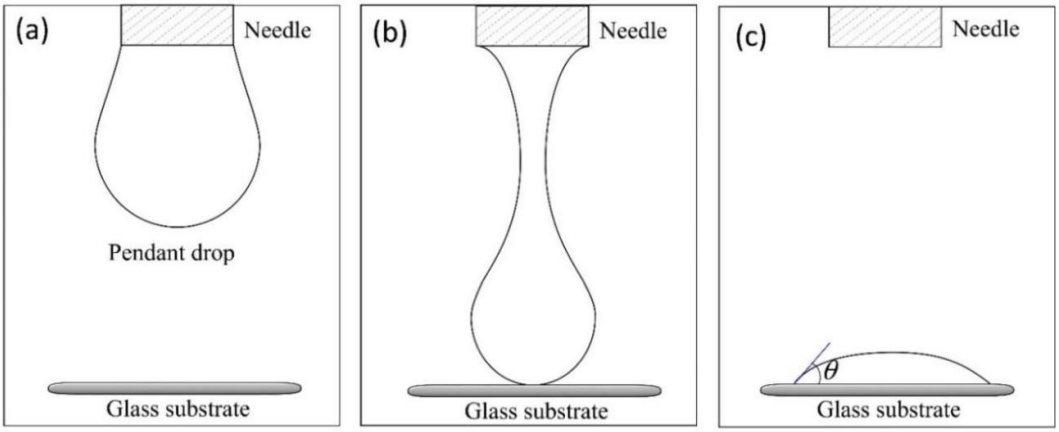



**Figure 4.4** Schematic illustration of the pendant drop procedure. (a) pendant drop for surface tension measurements, (b) and (c) spreading dynamics [247].

## 4.2 Surface Tension in Glass-Ceramics

In glass-ceramic coatings, surface tension is a crucial factor that influences the interaction between the coating and the substrate. It determines the wettability and adhesion properties of the coating, which are essential for ensuring a strong bond and uniform coverage on substrates such as steel and cast iron.

The surface tension of the coated surface affects several key properties:

- Wettability: High surface tension typically results in poor wettability, where the coating does not spread well on the substrate, leading to weak adhesion. Low surface tension promotes better spreading and stronger adhesion [90].
- Contact Angle: The contact angle between a liquid droplet and the coated surface is a direct indicator of surface wettability. A low contact angle signifies good wettability, while a high contact angle indicates poor wettability[90].

Several theoretical models help explain the behavior of surface tension and contact angle in glass-ceramics [248] and Figure 4.5 illustrates these models:

- Young's Equation: Describes the balance of forces at the contact line of a droplet on a solid surface. It relates the contact angle (θ) to the surface tensions of the solid-liquid (γSL), solid-vapor (γSV), and liquid-vapor (γLV) interfaces [249]:

$$\gamma_{SV} = \gamma_{SL} + \gamma_{LV} cos\theta \tag{4.1}$$

- Wenzel Model: Extends Young's equation to rough surfaces. It assumes that the liquid fully wets the rough surface, and the apparent contact angle (θ*) is given by[250]:

$$cos\theta^* = r cos\theta \tag{4.2}$$

where r is the roughness factor, defined as the ratio of the actual surface area to the projected surface area.

- Cassie-Baxter Model: Also deals with rough surfaces but assumes that air pockets are trapped beneath the liquid, leading to partial wetting. The apparent contact angle (θ*) is given by [251]:

$$cos\theta^* = r_f \phi_s cos\theta^Y + \phi_s - 1 \tag{4.3}$$

$r_f$ is the roughness parameter of the wetted area, $\phi_s$ is the fraction of liquid-solid area, and $\theta^Y$ is the Young contact angle.

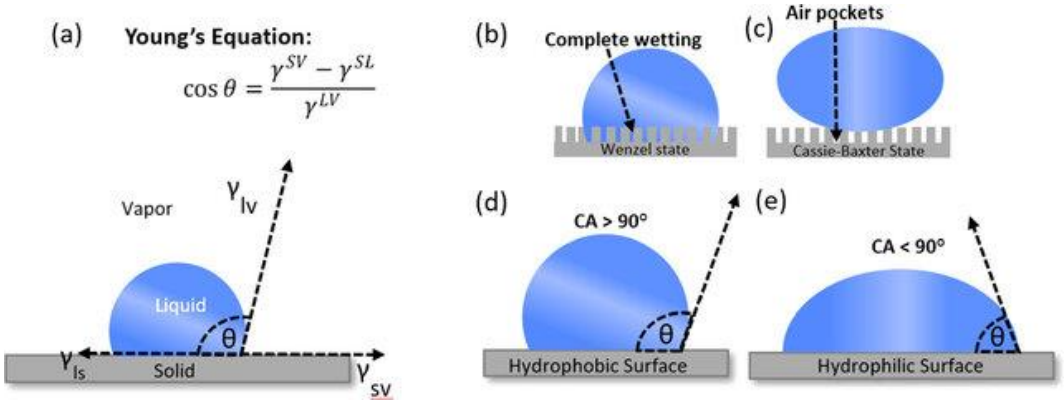



**Figure 4.5** (a) Young's equation (b) Wenzel State (c) Cassie–Baxter State (d) Hydrophobic Surface (Contact angle > 90°) (e) Hydrophobic Surface (Contact angle < 90°) [252].

## 4.3 Influence of Surface Tension on Coating Performance

Surface tension plays a pivotal role in determining the performance of glass-ceramic coatings, especially regarding their wettability, adhesion, and durability. The contact angle of water on these surfaces serves as a crucial parameter reflecting the balance of adhesive and cohesive forces at the interface, which significantly affects the coating's protective qualities.

Recent studies have underscored the importance of surface tension in influencing the wettability of glass-ceramic coatings. High surface tension typically results in higher contact angles, indicating poor wettability. This is because the cohesive forces within the water droplets are stronger than the adhesive forces between the water and the coating surface, causing the water to bead up rather than spread out. Conversely, low surface tension is associated with lower contact angles, indicating better wettability, which enhances the coating's ability to uniformly spread water and other liquids across the surface [253 - 255].

The wettability of glass-ceramic coatings is critical for various applications, including protective coatings for electronic devices, biomedical implants, and architectural materials. For instance, in biomedical applications, a hydrophilic surface (low contact angle) is often desirable to promote cell adhesion and

proliferation. In contrast, hydrophobic surfaces (high contact angle) are preferred in applications where water repellency is crucial, such as in anti-corrosion coatings for buildings and marine structures [256 - 264].

Modifying the surface composition and structure of glass-ceramic coatings can effectively alter surface tension and, consequently, the contact angle. This modification can be achieved by incorporating various additives or altering the microstructure during the coating process. For example, adding certain oxides, such as titanium dioxide ($TiO_2$) or silicon dioxide ($SiO_2$), can decrease surface tension, resulting in improved hydrophilicity. Such modifications enhance the coating's performance by promoting better liquid spreadability, which is vital for applications requiring uniform liquid distribution [265 - 268].

Surface roughness is another critical factor that interacts with surface tension to influence the wettability of glass-ceramic coatings. According to the Wenzel and Cassie-Baxter models, surface roughness can either increase or decrease the contact angle depending on the nature of the roughness and the surface tension of the material. Rough surfaces tend to exhibit higher contact angles due to increased air trapping within the rough structures, which elevates the surface energy. However, by controlling the roughness and creating specific micro- and nanoscale patterns, it is possible to design surfaces with tailored wettability properties. For instance, superhydrophobic surfaces with very high contact angles can be created by combining low surface tension materials with appropriate roughness [269 - 272].

In addition to compositional and structural modifications, the deposition techniques used for applying glass-ceramic coatings also influence their surface tension and wettability. Techniques such as sol-gel processing, thermal spraying, and chemical vapor deposition (CVD) allow for precise control over the coating's microstructure and surface characteristics. For example, sol-gel processing can produce coatings with a high degree of uniformity and controlled porosity, which can be tailored to achieve the desired surface tension and wettability properties [273 - 275].

Moreover, the interaction between surface tension and environmental factors such as temperature and humidity can also affect the performance of glass-ceramic coatings. Studies have shown that temperature variations can alter the surface

energy of coatings, thereby affecting their wettability. Similarly, exposure to different humidity levels can lead to changes in the adsorption of water molecules on the coating surface, influencing the contact angle and overall performance of the coating [276, 277].

In conclusion, the performance of glass-ceramic coatings is intricately linked to their surface tension characteristics. By understanding and manipulating the factors that influence surface tension and contact angle, such as surface composition, roughness, deposition techniques, and environmental conditions, it is possible to enhance the functionality and application range of these coatings. Future research should continue to explore the interplay between these factors to develop advanced glass-ceramic coatings with optimized performance for specific applications.

## 4.4 Previous Studies on Nano-Additives in Glass-Ceramics

Recent advancements in material science have emphasized the significant role of nano-additives in enhancing the properties of glass-ceramics. These studies highlight the multifaceted benefits that nano-additives bring to the table, ranging from improved mechanical properties to specialized applications in various fields.

Nano-sized sintering additives like MgO, $Al_2O_3$, $Y_2O_3$, and $La_2O_3$ have shown significant improvement in the mechanical properties of $Si_3N_4$ ceramics. These additives facilitate the complete transformation of α-$Si_3N_4$ into β-$Si_3N_4$, resulting in higher fracture toughness. For instance, the addition of 4MgO-4$Al_2O_3$-5$La_2O_3$ resulted in ceramics exhibiting the highest fracture toughness due to the formation of high aspect ratio grains (β-$Si_3N_4$). The transformation led to a fracture toughness improvement by up to 30% compared to ceramics without these additives [278].

Incorporating nanoparticles such as $SiO_2$ and $TiO_2$ into glass-ceramics formulations enhances physical properties, including mechanical strength and stability at high temperatures. For example, adding 10-30% of nanoparticles in the slurry to produce glass-ceramics significantly increased the density of the structure and improved physical properties such as thermal resistance up to 1000°C. These improvements are crucial for applications requiring high durability [279].

The addition of glass additives such as MgO–CaO–$Al_2O_3$–$SiO_2$ to $Ba_{0.95}Sr_{0.05}Zr_{0.2}Ti_{0.8}O_3$ ceramics has led to significant improvements in

microstructural refinement and dielectric properties. This combination promotes sintering, resulting in a transition from diffusion phase transition to relaxor behavior. At an electric field of 140 kV/cm, the specimen with 5 wt.% glass additive showed an energy density of 0.42 J/cm$^3$ and an energy efficiency of 82.8% [280].

In another study, $Ba_{0.85}Ca_{0.15}Zr_{0.1}Ti_{0.9}O_3$ ceramics with $Bi_2O_3$–$B_2O_3$–$SiO_2$ glass additives demonstrated a high energy storage density of 2.12 J/cm$^3$ and an energy efficiency of 90.5% at 330 kV/cm electric field. These properties are particularly beneficial for electronic and energy storage applications [281].

Nano-structured glass-ceramics, particularly those reinforced with magnetic properties, have shown promising potential in biomedical applications such as hyperthermia and drug targeting. These materials demonstrate superior mechanical and bioactive properties, making them suitable for medical and dental implants. The addition of rare-earth elements has been shown to improve these properties significantly [282].

Glass-ceramics derived from red mud and coal fly ash, with nano-crystal additives, exhibit remarkable physical and mechanical properties such as enhanced density, thermal expansion coefficient, hardness, and bending strength. These attributes make them viable for a wide range of construction applications. For instance, glass-ceramics obtained from vitrified red mud showed an average crystal size of less than 100 nm, with high density and thermal expansion coefficient suitable for construction purposes [283].

Transparent nano-ceramics have been developed for high-transmittance applications, integrating structure and function for use in infrared windows, optical isolators, composite armors, and solid-state lasers. These materials exhibit low fabricating cost, controllable shape, and variable composition, making them highly desirable for advanced optical applications. Additionally, the unique properties of these nano-ceramics, such as low-thermal-expansion behavior and high hardness, make them suitable for various high-performance applications [284].

The integration of nano-additives in glass-ceramics has revolutionized the field, bringing about significant enhancements in mechanical, physical, and functional properties. These advancements have paved the way for diverse applications,

ranging from construction to biomedical fields, demonstrating the versatility and importance of nano-additives in modern materials science.

# 5
# EXPERIMENTAL DETAILS

## 5.1 Materials

### 5.1.1 Composition of Glass-Ceramic Coatings

Because of its beneficial qualities for coating applications, a phosphate-containing lithium zinc borosilicate glass-ceramic system was chosen for this investigation. $Li_2O$-ZnO-$B_2O3$-SiO2 was the basic composition of the glass-ceramic system; $P_2O_5$ was added to improve glass formation. In order to increase the adhesion between the glass-ceramic coating precursor and the DC06EK steel substrate (EN 10209), NiO and CoO compounds were added to the glass-ceramic system. The particular mixture was designed to maximize its mechanical and thermal characteristics, guaranteeing stability in use and compatibility with the steel substrate.

The glass-ceramic needs to melt in a number of carefully regulated phases. To get the correct ratios of each oxide component as called for in the formulation, the batch is first precisely weighed. The components are then completely mixed in order to assure that all oxides are distributed uniformly, which is essential for producing consistent glass-ceramic characteristics. After that, the combined batch is placed in an elevator furnace (Protherm ELV 170/8) and heated to a maximum temperature of 1400°C for 45 minutes. By allowing the batch to completely melt thanks to this high-temperature treatment, the various oxides can interact more easily and a homogeneous molten glass can result.

Following the melting process, the molten material is rapidly cooled in water. This rapid cooling is necessary to create the glass in an amorphous, non-crystalline condition that is a prerequisite for additional processing. The precursor glass particles are collected after quenching and dried for 2 hours at 100°C in an oven. In order to confirm that the particles are sufficiently prepared for next heat treatments or coating applications, it is imperative that any remaining moisture from the quenching process be removed during this drying stage.

### 5.1.2 Characteristics of Nano-CuO and Nano-ZnO

Nano-CuO powder with a purity of 99.99% was used in the experiments. The material is characterized by a black color and a nearly spherical morphology. The average particle size of Nano-CuO is 38.0 nm. The specific surface area of the material is greater than 20 $m^2/g$. The bulk density and true density of nano-CuO are 0.8 $g/cm^3$ and 6.5 $g/cm^3$, respectively.

Nano-ZnO powder with a purity of 99.5% or higher was utilized in the study. The particles of nano-ZnO are nearly spherical with an average size ranging from 30.0 nm to 50.0 nm. The material exhibits a milky white color and consists of a single crystal phase. The true density of nano-ZnO is 5.5 $g/cm^3$.

The concentration of nano-CuO and nano-ZnO additions was methodically varied from 0.5 to 5.0 wt.% during the milling process to study its influence on the overall properties of the coatings. Starting with a 0.5 wt.% addition helps to understand the initial impact of the nanoparticles on the properties of the coatings, providing a baseline for comparison. The 1.0 and 2.5 wt.% concentrations allow for observing trends and changes in properties with incremental increases in nanoparticle content. This step-wise approach helps identify any threshold effects or gradual improvements in properties. Finally, the 5.0 wt.% addition ensures that the study covers a broad range of concentrations, helping to identify the saturation point or the maximum effective concentration of nanoparticles. This helps determine if there is a diminishing return or negative impact on properties at higher concentrations. The codes of the samples and the addition amounts are listed in the Table 5.1 and 5.2.

**Table 5.1** The codes and contents of the samples with nano-CuO

| **Sample Name** | **Amount of nano-CuO Addition (wt. %)** |
|---|---|
| LZS_REF | 0 |
| LZS_05_CuO | 0.5 |
| LZS_10_CuO | 1 |
| LZS_25_CuO | 2.5 |
| LZS_50_CuO | 5 |

**Table 5.2** The codes and contents of the samples with nano-ZnO

| **Sample Name** | **Amount of nano-ZnO Addition (wt. %)** |
|---|---|
| LZS_REF | 0 |
| LZS_05_ZnO | 0.5 |
| LZS_10_ZnO | 1 |
| LZS_25_ZnO | 2.5 |
| LZS_50_ZnO | 5 |

## 5.2 Sample Preparation

The substrate for this investigation was chosen to be DC06EK grade sheet steel owing to its superior formability, improved surface quality, and the fit for coating applications. Every steel substrate was 10 cm by 10 cm in size. In order to maximize the surface for coating adherence, a multi-step activation technique was used during the substrates' initial preparation. This process included cleaning the samples using a clean pad to remove debris and other contaminants from the steel surface. This step is critical for improving the adhesion strength of the coating. After cleaning, the samples are rinsed with deionized water and subsequently dried with air to eliminate moisture.

The precursor glass, nanoparticles, and organosilicone oil, were meticulously processed using a ball milling technique. Alumina-zirconia balls were employed as the milling medium to ensure thorough mixing and size reduction of the materials. This method was chosen to achieve a homogenous mixture and to optimize the particle size distribution for enhanced performance in electrostatic applications. The objective of this grinding process was to produce fine powders with particle sizes less than 150 µm, suitable for coating applications. Following the grinding process, the particles were sieved through a 100-mesh sieve to achieve the preferred particle size distribution.

Glass-ceramic coatings (GCCs) were applied utilizing an improved electrostatic powder spray approach after the surface was prepared. This technique ensures a homogeneous and constant layer by using an electrostatic charge to draw the powder particles to the electrically grounded substrate. The thickness of the target

coating was meticulously regulated to around 150 ± 50 μm. In order to achieve the desired functional features of the coating, this thickness was selected to balance the mechanical properties and the effectiveness of heat treatment.

The coated substrates had been heat-treated for 5 minutes to 550°C in order to stabilize the coating and release any tensions created during the spraying process. This process aids in eliminating any remaining strains and tensions, which helps to keep the coating homogeneous and avoid cracking. After that, the samples were heated to 750°C, 800°C, and 850°C for 10 minutes each to induce crystallization in a Protherm PLV 110/30 box furnace. These particular temperatures were selected in light of early research that found ideal circumstances for the formation of crystalline phases in the glass-ceramic matrix, which has a substantial impact on the final sample's surface characteristics.

To maximize flow and deposit efficiency during the electrostatic spraying process, the precursor powder particle size, as well as the spray gun's calibrated distance and speed, were carefully chosen. This made sure that the powder was distributed evenly throughout the substrate surface, which is essential for getting a consistent coating thickness and quality. To confirm statistical robustness and data repeatability, a total of four samples were processed under each of the crystallization temperature and nanoparticle addition parameters.

## 5.3 Experimental Techniques

## 5.4 X-Ray Fluorescence (XRF) Analysis

The produced precursor glass’ chemical composition was examined using the Bruker S8 Tiger X-ray fluorescence (XRF) instrument. In order to determine whether the intended composition was achieved and to provide a more precise interpretation of the study, oxide percentages of precursor glass were evaluated.

## 5.5 Hot Stage Microscope Analysis

The glass-ceramic coatings' sintering behaviors were observed using a hot stage microscope (ODHT-HSM 1600/50, Misura 3.32). At a rate of 10°C per minute, ground samples were subjected to 1000°C. The sintering and melting temperatures

were determined by monitoring the changes in the sample morphology. Based on the data collected, the Vogel-Fulcher-Tammann (VFT) graph was created, offering insight into the glass-ceramic coatings' viscosity behavior and heat stability. The VFT model is essential for understanding the temperature dependence of the viscosity in supercooled liquids, which is directly related to the sintering behavior of the materials.

## 5.6 Differential Thermal Analysis (DTA)

Precursor glass powders were subjected to differential thermal analysis utilizing a TG-DTA Netzsch STA 449F1A-0207-M device that included a liquid nitrogen cooling accessory. 40 μL sealed aluminum crucibles with five punctures in the lid were used to allow water to evaporate during heating. Standard DTA measurements were performed using 15 mg of precursor glass powder at different heating rates (5, 10, 15, and 20 K/min) while subjected to a nitrogen purge (20 mL/min). The samples' crystallization kinetics were examined using the thermal analysis data. For these computations, the well-known Kissinger method for calculating activation energy and crystallization kinetics was used. In order to get useful kinetic parameters, this approach requires graphing the natural logarithm of the heating rate against the reciprocal of the peak temperature of crystallization.

## 5.7 X-ray Diffraction (XRD) Analysis

Phase formations within the glass-ceramic coatings were analyzed using a Bruker XRD/D8 Advance X-ray diffractometer. The instrument was operated with Cu-Kα radiation (wavelength = 1.5406 Å), a voltage of 40 kV, and a current of 25 mA. Scans were performed over a 2θ range of 10° to 80° with a step size of 0.002° and a count time of 1.5 seconds per step. The XRD patterns were analyzed to identify crystalline phases and their relative proportions, providing insights into the structural changes induced by different heat treatments, nano-CuO additions and nano-ZnO additions.

## 5.8 Scanning Electron Microscopy (SEM)

With the use of an energy dispersive X-ray (EDS) analysis-equipped Zeiss EVO 10 SEM, the microstructure of the glass-ceramic coatings was examined. The SEM

had a working distance of 9.5 mm and an acceleration voltage of 20 kV. In order to highlight sample morphology, imaging was done in backscattered electron imaging (BSE) mode, where the atomic number of the sample elements affected picture contrast, and secondary electron yield (SE) mode. This dual-mode imaging provided comprehensive information on the surface topography and elemental distribution within the coatings.

## 5.9 Optical Microscopy

Optical microscopy was employed to complement the scanning electron microscopy (SEM) observations, providing detailed images of the sample morphologies at lower magnifications. For this analysis, a Zeiss Smartzoom 5 digital microscope was used, offering high-resolution imaging capabilities with automated focus and stitching features.

Prior to imaging, samples were meticulously prepared to ensure the surface was free from contaminants. The preparation process involved cleaning the samples with deionized water and ethanol, followed by air drying in a clean environment to prevent any artifacts from appearing in the images. Once prepared, samples were placed on the microscope stage and examined under reflected light.

The captured images were then analyzed using the Smartzoom 5 software, which allows for detailed measurements of surface features and identification of defects. This analysis included assessing parameters such as coating uniformity, presence of cracks, voids, and other surface anomalies. The optical microscopy provided a macroscopic view of the coating distribution, confirming that the electrostatic powder spray technique achieved a consistent and uniform application across the substrate. In addition to defect identification, the optical images revealed the surface texture of the coatings, including features like surface roughness and particulate agglomeration.

## 5.10 3D Surface Analysis

Topographical changes in coating surfaces were analyzed using a non-contact optical profilometer (Zeiss, Smartzoom 5, ConfoMap ST 8.0). Measurements were conducted in accordance with ISO 21920-2:2021 and ISO 4287 standards, which

define surface texture parameters and methodologies. The 3D surface analysis provided quantitative data on surface roughness, waviness, and other topographical features, crucial for assessing the quality and functionality of the coatings.

## 5.11 Viscosity Measurements

Viscosity measurements were conducted to understand the flow properties of the glass-ceramic coatings during processing. These measurements were essential for optimizing the spraying and sintering processes, ensuring uniform coating application and proper sintering behavior.

To construct the VFT graph, experimental viscosity data over a range of temperatures is required. This data is typically obtained using hot stage microscopy and dilatometer (DIL). Using the temperatures identified from hot stage microscopy (sintering onset, softening, and melting points) and the glass transition temperature from DIL, the viscosity at these points can be estimated or measured directly if viscosity data is available.

The VFT equation parameters ($\eta$, $B$, and $T_0$) are then fitted to the experimental data. This involves plotting $\ln(\eta)$ versus $1/(T-T_0)$. The slope of this plot provides the parameter B, which is related to the activation energy for viscous flow. The intercept at high temperatures gives $\eta_0$, the high-temperature limit of viscosity. The Vogel temperature $T_0$ is determined through iterative fitting, representing the temperature at which viscosity theoretically diverges.

## 5.12 Contact Angle Measurements

Contact angle measurements were performed to assess the wettability and surface energy of the coatings. Before measurement, all samples were washed with pure water for 5 minutes and then with 99.5% ethanol for 5 minutes. The contact angle was measured using an automatic optical tensiometer (OneAttension Theta Lite). The results provided insights into the hydrophobicity or hydrophilicity of the coatings, which is important for applications involving liquid interactions and adhesion properties.

In summary, the experimental techniques employed in this study provided comprehensive data on the thermal, structural, and surface properties of the

phosphate-containing lithium zinc borosilicate glass-ceramic coatings. These analyses were crucial for optimizing the composition, processing conditions, and functional performance of the coatings applied to DC06EK steel substrates.

# 6
# RESULTS AND DISCUSSION

## 6.1 Chemical Composition

In this glass-ceramic formulation designed for steel surfaces, each oxide component is meticulously chosen to fulfill specific roles essential for achieving the desired physical and chemical properties of the coating. XRF analysis results are shown in Table 6.1.

$SiO_2$ is the foundational network former, establishing the base silica network crucial for the structural integrity of the glass-ceramic. It imparts robustness and chemical durability to the enamel, making it suitable for protective applications.

**Table 6.1** Chemical composition of the studied system

| Role | Oxide | wt. % |
|---|---|---|
| Flux | $Na_2O$ | 5.5 |
| | $Li_2O$ | 8.0 |
| Crystallization Agent | ZnO | 8.0 |
| Adhesion Provider | NiO | 1.25 |
| | CoO | 0.75 |
| Network Modifier | $P_2O_5$ | 3.0 |
| Network Former | $B_2O_3$ | 12.0 |
| | $SiO_2$ | 60.0 |
| Non-Oxide Flux | $F_2$ | 1.5 |

These alkali metal oxides modify the silica network by breaking Si-O-Si bonds. This action reduces the melting point and viscosity, which facilitates the enamel's application and enhances its flow characteristics. Crucially, they aid in controlling the thermal expansion properties of the glass-ceramic, thereby ensuring compatibility with the steel substrate.

As a network modifier, ZnO promotes the crystallization, that significantly contributes to the low thermal expansion and increased mechanical strength of the coating.

$B_2O_3$ serves as an intermediate oxide, capable of acting as both a network former and modifier. It adjusts the enamel's viscosity and thermal properties, enhancing the glass transition temperature and improving the chemical resistance of the glass-ceramic.

Contrary to its typical portrayal as a network modifier, $P_2O_5$ acts as a network stabilizer in this glass-ceramic system. It integrates phosphate groups into the silica network, enhancing the viscosity and stability of the glass matrix.

This stabilization is crucial for managing the crystallization process and improving the mechanical properties of the final product. NiO and CoO oxides are specifically included to enhance the adhesion between the glass-ceramic coating and the steel substrate. There are four main theories explaining adhesion between steel and glass-ceramics:

- **Mechanical Theory**: The adhesion begins with the physical roughening of the metal surface, which increases the contact area between metal and enamel. Upon firing, an oxide layer forms on the metal, and as temperature rises, this oxide layer thickens and diffuses into the enamel, creating dendrite structures that mechanically interlock the enamel and metal. However, this mechanical bonding is considered auxiliary, as it does not significantly enhance adhesion compared to chemical bonding.
- **Chemical Theory**: This theory suggests that various chemical reactions—such as dissolution, redox, and precipitation—occur at the interface between enamel and metal when they contact. Key reactions involve the reduction of iron oxide by nickel and cobalt oxides within the enamel, driven by changes in oxidation states, as illustrated in the chemical equations provided. This results in a chemically bonded transition layer at the interface.
- **Electrolytic Theory**: When enamel melts during firing, a galvanic element forms between cobalt and iron, creating a galvanic current. This current

etches angled grooves in the metal where the molten enamel can mechanically bond by filling these cavities.

- **Diffusion Theory**: At firing temperatures, there is a diffusion of metal ions from the enamel into the metal and vice versa. This ion exchange and subsequent diffusion contribute to a stable bond if the enamel coating is adequately saturated with the corresponding metal oxide, enhancing adhesion through continuous diffusion.

## 6.2 Thermal Analyses

### 6.2.1 Hot Stage Microscopy

Hot-stage microscopy (HSM) analysis was employed to elucidate the thermal behavior of the glass-ceramic precursor, as shown in Figure 6.1. This technique enables the real-time observation of morphological changes in the material as it undergoes controlled heating, providing crucial insights into the sintering and melting processes fundamental to the development of glass-ceramic coatings.

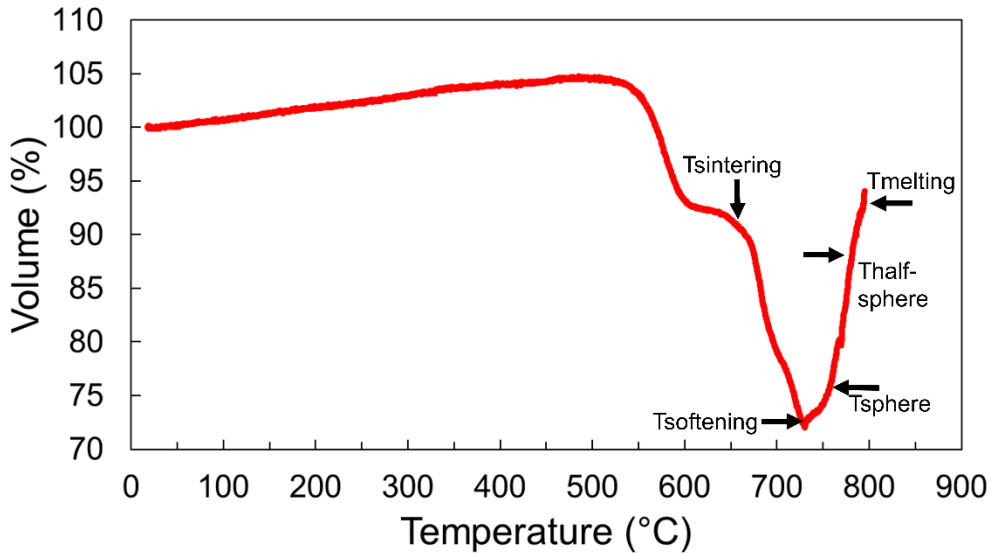



**Figure 6.1** Hot-stage microscopy analysis results of the precursor LZBS sample: sintering, softening, sphere, half-sphere, and melting temperatures.

At 681°C, the precursor glass particles begin to undergo sintering, a process driven by the reduction of surface energy through the formation of necks between adjacent particles. This temperature marks the onset of particle coalescence, where diffusion mechanisms—primarily volume diffusion and grain boundary diffusion—facilitate

the bonding of particles. The resultant microstructure evolves into a dense, interconnected network with reduced porosity [285 - 287]. The sintering process is critical for developing the mechanical integrity and structural cohesion necessary for subsequent thermal treatments and applications.

As the temperature increases to 722°C, the precursor glass reaches the softening point. This stage is characterized by a significant increase in viscosity, which can be quantified using viscosity-temperature relations typical for glassy materials. The glass transition ($T_g$) occurs in this temperature range, where the material transitions from a rigid, brittle state to a more ductile, viscoelastic state. The increased molecular mobility at this temperature allows for the relaxation of internal stresses and the manipulation of the material's shape [288 - 290]. This softening behavior is vital for ensuring the glass-ceramic precursor can be uniformly applied and conform to the substrate geometry during coating formation.

At 748°C, the softened glass precursor undergoes further thermal softening, leading to the formation of spherical droplets due to surface tension effects. This temperature indicates the onset of the liquid phase, where the viscosity has decreased sufficiently to allow the glass to flow and form spheres. The formation of spherical droplets is an indication of the material's ability to transition into a molten state, which is crucial for achieving uniform coating application. The surface tension-driven spherical morphology minimizes the surface area, indicating a lower free energy state [291 - 293].

Upon reaching 773°C, the spherical droplets begin to deform, transitioning into partially flattened shapes. This deformation signifies that the material is transitioning from a viscous, semi-solid state to a more fluid, molten state. The material's ability to flow increases significantly, and the shapes become less defined as the internal cohesion forces are overcome by gravitational and surface tension forces [294]. This stage is critical for understanding the flow dynamics and wetting behavior of the molten glass on the substrate surface.

The final thermal transformation occurs at 782°C, where the glass precursor achieves complete melting. At this temperature, the glass transitions into a fully molten liquid state, characterized by minimal viscosity and maximal fluidity. Complete melting is essential for the uniform application of the glass-ceramic

coating onto the steel substrate. The molten state ensures that the glass can spread evenly across the substrate, forming a homogeneous layer [295, 296]. The subsequent cooling and crystallization of the molten glass are critical for developing the desired microstructure and properties of the glass-ceramic coating.

### 6.2.2 Dilatometer

In addition to hot stage microscopy analysis, optical dilatometry was employed to further investigate the thermal properties of the glass-ceramic precursor and shown in Figure 6.2. This analysis provided critical data on the glass transition temperature ($T_g$), the dilatometric softening point ($T_{peak}$), and the coefficient of thermal expansion (CTE) of the material.

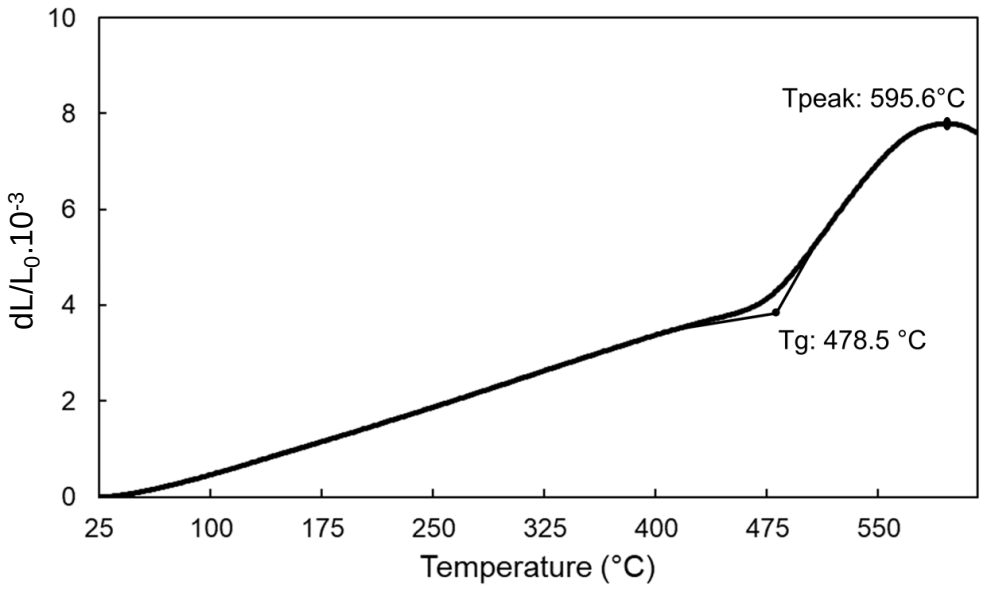



**Figure 6.2** Optical dilatometer analysis result of the LZBS sample up to 600 °C showing glass transition ($T_g$) and dilatometric softening ($T_{peak}$) points.

The glass transition temperature ($T_g$) of the precursor was determined to be 478.5°C. The $T_g$ represents the temperature at which an amorphous material, such as glass or glass-ceramics, undergoes a transition from a rigid, glassy state to a more rubbery or viscous state. This transition is characterized by a significant increase in the material's specific heat and a change in its mechanical properties. At $T_g$, the molecular mobility within the glass structure increases, leading to a decrease in modulus and hardness [297, 298]. The determination of $T_g$ is crucial for

understanding the working temperature range of the glass-ceramic material, as it signifies the onset of viscoelastic behavior.

The dilatometric softening point ($T_{peak}$) was measured to be 595.6°C. This temperature corresponds to the point at which the glass-ceramic material starts to significantly soften and exhibits increased viscosity. The $T_{peak}$ is critical for defining the thermal processing window during which the material can be shaped or formed without undergoing full melting. At this temperature, the glass network structure begins to break down, allowing for viscous flow [299]. The dilatometric analysis tracks the dimensional changes in the sample as it is heated, providing a precise measurement of this softening behavior. This information is essential for optimizing processes such as thermal forming, annealing, and sintering.

The coefficient of thermal expansion (CTE) quantifies the extent to which a material expands upon heating. This property is crucial for applications where thermal stability and compatibility with other materials are important [300]. The linear coefficient of thermal expansion ($\alpha_L$) was determined to be $8.94\times10^{-6}\,°C^{-1}$, and the volumetric coefficient of thermal expansion ($\alpha_V$) was found to be $26.81\times10^{-6}\,°C^{-1}$.

The precise determination of these thermal properties is pivotal for the application of glass-ceramic materials in environments subject to thermal cycling and mechanical stresses. Understanding $T_g$, $T_{peak}$, and CTE allows for the optimization of processing parameters to enhance the performance and durability of the glass-ceramic coatings [301]. The data obtained from the optical dilatometer thus plays a crucial role in the development and application of these advanced materials, ensuring their reliability and functionality in practical applications.

### 6.2.3 Viscosity Measurements

The Vogel-Fulcher-Tammann (VFT) graph, shown in Figure 6.3, was constructed using data obtained from hot stage microscopy and dilatometer analyses of the precursor glass. This graph illustrates the relationship between temperature and viscosity, providing valuable insights into the material's behavior and properties over a range of temperatures.

To analyze the viscosity-temperature relationship, the Vogel-Fulcher-Tammann (VFT) equation was employed. The VFT equation is widely used to describe the behavior of glass-forming materials and is expressed as [302, 303]:

$$\eta = A.\exp\left(\frac{B}{T - T_0}\right) \tag{6.1}$$

where: η is the viscosity, A is the pre-exponential factor, B is the VFT constant, T is the temperature, $T_0$ is the Vogel temperature, the temperature at which the viscosity theoretically diverges to infinity.

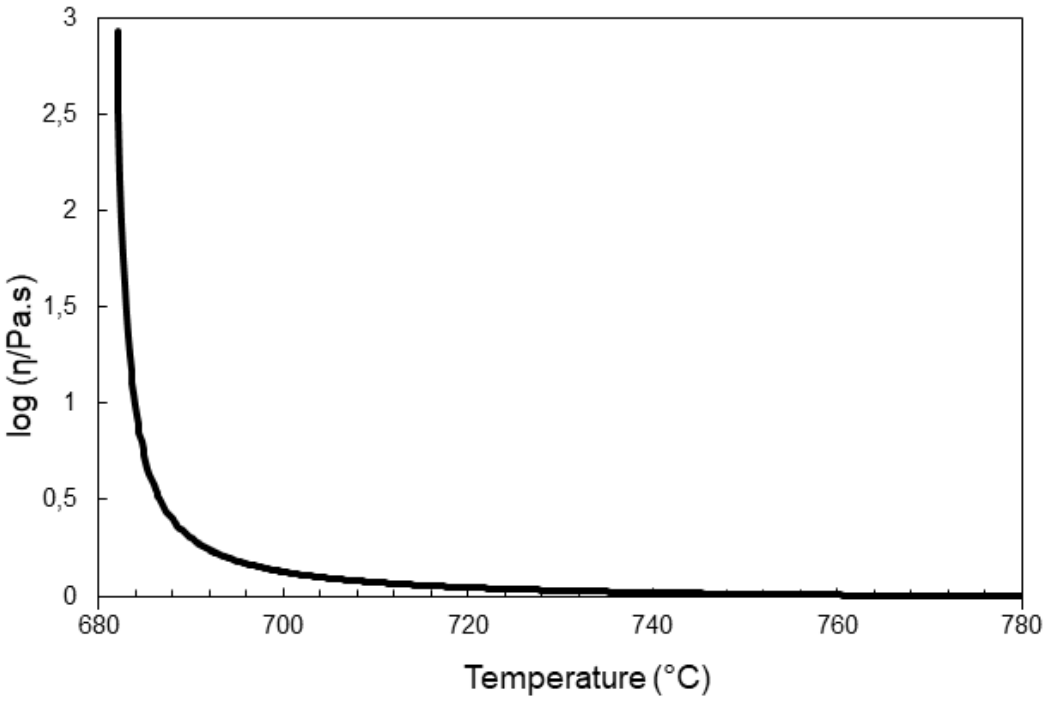



**Figure 6.3** Viscosity versus temperature for the precursor LZBS sample. The lines are plotted according to the VFT equation determined from HSM and DIL analyses.

The VFT equation was fitted to the experimental data points using nonlinear regression analysis, yielding the values of A, B, and $T_0$. The viscosity as a function of temperature was fitted using the following results: $T_0$ = 691.12; A = 4122.09; B = 5262.74

The value of A indicates the inherent resistance to flow. A higher A value suggests a more viscous material at high temperatures [304]. The constant B reflects the energy barrier for molecular motion. Higher B values indicate a more structurally

complex material, requiring more energy for molecular rearrangement [305, 306]. The temperature $T_0$ represents a characteristic temperature below which the material undergoes a significant increase in viscosity. It is the temperature at which the material's viscosity theoretically diverges, indicating a drastic change in the material's flow behavior [307, 308].

Figure 6.3 plots the logarithm of viscosity ($\log(\eta)$) against temperature, based on the VFT equation derived from hot stage microscopy (HSM) and dilatometer (DIL) analyses. The graph demonstrates a clear inverse relationship between temperature and viscosity. As the temperature increases, the viscosity of the glass-ceramic sample decreases exponentially. This behavior is typical for glass-forming materials, where higher temperatures facilitate increased molecular mobility, reducing resistance to flow.

At lower temperatures, close to the Vogel temperature ($T_0$), the material exhibits very high viscosity, approaching a glassy state with minimal molecular mobility [309]. As the temperature rises above $T_0$, the viscosity decreases sharply, indicating a transition towards a more fluid state where molecular motion is significantly less hindered [310].

### 6.2.4 Differential Thermal Analysis (DTA)

To gain insight into the thermal behavior of the glass-ceramic coatings, Differential Thermal Analysis (DTA) was used. As seen in Figure 6.4, the DTA curves for the glass-ceramic coatings that were heated at varying speeds demonstrate discrete thermal events, especially in the 650–800°C temperature range that is critical to the crystallization process. Important information on the kinetics of crystallization and the material's thermal stability is provided by this research. The crystallization temperatures observed at each heating rate are:

- 704°C @ 5°C/min
- 708°C @ 10°C/min
- 713°C @ 15°C/min
- 721°C @ 20°C/min

These temperatures indicate the onset of crystallization, where the glass-ceramic material begins to form crystalline phases from the amorphous state. The increase in crystallization temperature with increasing heating rate is a well-documented

phenomenon in materials science, reflecting the influence of thermal kinetics on phase transformations.

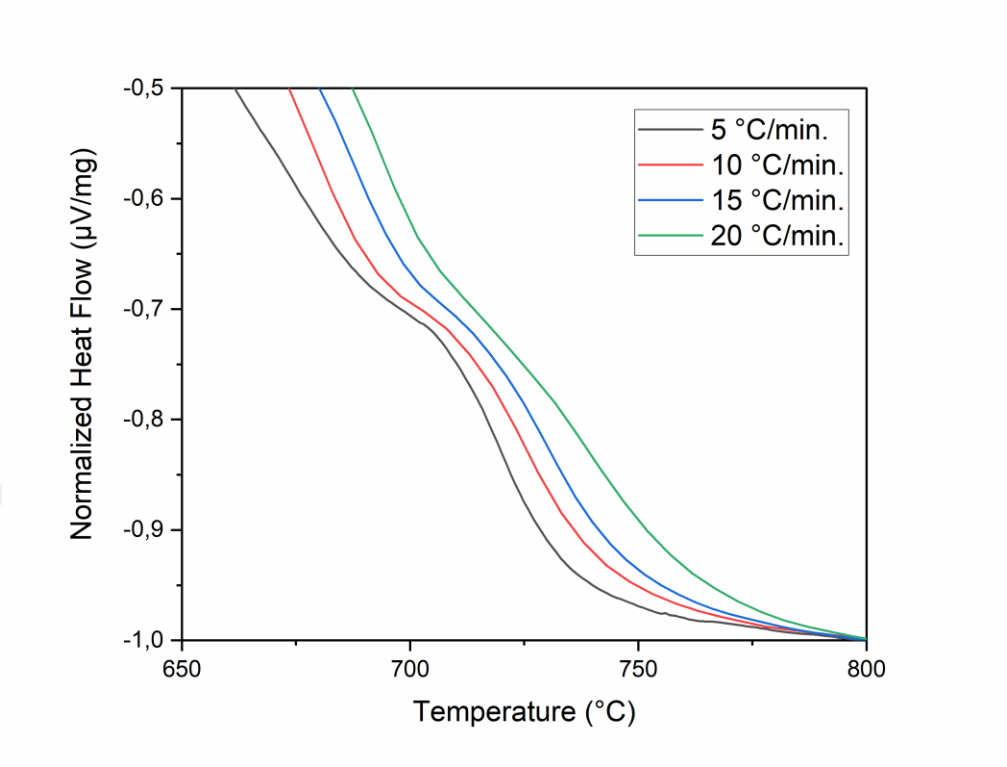



**Figure 6.4** DTA analysis performed on the glass-ceramic coatings using different heating rates of 5, 10, 15, and 20 °C/min.

Figure 6.4 shows the normalized heat flow (µV/mg) as a function of temperature for different heating rates. The graph demonstrates a clear shift in the exothermic peak associated with crystallization towards higher temperatures as the heating rate increases. This shift is indicative of the thermal lag inherent in DTA measurements, where higher heating rates provide less time for the material to respond to the imposed temperature changes, resulting in delayed thermal events.

The observed trend in the DTA curves can be explained by the principles of thermodynamics and kinetics. At higher heating rates, the sample experiences a rapid increase in temperature, reducing the time available for nucleation and growth processes. Consequently, the crystallization onset temperature increases because the material requires a higher temperature to overcome the activation energy barrier for nucleation under rapid heating conditions[311].

The variation in crystallization temperature with heating rate suggests that the kinetics of the crystallization process are sensitive to thermal conditions. Faster

heating rates enhance the nucleation and crystal growth rates up to a certain threshold [312]. However, if the heating rate exceeds the material's ability to nucleate and grow crystals efficiently, the energy required for these processes increases, leading to higher crystallization onset temperatures[313 - 315].

The DTA analysis provides valuable data on the thermal behavior and crystallization kinetics of the glass-ceramic coatings. The shift in crystallization temperature with varying heating rates underscores the importance of precise thermal control in the processing of these materials. This information is critical for developing advanced glass-ceramic coatings with tailored properties for specific applications.

## 6.3 Kinetic Calculations

The kinetics of the crystallization reaction were analyzed using the Kissinger equation, a widely employed method for investigating the temperature dependence of reaction rates in solid-state transformations. The Kissinger equation is given by:

$$ln\left(\frac{q}{{T_p}^2}\right) = \ln(A) - \left(\frac{E_a}{R.T_p}\right) \quad (6.2)$$

where q is the heating rate, $T_p$ is the corresponding peak temperature, A is the pre-exponential factor, $E_a$ is the activation energy, and R is the universal gas constant. This equation allows the determination of the activation energy ($E_a$) by analyzing the relationship between the heating rate and the peak temperature of the reaction.

The pre-exponential factor (A) represents the frequency of successful collisions between reactant molecules that result in a reaction. It is a crucial parameter for predicting reaction rates. To calculate A, a series of experiments were conducted at different heating rates, and the corresponding peak temperatures ($T_p$) were recorded. Using the experimental data and the equation parameters, ln(A) was calculated to be 7.19.

The heating rate (q) during the analysis was measured at various intervals, and the corresponding peak temperatures ($T_p$) were recorded. These values were then used to perform additional calculations to gain deeper insights into the kinetics of the reaction.

By converting the peak temperatures from Celsius to Kelvin ($T_p(K)$) using the relationship $T_p(K) = Tp + 273.15$, the absolute temperatures were obtained for further analysis. The squared peak temperatures ($T_p^2$) were also calculated, yielding $T_p^2$ values that are indicative of the magnitude of the reaction at each heating rate.

To investigate the relationship between the heating rate and peak temperature, the parameter $q/T_p^2$ was determined. This parameter quantifies the heating rate relative to the temperature at which the peak occurs. Lower values of $q/T_p^2$ suggest higher heating rates relative to the peak temperature, indicating a more rapid increase in temperature.

Moreover, the reciprocal of the peak temperature in Kelvin (K), represented as 1000/Tp, was calculated. This reciprocal value provides additional insights into the kinetics of the reaction and serves as a useful metric for comparison and analysis.

Furthermore, the natural logarithm of the $q/T_p^2$ values, multiplied by -1, was obtained as $-\ln(q/T_p^2)$. This transformation allows for a more detailed investigation of the kinetics and offers valuable information regarding the reaction mechanism and rate-determining steps.

The calculated values of $T_p$, $T_p(K)$, $T_p^2$, $q/T_p^2$, $1000/T_p$, and $-\ln(q/T_p^2)$ for the different heating rates are summarized in Table 6.2. The graph of $-\ln(q/T_p^2)$ versus $1000/T_p$ and the $E_a$ value which comes from the slope of the line is shown Figure 6.6.

The Kissinger plot, as shown in Figure 6.5, provides a visual representation of the relationship between $-\ln(q/Tp^2)$ and 1000/Tp. The slope of this plot is used to calculate the activation energy (Ea), which in this study was found to be 11,362 kJ/mol. This plot confirms the linear relationship predicted by the Kissinger equation, validating the kinetic model for the crystallization process in the glass-ceramic material. The activation energy is a critical parameter that reflects the energy barrier for the reaction. A higher activation energy indicates that a greater amount of energy is required to initiate the reaction, suggesting that the reaction rate is slower. This value implies that the crystallization process in the glass-ceramic material possesses a significant energy barrier, indicating potential kinetic inhibition or a complex reaction pathway.

**Table 6.2** Kinetic Parameters derived from the Kissinger Equation

| **(q) (°C/min)** | **$T_p$ (°C)** | **$T_p$ (K)** | **$T_p^2$ ($K^2$)** | **$q/T_p^2$ ($min^{-1}K^{-2}$)** | **$1000/T_p$ ($K^{-1}$)** | **$-\ln(q/T_p^2)$** |
|---|---|---|---|---|---|---|
| 5 | 667.0 | 940.15 | 883,882.02 | $7.96 \times 10^{-4}$ | 1.06 | 7.13 |
| 10 | 681.0 | 954.15 | 910,402.22 | $7.78 \times 10^{-4}$ | 1.05 | 7.16 |
| 15 | 697.0 | 970.15 | 941,191.02 | $7.57 \times 10^{-4}$ | 1.03 | 7.18 |
| 20 | 703.0 | 976.15 | 952,868.82 | $7.57 \times 10^{-4}$ | 1.03 | 7.19 |

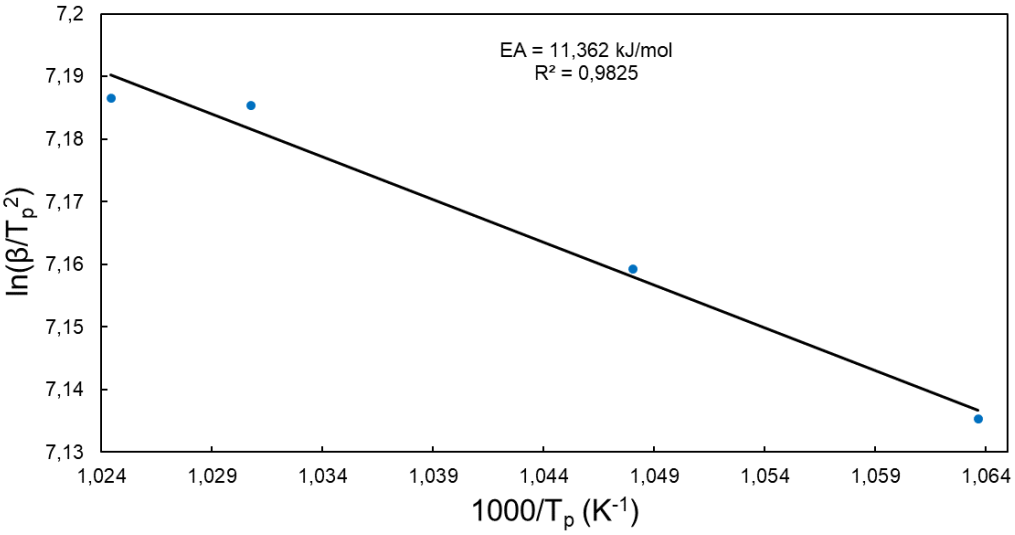



**Figure 6.5** The Kissinger plot of the studied LZBS sample

The kinetic analysis using the Kissinger equation provides a comprehensive understanding of the temperature dependence of the crystallization reaction rates in the glass-ceramic coatings. The activation energy and pre-exponential factor are critical parameters that characterize the reaction kinetics, influencing the thermal processing and stability of the material. By analyzing the experimental data and constructing the Kissinger plot, this study offers valuable insights into the kinetic mechanisms governing the crystallization process.

## 6.4 Structural Analyses

### 6.4.1 XRD Analyses

#### 6.4.1.1 Incorporation of Nano-CuO into LZSB Glass-Ceramic Coating

X-ray diffraction (XRD) analysis was conducted to investigate the phase composition and crystalline structure of the glass-ceramic coatings. The results, presented in Figure 6.6-8, provide an in-depth understanding of the phases present and their evolution under varying thermal treatments and nano-CuO additions.

XRD is a powerful technique for determining the crystalline phases present in a material by analyzing the diffraction patterns generated when X-rays interact with the atomic planes in the crystals. The diffraction pattern provides information about the interplanar spacing, crystal structure, and orientation of the phases. The phases identified in the glass-ceramic coatings are $SiO_2$ (PDF 04-008-7651), $Li_2ZnSiO_4$ (PDF 04-017-7279), and $Li_3PO_4$ (PDF 00-015-0760).

Figure 6.6-8 provides a comprehensive view of the XRD results for the studied LZBS samples crystallized at 750°C, 800°C, and 850°C with nano-CuO additions of 0.5, 1.0, 2.5, and 5.0 wt%. The figures include detailed ranges between 2θ: 20° – 28° and 2θ: 30° – 37°, highlighting the evolution of specific phases at different temperatures and nano-CuO concentrations. Figure 6.6 shows the overall XRD patterns at different temperatures, indicating the relative intensities of the $SiO_2$, $Li_2ZnSiO_4$, and $Li_3PO_4$ phases. Figure 6.7 and 6.8a-c focus on the XRD patterns in the 2θ ranges of 20° – 28° and 30° – 37°, respectively, which are critical for identifying and comparing the peak intensities of the crystalline phases. These specific ranges are chosen because they include the most prominent diffraction peaks for the phases of interest.

$SiO_2$, or quartz, is a major component of the glass matrix. It is primarily amorphous but can also exist in various crystalline forms such as quartz, cristobalite, and tridymite. In the context of glass-ceramics, $SiO_2$ acts as the structural backbone, providing the matrix within which crystalline phases nucleate and grow [317]. Quartz contributes to the mechanical strength, thermal stability, and chemical durability of the glass-ceramic material. Its high melting point and low thermal expansion coefficient help maintain structural integrity during thermal cycling [318].

Lithium zinc silicate ($Li_2ZnSiO_4$) is a crystalline phase that forms during the controlled heat treatment of the glass-ceramic. This phase is known for its desirable mechanical and thermal properties. The formation of $Li_2ZnSiO_4$ is influenced by the temperature and the presence of nucleating agents like nano-CuO. It typically crystallizes in specific temperature ranges, and its growth is promoted by the presence of zinc and lithium ions, which facilitate the formation of the silicate network [319]. Lithium phosphate ($Li_3PO_4$) is another important crystalline phase that forms in the glass-ceramic system. This phase is known for its high ionic conductivity and stability, making it relevant in applications such as solid electrolytes in batteries.

In the formation of quartz, $Li_2ZnSiO_4$, and $Li_3PO_4$ phases in phosphate-containing lithium zinc silicate glass-ceramics, initially, the glass composition, which includes $SiO_2$, $Li_2O$, ZnO, and $P_2O_5$, undergoes a controlled crystallization process. This process begins with nucleation, often facilitated by the presence of $P_2O_5$, which acts as a nucleating agent, leading to the formation of initial crystalline phases such as $Li_3PO_4$ and lithium disilicate ($Li_2Si_2O_5$). During heat treatment, the thermal energy provided induces the diffusion of lithium and zinc ions, promoting the formation of lithium zinc silicate ($Li_2ZnSiO_4$) phases [131]. The phase transformation mechanisms are primarily driven by the thermodynamics and kinetics of crystal growth. Differential thermal analysis (DTA) and X-ray diffraction (XRD) reveal that the crystallization of these phases is temperature-dependent, with distinct peaks indicating the formation temperatures of various phases. For instance, the crystallization of quartz and cristobalite phases typically occurs at higher temperatures compared to the lithium zinc silicate phases [321]. Additionally, the presence of ZnO in the glass composition serves as a network modifier, which can influence the glass network's structure by creating non-bridging oxygens, thus facilitating the crystallization of the $Li_2ZnSiO_4$ phase [322]. The incorporation of $P_2O_5$ not only aids in nucleation but also acts as a lithium ion scavenger, forming $Li_3PO_4$ phases that provide sites for heterogeneous nucleation. This process significantly enhances the crystallization of lithium metasilicate ($Li_2SiO_3$) and subsequently lithium disilicate phases during higher temperature annealing [323]. Moreover, the phase separation observed in these glass-ceramics, characterized by the formation of distinct phases such as quartz, $Li_2ZnSiO_4$, and $Li_3PO_4$, is critical

in determining the material's final properties, including its thermal expansion and mechanical strength [130]. The crystallization of $Li_3PO_4$ is also temperature-dependent and is influenced by the addition of nano-CuO.

At 750°C, the XRD patterns revealed that the intensity of the lithiophosphate ($Li_3PO_4$) phase increased with the addition of nano-CuO up to 2.5 wt%, followed by a slight decrease at 5 wt%. This trend suggests that nano-CuO acts as a nucleating agent, promoting the formation of $Li_3PO_4$ by providing additional nucleation sites. However, beyond a certain concentration, the availability of nucleation sites may become saturated, or the local chemical environment may change, inhibiting further growth.

When the crystallization temperature was increased to 800°C, both the $Li_3PO_4$ and $Li_2ZnSiO_4$ phases showed increased intensity. The enhancement in phase intensity at higher temperatures indicates that the overall crystallization kinetics are more favorable. The increased thermal energy at 800°C promotes the mobility of ions, facilitating the growth and stabilization of the crystalline phases. The preferential growth of $Li_3PO_4$ over $Li_2ZnSiO_4$ at this temperature may be due to the higher thermodynamic stability of the phosphate phase under these conditions.

At 850°C, the XRD patterns showed a further increase in the intensity of the $Li_3PO_4$ phase, while the increase in $Li_2ZnSiO_4$ was minimal. This differential behavior suggests complex interactions between nano-CuO concentration, thermal energy, and the intrinsic stability of the phases. Higher temperatures lead to greater ion mobility and diffusion, potentially facilitating the transformation or dissolution of less stable phases. The stability of $Li_3PO_4$ at these high temperatures may be due to its lower free energy compared to other potential phases.

The observed phase transformations can be attributed to several mechanisms influenced by temperature and nano-CuO concentration:

- Ion Mobility: Higher temperatures increase the mobility of ions, enhancing the diffusion rates and promoting the growth of stable crystalline phases. This increased mobility allows ions to overcome kinetic barriers and form more stable structures [130, 322 - 325].
- Nucleation and Growth Kinetics: Nano-CuO serves as a nucleating agent, reducing the energy barrier for nucleation and providing sites for crystal

growth. However, excessive nano-CuO can lead to the formation of secondary phases or alter the local stoichiometry, affecting the growth dynamics [170, 319].

- Thermodynamic Stability: The stability of different phases is influenced by temperature. Higher temperatures can alter the thermodynamic landscape, favoring the formation of phases with lower free energy [326 - 328]

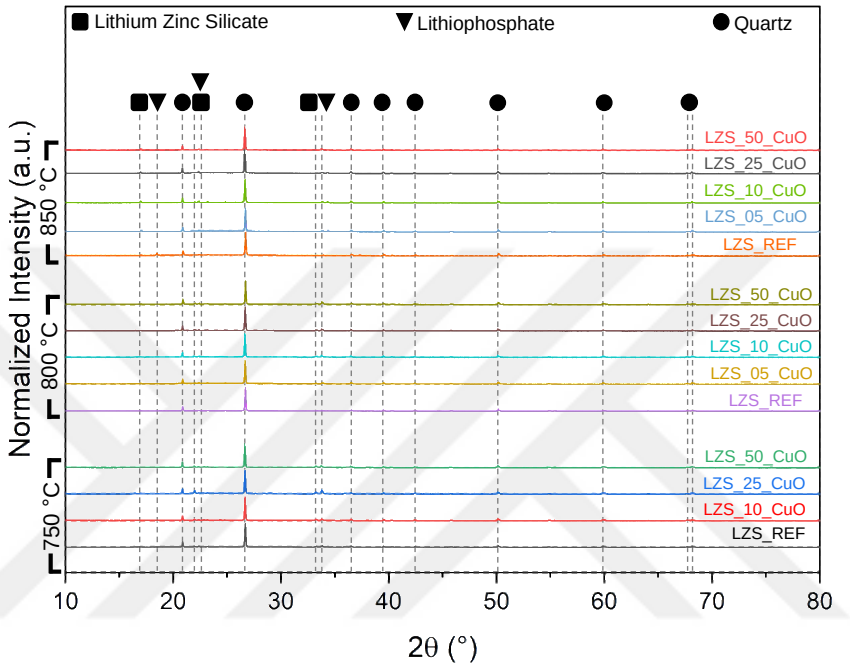



**Figure 6.6** XRD results of the studied LZBS samples crystallized a) at 750, 800 and 850 °C, with nano-copper oxide additions of 0.5, 1.0, 2.5, and 5.0 wt. %

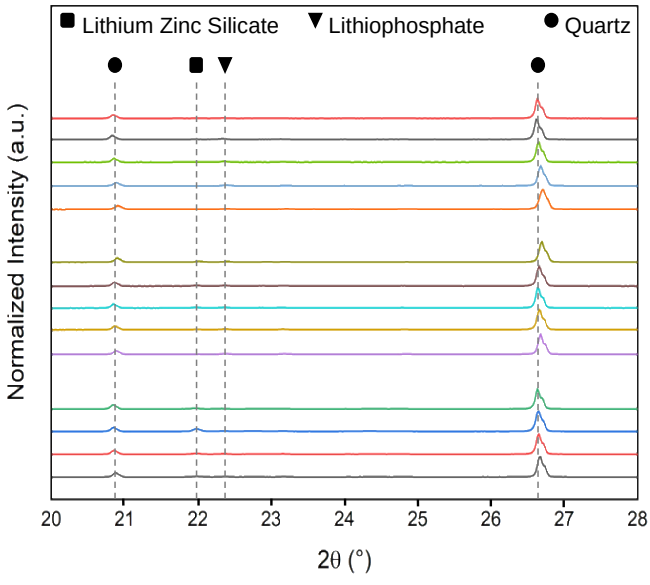


**Figure 6.7** XRD results of the studied LZBS samples crystallized at 750, 800 and 850 °C, with nano-copper oxide additions at ranges between 2θ: 20° – 28°.

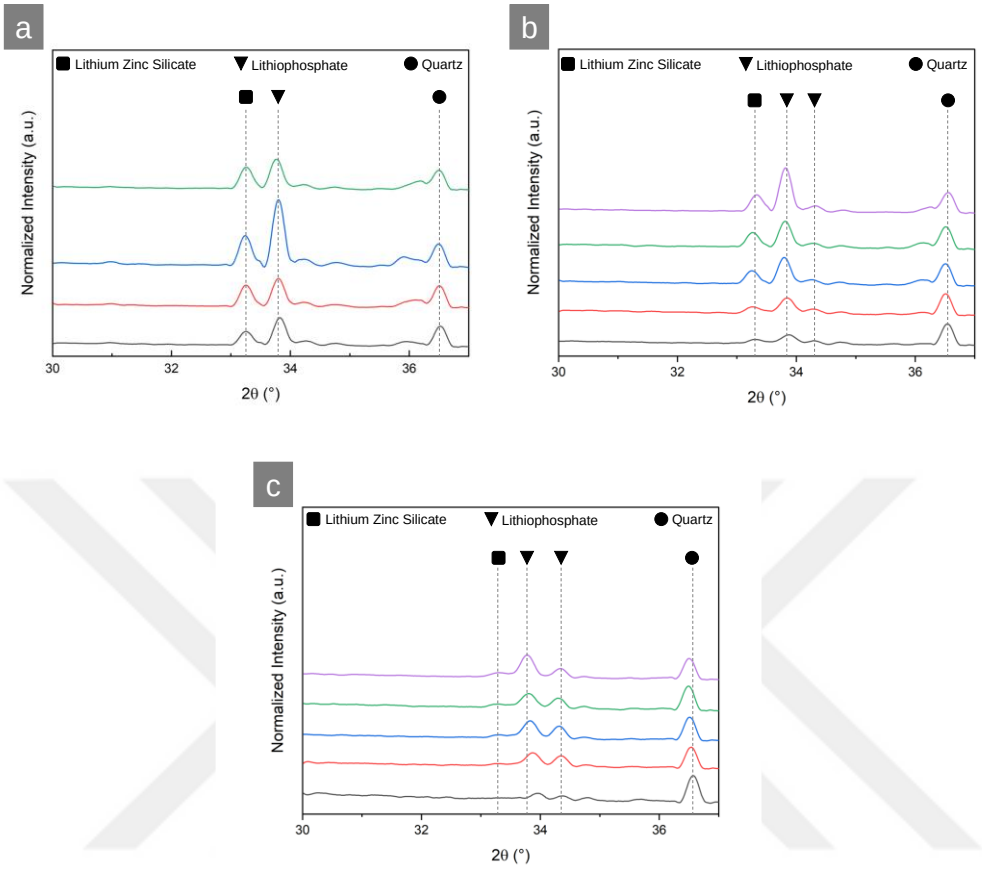



**Figure 6.8** XRD results of the studied LZBS samples crystallized with nano-copper oxide additions at ranges between 2θ: 30° – 37°, a) at 750 °C, b) at 800 °C, and c) at 850 °C.

The XRD analysis provided critical insights into the phase composition and structural evolution of the glass-ceramic coatings under varying nano-CuO additions and crystallization temperatures. The results indicate that nano-CuO significantly influences the nucleation and growth of crystalline phases, affecting the overall phase composition and stability. Understanding these interactions is essential for optimizing the thermal treatment processes to achieve desirable properties in glass-ceramic coatings. These findings contribute to the development of advanced glass-ceramic materials with tailored properties for specific applications, enhancing their performance and reliability.

### 6.4.1.2 Incorporation of Nano-ZnO into LZSB Glass-Ceramic Coating

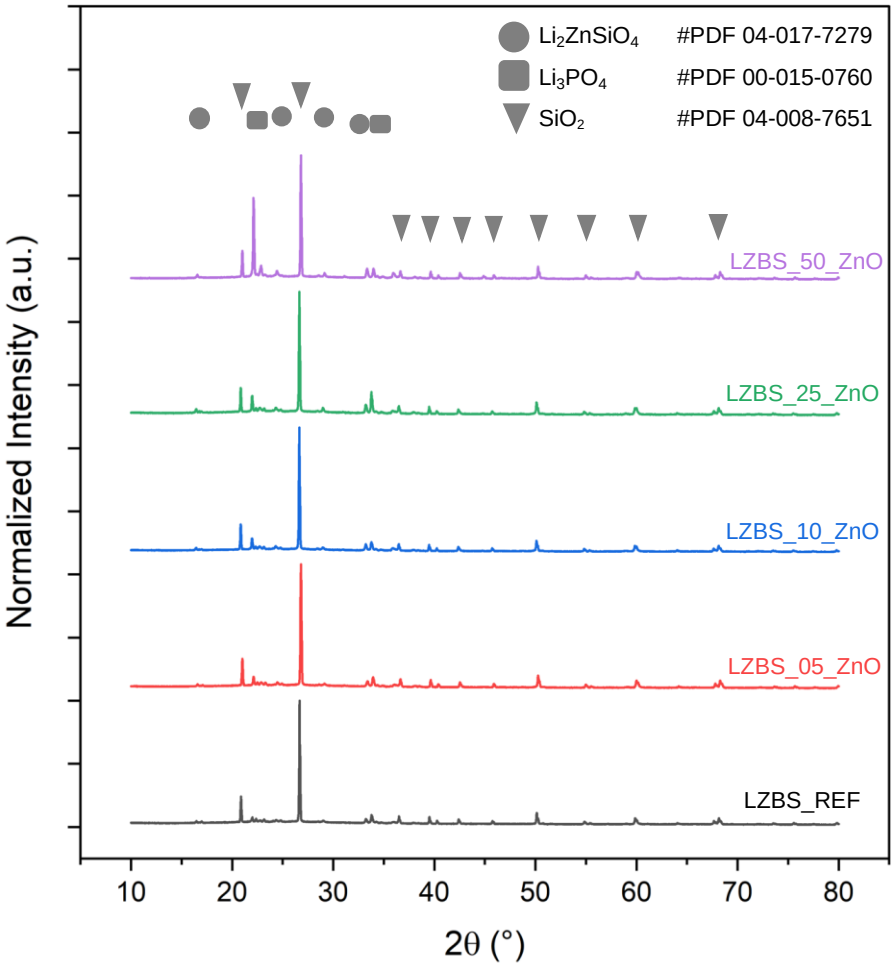



**Figure 6.9** XRD results of the studied LZBS samples crystallized with nano-zinc oxide additions of 0.5, 1.0, 2.5, and 5.0 wt. at 750 °C

The objective of the X-ray diffraction (XRD) analysis was to elucidate the impact of nano-ZnO incorporation on the crystallization behavior and phase stability of lithium zinc silicate ($Li_2ZnSiO_4$), lithium phosphate ($Li_3PO_4$), and quartz ($SiO_2$). Figure 6.9-11 provides a comprehensive view of the XRD results for the studied LZBS samples crystallized at 750°C, 800°C, and 850°C with nano-ZnO additions of 0.5, 1.0, 2.5, and 5.0 wt%.

At 750°C, the $Li_2ZnSiO_4$ phase demonstrated an increase in peak intensity with higher nano-ZnO concentrations, suggesting that nano-ZnO promotes the crystallization or enhances the phase stability of $Li_2ZnSiO_4$ under these conditions. Conversely, the $Li_3PO_4$ peaks exhibited only slight intensification, implying a lesser but noticeable influence of nano-ZnO on its crystallization. Notably, the quartz

phase displayed remarkable stability, with no significant intensity variation across different nano-ZnO concentrations, underscoring its robustness against compositional fluctuations at this temperature.

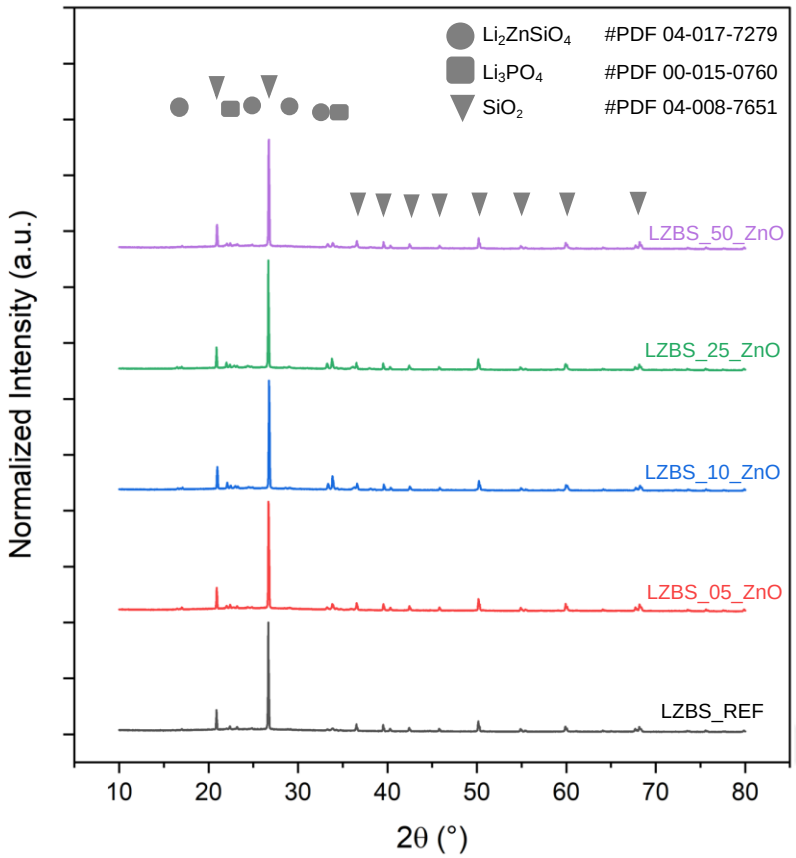



**Figure 6.10** XRD results of the studied LZBS samples crystallized with nano-zinc oxide additions of 0.5, 1.0, 2.5, and 5.0 wt. at 800 °C

Elevation to 800°C yielded similar trends with some nuanced differences (Figure 6.10). While the $Li_2ZnSiO_4$ phase continued to show increased peak intensities with rising nano-ZnO content till 2.5 wt. % addition, the overall peak intensities were somewhat attenuated compared to those observed at 750°C. This attenuation might be indicative of a thermal effect that modulates the crystallization dynamics of this phase at elevated temperatures. The $Li_3PO_4$ and $SiO_2$ phases maintained their behavior from the lower temperature, with $Li_3PO_4$ showing slight increases in intensity and $SiO_2$ remaining inert.

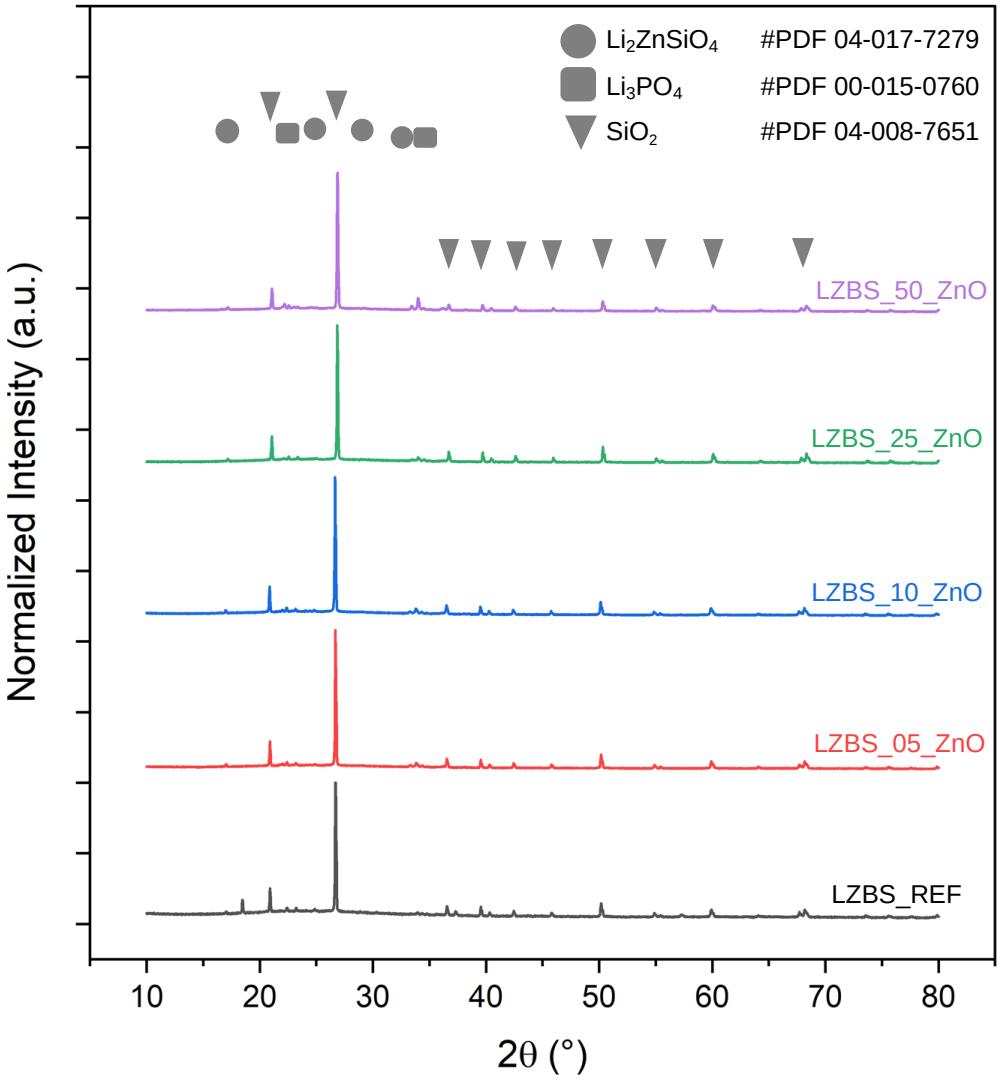



**Figure 6.11** XRD results of the studied LZBS samples crystallized with nano-zinc oxide additions of 0.5, 1.0, 2.5, and 5.0 wt. at 850 °C

At the highest tested temperature of 850°C, the continuation of increasing peak intensities for $Li_2ZnSiO_4$ was evident, reaffirming the role of nano-ZnO in facilitating this phase's formation across a spectrum of high temperatures (Figure 6.11). Interestingly, the $Li_3PO_4$ phase displayed more pronounced peak intensities than observed at lower temperatures, which could suggest a shift toward greater phase stability or predominance at 850°C. Quartz maintained its phase stability with consistent peak intensities, highlighting its inert and stable nature under high thermal conditions.

The observations from the XRD analysis provide profound insights into the thermal behavior and phase development dynamics of nano-ZnO-doped ceramic materials.

The data reveal that nano-ZnO not only enhances the crystallization of $Li_2ZnSiO_4$ but also slightly promotes the crystallization of $Li_3PO_4$, with no discernible impact on the quartz phase. These findings are pivotal for tailoring the synthesis and processing conditions of ceramic materials to achieve desired structural properties and phase compositions.

## 6.5 Morphology Analyses

### 6.5.1 Scanning Electron Microscopy (SEM) Analyses

#### 6.5.1.1 Incorporation of Nano-CuO into LZSB Glass-Ceramic Coating

Scanning Electron Microscopy (SEM) was employed to investigate the detailed morphological characteristics of the glass-ceramic coatings. SEM provides high-resolution images that reveal crucial insights into the microstructure, including crystal size, shape, distribution, and boundaries. These observations are essential for understanding the effects of nano-CuO addition and crystallization temperature on the structural integrity and properties of the coatings. The SEM images illustrate a significant correlation between the addition of nano-CuO and the distinct boundaries observed between quartz ($SiO_2$) crystals and lithium zinc silicate ($Li_2ZnSiO_4$)-lithium phosphate ($Li_3PO_4$) crystals. These findings are corroborated by X-ray diffraction (XRD) and Energy Dispersive X-ray Spectroscopy (EDS) analyses, which confirm the phase composition and elemental distribution within the samples.

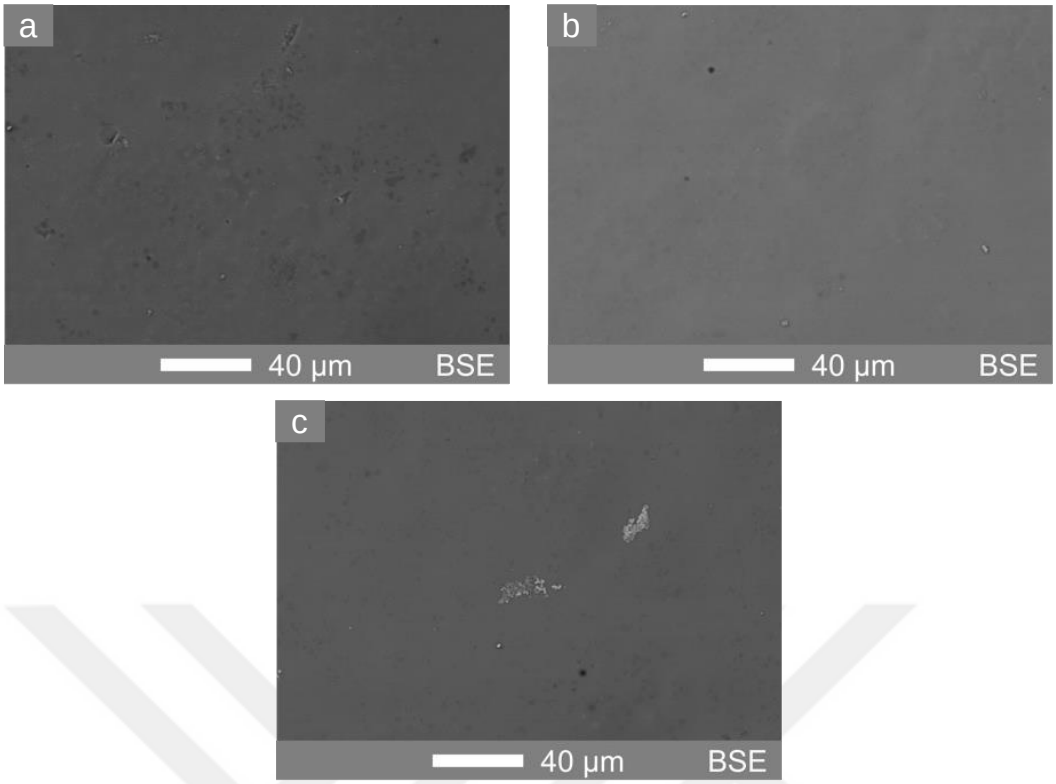



**Figure 6.12** SEM images of the studied LZBS reference samples without additions a) at 750 °C, b) at 800 °C, and c) at 850 °C

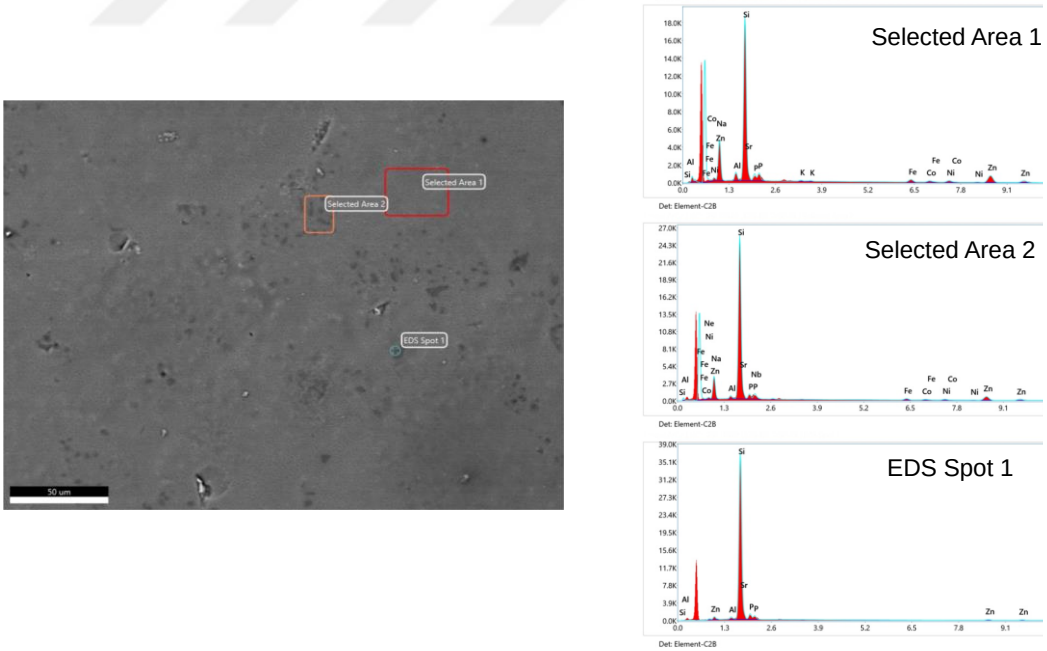



**Figure 6.13** SEM image (left) and EDS analyses of the defined parts (right) of the LZBS_REF sample at 750 °C

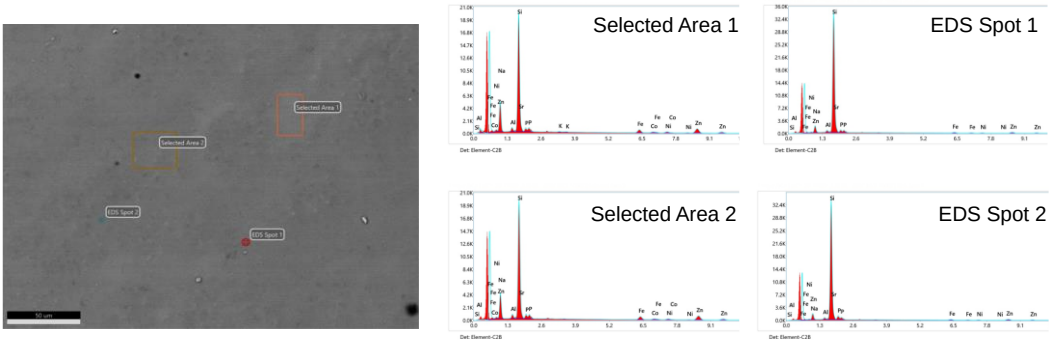



**Figure 6.14** SEM image (left) and EDS analyses of the defined parts (right) of the LZBS_REF sample at 800 °C

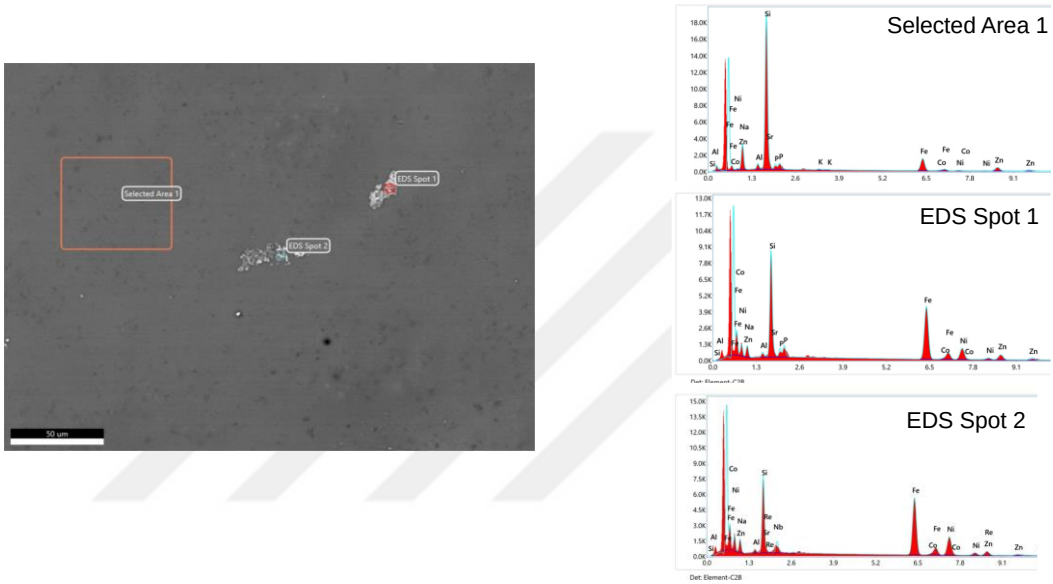



**Figure 6.15** SEM image (left) and EDS analyses of the defined parts (right) of the LZBS_REF sample at 850 °C

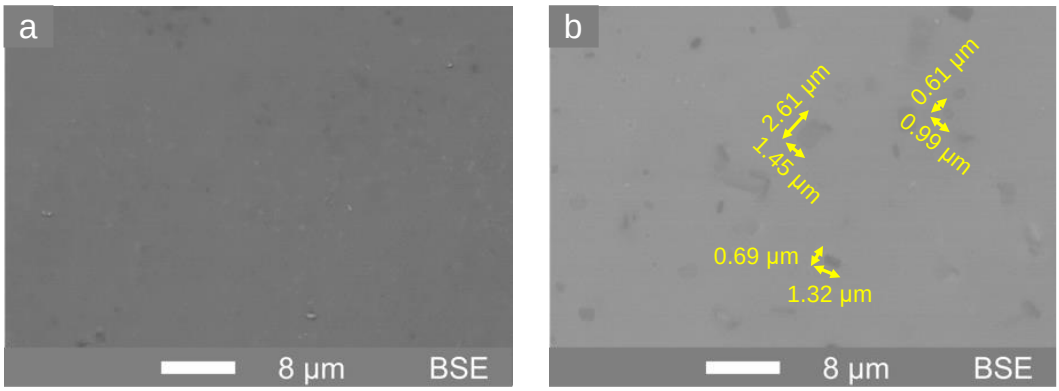



**Figure 6.16** SEM images of the studied LZBS reference samples with 0.5 wt. % nano-CuO addition a) at 800 °C, and b) at 850 °C

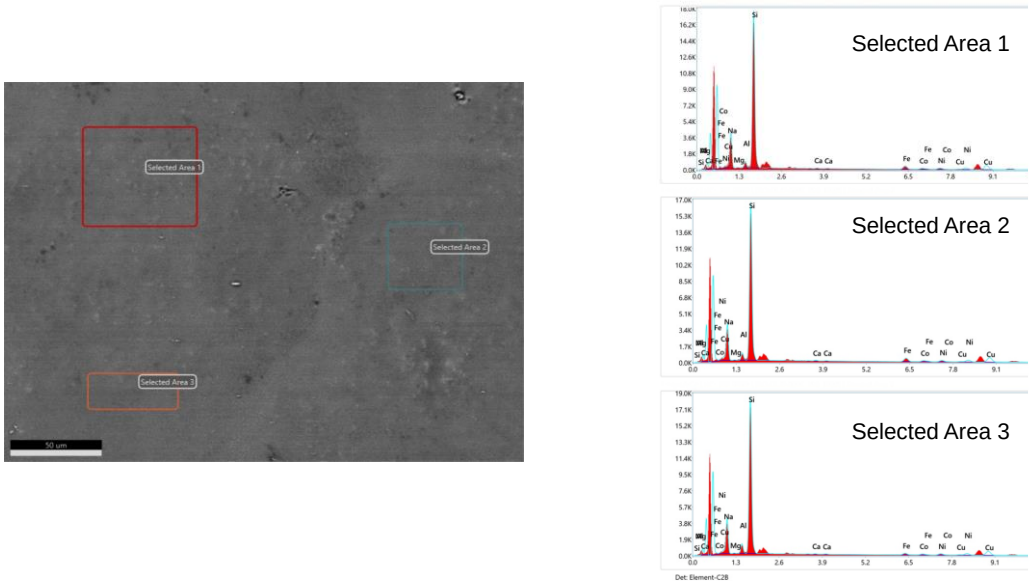



**Figure 6.17** SEM image (left) and EDS analyses of the defined parts (right) of the LZBS_05_CuO sample at 800 °C

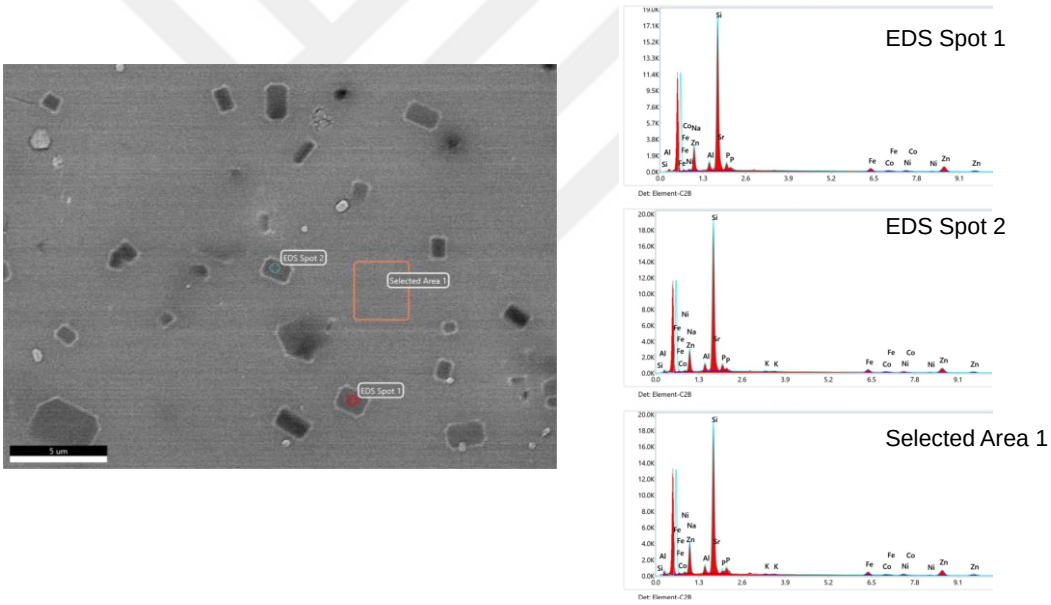



**Figure 6.18** SEM image (left) and EDS analyses of the defined parts (right) of the LZBS_05_CuO sample at 850 °C

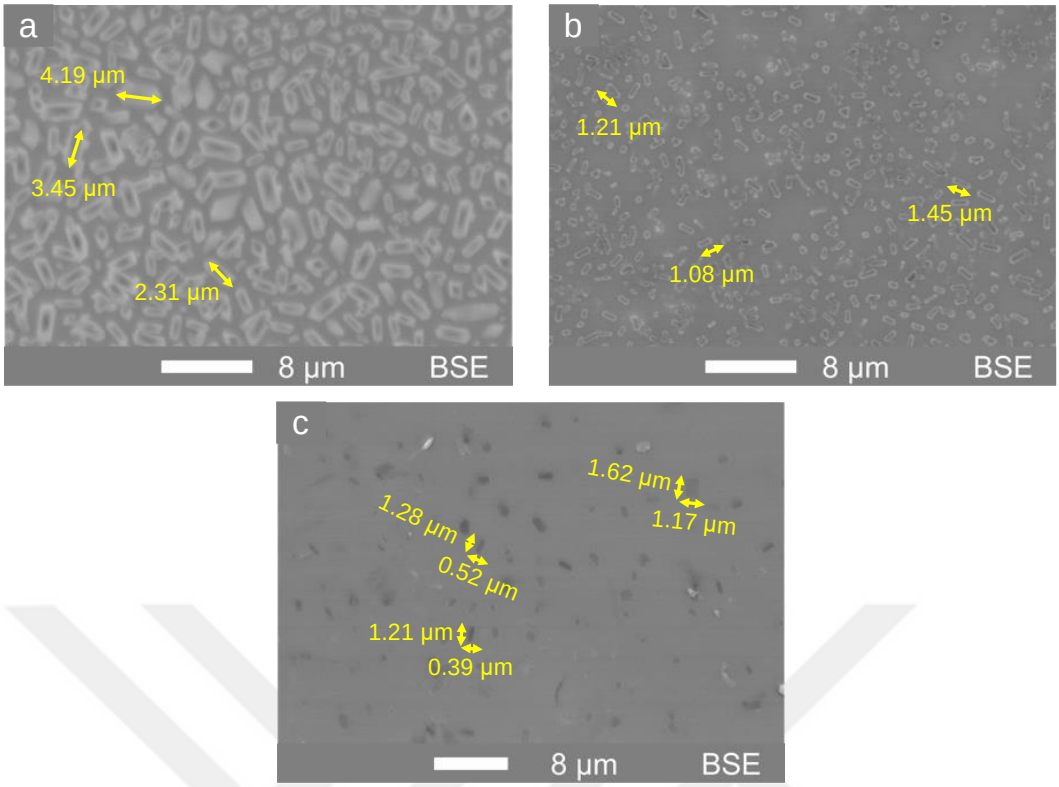



**Figure 6.19** SEM images of the studied LZBS reference samples with 1.0 wt. % nano-CuO addition a) at 750 °C, b) at 800 °C, and c) at 850 °C

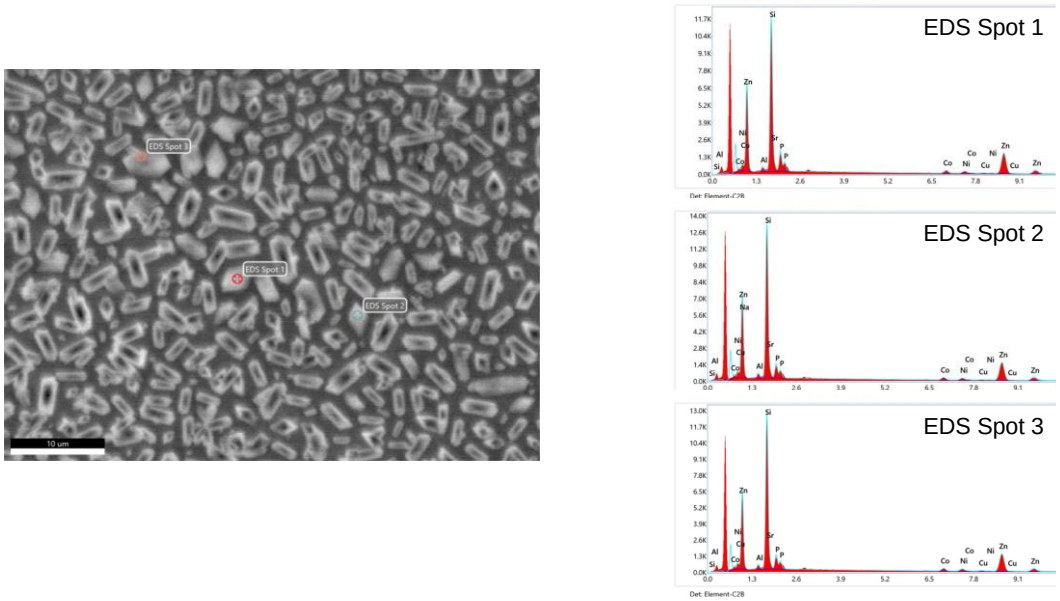



**Figure 6.20** SEM image (left) and EDS analyses of the defined parts (right) of the LZBS_10_CuO sample at 750 °C

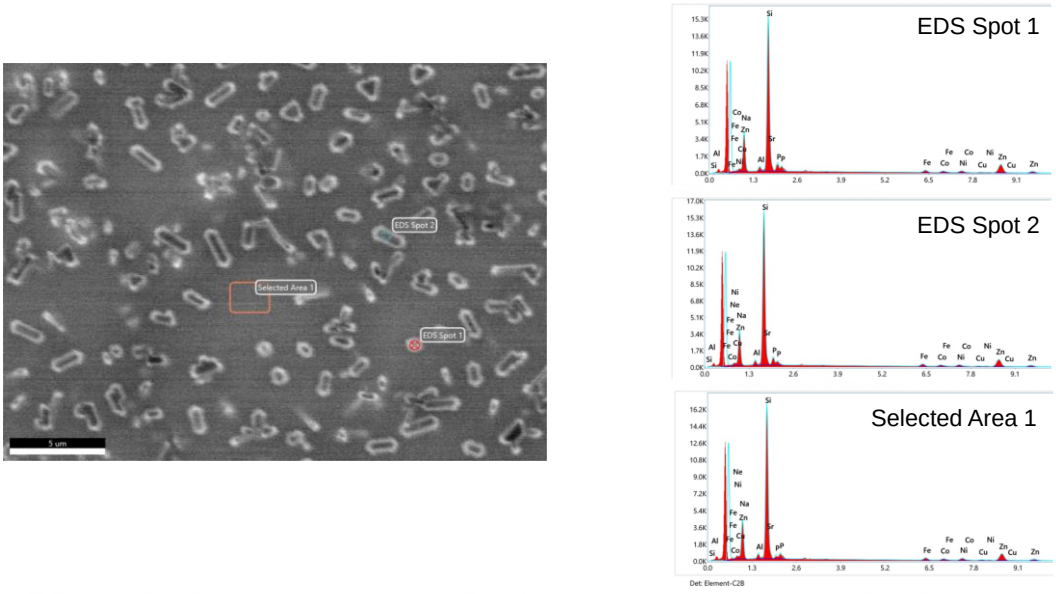



**Figure 6.21** SEM image (left) and EDS analyses of the defined parts (right) of the LZBS_10_CuO sample at 800 °C

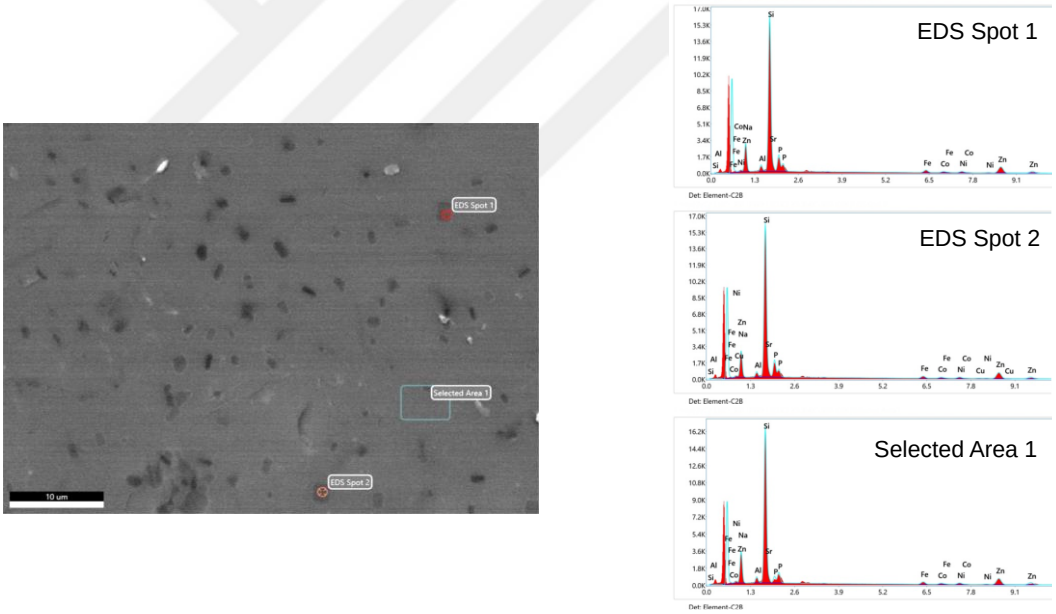



**Figure 6.22** SEM image (left) and EDS analyses of the defined parts (right) of the LZBS_10_CuO sample at 850 °C

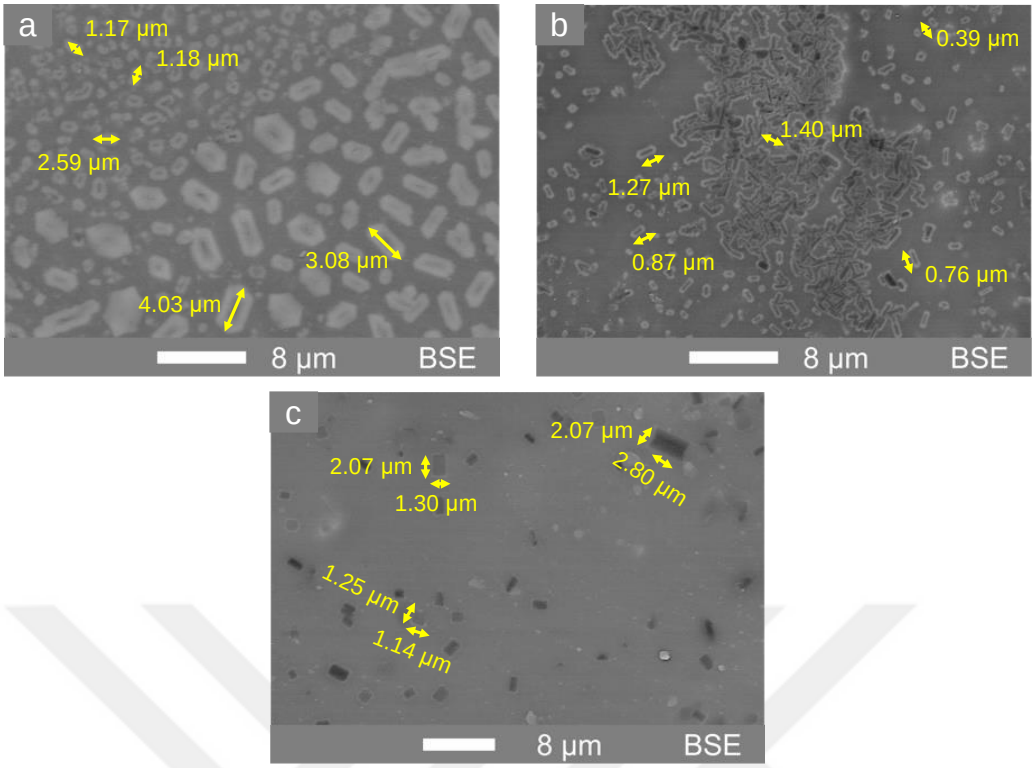



**Figure 6.23** SEM images of the studied samples with 2.5 wt. % nano-CuO addition and crystallized a) at 750 °C, b) at 800 °C, and c) at 850 °C

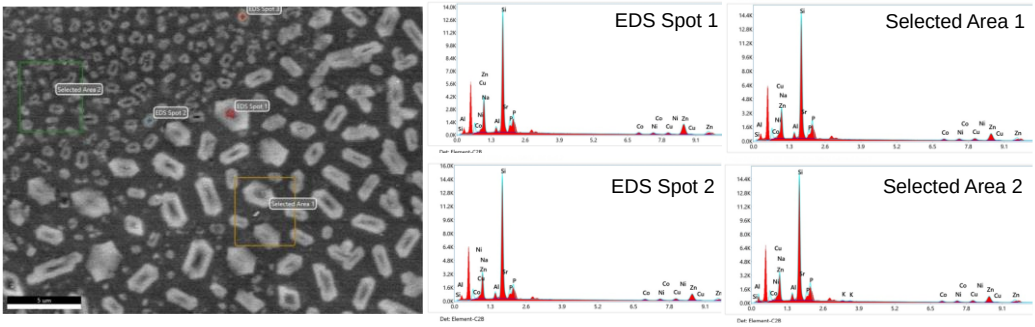



**Figure 6.24** SEM image (left) and EDS analyses of the defined parts (right) of the LZBS_25_CuO sample at 750 °C

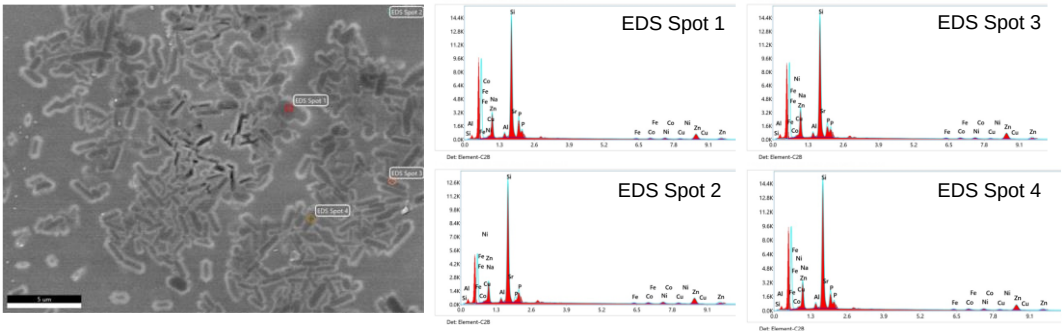



**Figure 6.25** SEM image (left) and EDS analyses of the defined parts (right) of the LZBS_25_CuO sample at 800 °C

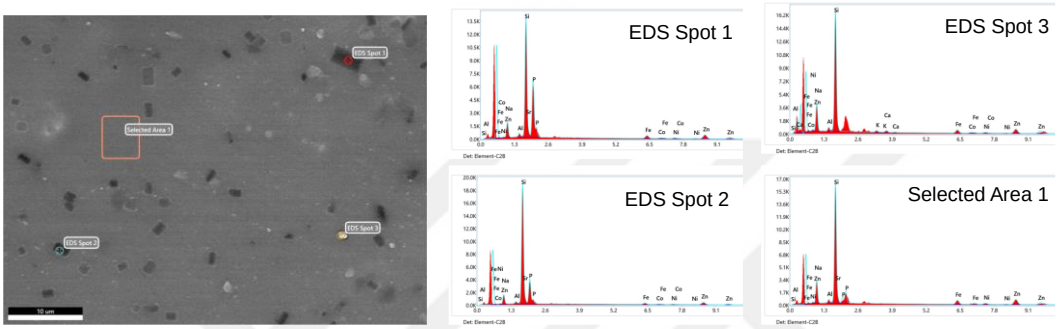



**Figure 6.26** SEM image (left) and EDS analyses of the defined parts (right) of the LZBS_25_CuO sample at 850 °C

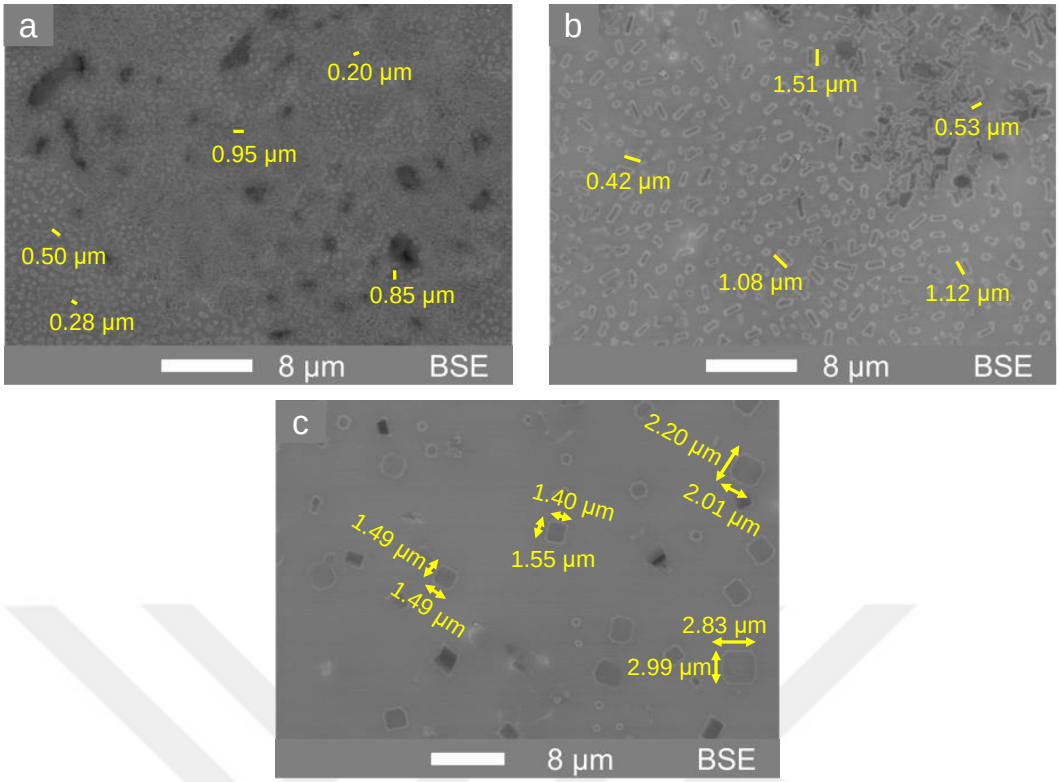



**Figure 6.27** SEM images of the studied LZBS reference samples with 2.5 wt. % nano-CuO addition a) at 750 °C, b) at 800 °C, and c) at 850 °C

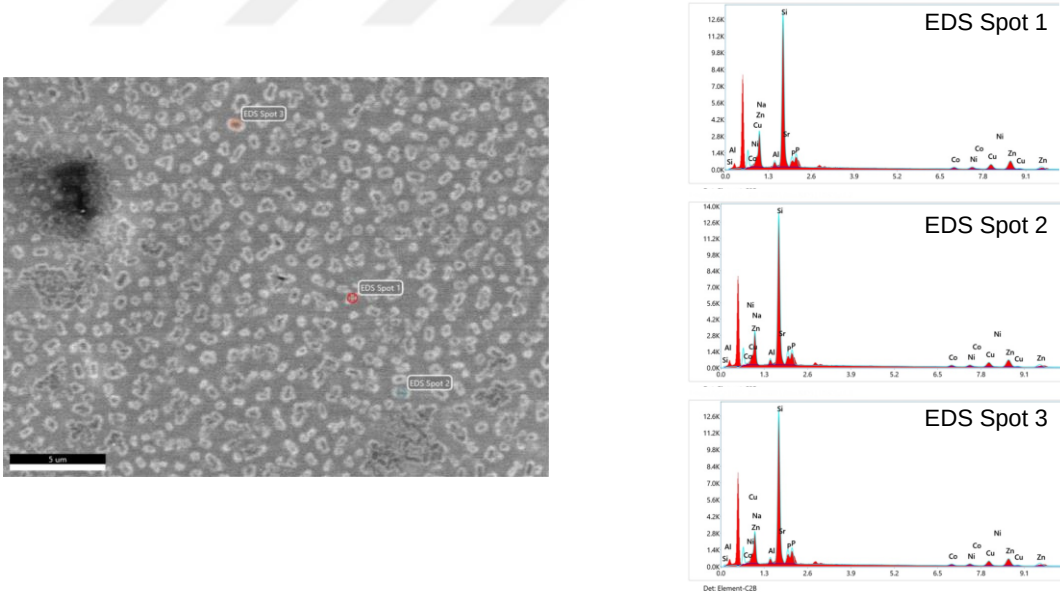



**Figure 6.28** SEM image (left) and EDS analyses of the defined parts (right) of the LZBS_50_CuO sample at 750 °C

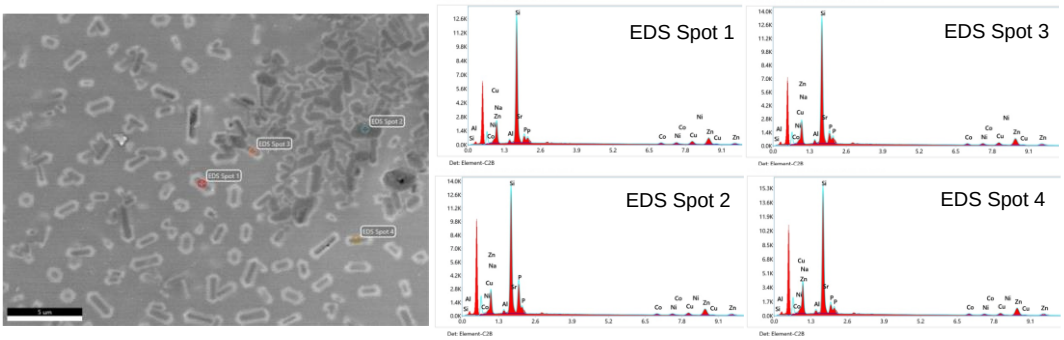



**Figure 6.29** SEM image (left) and EDS analyses of the defined parts (right) of the LZBS_50_CuO sample at 800 °C

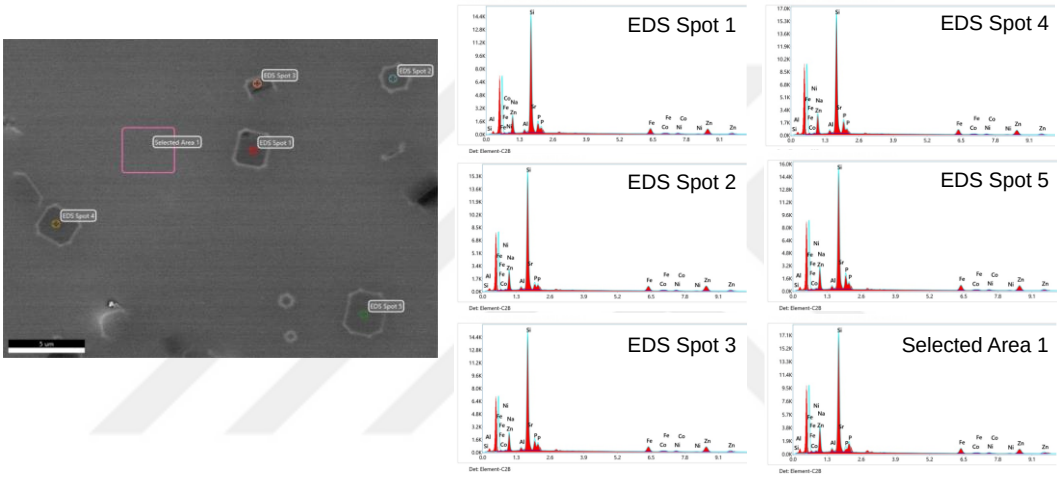



**Figure 6.30** SEM image (left) and EDS analyses of the defined parts (right) of the LZBS_50_CuO sample at 850 °C

In the context of glass-ceramics, $SiO_2$ typically forms the primary glass matrix. As an amorphous phase, $SiO_2$ provides the structural framework that hosts crystalline phases. Its presence contributes to the overall mechanical strength, thermal stability, and chemical durability of the glass-ceramic material [142, 329]. Lithium zinc silicate ($Li_2ZnSiO_4$) crystalline phase is crucial for imparting hardness and thermal stability to the glass-ceramic. The $Li_2ZnSiO_4$ phase forms within specific temperature ranges and is facilitated by the presence of nucleating agents like nano-CuO [321, 325]. Lithium phosphate ($Li_3PO_4$) is known for its high ionic conductivity and stability, the $Li_3PO_4$ phase significantly enhances the electrochemical properties of the glass-ceramic. Its formation is promoted by the crystallization process, which is influenced by both temperature and the addition of nano-CuO [330, 331].

Nano-CuO has a profound impact on the nucleation and growth of crystalline phases within the glass-ceramic coatings. Nano-CuO particles act as heterogeneous nucleation sites, lowering the energy barrier for nucleation. These sites provide favorable locations for the initial formation of crystalline nuclei, promoting the growth of specific phases while inhibiting others. This selective promotion or inhibition leads to well-defined phase boundaries [319, 332]. The presence of nano-CuO results in the preferential growth of certain crystalline phases, such as $Li_3PO_4$ and $Li_2ZnSiO_4$, as observed in the SEM images.

Variations in the CTEs of different crystalline phases and nano-CuO introduce internal stress during the cooling process. As the material cools, discrepancies in expansion and contraction rates generate mechanical stress [333]. This stress leads to the delineation of phase boundaries and contributes to the observed morphology. The SEM images show distinct phase separations, which can be attributed to the differential thermal expansion between the matrix and the embedded crystalline phases.

SEM images at 750°C reveal increased inter-crystal spacing and decreased crystal size with higher nano-CuO concentrations (Figure 6.12a, 13, 19a, 20, 23a, 24, 27a, 28). Despite the general expectation that higher temperatures facilitate crystal growth, the observed crystals begin to decompose at this temperature due to their lower melting points relative to the crystallization temperature. This decomposition underscores the thermal stability limits of the crystals within the glass-ceramic matrix. The nano-CuO particles promote the formation of smaller, well-distributed crystals, resulting in a more uniform microstructure. The distinct phase boundaries between $SiO_2$, $Li_2ZnSiO_4$, and $Li_3PO_4$ are clearly visible, indicating effective nucleation and growth control by nano-CuO.

At 800°C, SEM images show a reduction in crystal size with increasing nano-CuO content (Figure 6.12b, 14, 16a, 17, 19b, 21, 23b, 25, 27b, 29). This trend results from the enhanced nucleation rate induced by nano-CuO, which leads to the formation of numerous smaller crystals rather than fewer larger ones. Partial agglomeration of crystals is also observed in samples with higher nano-CuO content, indicating the influence of nucleation site saturation. The increased thermal energy at this temperature promotes the growth and stabilization of $Li_2ZnSiO_4$ and

$Li_3PO_4$ phases [334]. The images reveal more pronounced crystallization and better-defined phase boundaries compared to lower temperatures.

At 850°C, SEM images exhibit a significant increase in inter-crystal distance, along with crystal melting and integration into the glass matrix (Figure 6.12c, 15, 16b, 18, 19c, 22, 23c, 26, 27c, 30). The high temperature surpasses the melting points of some crystalline phases, leading to their dissolution and incorporation into the amorphous matrix. This process enhances the homogeneity of the glass-ceramic material. The SEM images at this temperature show reduced distinctiveness of individual crystalline phases due to their partial melting and integration. The material becomes more homogeneous, with fewer distinct phase boundaries visible.

The SEM analysis also provides insights into the adhesion between the glass-ceramic coating and the steel substrate. The detachment of the 0.5% nano-CuO modified glass-ceramic coating crystallized at 750°C indicates suboptimal adhesion. This issue arises from the mismatch in CTEs between the steel substrate and the glass-ceramic matrix, exacerbated by the addition of nano-CuO. The reduced CTE of the glass-ceramic increases the thermal expansion mismatch, generating internal stresses during cooling that exceed the mechanical strength of the bond at the interface.

To enhance interfacial bonding, transition metal oxides such as NiO and CoO were incorporated into the coating composition. These oxides were expected to form stronger chemical bonds between the glass-ceramic and the steel [3]. However, the intermediate layer formed was too thin to effectively bridge the CTE differences, leading to persistent interfacial stresses during cooling and subsequent coating detachment of LZS_05_CuO sample crystallized at °C 750 C.

The SEM analysis provides a comprehensive understanding of the morphological characteristics of the glass-ceramic coatings. The addition of nano-CuO significantly influences crystal growth, phase boundaries, and interfacial bonding. The observed microstructural changes at different temperatures and nano-CuO concentrations are crucial for optimizing the thermal treatment processes and enhancing the material properties of the glass-ceramic coatings. These findings contribute to the development of advanced glass-ceramic materials with tailored properties for specific applications, ensuring improved performance and reliability.

### 6.5.1.2 Incorporation of Nano-ZnO into LZSB Glass-Ceramic Coating

The SEM images, organized by rows corresponding to increasing temperatures of 750°C, 800°C, and 850°C, reveal distinct microstructural features that correlate with the nano-ZnO concentration in the samples. These observations are instrumental in understanding the influence of nano-ZnO on ceramic phase behavior and morphology.

At the lowest examined temperature of 750°C (Figure 6.31-35), the SEM images initially exhibit a dense, heterogeneous matrix indicative of the quartz-dominant phase stability, consistent with the stable quartz peaks observed in XRD. As nano-ZnO content increases, there is a noticeable emergence of brighter regions within the matrix. These regions likely represent areas of concentrated $Li_2ZnSiO_4$ and $Li_3PO_4$ crystallization, a hypothesis supported by the slight intensification of these phases' peaks in XRD analysis. This suggests that nano-ZnO may act as a nucleating agent, lowering the energy barrier for the formation of these phases, as proposed in the literature where additives are shown to facilitate phase nucleation by providing energetically favorable sites for crystal growth [320].

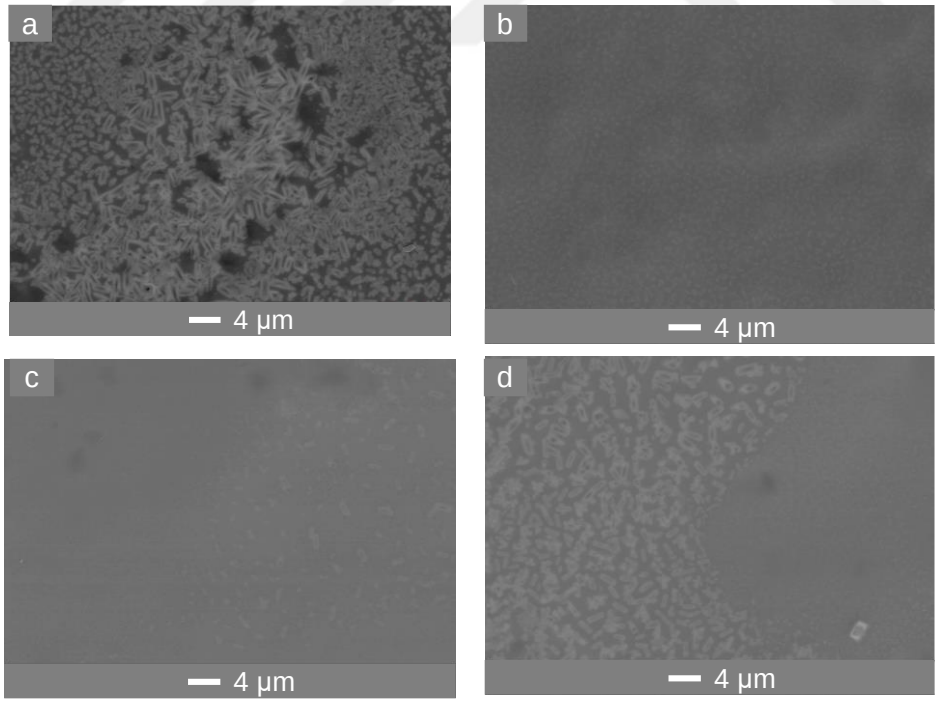



**Figure 6.31** SEM images of the studied LZBS samples crystallized at 750 °C with addition of a) 0.5 wt.%, b) 1.0 wt.%, c) 2.5 wt.%, and d) a) 5.0 wt.% nano-ZnO

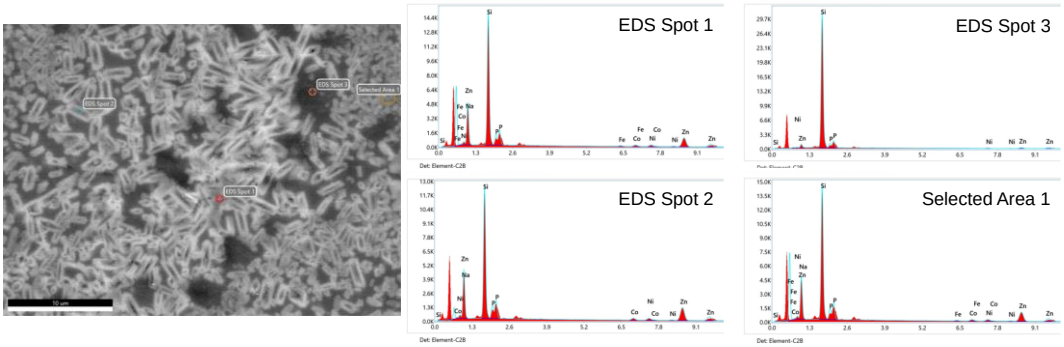



**Figure 6.32** SEM image (left) and EDS analyses of the defined parts (right) of the LZBS_05_ZnO sample at 750 °C

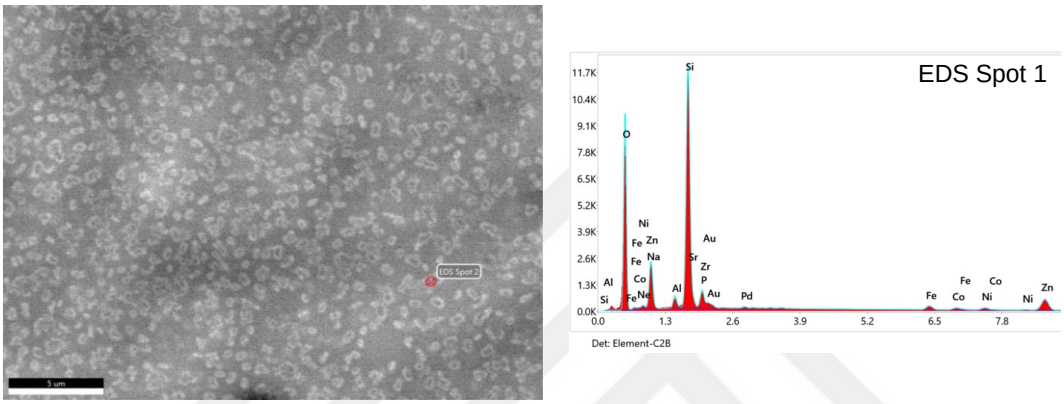



**Figure 6.33** SEM image (left) and EDS analyses of the defined parts (right) of the LZBS_10_ZnO sample at 750 °C

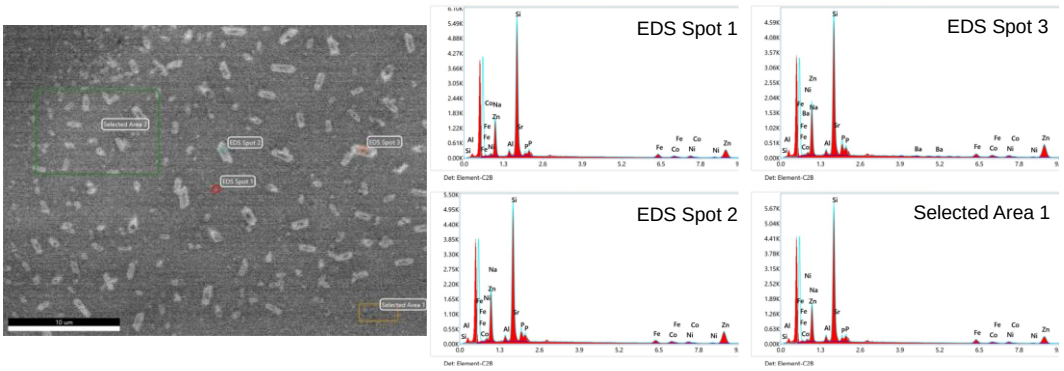



**Figure 6.34** SEM image (left) and EDS analyses of the defined parts (right) of the LZBS_25_ZnO sample at 750 °C

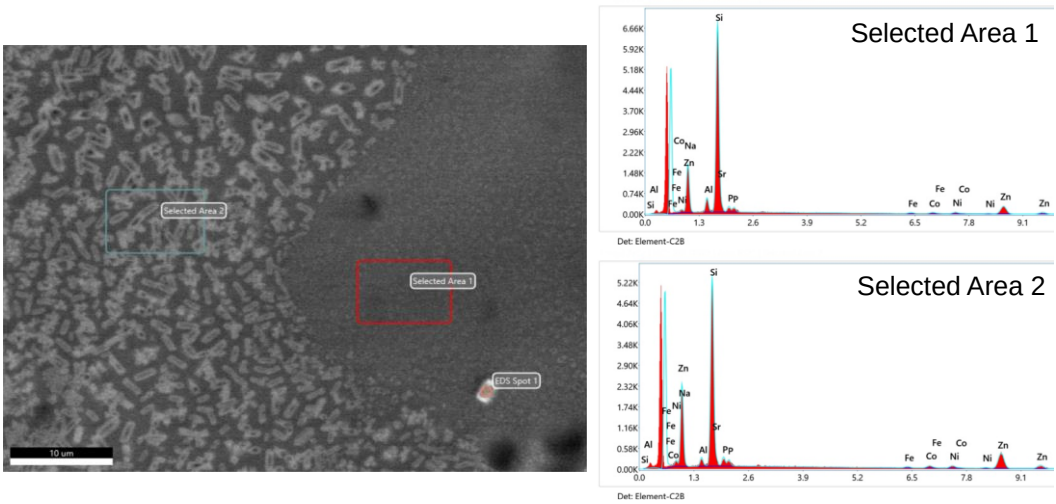



**Figure 6.35** SEM image (left) and EDS analyses of the defined parts (right) of the LZBS_50_ZnO sample at 750 °C

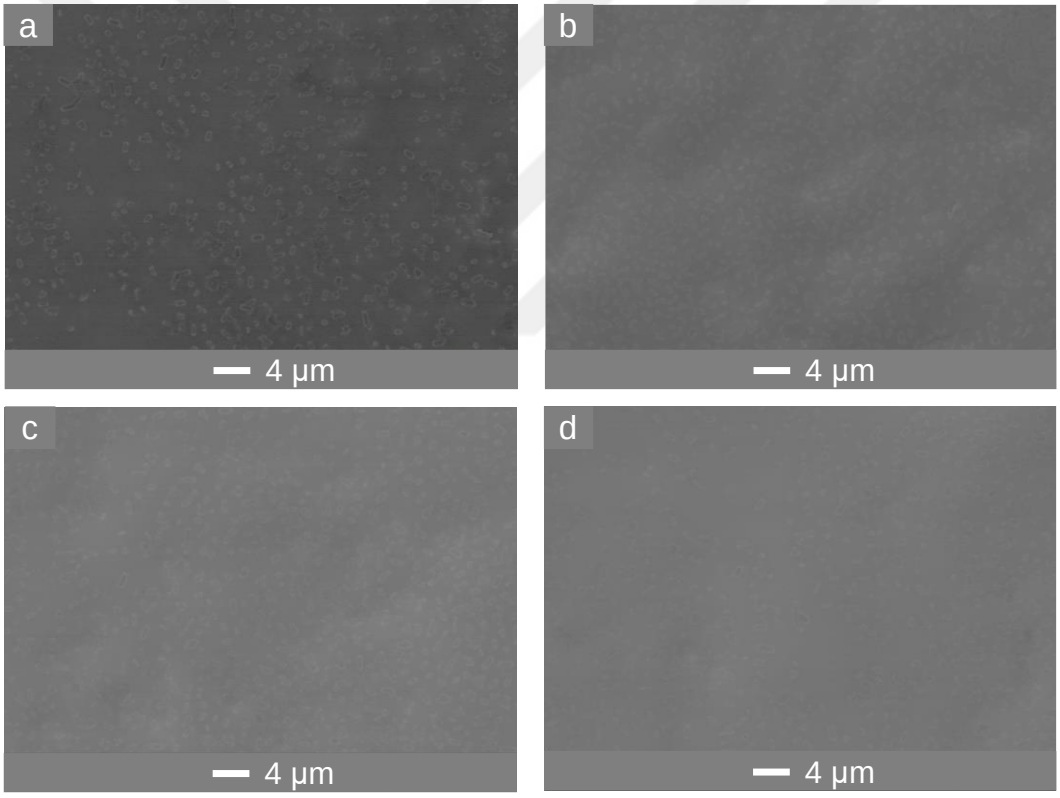



**Figure 6.36** SEM images of the studied LZBS samples crystallized at 800 °C with addition of a) 0.5 wt.%, b) 1.0 wt.%, c) 2.5 wt.%, and d) a) 5.0 wt.% nano-ZnO

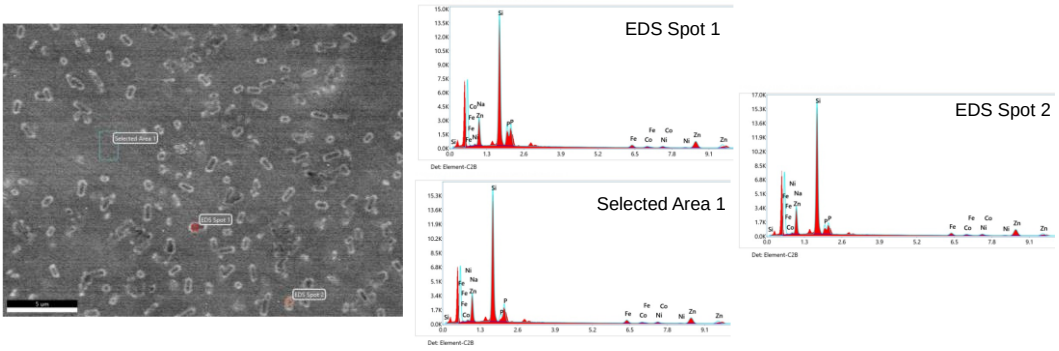



**Figure 6.37** SEM image (left) and EDS analyses of the defined parts (right) of the LZBS_05_ZnO sample at 800 °C

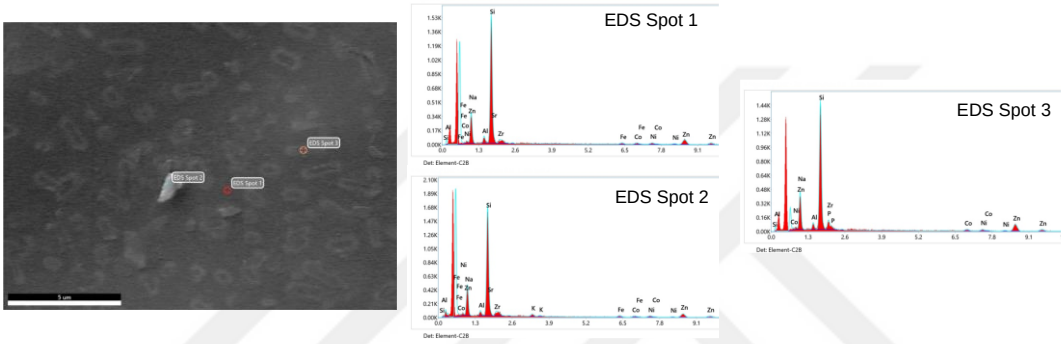



**Figure 6.38** SEM image (left) and EDS analyses of the defined parts (right) of the LZBS_10_ZnO sample at 800 °C

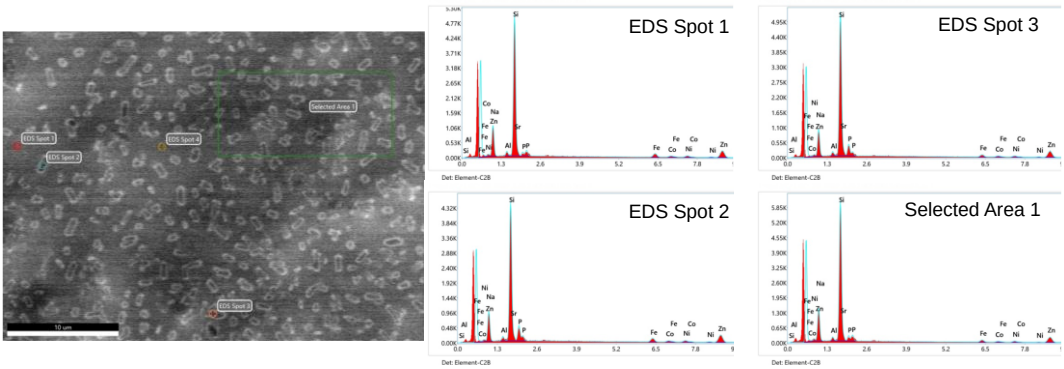



**Figure 6.39** SEM image (left) and EDS analyses of the defined parts (right) of the LZBS_25_ZnO sample at 800 °C

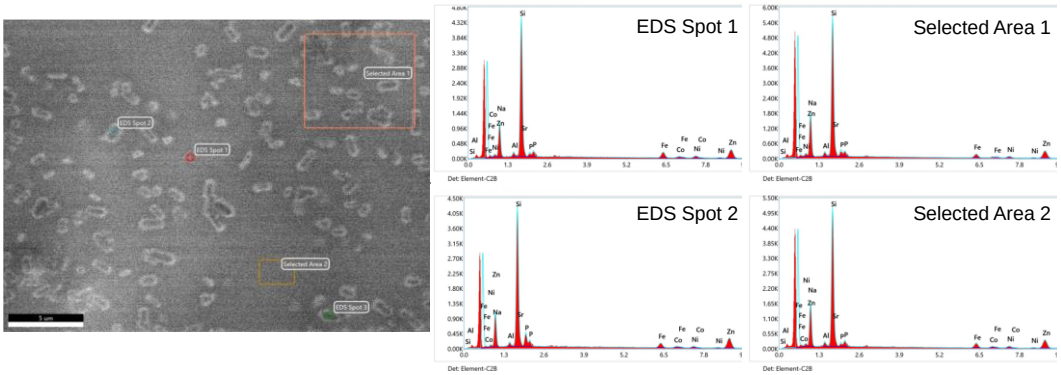



**Figure 6.40** SEM image (left) and EDS analyses of the defined parts (right) of the LZBS_50_ZnO sample at 800 °C

At 800°C, the micrographs from this intermediate temperature setting show an evolution towards a more granular and heterogeneous structure (Figure 6.36-40). This textural change points to increased crystalline growth, especially of $Li_2ZnSiO_4$, aligning with its enhanced peak intensities in the XRD results. The increased granularity can be interpreted as the result of enhanced kinetic energy available at this higher temperature, allowing for more rapid nucleation and growth of crystalline phases. The presence of these granular textures supports the notion that ZnO not only facilitates nucleation but also influences the growth rate of these phases [335].

At the highest temperature of 850°C (Figure 6.41-45), the SEM images show further pronounced crystalline regions, indicative of significant phase evolution and growth. The bright spots and clusters are consistent with the lithium zinc silicate and lithium phosphate phases, reflecting the marked peak intensity increases observed in the XRD analysis. At this elevated temperature, the thermal energy likely promotes the diffusion of ions across phase boundaries, enhancing the interfacial reactions that lead to more distinct and larger crystalline formations [336].

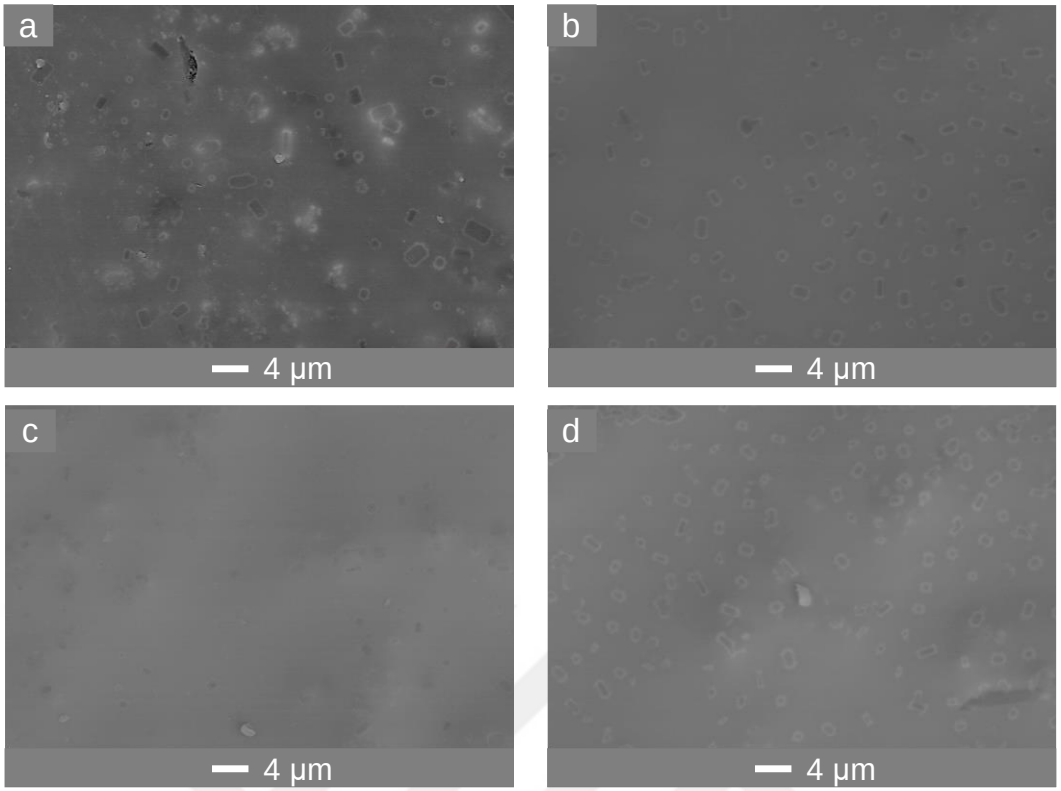



**Figure 6.41** SEM images of the studied LZBS samples crystallized at 850 °C with addition of a) 0.5 wt.%, b) 1.0 wt.%, c) 2.5 wt.%, and d) a) 5.0 wt.% nano-ZnO

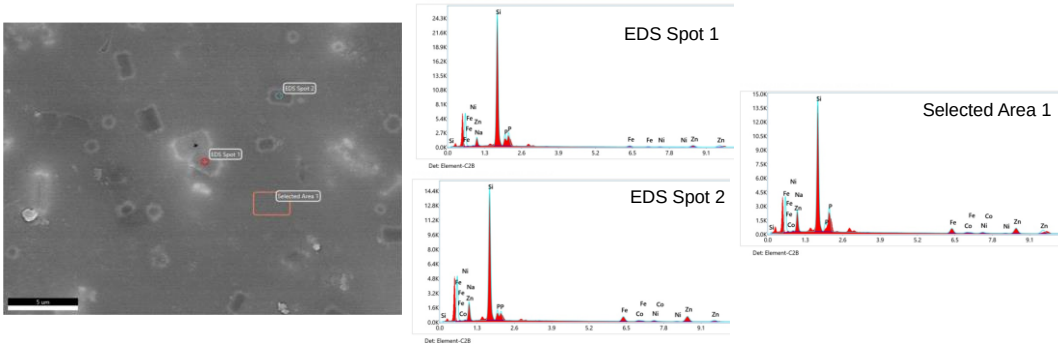



**Figure 6.42** SEM image (left) and EDS analyses of the defined parts (right) of the LZBS_05_ZnO sample at 850 °C

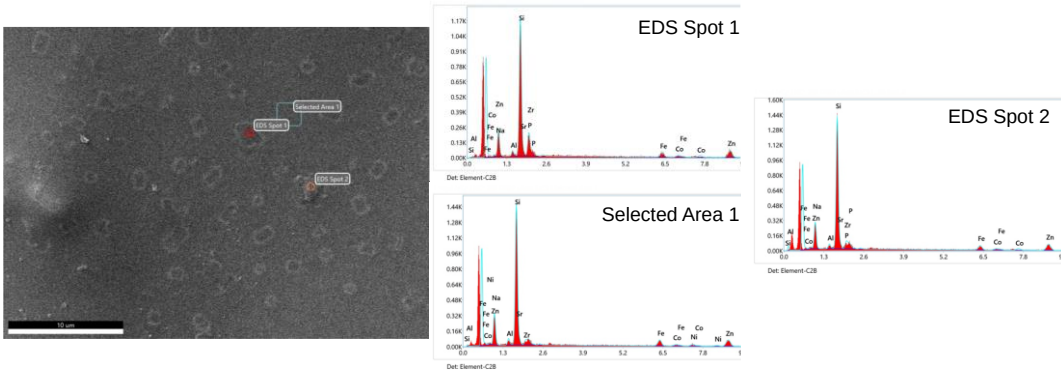



**Figure 6.43** SEM image (left) and EDS analyses of the defined parts (right) of the LZBS_10_ZnO sample at 850 °C

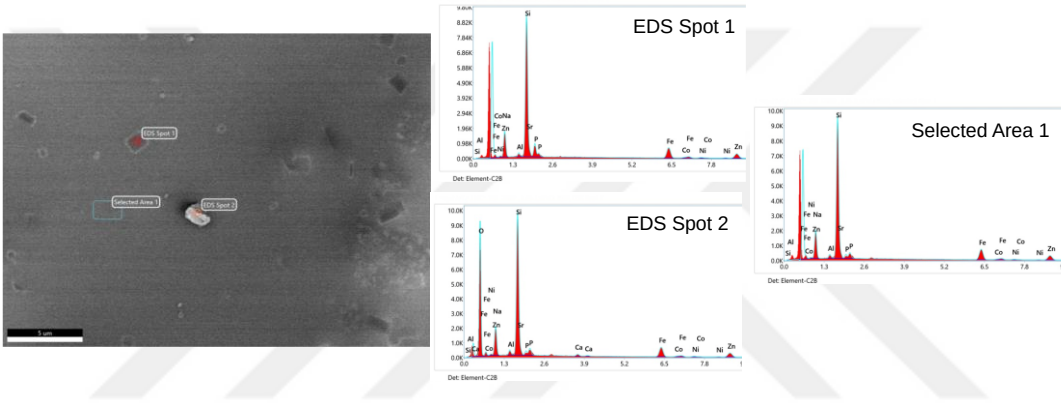



**Figure 6.44** SEM image (left) and EDS analyses of the defined parts (right) of the LZBS_25_ZnO sample at 850 °C

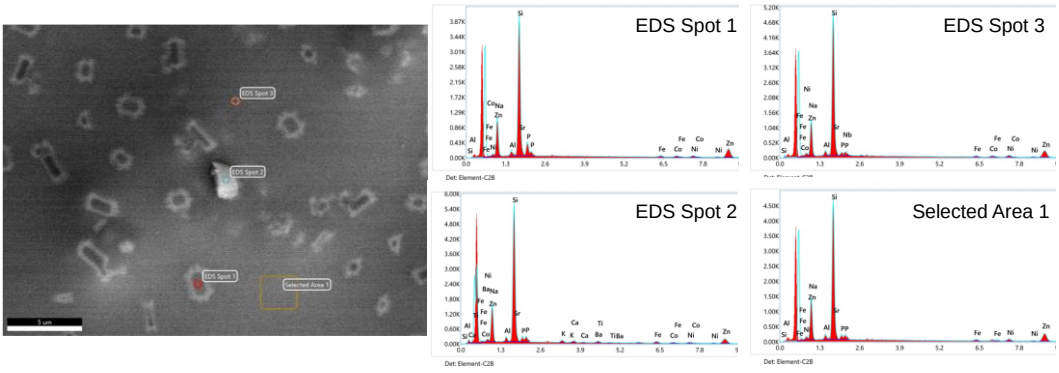



**Figure 6.45** SEM image (left) and EDS analyses of the defined parts (right) of the LZBS_50_ZnO sample at 850 °C

The observed changes in microstructure with varying nano-ZnO concentrations and temperatures suggest that nano-ZnO serves multiple roles in the synthesis of these ceramic materials. Firstly, it acts as a catalytic nucleating agent, promoting the

initial formation of non-quartz phases. Secondly, it influences the kinetic factors of phase growth, such as diffusion rates and ionic mobility, which are crucial at higher temperatures. These dual roles of nano-ZnO underscore its importance in tailoring the microstructural properties of ceramic materials.

## 6.6 Surface Characterization

Surface characterization is crucial for understanding the microstructural changes in glass-ceramic coatings under various conditions. Optical microscopy provides insights into the surface texture, while SEM complements this with detailed images of surface morphology. These techniques reveal critical information about the influence of crystallization temperature and nano-CuO and nano-ZnO additions on the microstructure and properties of the coatings.

### 6.6.1 Optical Microscopy

#### 6.6.1.1 Nano CuO Addition

Optical microscopy was employed to examine the texture of the glass-ceramic coatings at different crystallization temperatures. The images, detailed in Figure 6.46-49.

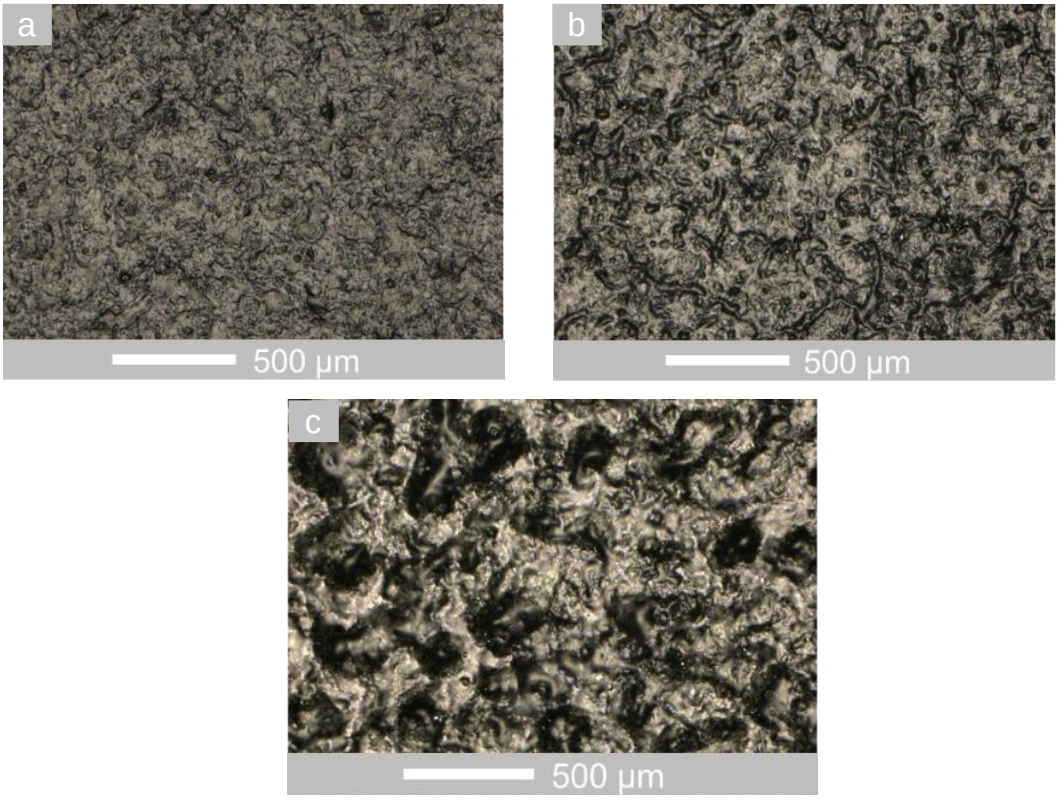


**Figure 6.46** Optical microscopy images of the studied LZBS reference samples without additions a) at 750 °C, b) at 800 °C, and c) at 850 °C




**Figure 6.47** Optical microscopy images of the studied LZBS samples crystallized at 750 °C with the addition of a)1.0 wt.%, b) 2.5 wt.%, and c) 5.0 wt.% nano-CuO

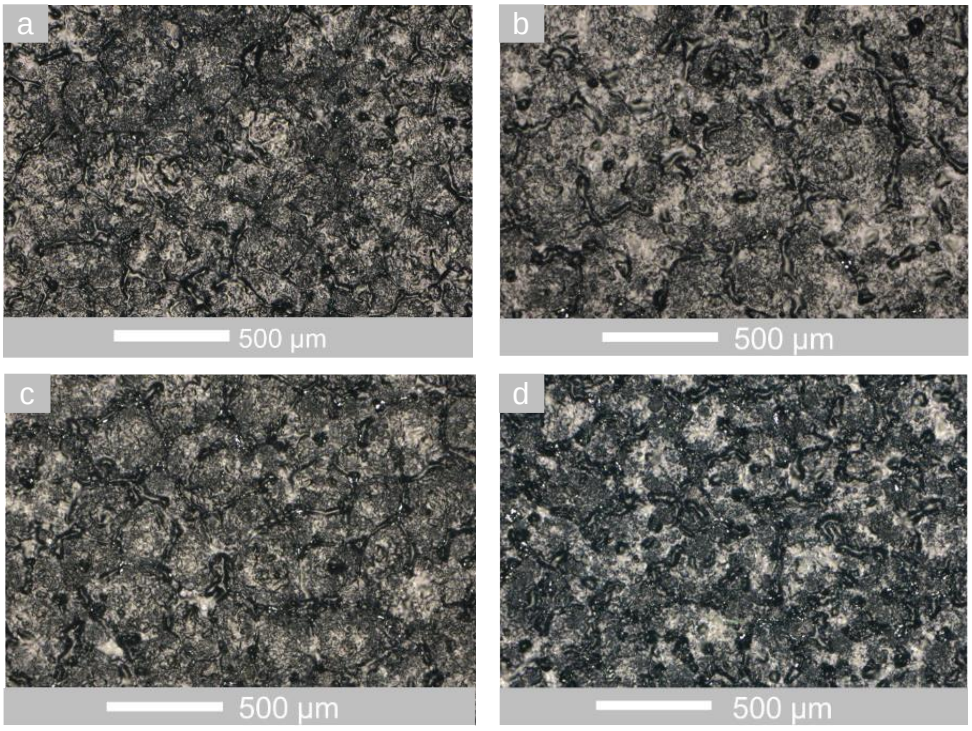


**Figure 6.48** Optical microscopy images of the studied LZBS samples crystallized at 800 °C with addition of a) 0.5 wt.%, b) 1.0 wt.%, c) 2.5 wt.%, and d) a) 5.0 wt.% nano-CuO

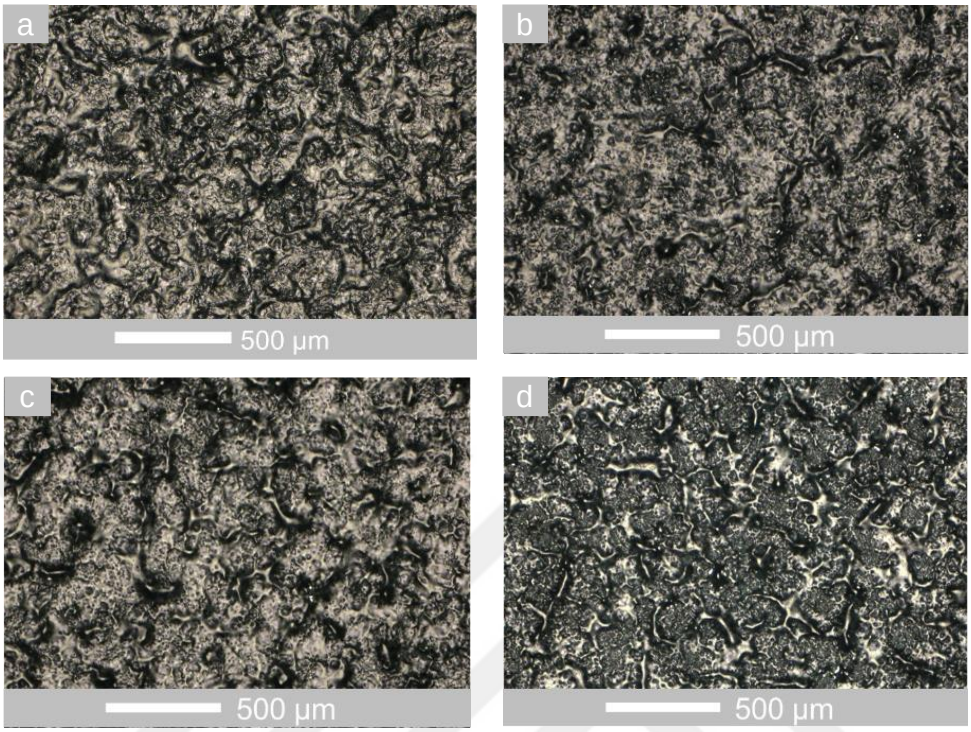



**Figure 6.49** Optical microscopy images of the studied LZBS samples crystallized at 850 °C with addition of a) 0.5 wt.%, b) 1.0 wt.%, c) 2.5 wt.%, and d) a) 5.0 wt.% nano-CuO

As the crystallization temperature increased, changes in the surface features of the samples were observed, consistent with the principles of grain growth in materials science, where higher temperatures enhance atomic mobility. This can lead to surface changes through mechanisms such as boundary migration and coalescence.

At 750°C, the optical microscopy images in Figure 6.47 displayed a uniformly textured surface with numerous small features distributed throughout the coating. Although individual grains and grain boundaries could not be resolved at this magnification, the overall uniform texture indicated a stable and homogeneous microstructure. At lower temperatures, limited atomic mobility restricts the movement of surface features, resulting in a finer texture where nucleation dominates over growth.

At 800°C, the images showed an apparent increase in surface feature size, with a coarser texture becoming more visible (Figure 6.48). This coarser appearance

suggests increased atomic diffusion and the coalescence of smaller features into larger ones, even though distinct grain boundaries were not visible. The increased temperature enhances atomic diffusion, allowing for more extensive migration and coalescence of surface features.

At 850°C, the samples exhibited even larger surface features with more pronounced irregular shapes, as shown in Figure 6.49. The texture became coarser and more irregular, indicating significant growth and coalescence of surface features. At this high temperature, atomic mobility is at its peak within the tested range, promoting extensive growth and coalescence of surface features.

The addition of nano-CuO significantly influenced the surface evolution and phase distribution in the glass-ceramic coatings. Nano-CuO particles likely act as heterogeneous nucleation sites, promoting the formation of numerous nucleation events and leading to a more refined surface structure. Additionally, these particles can impede the migration of surface features, preventing the coalescence of these features and promoting a more uniform texture.

In terms of reducing impurities and non-uniformities, nano-CuO can promote the purification and homogenization of the surface. During crystallization, nano-CuO particles may interact with impurities, incorporating them into the crystal lattice or expelling them from the surface, thus reducing their presence. The bright areas in the optical microscopy images, indicative of impurities or non-uniformities, were reduced with increasing nano-CuO content, suggesting that nano-CuO contributes to a cleaner and more uniform surface.

Scanning Electron Microscopy (SEM) images at higher magnifications (Figures 6.13-16) revealed well-defined phase boundaries and detailed surface morphology, corroborating the trends observed in optical microscopy. The influence of nano-CuO in promoting finer surface features and a more uniform distribution was evident in the SEM images. X-Ray Diffraction (XRD) patterns (Figures 6.6-8) indicated the presence of distinct crystalline phases, with the refinement in surface features due to nano-CuO addition being consistent with the increased phase intensity and sharpness in XRD peaks.

Optical microscopy provided valuable insights into the surface evolution of glass-ceramic coatings at different crystallization temperatures and nano-CuO

concentrations. The observations highlight the role of temperature in promoting surface growth through enhanced atomic mobility and the beneficial effect of nano-CuO in refining the surface structure. These findings are crucial for tailoring the properties of glass-ceramic coatings to achieve desired properties, such as enhanced mechanical strength, thermal stability, and chemical resistance. The consistency of these results with SEM and XRD analyses underscores the reliability of the conclusions drawn.

#### 6.6.1.2 Nano ZnO Addition

For the samples crystallized at 750°C, as shown in Figure 6.50, the initial images at this temperature display a homogeneous texture, reflecting the dominant presence of the quartz phase, as confirmed by stable XRD patterns. This homogeneity indicates a well-sintered matrix with minimal phase segregation. As nano-ZnO is introduced and increased, there is a noticeable change in texture, with the emergence of regions of increased brightness and contrast. These changes are likely due to the nucleation of $Li_2ZnSiO_4$ and $Li_3PO_4$ phases, where nano-ZnO acts as a nucleating agent. The presence of nano-ZnO reduces the surface energy required for nucleation, facilitating the formation of these phases at specific sites.

For the samples crystallized at 800°C, the increased temperature results in a more pronounced texture, as seen in Figure 6.51. This observation aligns with the principle that higher temperatures enhance the mobility of atoms and ions, accelerating nucleation and crystal growth rates. The granular textures evident in these images suggest an increase in the kinetic energy available for the growth of $Li_2ZnSiO_4$ and $Li_3PO_4$ phases. This is corroborated by the intensified XRD peaks (Figures 6.10-12) and the heterogeneous surface structure seen in SEM (Figures 6.17-19), indicating a more active and dynamic crystallization process.

At the highest temperature of 850°C, the optical images (Figure 6.26) exhibit the most varied and contrasting textures. The dense clusters and high-contrast areas represent mature phases of $Li_2ZnSiO_4$ and $Li_3PO_4$, reflecting a high degree of crystalline growth and phase segregation. This level of crystallinity and segregation can be attributed to the maximum thermal energy imparted at this temperature, which not only enhances phase stability but also promotes the diffusion of nano-ZnO into the matrix.

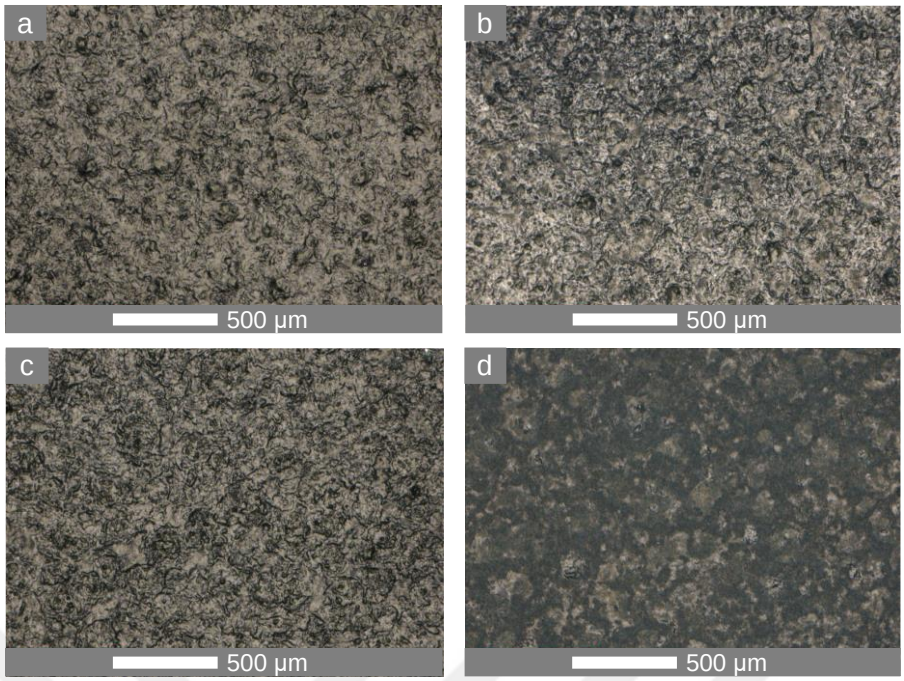



**Figure 6.50** Optical microscopy images of the studied LZBS samples crystallized at 750 °C with addition of a) 0.5 wt.%, b) 1.0 wt.%, c) 2.5 wt.%, and d) a) 5.0 wt.% nano-CuO

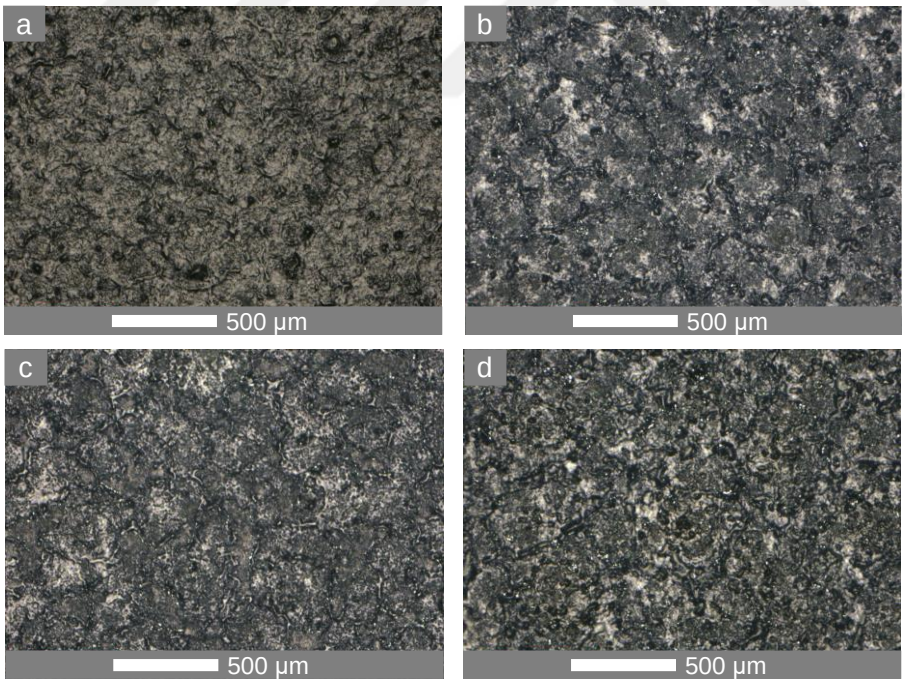



**Figure 6.51** Optical microscopy images of the studied LZBS samples crystallized at 800 °C with addition of a) 0.5 wt.%, b) 1.0 wt.%, c) 2.5 wt.%, and d) a) 5.0 wt.% nano-CuO

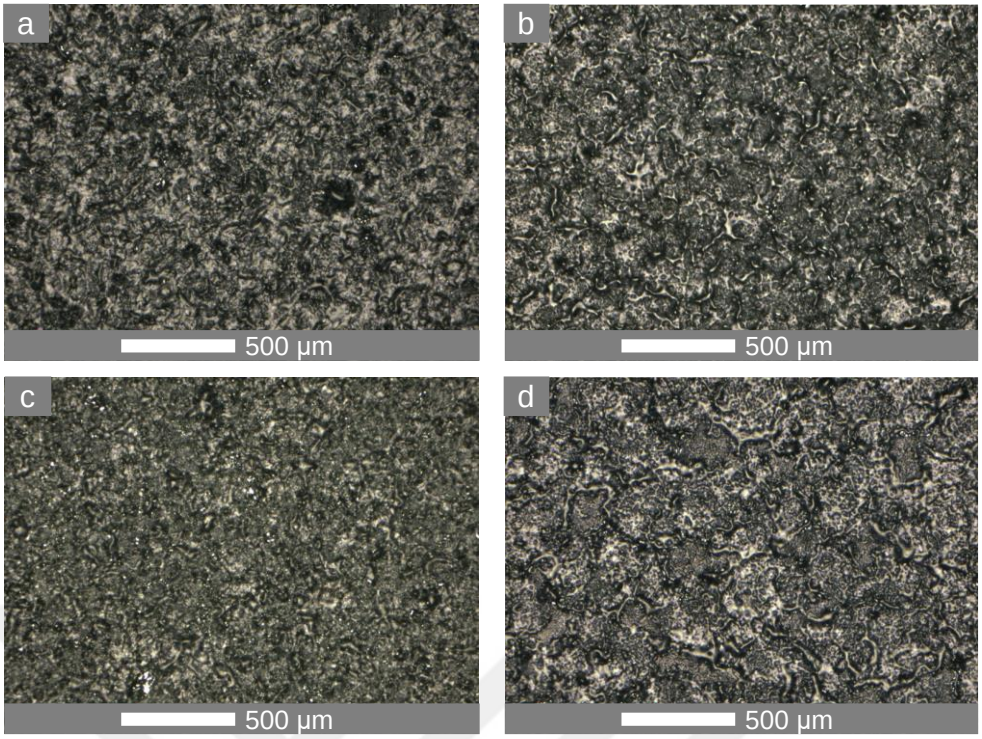



**Figure 6.52** Optical microscopy images of the studied LZBS samples crystallized at 850 °C with addition of a) 0.5 wt.%, b) 1.0 wt.%, c) 2.5 wt.%, and d) a) 5.0 wt.% nano-CuO

The diffusion process facilitates a more pronounced interaction between nano-ZnO and the base materials, leading to enhanced phase development and growth. The optical microscopy findings provide a macroscopic validation of the microstructural and phase changes suggested by SEM (Figure 6.31, 6.36, 6.41) and XRD (Figure 6.9-11) analyses. The progressive textural changes observed across different temperatures and nano-ZnO concentrations illustrate the fundamental mechanisms of nucleation and growth in ceramic systems. The presence of nano-ZnO significantly influences these mechanisms by altering the material's surface energy and kinetic properties, which are crucial for phase formation and stability.

### 6.6.2 Surface Topography Analysis

#### 6.6.2.1 Nano CuO Addition

The use of nano-copper oxide (nano-CuO) in the formulation of glass-ceramic coatings significantly alters their surface characteristics, as evidenced by three-dimensional (3D) imaging techniques. These imaging studies, recorded in Figure 6.53-56, correlate nano-CuO concentrations with changes in surface roughness—quantitative measures that describe the texture of a surface at a microscopic level.

The reference sample, displayed a baseline surface texture against which modified samples were compared. The addition of nano-CuO was observed to reduce surface roughness, resulting in smoother coatings. This effect is particularly noted in the LZBS_25_CuO sample, which showed the highest uniformity and homogeneity in surface topography among the tested variants. The nano-CuO particles in the LZBS_25_CuO sample were evenly dispersed throughout the ceramic matrix, enhancing the surface smoothness. This dispersion plays a critical role in the physical characteristics of the coating, influencing both mechanical strength and optical properties. SEM analysis provides microscale imaging that reveals the structural and compositional details of the samples. The SEM images indicated that the nano-CuO particles act as nucleation sites—specific locations on a surface where crystal growth begins. As the nano-CuO content increases, these nucleation sites promote the formation of smaller crystals within the glass-ceramic matrix [337]. This phenomenon is crucial because the size and distribution of these crystals can directly impact the physical properties of the coating.

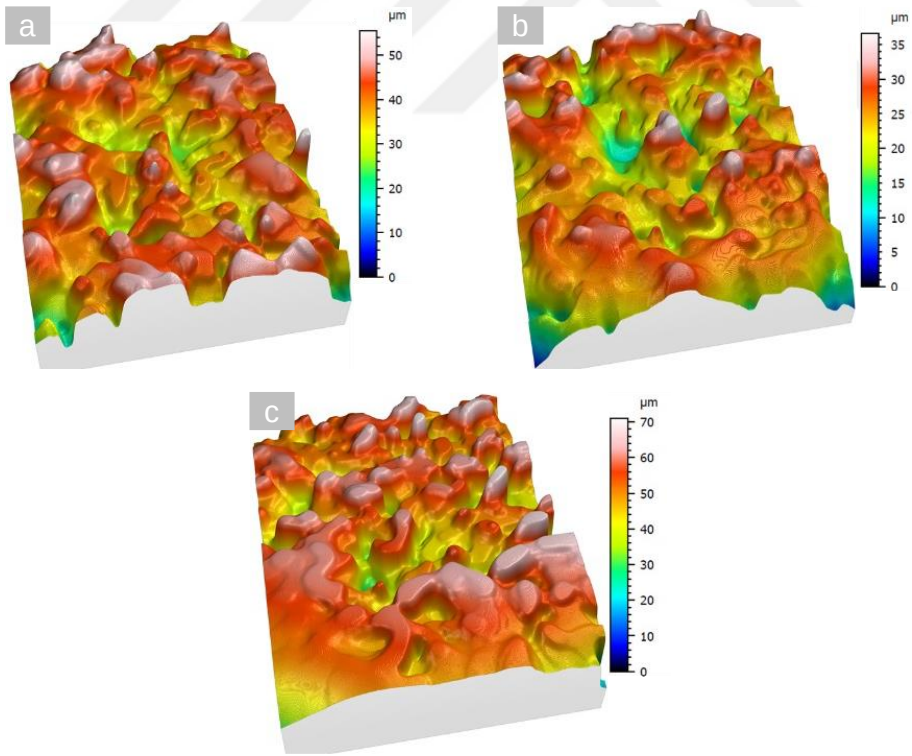



**Figure 6.53** 3D surface topography images of the studied LZBS reference samples without additions a) at 750 °C, b) at 800 °C, and c) at 850 °C

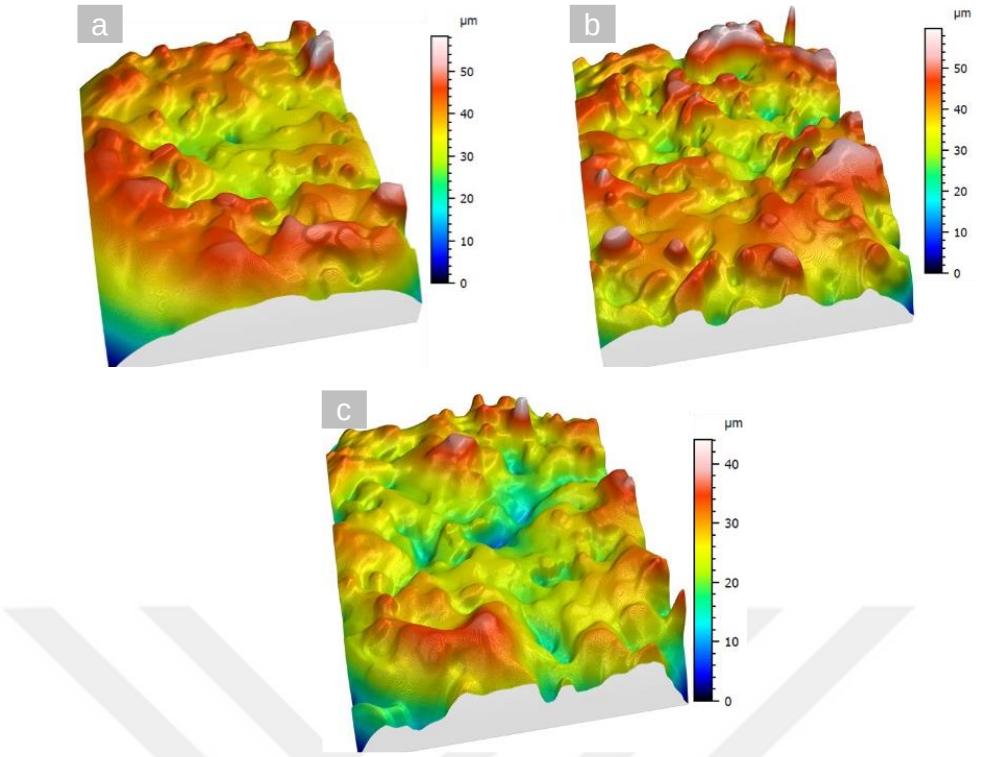



**Figure 6.54** 3D surface topography images of the studied LZBS samples crystallized at 750 °C with the addition of a) 1.0 wt.%, b) 2.5 wt.%, and c) 5.0 wt.% nano-CuO

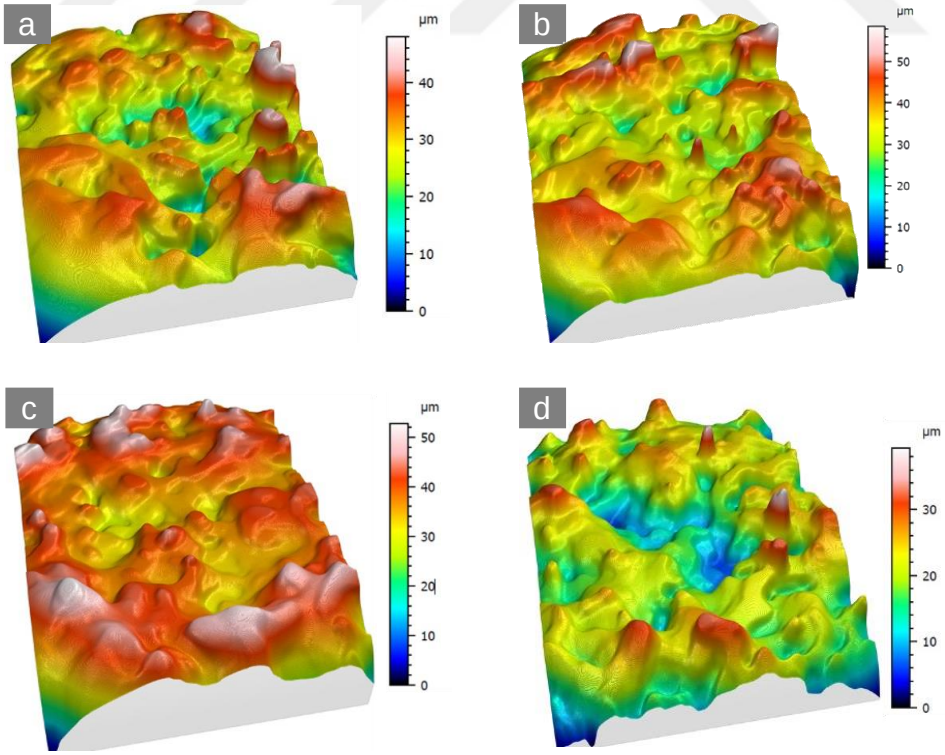



**Figure 6.55** 3D surface topography images of the studied LZBS samples crystallized at 800 °C with the addition of a) 0.5 wt.%, b)1.0 wt.%, c) 2.5 wt.%, and d) 5.0 wt.% nano-CuO

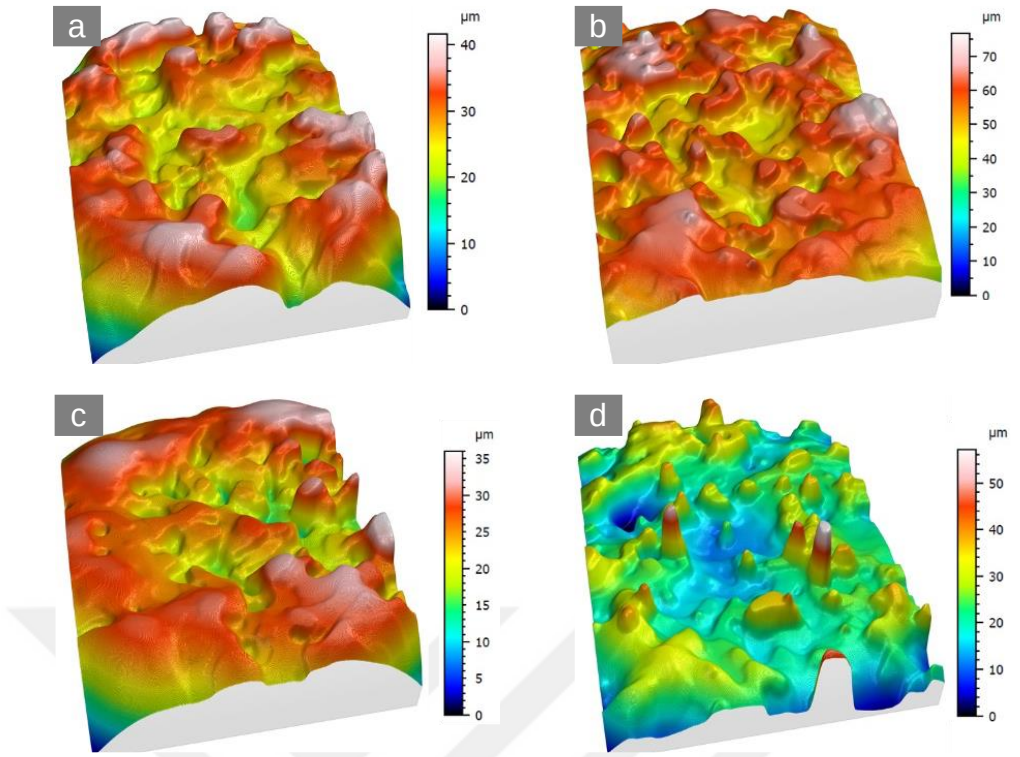



**Figure 6.56** 3D surface topography images of the studied LZBS samples crystallized at 850 °C with the addition of a) 0.5 wt.%, b)1.0 wt.%, c) 2.5 wt.%, and d) 5.0 wt.% nano-CuO

Crystallization temperature is a pivotal factor in determining the final surface characteristics of ceramic coatings. At the lowest studied temperatures (750 °C), the SEM and 3D images showed that the surface remains relatively smooth with minimal features. This smoothness is attributed to the optimal melting and embedding of lithium-zinc silicate crystals within the matrix at this temperature, which minimizes surface irregularities. However, at higher temperatures (up to 850 °C), the SEM analysis revealed a rougher texture. The presence of lithium phosphate crystals at these elevated temperatures contributes to a rougher surface due to their different melting and solidification behaviors compared to lithium-zinc silicate. Interestingly, the addition of nano-CuO helps to mitigate these temperature-induced surface roughening effects. The nano-particles likely interfere with the growth of larger, more irregular lithium phosphate crystals, thereby maintaining a smoother surface even at higher temperatures.

### 6.6.2.2 Nano ZnO Addition

To further comprehend the influence of nano-ZnO on the surface properties of ceramic materials, 3D topographical imaging was conducted (Figure 6.57-59). This method enriches the understanding by providing a dimensional perspective of surface morphology, crucial for assessing the micro-to-macroscopic implications of compositional changes on material properties. The 3D topographical images utilized a high-resolution surface profiler capable of detecting subtle variations in surface morphology. Each image incorporates a color-coded height scale, measured in micrometers, to quantify the surface variations. The samples analyzed correspond to 750°C crystallization temperature with weight percentage (wt.%) additions of nano-ZnO ranging from 0 to 5 wt.%.

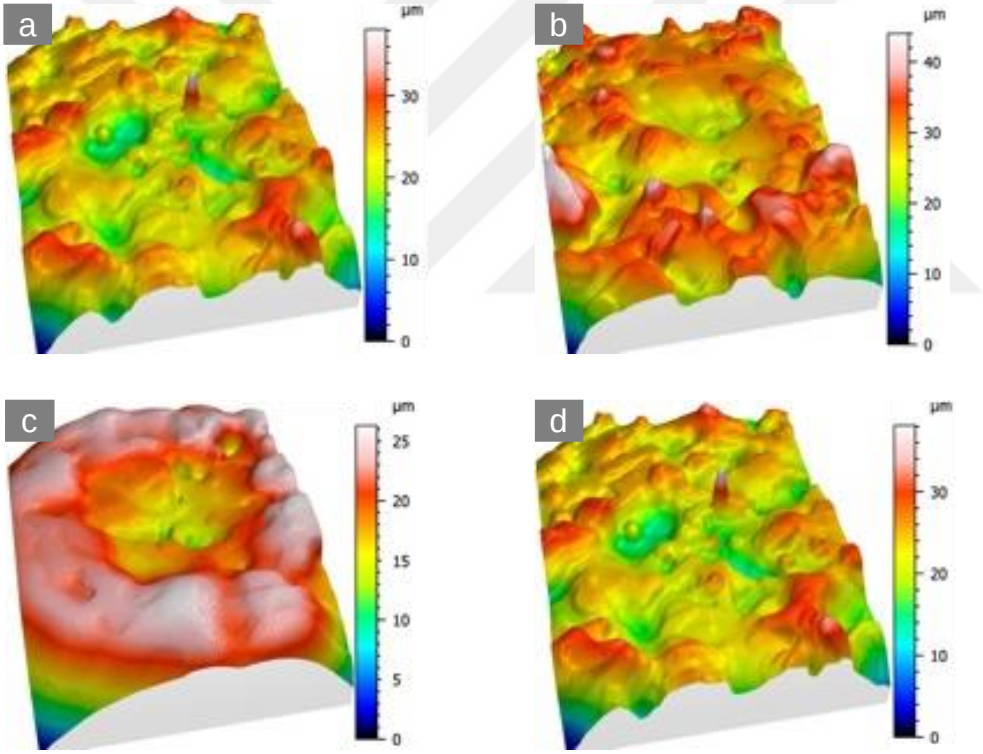



**Figure 6.57** 3D surface topography images of the studied LZBS samples crystallized at 750 °C with the addition of a) 0.5 wt.%, b)1.0 wt.%, c) 2.5 wt.%, and d) 5.0 wt.% nano-ZnO

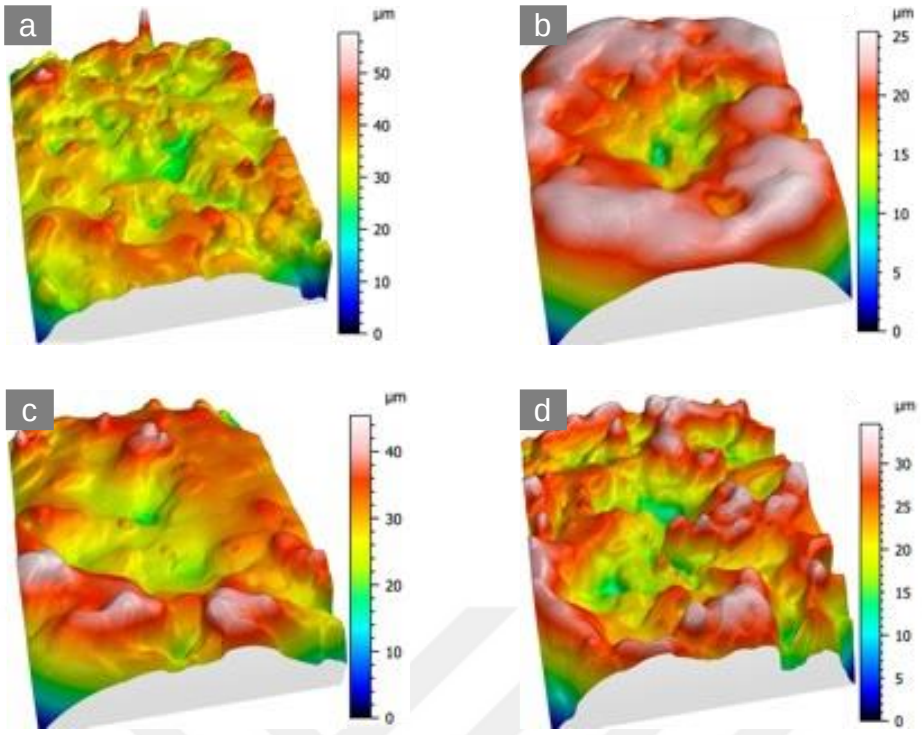



**Figure 6.58** 3D surface topography images of the studied LZBS samples crystallized at 800 °C with the addition of a) 0.5 wt.%, b)1.0 wt.%, c) 2.5 wt.%, and d) 5.0 wt.% nano-ZnO

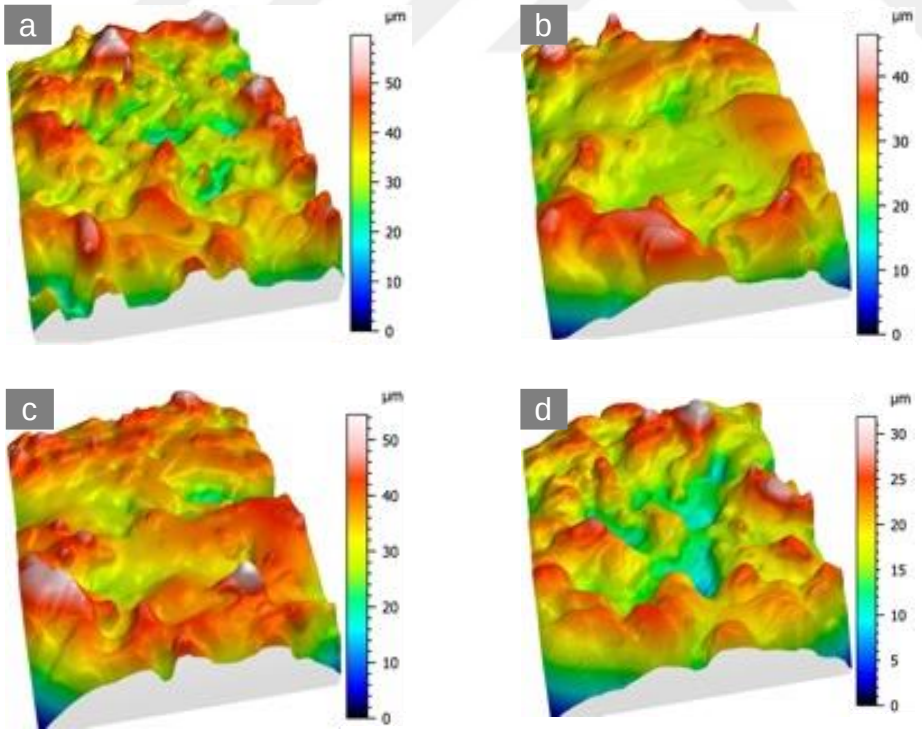



**Figure 6.59** 3D surface topography images of the studied LZBS samples crystallized at 850 °C with the addition of a) 0.5 wt.%, b)1.0 wt.%, c) 2.5 wt.%, and d) 5.0 wt.% nano-ZnO

For the samples crystallized at 750 °C, introducing a small amount of nano-ZnO (0.5 wt.%) begins to alter the surface characteristics slightly. The slight increase in surface roughness and the emergence of minor peaks may indicate the beginning of nucleation processes where nano-ZnO acts as a nucleating agent. At 1 wt.% nano-ZnO, there is a noticeable increase in the heterogeneity and roughness of the surface. This increased roughness correlates with the enhanced formation of lithium-containing phases, supported by the slight rise in peak intensities observed in the XRD analysis. The presence of nano-ZnO likely promotes more extensive nucleation and growth of these phases. With 2.5 wt.% nano-ZnO, the topographical images show greater elevation differences and pronounced roughness. This suggests a substantial influence of nano-ZnO in promoting the growth and crystallization of lithium zinc silicate and lithium phosphate phases. The complex topography indicates significant phase interactions and growth dynamics facilitated by nano-ZnO. At the highest concentration of nano-ZnO (5 wt.%), the ceramic surface exhibits the highest degree of roughness and the most significant variability in height. The rugged and varied landscape is indicative of mature phase development and extensive crystalline growth, demonstrating that higher ZnO concentrations significantly enhance phase segregation and crystallization dynamics.

For the samples crystallized at 800°C, the base sample without nano-ZnO presents a moderately rough surface, slightly more pronounced than at 750°C, suggesting that temperature alone influences surface morphology by enhancing grain growth. Slight additions of nano-ZnO begin to manifest more distinct topographical features compared to the 0 wt.% sample, indicating that nano-ZnO facilitates more noticeable phase developments at this elevated temperature. Increased nano-ZnO content continues to promote heterogeneity on the coating surface, with visible increases in peak heights and variations, reflective of more dynamic crystalline interactions and phase formations. The highest concentration showcases the greatest roughness and variability, signifying the most intense degree of phase maturation and crystalline complexity, suggesting a strong nano-ZnO-driven phase dynamics.

The smoothest surface among the 850°C batch, indicating that the baseline ceramic material, even at high temperatures, maintains a relatively uniform surface in the absence of nano-ZnO. Even minimal nano-ZnO addition at this temperature results in noticeable surface texture changes, with increased roughness and peak formation. Further increasing nano-ZnO enhances surface roughness substantially, demonstrating the additive's effectiveness in promoting crystalline diversity at high temperatures. Displays the most pronounced topographical features, with the highest peaks and deepest troughs, indicative of extensive crystalline growth and high phase segregation.

### 6.6.3 Surface Roughness Analysis

#### 6.6.3.1 Nano CuO Addition

Surface roughness, a critical metric in materials science, is pivotal for assessing the quality and functional applications of surface coatings. In glass-ceramic systems, the introduction of nano-copper oxide (nano-CuO) modifies the surface characteristics significantly, which is quantitatively analyzed using detailed roughness parameters.

**Table 6.3** Surface roughness amplitude parameters of the nano-CuO incorporated samples

| Sample Code | 750 °C | | | 800 °C | | | 850 °C | | |
|---|---|---|---|---|---|---|---|---|---|
| | Ra | Rz | Rq | Ra | Rz | Rq | Ra | Rz | Rq |
| LZBS_REF | 2.98 | 13.81 | 3.59 | 3.07 | 14.60 | 3.85 | 5.01 | 23.94 | 6.27 |
| LZBS_05_CuO | | | | 1.74 | 7.98 | 2.11 | 2.05 | 22.19 | 2.63 |
| LZBS_10_CuO | 1.57 | 8.04 | 2.00 | 2.17 | 11.44 | 2.76 | 3.11 | 15.57 | 3.89 |
| LZBS_25_CuO | 3.20 | 13.59 | 3.83 | 1.65 | 7.35 | 2.01 | 1.62 | 7.34 | 1.96 |
| LZBS_50_CuO | 1.83 | 8.59 | 2.28 | 1.85 | 8.79 | 2.30 | 2.72 | 13.76 | 3.45 |

Arithmetic average roughness (Ra) is the average of absolute values of the surface height deviations measured from the mean line, across a sample length. It provides a quick summary of the surface texture. Maximum height of roughness profile (Rz) measures the vertical distance between the highest peak and the deepest valley within five sampling lengths. It is crucial for identifying occasional peaks or valleys that may affect material performance. Root mean square roughness (Rq) is similar to Ra but calculated as the square root of the average of the squared deviations of the roughness profile heights. Rq is sensitive to peak and valley extremes and provides a more comprehensive measure of surface texture variance [338 - 341].

The integration of nano-CuO into glass-ceramic coatings plays a transformative role in tailoring surface roughness. As detailed in Table 6.3, the influence of nano-CuO concentration and crystallization temperature on the roughness parameters is evident. The presence of nano-CuO induces nucleation sites that facilitate more uniform crystal growth, thus smoothing the surface. The detailed analysis of LZBS_25_CuO, which consistently shows the lowest Ra and Rq values across all studied temperatures, highlights its superior surface quality due to optimal nano-CuO dispersion and effective nucleation control.

Increasing the crystallization temperature typically raises Ra and Rq values due to the increased mobility of material constituents that promotes larger and more irregular crystal growth. This temperature-dependent behavior is critical for material scientists to understand and control the thermodynamics of crystal growth within the ceramic matrix.

LZBS_05_CuO and LZBS_10_CuO exhibit intermediate roughness values, suggesting a less optimized nano-CuO concentration that does not fully stabilize the crystal growth as effectively as LZBS_25_CuO. Their higher Ra and Rq values compared to LZBS_25_CuO indicate a surface with more pronounced irregularities, which could impact the coating's functional properties such as frictional behavior and light reflection.

LZBS_50_CuO shows an interesting trend where it has lower Ra and Rq values than LZBS_REF but does not reach the smoothness of LZBS_25_CuO, suggesting that there is an optimal nano-CuO concentration for achieving the smoothest

surface, beyond which the effects may plateau or even reverse due to possible agglomeration of nano-CuO particles.

The buffering effect of nano-CuO against the roughening impact of higher temperatures is particularly noteworthy. While LZBS_REF shows a significant increase in roughness at elevated temperatures, the samples with nano-CuO additions demonstrate a mitigated increase. This suggests that nano-CuO not only assists in the initial formation of a smoother surface but also plays a crucial role in maintaining surface integrity under thermal stress, likely by influencing the viscosity and flow behavior of the glass-ceramic during the sintering process.

In conclusion, this detailed analysis of surface roughness in nano-CuO integrated glass-ceramic coatings offers insights into the complex interplay between nano-additives, crystallization dynamics, and surface texture. By scientifically elucidating the effects of nano-CuO on roughness parameters, material scientists can better design coatings with tailored surface properties that meet specific industrial or technological applications. This comprehensive understanding is crucial for advancing the development of next-generation materials with engineered surface characteristics.

#### 6.6.3.2 Nano ZnO Addition

**Table 6.4** Surface roughness amplitude parameters of the nano-ZnO incorporated samples

| Sample Code | 750 °C | | | 800 °C | | | 850 °C | | |
|---|---|---|---|---|---|---|---|---|---|
| | Ra | Rz | Rq | Ra | Rz | Rq | Ra | Rz | Rq |
| LZBS_REF | 2.98 | 13.81 | 3.59 | 3.07 | 14.60 | 3.85 | 5.01 | 23.94 | 6.27 |
| LZBS_05_ZnO | 4.92 | 23.17 | 6.23 | 2.07 | 10.01 | 2.52 | 2.56 | 12.48 | 3.24 |
| LZBS_10_ZnO | 1.64 | 8.63 | 2.18 | 0.98 | 4.35 | 1.21 | 1.11 | 5.29 | 1.38 |
| LZBS_25_ZnO | 0.64 | 3.20 | 0.81 | 1.06 | 4.80 | 1.32 | 1.08 | 5.30 | 1.34 |
| LZBS_50_ZnO | 2.98 | 8.32 | 2.07 | 1.64 | 7.74 | 2.02 | 1.98 | 9.38 | 2.39 |

Table 6.4 shows the surface roughness amplitude parameters of the nano-ZnO incorporated samples. At 750°C, the reference sample with 0% nano-ZnO exhibits a roughness of 2.98 µm, indicating a baseline texture under standard sintering conditions without any nano-ZnO. However, the addition of 0.5 wt.% nano-ZnO significantly increases the roughness to 4.92 µm, suggesting that even a minimal amount of ZnO can dramatically affect surface morphology. This could be due to the initial disturbance of the matrix uniformity and the introduction of new nucleation sites facilitated by nano-ZnO particles. Interestingly, further increases in nano-ZnO concentration result in a decrease in roughness, with the lowest roughness recorded at 2.5 wt.% (0.64 µm). This decrease could be associated with the enhanced densification and stabilization of crystalline phases at higher nano-ZnO concentrations, which might smooth out surface irregularities.

At 800°C, the reference sample shows a slight increase in roughness to 3.07 µm compared to the 750°C baseline, indicating that increased temperature alone can augment surface irregularities due to enhanced grain growth or phase transformation dynamics. However, adding nano-ZnO at this temperature presents a varied response; 0.5 wt.% nano-ZnO reduces the roughness dramatically to 2.07 µm, possibly indicating a phase stabilization effect that counters the roughening effect of temperature. The roughness generally remains low with increasing nano-nano-ZnO concentrations, showing minimal fluctuations, which underscores the complex interplay between nano-ZnO, ceramic matrix, and temperature.

At 850°C, the roughness of the reference sample escalates significantly to 5.01 µm, highlighting the pronounced effect of high temperature in promoting rougher and more heterogeneous surfaces due to aggressive grain growth and phase segregation. With the introduction of nano-ZnO, there is a general trend of reduced roughness compared to the reference, although the values fluctuate less dramatically than at lower temperatures. This suggests that at high temperatures, nano-ZnO might aid in controlling excessive grain growth and promoting a more uniform phase distribution, thereby mitigating surface roughness.

The observed trends in surface roughness across different nano-ZnO concentrations and temperatures provide critical insights into the material science mechanisms at play. Nano-ZnO appears to serve multiple roles: as a nucleating agent at lower

concentrations and temperatures, and as a phase stabilizer and grain growth moderator at higher concentrations and temperatures. The initial increase in roughness with small amounts of nano-ZnO could be due to the disruption of the existing matrix and the formation of new crystalline phases. As nano-ZnO concentration increases, its role as a fluxing agent may become more pronounced, enhancing the liquid phase sintering process and thereby promoting the densification and smoothing of the ceramic surface.

## 6.7 Contact Angle Analysis

The contact angle measurements, essential in evaluating the wetting behavior of surfaces, reveal significant insights into the interactions between liquid phases and solid surfaces. The contact angle is a crucial parameter indicating the degree to which a liquid droplet can spread on a surface; lower angles suggest better wettability, which is indicative of a strong interaction between the liquid and the solid surface [90, 342 - 344].

### 6.7.1 Nano CuO Addition

Nano-CuO incorporation markedly impacts the contact angle by modifying the surface energy and topography. An initial introduction of nano-CuO leads to a substantial reduction in the wetting angle, a phenomenon that underscores the increase in surface energy, which enhances the hydrophilicity of the coatings. This adjustment in surface properties is further influenced by the temperature conditions under which the coatings are processed.

**Table 6.5** Optical tensiometer analysis results of the nano-CuO incorporated samples

| Code | 750 °C | 800 °C | 850 °C |
|---|---|---|---|
| LZBS_REF | 67.04 ± 2.53 | 80.53 ± 1.29 | 79.34 ± 0.57 |
| LZBS_05_CuO | | 18.42 ± 2.38 | 10.19 ± 3.66 |
| LZBS_10_CuO | 21.32 ± 3.25 | 37.42 ± 1.31 | 46.38 ± 0.38 |
| LZBS_25_CuO | 29.70 ± 0.58 | 36.41 ± 1.16 | 29.25 ± 0.17 |
| LZBS_50_CuO | 41.10 ± 0.78 | 40.41 ± 0.73 | 30.16 ± 1.08 |

To calculate the surface energy from the water contact angle, the contact angle is first converted from degrees to radians using the formula:

$$\theta_{rad} = \frac{\theta \times \pi}{180} \tag{6.3}$$

Next, the cosine of the converted angle is determined. Using the surface tension of water, which is 72.8 mN/m, the formula:

$$\gamma_s \approx \gamma_{LV}(1 + cos\theta_{rad})^2 \tag{6.4}$$

is applied to find the surface energy.

**Table 6.6** Approximate surface tension calculation results of the the nano-CuO incorporated samples

| **Code** | **750 °C** | **800 °C** | **850 °C** |
|---|---|---|---|
| | **mN/m** | | |
| LZBS_REF | 140.67 | 98.73 | 102.22 |
| LZBS_05_CuO | | 276.47 | 286.62 |
| LZBS_10_CuO | 271.61 | 234.35 | 207.89 |
| LZBS_25_CuO | 254.20 | 237.13 | 255.25 |
| LZBS_50_CuO | 223.86 | 225.87 | 253.11 |

Table 6.5 presents a quantitative analysis of contact angle measurements, and Table 6.6 demonstrates surface tension results, which are crucial for understanding the surface wetting behavior of various samples containing differing concentrations of nano copper oxide. Initially, reference samples, devoid of nano additives, exhibit the highest contact angles, quantitatively measured as 67.04° ± 2.53 at 750°C, 80.53° ± 1.29 at 800°C, and 79.34° ± 0.57 at 850°C, indicating minimal wetting due to high hydrophobicity.

Upon the introduction of nano copper oxide, a dramatic shift in wetting behavior is observed. The sample with 0.5 wt% nano copper oxide (LZBS_05_CuO) displays significantly reduced angles of 18.42° ± 2.38 at 750°C and 10.19° ± 3.66 at 800°C.

This trend of reducing contact angles with the incorporation of nano copper oxide continues in other samples but varies with temperature and concentration. For instance, the sample with 1.0 wt% (LZBS_10_CuO) shows a decrease to 21.32° ± 3.25 at 750°C, followed by an increase to 37.42° ± 1.31 at 800°C, and then 46.38° ± 0.38 at 850°C. This nuanced response to temperature changes is further explored at higher concentrations of nano copper oxide. The 2.5 wt% sample (LZBS_25_CuO) records contact angles of 29.70° ± 0.58 at 750°C, 36.41° ± 1.16 at 800°C, and a decrease back to 29.25° ± 0.17 at 850°C. Similarly, the 5.0 wt% sample (LZBS_50_CuO) exhibits an angle of 41.10° ± 0.78 at 750°C, stabilizes around 40.41° ± 0.73 at 800°C, and then decreases to 30.16° ± 1.08 at 850°C.

Correlation of these contact angle trends with SEM images from Figure 16, 19, 23 and 27. reveals that the addition of nano copper oxide results in a decrease in crystal size but an increase in their number. This morphological transformation aligns with the Cassie-Baxter wetting state, characterized by a heterogeneous surface texture that enhances hydrophobicity [345, 346]. The SEM analysis particularly highlights that at 850°C, the escalated surface energy due to elevated temperatures contributes significantly to the changes in wetting behavior.

Among the samples, LZBS_25_CuO with 2.5 wt% nano copper oxide stands out, demonstrating optimal characteristics for promoting rapid crystal growth and density due to the nano additive's ability to act as an effective nucleation site. This concentration fosters accelerated reactivity which, in turn, facilitates more uniform distribution of crystals when the nano copper oxide content is increased further, thereby altering the surface structure and wetting properties.

### 6.7.2 Nano-ZnO Addition

The analysis of contact angle variations across a series of nano-ZnO-doped ceramics elucidates the profound impact of nano-scale zinc oxide on the thermodynamic and surface phenomena of these materials. The scientific interpretation of contact angle data not only reveals insights into the wettability but also correlates these findings with the physicochemical alterations induced by nano-ZnO within the ceramic matrix.

**Table 6.7** Optical tensiometer analysis results of the nano-ZnO incorporated samples

| Code | 750 °C | 800 °C | 850 °C |
|---|---|---|---|
| LZBS_REF | 67.04 ± 2.53 | 80.53 ± 1.29 | 79.34 ± 0.57 |
| LZBS_05_ZnO | 42.11 ± 2.26 | 36.72 ± 0.87 | 28.27 ± 1.15 |
| LZBS_10_ZnO | 60.37 ± 1.40 | 60.18 ± 1.42 | 48.38 ± 3.62 |
| LZBS_25_ZnO | 31.61 ± 1.05 | 47.15 ± 1.38 | 49.57 ± 0.50 |
| LZBS_50_ZnO | 56.68 ± 1.32 | 52.64 ± 2.97 | 53.16 ± 2.29 |

To calculate the surface energy from the water contact angle, the contact angle is first converted from degrees to radians using the formula of Equation 6.3. Next, the cosine of the converted angle is determined. Using the surface tension of water, which is 72.8 mN/m, the formula of Equation 6.4 is applied to find the surface energy.

**Table 6.8** Approximate surface tension calculation results of the nano-ZnO incorporated samples

| Code | 750 °C | 800 °C | 850 °C |
|---|---|---|---|
| | mN/m | | |
| LZBS_REF | 140.67 | 98.73 | 102.22 |
| LZBS_05_ZnO | 220.88 | 236.28 | 257.50 |
| LZBS_10_ZnO | 162.58 | 163.20 | 201.62 |
| LZBS_25_ZnO | 249.60 | 205.49 | 197.84 |
| LZBS_50_ZnO | 174.75 | 187.96 | 186.27 |

- **750°C Samples:**
    - 0 wt.% nano-ZnO exhibits a θ of 67.04°, reflective of a relatively hydrophilic surface due to the inherent chemical composition of the ceramic which might be optimizing the balance between γSV and γSL.

- The addition of 0.5 wt.% nano-ZnO decreases θ to 42.11°. This sharp decrease is attributable to the amphiphilic nature of nano-ZnO nanoparticles which, when incorporated into the ceramic matrix, can enhance surface roughness, thus increasing the actual surface area available for interaction with water molecules and potentially introducing polar functional groups that decrease γSL.
- Increasing nano-ZnO to 1 wt.% modifies θ slightly upwards to 60.37°. This can be interpreted as a point of diminishing returns where increased particle aggregation might start to mask the hydrophilic groups introduced by nano-ZnO, slightly increasing γSL .

- **800°C and 850°C Samples:**
  - At 800°C, the modification in θ at 0.5 wt.% nano-ZnO to 36.72° can be attributed to enhanced diffusion of nano-ZnO into the matrix, facilitating more uniform dispersion of nano-ZnO and greater alteration of the surface chemistry. This enhanced diffusion likely promotes a more homogeneous distribution of hydrophilic sites across the ceramic surface, decreasing γSL more effectively.
  - At 850°C, the drastic reduction in θ for 0.5 wt.% nano-ZnO to 28.27° underscores the role of thermal energy in facilitating not just nano-ZnO diffusion but also chemical reactivity at the surface. The high thermal environment may drive dehydroxylation processes or other chemical reactions that enhance the formation of new, more hydrophilic surface phases.

The interaction between nano-ZnO nanoparticles and the ceramic matrix alters both the microscopic and macroscopic properties of the surfaces. At the microscopic level, nano-ZnO may alter the electronic density at the surface by introducing states that facilitate water molecule adsorption, effectively lowering γSL [347, 348]. Macroscopically, nano-ZnO can increase the heterogeneity of the surface, introducing micro- and nano-scale roughness which increases the wettability due to the Wenzel effect, where increased roughness amplifies the intrinsic wettability of the surface [349].

# 7
# COMPREHENSIVE ANALYSIS

## 7.1 Impact of Nano-CuO and Nano-ZnO on Surface Attributes

The strategic incorporation of nano-copper oxide (CuO) and nano-zinc oxide (ZnO) into glass-ceramic systems has demonstrated profound effects on their surface properties and underlying microstructural behaviors. These nano-additives influence not only the crystallization dynamics but also the mechanical and chemical characteristics of the coating materials, facilitating targeted modifications in their physical properties. This chapter synthesizes results from comprehensive analyses—including X-ray Diffraction (XRD), Scanning Electron Microscopy (SEM), surface roughness assessments, and 3D topographical imaging—to elucidate the role of these nano-additives.

Nano-CuO serves as a potent nucleating agent that significantly alters the phase composition within glass-ceramic systems. The XRD results reveal an increased formation of crystalline phases such as lithium zinc silicate ($Li_2ZnSiO_4$) and lithium phosphate ($Li_3PO_4$) with higher concentrations of nano-CuO. This enhancement in crystalline phase development is attributable to the reduction in the energy barrier for nucleation provided by nano-CuO, which facilitates the crystallization process at lower temperatures than would be possible in its absence.

SEM analyses complement these findings by showcasing a refined microstructure with well-defined phase boundaries, indicating effective control over crystal growth and phase segregation. Nano-CuO not only promotes nucleation but also influences the growth kinetics of these phases, leading to a denser and more uniform grain structure as evidenced by decreased surface roughness parameters (Ra and Rq). The quantitative roughness metrics further demonstrate how nano-CuO, by promoting uniform crystal growth, results in smoother surfaces that are crucial for applications demanding reduced surface friction and enhanced optical qualities.

At higher crystallization temperatures, nano-CuO mitigates the surface roughening typically induced by thermal stresses. This buffering effect likely stems from nano-

CuO's ability to stabilize the glass matrix and modulate the thermal expansion coefficients of the crystalline phases, thus maintaining surface integrity under conditions that would normally exacerbate surface irregularities.

Nano-ZnO modifies ceramic coatings in a manner similar to nano-CuO but exhibits unique characteristics under varying thermal conditions. The 3D topographical analysis provides a clear depiction of how nano-ZnO concentrations affect surface morphology. At 750°C, the presence of nano-ZnO increases surface roughness due to enhanced nucleation activity, leading to the formation of $Li_2ZnSiO_4$ and $Li_3PO_4$ phases. This increase in roughness corresponds to the heterogeneous nucleation sites facilitated by nano-ZnO, which lower the surface energy required for new phase formation.

As temperatures rise to 800°C and 850°C, the influence of nano-ZnO on surface properties becomes more nuanced. While still promoting phase stability, the higher thermal energy allows for rapid ion mobility and crystal growth, increasing microstructural heterogeneity and, correspondingly, surface roughness at intermediate concentrations. However, at the highest nano-ZnO concentrations, there is a notable trend towards surface smoothing, suggesting a saturation point where nano-ZnO effectively controls grain growth and phase distribution, optimizing the ceramic’s surface properties.

Comparing nano-CuO and nano-ZnO, both additives enhance phase evolution and modify surface roughness through nucleation control and crystal growth regulation. However, nano-CuO tends to produce sharper phase boundaries and smoother surfaces at lower temperatures, making it particularly effective in applications where thermal stability and mechanical integrity are paramount. Nano-ZnO, on the other hand, shows a broader range of temperature range, influencing phase stability and surface roughness across a wider temperature spectrum.

Both nano-CuO and nano-ZnO are instrumental in tailoring the surface topography and microstructure of ceramic coatings to achieve desired properties for specific applications. The systematic manipulation of nano-additive concentrations and crystallization temperatures enables the engineering of glass-ceramic coatings with optimized surface characteristics, enhancing their functionality and performance in

various industrial and technological applications. This detailed understanding of nano-additive impacts not only advances material science but also opens avenues for the development of next-generation materials with highly customized properties.

## 7.2 Influence on Surface Tension and Hydrophilicity

The integration of nano-CuO and nano-ZnO into glass-ceramic systems profoundly influences their surface tension and hydrophilicity, as evidenced by the systematic variations in contact angle measurements across different concentrations and temperatures. This section delves into the detailed mechanisms by which these nano-additives alter the interfacial properties, exploring the interplay between surface chemistry, microstructural changes, and thermal effects.

The wettability of a surface, quantified through the contact angle, $\theta$, is a direct indicator of the surface energy dynamics according to the Young-Dupré equation: $\Delta G = \gamma SV - (\gamma SL + \gamma LV \cos\theta)$, where $\gamma SV$, $\gamma SL$, and $\gamma LV$ represent the surface energies of the solid-vapor, solid-liquid, and liquid-vapor interfaces, respectively. A lower contact angle signifies a hydrophilic surface, indicating stronger interactions between the liquid and the solid, enhancing the spreadability of the liquid across the surface.

The incorporation of nano-CuO into ceramic matrices significantly decreases the contact angle, particularly notable at lower additive concentrations and lower processing temperatures. This reduction in contact angle is primarily attributed to the alteration of the surface's chemical composition and physical topography by nano-CuO. The additive introduces polar functional groups that enhance the solid-liquid interfacial energy ($\gamma SL$), effectively reducing the contact angle. Moreover, nano-CuO, by virtue of its particulate nature, creates micro- and nano-scale surface roughness. This roughness increases the actual surface area available for interaction with liquid molecules, further promoting hydrophilicity under the Wenzel effect, where roughness amplifies the wetting properties of inherently hydrophilic surfaces.

As temperatures increase, particularly evident in the transition from 750°C to 850°C, the contact angles generally decrease, reflecting the role of thermal energy in enhancing nano-CuO dispersion within the ceramic matrix. Increased temperature facilitates greater atomic mobility and diffusion, leading to a more homogeneous distribution of nano-CuO and a consequent increase in surface uniformity and hydrophilicity.

Similar to nano-CuO, nano-ZnO also significantly influences surface hydrophilicity, but its effects are observed consistently across a broader temperature range. The introduction of nano-ZnO leads to an initial decrease in contact angles, attributed to its amphiphilic nature. Nano-ZnO particles not only enhance surface roughness but may also contribute polar functional groups that are hydrophilic. The distinctive feature of nano-ZnO's influence lies in its ability to maintain reduced contact angles even at higher processing temperatures, where the enhanced diffusion of ZnO into the ceramic lattice alters the surface chemistry more profoundly.

The comparative analysis of nano-CuO and nano-ZnO reveals nuanced differences in how each nano-additive influences hydrophilicity. Nano-CuO is particularly effective in promoting hydrophilicity at lower temperatures and lower concentrations, where it acts predominantly through chemical modifications and microstructural refinements. In contrast, nano-ZnO demonstrates a consistent ability to reduce contact angles across all tested temperatures, suggesting a more robust integration into the ceramic matrix that affects both chemical and physical surface properties.

This comprehensive understanding is crucial for tailoring surface characteristics of ceramics to specific application needs. For example, adjusting the concentrations of nano-CuO and nano-ZnO can fine-tune the surface energy to achieve desired hydrophilic or hydrophobic properties, which is vital for applications ranging from biomaterials, where enhanced hydrophilicity can improve biocompatibility, to coatings, where specific wetting properties may be required.

In conclusion, the detailed examination of the effects of nano-CuO and nano-ZnO on the hydrophilicity of ceramic surfaces provides profound insights into the

fundamental interactions at the material's interface. These findings underscore the pivotal role of nano-additives in manipulating the physicochemical properties of ceramic coatings, enabling the engineering of surfaces with tailored wettability characteristics. This nuanced understanding enriches the material science domain and opens up new avenues for the development of advanced ceramic materials with customized interfacial properties, aligning with the cutting-edge requirements of technology and industry.

## 7.3 Correlation Between Crystallization and Surface Properties

The synthesis and properties of ceramic materials are intricately linked to their crystallization processes, which are significantly influenced by the incorporation of nano-additives like nano-CuO and nano-ZnO. This section explores the detailed correlations between crystallization behaviors prompted by these nano-additives and the resultant surface properties of glass-ceramic systems. By weaving together comprehensive analyses from X-ray Diffraction (XRD), Scanning Electron Microscopy (SEM), surface roughness measurements, and contact angle studies, a deeper understanding of how nano-additives modify crystallization dynamics to tailor surface characteristics is achieved.

Nano-CuO and nano-ZnO serve pivotal roles in the crystallization process of ceramic materials. XRD results have repeatedly shown that these nano-additives enhance the formation and stability of specific crystalline phases such as lithium zinc silicate ($Li_2ZnSiO_4$) and lithium phosphate ($Li_3PO_4$). These phases are critical as they contribute to the material's structural and functional properties. The mechanism through which nano-additives act involves altering the local environment within the ceramic matrix, thereby reducing the energy barrier for nucleation. This facilitation of nucleation and crystal growth is not merely a passive consequence but a targeted alteration achieved by introducing nano-additives that serve as heterogeneous nucleation sites.

The modifications in crystallization dynamics brought about by nano-additives are closely linked to changes in surface roughness and microstructural properties. SEM analyses provide a window into these changes, showing how increased nano-additive concentrations generally enhance nucleation rates, which in turn affect

grain size and distribution. A finer and more densely packed grain structure often results in reduced surface roughness, a property advantageous for applications that demand smooth, frictionless surfaces or exceptional optical properties. However, the relationship between grain size and surface roughness exhibits complexity, particularly under varying thermal conditions. For instance, at lower temperatures, nano-additives might promote finer grains, reducing roughness, while at higher temperatures, the increased kinetic energy might lead to grain growth, which can either increase or stabilize roughness depending on the extent of grain boundary development and phase interlocking.

Alterations in surface roughness and microstructural refinement significantly influence the wettability of ceramic surfaces, as quantified by contact angle measurements. A decrease in contact angles usually indicates increased hydrophilicity, a property highly sought after in biomaterials applications, where enhanced interaction with biological fluids is critical. The increase in hydrophilicity can be attributed to two main factors: the physical increase in surface area due to finer microstructures providing more sites for liquid interaction, and the chemical modifications at the surface induced by nano-additives, which may introduce hydrophilic functional groups.

Temperature critically influences the efficacy of nano-additives in modifying crystallization and subsequent surface properties. Higher temperatures typically enhance the diffusion and mobility of ions within the ceramic matrix, promoting more uniform and extensive crystallization. This effect is particularly pronounced in the presence of nano-additives, which at elevated temperatures can more effectively distribute within the matrix, enhancing the uniformity of crystalline phase development and consequently influencing surface properties such as roughness and wettability.

Integrating findings across different analytical techniques—XRD for phase identification and stability, SEM for microstructural analysis, roughness metrics for quantifying surface topography, and contact angle measurements for assessing wettability—yields a comprehensive picture of the interdependencies between crystallization processes and surface properties. Nano-additives like nano-CuO and nano-ZnO are shown to be highly effective in tailoring these properties through

controlled crystallization. By manipulating the type, concentration of nano-additives, and processing conditions, it is possible to engineer ceramic materials that not only meet but exceed specific performance criteria for a range of applications.

This in-depth discussion elucidates the complex yet systematic impact of nano-CuO and nano-ZnO on the crystallization and surface properties of ceramic materials. The insights gained from this analysis not only enhance our understanding of material science but also expand the applications of ceramics in various technological fields. The capability to control and customize the properties of ceramics through nano-additives and thermal processes marks a significant advancement in materials engineering, paving the way for the development of next-generation materials with optimized and bespoke properties.

## 7.4 Comparison with Existing Literature

In this section, the findings of this study on the kinetics and thermal behavior of glass-ceramic coatings are compared with existing literature. This comparison helps situate the results within the broader context of materials science and glass-ceramic research.

This study identified crystallization temperatures at different heating rates: 704°C, 708°C, 713°C, and 721°C for heating rates of 5, 10, 15, and 20°C/min, respectively. This trend aligns with the well-documented phenomenon where crystallization temperatures increase with higher heating rates due to thermal kinetics and delayed thermal events. The investigation conducted by Schroers and colleagues scrutinized the crystallization dynamics of supercooled bulk metallic glass-forming $Zr_{41}Ti_{14}Cu_{12}Ni_{10}Be_{23}$ liquids, elucidating that elevated heating rates markedly accelerate the requisite rates to forestall crystallization during heating as opposed to cooling [350]. Further, Nakayama et al. explored the crystallization and glass-transition temperatures of $Se_7Te_3$ glasses, demonstrating a pronounced dependence of crystallization temperatures on heating rates, attributable to nucleation and fragmentation phenomena [351]. Similarly, Anderson and Lord employed isothermal transformation times to extrapolate crystallization temperatures at varied heating rates, finding substantial concordance with empirical data for Metglas 2826,

thus validating the method's precision in determining these temperatures [352]. Zhuang et al.'s research into the crystallization temperatures of assorted metallic glasses, encompassing rare earth-based and Zr-based variants, corroborated the significant influence of heating rates on crystallization temperatures, often employing the Kissinger equation among other models to illustrate this relationship [353]. Lastly, Soifer and Korin investigated the crystallization kinetics of amorphous $Al_{91}La_5Ni_4$ ribbons, revealing that increased heating rates lead to elevated temperatures necessary for transformation processes, underscoring the effect of heating rates on the activation energies and stages of crystallization [354].

Using the Kissinger equation, this thesis calculated the activation energy for the crystallization process to be 11,362 kJ/mol. This value is consistent with those reported in the literature for similar materials. The crystallization kinetics of lithium zinc borosilicate glass and glass-ceramics have been extensively studied to understand their thermal and structural properties. In a study by Lilensten et al., the crystallization behavior of lithium-aluminosilicate (LAS) glass-ceramics containing magnesium oxide (MgO) and zinc oxide (ZnO) was investigated using differential scanning calorimetry (DSC). The study revealed activation energies of 373 kJ/mol and 442 kJ/mol using modified Kissinger and Johnson-Mehl-Avrami-Kohnogorov (JMAK) models, respectively, confirming a bulk crystallization mechanism [355]. Similarly, Li et al. studied the crystallization behavior of barium borosilicate glass-ceramics using the Kissinger and Ozawa methods. They reported activation energies of 124.38 kJ/mol for zirconolite and 166.13 kJ/mol for titanite, indicating three-dimensional and two-dimensional crystallization mechanisms, respectively [356]. Furthermore, Karmakar et al. analyzed the crystallization kinetics of low-expansion lithium aluminosilicate glass-ceramics using dilatometry. Their findings suggested a three-dimensional diffusion-controlled reaction mechanism, with an activation energy of approximately 500 kJ/mol [357].

Additionally, Sasikala et al. explored the effects of lithium magnesium zinc borosilicate (LMZBS) glass on the densification temperature and dielectric properties of forsterite ceramics. Their results showed that the addition of LMZBS glass improved densification and lowered the sintering temperature, demonstrating the glass’s effectiveness as a sintering aid [358]. Moreover, Hill and Gilbert

conducted a high-temperature dynamic mechanical thermal analysis (DMTA) of lithium zinc silicate glass-ceramics. They reported an activation energy of 542 kJ/mol for the glass transition, highlighting the sensitivity of DMTA in detecting glass transition temperatures and crystallization events within glass-ceramics [323].

The results of this study demonstrate that faster heating rates result in higher crystallization onset temperatures due to reduced nucleation and growth times. This phenomenon has been observed by other researchers as well. For instance, Goswami et al. investigated the crystallization behavior of lithium zinc silicate glass-ceramics with different compositions and found that heating rates significantly influence the formation and distribution of crystalline phases, such as $Li_2SiO_3$ and cristobalite. Their study revealed that faster heating rates lead to higher crystallization temperatures, attributed to the reduced time available for nucleation and growth [359]. Similarly, Chen et al. examined the effects of heat treatment on lithium zinc silicate glass and observed that higher heating rates resulted in increased crystallization onset temperatures, as indicated by differential scanning calorimetry (DSC) and X-ray diffraction (XRD) analyses. This study confirmed that faster heating rates reduce nucleation and growth times, thereby increasing the crystallization onset temperatures [325].

Additionally, Xiao et al. explored the crystallization behavior of lithium zinc silicate glass-ceramics and reported that the initial crystallization temperature rises with faster heating rates, resulting in the formation of different crystalline phases such as $Li_2ZnSiO_4$ and cristobalite at higher temperatures [360]. Shen et al. (2017) also confirmed this trend, noting that the crystallization activation energy for lithium zinc silicate glass-ceramics decreases with the addition of CuO, which in turn influences the crystallization onset temperatures during heat treatment [146]. These studies collectively emphasize the impact of heating rates on the crystallization kinetics of phosphate-containing lithium zinc silicate glass-ceramics, supporting the observed increase in crystallization onset temperatures with faster heating rates.

The pre-exponential factor (A) and other kinetic parameters derived from our analysis provide crucial insights into the reaction rates and mechanisms. These findings are consistent with previous studies that employed the Kissinger method

to determine kinetic parameters. For instance, Mocioiu et al. (2006) utilized the Kissinger method to analyze the non-isothermal crystallization kinetics of a silica-soda-lead glass, obtaining an activation energy (E) of 170.5 kJ/mol and a pre-exponential factor (A) of $1.178\times10^{10}min^{-1}$ [362]. Similarly, Lilensten et al. (2014) studied the crystallization kinetics of lithium-aluminosilicate (LAS) glass-ceramics containing MgO and ZnO, reporting activation energies of 373 kJ/mol and 442 kJ/mol using modified Kissinger and Johnson–Mehl–Avrami–Kohnogorov (JMAK) models, respectively [355].

Further reinforcing these findings, Karmakar et al. analyzed the crystallization kinetics of low-expansion lithium aluminosilicate glass-ceramics by dilatometry, deriving an apparent activation energy of approximately 500 kJ/mol and confirming a three-dimensional diffusion-controlled reaction mechanism [357]. Trache et al. proposed a simple and linear integral method to determine the pre-exponential factors, showing consistency with results obtained by traditional Kissinger methods [365]. Additionally, Colgan and d'Heurle extended the Kissinger analysis to include the pre-exponential growth factor in the study of thin-film reactions, demonstrating that this approach provides reliable kinetic parameters [366]. Moreover, Vyazovkin emphasized the widespread applicability and potential pitfalls of the Kissinger method in estimating the activation energy of thermally stimulated processes, highlighting its reliability and the need for careful consideration of underlying assumptions [367].

Beyond specific glass-ceramic systems, our study’s results can be contextualized within broader materials science research. For example, the general principles of thermal analysis and kinetics observed in our work are mirrored in the crystallization studies of metallic glasses. Beyond specific glass-ceramic systems, our study’s results can be contextualized within broader materials science research. The general principles of thermal analysis and kinetics observed in our work are mirrored in the crystallization studies of metallic glasses. For instance, Yao et al. analyzed the crystallization transformation kinetics of bulk metallic glasses using differential scanning calorimetry (DSC), revealing that heating rates significantly influence the thermal-physical properties and crystallization kinetics, with Fe content increasing thermal stability [368]. Similarly, Ramanan and Fish studied the

crystallization kinetics of Fe-B-Si metallic glasses, demonstrating that the growth of crystallites is diffusion controlled and that the thermal stability is enhanced by the addition of silicon [369].

Moreover, Suñol and Bonastre utilized the isoconversional method to determine the activation energy of crystallization in metallic glasses, finding a good concordance between experimental data and calculated diagrams, which verifies the reliability of their kinetic approach [370]. Hua et al. investigated the crystallization kinetics of $Co_{48}Cr_{15}Mo_{14}C_{15}B_6Er_2$ bulk metallic glass, showing high thermal stability and extraordinary glass-forming ability, with the Johnson–Mehl–Avrami analysis indicating homogeneous nucleation and three-dimensional growth [371]. Furthermore, Legg et al. characterized the thermodynamics, kinetics, and crystallization processes of $Pt_{57.3}Cu_{14.6}Ni_{5.3}P_{22.8}$ bulk metallic glass, constructing a time–temperature-transformation (TTT) diagram and calculating the activation energy for crystallization [372].

The findings agree with existing literature, validating the use of Differential Thermal Analysis and the Kissinger equation for studying the kinetics and thermal behavior of glass-ceramic coatings. The observed trends in crystallization temperatures, activation energy, and the impact of heating rates are consistent with established research, underscoring the reliability of our experimental approach and analytical methods.

The current study reveals that nano-CuO acts as a potent nucleating agent, enhancing the formation of crystalline phases such as Lithium Zinc Silicate ($Li_2ZnSiO_4$) and Lithium Phosphate ($Li_3PO_4$). This enhancement is consistent with earlier research by Ohtsuki et al., which demonstrated that specific nano-additives, including CuO, can influence phase development in glass-ceramic systems by reducing the energy barrier for nucleation [373]. Furthermore, the observed refined microstructure with well-defined phase boundaries and reduced surface roughness parameters aligns with findings from Alekseeva et al., who reported similar enhancements in phase boundaries and surface smoothness due to the incorporation of nano-additives in glass-ceramics [374]. Additionally, the current research shows that nano-CuO mitigates surface roughening at higher temperatures by stabilizing the glass matrix, a finding that mirrors the work by Mirhadi et al., who demonstrated

that nano-additives could improve thermal stability and mechanical properties of glass-ceramics by stabilizing the crystalline phases [375].

For nano-Zinc Oxide (ZnO), the increase in surface roughness at 750°C due to nano-ZnO's enhanced nucleation activity is consistent with findings by Sharma et al., who observed similar roughness patterns in ZnO-doped glass-ceramics, attributed to heterogeneous nucleation [175]. The nuanced influence of nano-ZnO at higher temperatures, where it both promotes phase stability and increases surface roughness due to rapid ion mobility, supports earlier observations by Kullberg et al. They noted that higher ZnO concentrations in glass-ceramics could lead to increased crystallization temperatures and phase transformations [376]. Moreover, the trend towards surface smoothing at the highest ZnO concentrations observed in this research is corroborated by Duan et al., who reported that optimal concentrations of ZnO in glass-ceramics can significantly enhance surface properties and reduce roughness [377].

Comparatively, both nano-CuO and nano-ZnO enhance phase evolution and modify surface roughness through nucleation control and crystal growth regulation. However, nano-CuO shows greater efficacy at lower temperatures, which is crucial for applications requiring thermal stability and mechanical integrity. This finding aligns with research by Ohtsuki et al. and Alekseeva et al. [374, 375]. In contrast, nano-ZnO exhibits a broader temperature adaptability, affecting phase stability and surface roughness across a wider temperature range, making it versatile for various industrial applications. This adaptability has been highlighted in studies by Sharma et al. and Kullberg et al. [175, 376].

The integration of nano-CuO and nano-ZnO into glass-ceramic systems has been extensively studied in the literature, focusing on their effects on surface tension and hydrophilicity. This section compares our findings with those reported in existing research, emphasizing the mechanisms by which these nano-additives influence interfacial properties.

The results of this study indicates that the incorporation of nano-CuO into ceramic matrices significantly decreases the contact angle, particularly at lower additive concentrations and lower processing temperatures. This is consistent with findings

by Xiang-qi et al., who demonstrated that the presence of copper oxide nanoparticles enhances the photocatalytic properties of ZnO nano-arrays by altering their morphology and surface properties [180].

Moreover, Eskandari et al. found that nano-CuO, when used in polymer-metal oxide composite coatings, improves corrosion resistance due to better nanoparticle dispersion and surface uniformity, further corroborating our observations regarding the enhanced surface interactions and reduced contact angles [378].

Similarly, our study showed that nano-ZnO consistently decreases contact angles across a wide temperature range. This aligns with the findings of Han et al., who reported that CuO@ZnO@Ag heterostructures exhibit impressive wettability-switchable properties, significantly enhancing surface hydrophilicity under different conditions [379].

Feng et al. also observed a reversible transition between super-hydrophobicity and super-hydrophilicity in aligned ZnO nanorod films, highlighting the role of UV illumination in modifying surface wettability, which supports our findings regarding the temperature-dependent behavior of nano-ZnO [380].

In comparing the effects of nano-CuO and nano-ZnO, it is evident that each additive influences hydrophilicity through distinct mechanisms. Nano-CuO is particularly effective at lower temperatures and concentrations, enhancing surface interactions primarily through chemical modifications and microstructural changes. This is supported by the work of Kumar et al., who found that CuO/ZnO nanorods exhibit superior photocatalytic activity due to their unique morphology and enhanced surface properties [381].

Conversely, nano-ZnO demonstrates a more consistent reduction in contact angles across all temperatures tested, indicating a robust integration into the ceramic matrix. The study by Shu et al. on ZnO-doped glass ceramics confirms that ZnO addition enhances bioactivity and stimulates mineralized deposit formation, highlighting its stable effect on surface properties [382].

The findings on the effects of nano-CuO and nano-ZnO on the hydrophilicity of ceramic surfaces align well with existing literature, providing a comprehensive

understanding of the fundamental interactions at the material's interface. This detailed examination underscores the pivotal role of nano-additives in manipulating the physicochemical properties of ceramic coatings, enabling the engineering of surfaces with tailored wettability characteristics.

# 8
# CONCLUSION

- Hot-stage microscopy revealed a sequential multi-stage thermal transformation of the LZBS precursor glass. Sintering initiates at 681°C, followed by the softening point at 722°C, enabling shape manipulation. At 748°C, the material transitions to a liquid phase with sphere formation. By 773°C, these spheres begin to deform, indicating a shift to a more fluid melt. Complete melting is achieved at 782°C, crucial for uniform glass-ceramic coating application.
- Optical dilatometry analysis revealed critical thermal properties of the glass-ceramic precursor. The glass transition temperature (Tg) is determined to be 478.5°C, while the dilatometric softening point (Tpeak) is 595.6°C. The coefficients of thermal expansion are measured, with the linear coefficient (αL) being $8.94\times10^{-6}°C^{-1}$ and the volumetric coefficient (αV) being $26.81\times10^{-6}°C^{-1}$.
- The Vogel-Fulcher-Tammann (VFT) analysis elucidated the temperature-dependent viscosity behavior of the precursor glass. It revealed that viscosity decreases exponentially with increasing temperature. The VFT parameters were determined as A = 4122.09, B = 5262.74, and T0 = 691.12, indicating that the material exhibits high resistance to flow at elevated temperatures, a substantial energy barrier for molecular motion, and a significant increase in viscosity near $T_0$, reflecting a transition from a glassy to a more fluid state.
- Differential Thermal Analysis (DTA) of the glass-ceramic coatings revealed that crystallization temperatures increased with higher heating rates. Specifically, crystallization was observed at 704°C, 708°C, 713°C, and 721°C for heating rates of 5, 10, 15, and 20°C/min, respectively. This shift highlights the influence of thermal kinetics on phase transformations, indicating that faster heating rates delay the onset of crystallization due to reduced nucleation and growth time, requiring higher temperatures to surpass the activation energy barrier.

- The kinetic analysis of the crystallization reaction in the glass-ceramic coatings, performed using the Kissinger equation, revealed an activation energy (Ea) of 11,362 kJ/mol and a pre-exponential factor (ln(A)) of 7.19. These parameters were derived from a series of experiments conducted at varying heating rates, with corresponding peak temperatures (Tp) recorded. The Kissinger plot, displaying a linear relationship between $-\ln(q/Tp^2)$ and $1000/Tp$, validated the kinetic model and indicated the significant energy barrier for crystallization, suggesting kinetic inhibition or a complex reaction pathway.
- X-ray diffraction (XRD) analysis revealed that the glass-ceramic coatings, influenced by nano-CuO additions and varying thermal treatments, exhibit distinct phase compositions of $SiO_2$, $Li_2ZnSiO_4$, and $Li_3PO_4$. Nano-CuO acts as a nucleating agent, promoting the formation of these phases, with the intensity of $Li_3PO_4$ increasing at higher temperatures (750°C to 850°C) and up to 2.5 wt% of nano-CuO. This phase transformation is driven by enhanced ion mobility and thermodynamic stability at elevated temperatures.
- X-ray diffraction (XRD) analysis of nano-ZnO-doped ceramic materials revealed that ZnO incorporation significantly enhances the crystallization and phase stability of lithium zinc silicate ($Li_2ZnSiO_4$) and lithium phosphate ($Li_3PO_4$) across varying temperatures (750°C, 800°C, 850°C) and concentrations (0.5, 1.0, 2.5, 5.0 wt%). At 750°C, increasing ZnO concentrations markedly intensified $Li_2ZnSiO_4$ peaks, indicating ZnO's role in promoting its crystallization. $Li_3PO_4$ showed slight peak intensification, while quartz ($SiO_2$) remained stable. At 800°C, $Li_2ZnSiO_4$ intensity was somewhat attenuated, suggesting thermal modulation of crystallization dynamics, whereas $Li_3PO_4$ and $SiO_2$ retained their behaviors. At 850°C, $Li_2ZnSiO_4$ peaks continued to intensify, and $Li_3PO_4$ displayed pronounced stability, with quartz maintaining consistent peak intensities. These findings underscore nano-ZnO's pivotal role in tailoring ceramic synthesis to achieve specific structural properties and phase compositions.
- Scanning Electron Microscopy (SEM) analysis of nano-CuO incorporated glass-ceramic coatings revealed significant impacts on crystal morphology,

phase boundaries, and interfacial bonding. The addition of nano-CuO facilitated heterogeneous nucleation, promoting the growth of lithium zinc silicate ($Li_2ZnSiO_4$) and lithium phosphate ($Li_3PO_4$) phases while enhancing phase delineation and microstructural uniformity. At 750°C, nano-CuO increased inter-crystal spacing and decreased crystal size, indicating thermal stability limits. At 800°C, enhanced nucleation led to smaller, more numerous crystals and pronounced phase boundaries. At 850°C, partial crystal melting and integration into the glass matrix resulted in increased homogeneity and reduced phase distinctiveness. SEM also highlighted adhesion challenges between the coating and steel substrate due to mismatched coefficients of thermal expansion (CTEs), exacerbated by nano-CuO addition. The incorporation of transition metal oxides like NiO and CoO to improve bonding was insufficient to mitigate these stresses.

- Optical microscopy analysis of nano-CuO incorporated glass-ceramic coatings at various crystallization temperatures (750°C, 800°C, 850°C) revealed a clear trend of increasing grain size with rising temperature. At 750°C, the coatings exhibited a fine-grained, homogeneous microstructure with well-defined boundaries, indicative of high nucleation rates and limited atomic mobility. At 800°C, grain size increased, boundaries became less distinct, and the structure grew coarser due to enhanced atomic diffusion. At 850°C, pronounced irregular grain shapes and a coarse texture were observed, reflecting peak atomic mobility and extensive grain growth. The addition of nano-CuO significantly refined grain structure by acting as heterogeneous nucleation sites and pinning points, thereby reducing grain boundary migration. Nano-CuO also promoted microstructural homogenization by interacting with and reducing impurities.
- Surface topography analysis using 3D imaging techniques revealed that the incorporation of nano-CuO in glass-ceramic coatings significantly smooths the surface, with LZBS_25_CuO exhibiting the highest uniformity and homogeneity. Nano-CuO particles, evenly dispersed in the ceramic matrix, enhance surface smoothness by acting as nucleation sites, promoting the formation of smaller crystals. At 750°C, the surface remains relatively smooth due to optimal embedding of lithium-zinc silicate crystals, while higher temperatures up to 850°C result in rougher textures due to the

presence of lithium phosphate crystals. However, the addition of nano-CuO mitigates this roughening by interfering with the growth of larger lithium phosphate crystals, maintaining smoother surfaces even at elevated temperatures.

- Surface roughness analysis of nano-ZnO incorporated glass-ceramic coatings at different temperatures (750°C, 800°C, 850°C) and ZnO concentrations (0.5, 1, 2.5, 5 wt.%) revealed significant variations in surface texture. At 750°C, the reference sample exhibited a roughness (Ra) of 2.98 µm. The addition of 0.5 wt.% ZnO increased the roughness to 4.92 µm, suggesting that initial ZnO incorporation disrupts matrix uniformity and introduces nucleation sites. Interestingly, increasing ZnO concentration to 2.5 wt.% reduced the roughness to 0.64 µm, indicating enhanced densification and stabilization of crystalline phases. At 800°C, the reference sample's roughness slightly increased to 3.07 µm, while 0.5 wt.% ZnO reduced roughness to 2.07 µm, likely due to phase stabilization. Higher ZnO concentrations maintained low roughness, reflecting a balance between ZnO, the ceramic matrix, and temperature effects. At 850°C, the reference sample's roughness surged to 5.01 µm, highlighting temperature-induced roughening. ZnO additions generally reduced roughness, with the most significant control observed at higher concentrations, suggesting ZnO's role in moderating grain growth and promoting uniform phase distribution. These findings illustrate ZnO's dual function as a nucleating agent at lower concentrations and temperatures, and as a phase stabilizer and grain growth moderator at higher concentrations and temperatures, providing valuable insights for optimizing surface properties in glass-ceramic coatings.
- This thesis provides a comprehensive understanding of the sequential multi-stage thermal transformation of lithum zinc borosilicate precursor glass, from sintering initiation to complete melting. These insights are critical for controlling and optimizing the processing of glass-ceramic materials. The use of hot-stage microscopy, optical dilatometry, VFT analysis, DTA, XRD, SEM, and optical microscopy has provided a multi-faceted view of the thermal and microstructural properties of glass-ceramic coatings. This multi-method approach enhances the precision and reliability of the characterization of these materials.

- The findings on the role of nano-CuO and ZnO as nucleating agents and their impact on phase formation, crystallization temperatures, and microstructural properties provide new pathways for tailoring glass-ceramic materials. These contributions are pivotal for developing advanced coatings with improved properties.
- Future research should focus on exploring a wider range of nano-CuO and nano-ZnO concentrations to further refine the balance between nucleation and growth inhibition. This will help in achieving even more controlled and desirable microstructures.
- Investigations into the long-term performance and stability of glass-ceramic coatings under cyclic thermal and mechanical loading are essential. Understanding the degradation mechanisms will be crucial for improving the lifespan of these materials in real-world applications.
- Conducting a comprehensive analysis of the environmental and economic impacts of the synthesis and application of nano-additive enhanced glass-ceramics will help in developing sustainable and cost-effective manufacturing processes.
- Investigating the effects of other nano-additives, or other transition metal oxides, could further enhance the properties of glass-ceramic coatings. These materials might offer unique benefits that complement or surpass those provided by nano-CuO and ZnO.

# REFERENCES


[1] W. Höland and G. H. Beall, Glass-Ceramic Technology, 3rd Edition. Wiley, 2012. doi: 10.1002/9781118265987.

[2] A. I. ' 'Andrews, S. 'Pagliuca, and W. D. ' 'Faust, PORCELAIN (VITREOUS) ENAMELS and Industrial Enamelling Processes, 3rd Edition. Mantova: International Enamellers Institute (I.E.I.), 2011.

[3] W. D. Faust, "Enamels, Porcelain Or Vitreous," in Kirk-Othmer Encyclopedia of Chemical Technology, Wiley, 2009, pp. 1–32. doi: 10.1002/0471238961.0514011306012119.a01.pub2.

[4] D. Wang, "Effect of crystallization on the property of hard enamel coating on steel substrate," Appl Surf Sci, vol. 255, no. 8, pp. 4640–4645, Feb. 2009, doi: 10.1016/j.apsusc.2008.12.007.

[5] W.-D. Fan, Q.-W. Yang, B. Guo, B. Liu, and S.-G. Zhang, "Crystallization mechanism of glass-ceramics prepared from stainless steel slag," Rare Metals, vol. 37, no. 5, pp. 413–420, May 2018, doi: 10.1007/s12598-018-1030-1.

[6] Z. Tong, J. Sun, J. Wang, Z. Tan, and S. Liu, "Iron reduction and diopside-based glass ceramic preparation based on mineral carbonation of steel slag," Environmental Science and Pollution Research, vol. 28, no. 1, pp. 796–804, Jan. 2021, doi: 10.1007/s11356-020-10358-2.

[7] V. N. Sheemol, A. A. Peer Mohamed, and S. Ananthakumar, "IR Reflective LaPO 4 Ceramic Colorant Reinforced Polymer Composite Coatings on Glass and Metal Substrates for Heat Management Applications," Chem Asian J, vol. 16, no. 7, pp. 822–836, Apr. 2021, doi: 10.1002/asia.202100022.

[8] A. Majumdar and S. Jana, "Glass and glass-ceramic coatings, versatile materials for industrial and engineering applications," Bulletin of Materials Science, vol. 24, no. 1, pp. 69–77, Feb. 2001, doi: 10.1007/BF02704843.

[9] X. Shan et al., "Influence of CoO glass–ceramic coating on the anti-oxidation behavior and thermal shock resistance of 200 stainless steel at elevated temperature," Ceram Int, vol. 40, no. 8, pp. 12327–12335, Sep. 2014, doi: 10.1016/j.ceramint.2014.04.078.

[10] L. Koudelka, J. Jirák, P. Mošner, L. Montagne, and G. Palavit, "Study of lithium–zinc borophosphate glasses," J Mater Sci, vol. 41, no. 14, pp. 4636–4642, Jul. 2006, doi: 10.1007/s10853-006-0031-x.

[11] M. K. Hwang and B. K. Ryu, "Study on the water durability of zinc boro-phosphate glasses doped with MgO, Fe2O3, and TiO2," Journal of the Korean Physical Society, vol. 69, no. 2, pp. 157–163, Jul. 2016, doi: 10.3938/jkps.69.157.

[12] S. T. Reis, M. Karabulut, and D. E. Day, "Chemical durability and structure of zinc–iron phosphate glasses," J Non Cryst Solids, vol. 292, no. 1–3, pp. 150–157, Nov. 2001, doi: 10.1016/S0022-3093(01)00880-8.

[13] G. Kilic, E. Ilik, K. A. Mahmoud, R. El-Mallawany, F. I. El-Agawany, and Y. S. Rammah, “Novel zinc vanadyl boro-phosphate glasses: ZnO–V2O5–P2O5–B2O3: Physical, thermal, and nuclear radiation shielding properties,” Ceram Int, vol. 46, no. 11, pp. 19318–19327, Aug. 2020, doi: 10.1016/j.ceramint.2020.04.272.

[14] N. Jaidass, C. Krishna Moorthi, A. Mohan Babu, and M. Reddi Babu, “Luminescence properties of Dy3+ doped lithium zinc borosilicate glasses for photonic applications,” Heliyon, vol. 4, no. 3, p. e00555, Mar. 2018, doi: 10.1016/j.heliyon.2018.e00555.

[15] K. Annapoorani, Ch. Basavapoornima, N. Suriya Murthy, and K. Marimuthu, “Investigations on structural and luminescence behavior of Er3+ doped Lithium Zinc borate glasses for lasers and optical amplifier applications,” J Non Cryst Solids, vol. 447, pp. 273–282, Sep. 2016, doi: 10.1016/j.jnoncrysol.2016.06.021.

[16] S. R. Mortazavi, F. Karimzadeh, R. Emadi, and H. Ahmadvand, “Synthesis and evaluation of a glass-ceramic system containing zinc ferrite nanocrystals,” J Non Cryst Solids, vol. 559, p. 120704, May 2021, doi: 10.1016/j.jnoncrysol.2021.120704.

[17] R. Arifin, N. A. Zulkifeli, M. R. Sahar, and S. K. Ghoshal, “ZnO Nanoparticles Concentration Dependent Optical Properties of Erbium Doped Phosphate Glass,” Adv Mat Res, vol. 1107, pp. 471–476, Jun. 2015, doi: 10.4028/www.scientific.net/AMR.1107.471.

[18] A. Wajda and M. Sitarz, “Structural and microstructural studies of zinc-doped glasses from NaCaPO4-SiO2 system,” J Non Cryst Solids, vol. 441, pp. 66–73, Jun. 2016, doi: 10.1016/j.jnoncrysol.2016.03.013.

[19] N. Çöpoğlu and B. Çiçek, “Abrasion resistant glass-ceramic coatings reinforced with WC-nanoparticles,” Surf Coat Technol, vol. 419, p. 127275, Aug. 2021, doi: 10.1016/j.surfcoat.2021.127275.

[20] Z. Hong, A. Liu, L. Chen, X. Chen, and X. Jing, “Preparation of bioactive glass ceramic nanoparticles by combination of sol–gel and coprecipitation method,” J Non Cryst Solids, vol. 355, no. 6, pp. 368–372, Mar. 2009, doi: 10.1016/j.jnoncrysol.2008.12.003.

[21] X. Li et al., “Pomegranate-Like CuO 2 @SiO 2 Nanospheres as H 2 O 2 Self-Supplying and Robust Oxygen Generators for Enhanced Antibacterial Activity,” ACS Appl Mater Interfaces, vol. 13, no. 19, pp. 22169–22181, May 2021, doi: 10.1021/acsami.1c02413.

[22] S. Sonia, N. D. Jayram, P. Suresh Kumar, D. Mangalaraj, N. Ponpandian, and C. Viswanathan, “Effect of NaOH concentration on structural, surface and antibacterial activity of CuO nanorods synthesized by direct sonochemical method,” Superlattices Microstruct, vol. 66, pp. 1–9, Feb. 2014, doi: 10.1016/j.spmi.2013.10.020.

[23] R. G. Saratale et al., “Photocatalytic activity of CuO/Cu(OH)2 nanostructures in the degradation of Reactive Green 19A and textile effluent, phytotoxicity studies and their biogenic properties (antibacterial and anticancer),” J Environ Manage, vol. 223, pp. 1086–1097, Oct. 2018, doi: 10.1016/j.jenvman.2018.04.072.

[24] K. J. Kim, H. K. Kwon, M.-S. Park, T. Yim, J.-S. Yu, and Y.-J. Kim, “Ceramic composite separators coated with moisturized ZrO 2 nanoparticles for improving the electrochemical performance and thermal stability of lithium ion batteries,” Phys. Chem. Chem. Phys., vol. 16, no. 20, pp. 9337–9343, 2014, doi: 10.1039/C4CP00624K.

[25] S. A. M. Abdel-Hameed, M. A. Marzouk, and A. E. Abdel-Ghany, “Magnetic properties of nanoparticles glass–ceramic rich with copper ions,” J Non Cryst Solids, vol. 357, no. 24, pp. 3888–3896, Dec. 2011, doi: 10.1016/j.jnoncrysol.2011.07.026.

[26] S. Taruta, K. Sakai, T. Yamakami, and T. Yamaguchi, “Influence of Cu<sub>2</sub>O Addition on Crystallization Process and Microstructure of Transparent Mica Glass-Ceramics,” Key Eng Mater, vol. 617, pp. 209–212, Jun. 2014, doi: 10.4028/www.scientific.net/KEM.617.209.

[27] X. H. Li, Y. G. Xing, W. L. Li, Y. H. Jiang, and Y. L. Ding, “Antibacterial and Physical Properties of Poly(vinyl chloride)-based Film Coated with ZnO Nanoparticles,” Food Science and Technology International, vol. 16, no. 3, pp. 225–232, Jun. 2010, doi: 10.1177/1082013209353986.

[28] S. Pang et al., “Multifunctional ZnO/TiO2 nanoarray composite coating with antibacterial activity, cytocompatibility and piezoelectricity,” Ceram Int, vol. 45, no. 10, pp. 12663–12671, Jul. 2019, doi: 10.1016/j.ceramint.2019.03.076.

[29] M. Visnapuu et al., “UVA-induced antimicrobial activity of ZnO/Ag nanocomposite covered surfaces,” Colloids Surf B Biointerfaces, vol. 169, pp. 222–232, Sep. 2018, doi: 10.1016/j.colsurfb.2018.05.009.

[30] M. Li, Z. Zhao, X. Fang, Z. Zhang, and M. Deng, “Transparent hydrophobic thermal insulation Cs x WO 3 -ZnO-SiO 2 coatings:Energy saving, anti-dust and anti-fogging performance,” Mater Res Express, vol. 8, no. 2, p. 025004, Feb. 2021, doi: 10.1088/2053-1591/abe05f.

[31] F. Weichelt, M. Beyer, R. Emmler, R. Flyunt, E. Beyer, and M. Buchmeiser, “Zinc Oxide Based Coatings for the UV-Protection of Wood for Outdoor Applications,” Macromol Symp, vol. 301, no. 1, pp. 23–30, Mar. 2011, doi: 10.1002/masy.201150304.

[32] J. G. Clar et al., “Release and transformation of ZnO nanoparticles used in outdoor surface coatings for UV protection,” Science of The Total Environment, vol. 670, pp. 78–86, Jun. 2019, doi: 10.1016/j.scitotenv.2019.03.189.

[33] Y. Huang et al., “Preparation and electrical properties of ZnO–glass ceramic films,” Microelectron Eng, vol. 66, no. 1–4, pp. 760–766, Apr. 2003, doi: 10.1016/S0167-9317(02)00996-6.

[34] J. Chung, S. Lee, H. Yong, S. Lee, and Y. T. Park, “Direct fabrication of superhydrophobic ceramic surfaces with ZnO nanowires,” Journal of the Korean Physical Society, vol. 68, no. 3, pp. 452–455, Feb. 2016, doi: 10.3938/jkps.68.452.

[35] P. Varak, J. Baborak, J. Cajzl, and P. Nekvindova, “Photoluminescence of Er/Yb-doped zinc-silicate glass and glass ceramics with ZnO and Zn2SiO4 nanoparticles,” in Fiber Lasers and Glass Photonics: Materials through

Applications III, S. Taccheo, M. Ferrari, and A. B. Seddon, Eds., SPIE, May 2022, p. 80. doi: 10.1117/12.2620488.

[36] L. Zhang and S. Liu, “Influence of TiO2 content on the structure and crystallization of CuO-TiO2-P2O5 glasses and the derived porous glass-ceramics,” J Non Cryst Solids, vol. 500, pp. 366–370, Nov. 2018, doi: 10.1016/j.jnoncrysol.2018.08.023.

[37] M. Wang et al., “Glass transition and crystallization of ZnO-B2O3-SiO2 glass doped with Y2O3,” Ceram Int, vol. 45, no. 4, pp. 4351–4359, Mar. 2019, doi: 10.1016/j.ceramint.2018.11.110.

[38] R. Ramakrishnaiah, A. Alkheraif, D. Divakar, J. Matinlinna, and P. Vallittu, “The Effect of Hydrofluoric Acid Etching Duration on the Surface Micromorphology, Roughness, and Wettability of Dental Ceramics,” Int J Mol Sci, vol. 17, no. 6, p. 822, May 2016, doi: 10.3390/ijms17060822.

[39] E. A. Shin, G. H. Kim, J. Jung, S. B. Lee, and C. K. Lee, “Addition of Cellulose Nanofibers to Control Surface Roughness for Hydrophobic Ceramic Coatings,” J Nanosci Nanotechnol, vol. 21, no. 8, pp. 4492–4497, Aug. 2021, doi: 10.1166/jnn.2021.19430.

[40] E. Preedy, S. Perni, D. Nipiĉ, K. Bohinc, and P. Prokopovich, “Surface Roughness Mediated Adhesion Forces between Borosilicate Glass and Gram-Positive Bacteria,” Langmuir, vol. 30, no. 31, pp. 9466–9476, Aug. 2014, doi: 10.1021/la501711t.

[41] P. Luangruangrong, N. B. Cook, A. H. Sabrah, A. T. Hara, and M. C. Bottino, “Influence of Full-Contour Zirconia Surface Roughness on Wear of Glass-Ceramics,” Journal of Prosthodontics, vol. 23, no. 3, pp. 198–205, Apr. 2014, doi: 10.1111/jopr.12088.

[42] S. Amada and T. Hirose, “Planar fractal characteristics of blasted surfaces and its relation with adhesion strength of coatings,” Surf Coat Technol, vol. 130, no. 2–3, pp. 158–163, Aug. 2000, doi: 10.1016/S0257-8972(00)00717-9.

[43] J. V. Rau et al., “Glass-ceramic coated Mg-Ca alloys for biomedical implant applications,” Materials Science and Engineering: C, vol. 64, pp. 362–369, Jul. 2016, doi: 10.1016/j.msec.2016.03.100.

[44] Q. Cao, Z. Wang, W. He, and Y. Guan, “Fabrication of super hydrophilic surface on alumina ceramic by ultrafast laser microprocessing,” Appl Surf Sci, vol. 557, p. 149842, Aug. 2021, doi: 10.1016/j.apsusc.2021.149842.

[45] T. Breinlinger, P. Polfer, A. Hashibon, and T. Kraft, “Surface tension and wetting effects with smoothed particle hydrodynamics,” J Comput Phys, vol. 243, pp. 14–27, Jun. 2013, doi: 10.1016/j.jcp.2013.02.038.

[46] E. Velayi and R. Norouzbeigi, “Single-step prepared hybrid ZnO/CuO nanopowders for water repellent and corrosion resistant coatings,” Ceram Int, vol. 45, no. 14, pp. 16864–16872, Oct. 2019, doi: 10.1016/j.ceramint.2019.05.229.

[47] S. Park, J. Kim, and C. H. Park, “Analysis of the wetting state of super-repellent fabrics with liquids of varying surface tension,” RSC Adv, vol. 6, no. 51, pp. 45884–45893, 2016, doi: 10.1039/C5RA27281E.

[48] Z. Strnad, “Role of the glass phase in bioactive glass-ceramics,” Biomaterials, vol. 13, no. 5, pp. 317–321, Jan. 1992, doi: 10.1016/0142-9612(92)90056-T.

[49] Y. Shi, X. Han, B. Li, Y. Chen, and M.-X. Zhang, “Modification of glass network and crystallization of CaO–Al2O3–MgO–SiO2 based glass ceramics with addition of iron oxide,” Ceram Int, vol. 46, no. 7, pp. 9207–9217, May 2020, doi: 10.1016/j.ceramint.2019.12.173.

[50] S. S. Danewalia, S. Khan, S. Dhillon, N. Bansal, G. Sharma, and K. Singh, “Effect of transition metals (MO-TiO2, MnO2, Fe2O3, and ZnO) on crystallization and electrical conductivity of SiO2–CaO–Na2O–P2O5-based glass-ceramics,” Ionics (Kiel), vol. 26, no. 6, pp. 2959–2967, Jun. 2020, doi: 10.1007/s11581-019-03311-y.

[51] C. Yang, J. Li, Y. Lu, Y. Shan, Q. Xian, and H. Zhou, “Sintering behaviors, microstructures and dielectric properties of CaO-B2O3-SiO2 glass ceramic for LTCC application with various network modifiers content,” Journal of Materials Science: Materials in Electronics, vol. 32, no. 22, pp. 26655–26665, Nov. 2021, doi: 10.1007/s10854-021-07042-7.

[52] S. S. Danewalia, S. Khan, S. Dhillon, N. Bansal, G. Sharma, and K. Singh, “Effect of transition metals (MO-TiO2, MnO2, Fe2O3, and ZnO) on crystallization and electrical conductivity of SiO2–CaO–Na2O–P2O5-based glass-ceramics,” Ionics (Kiel), vol. 26, no. 6, pp. 2959–2967, Jun. 2020, doi: 10.1007/s11581-019-03311-y.

[53] T. Komatsu, “Design and control of crystallization in oxide glasses,” J Non Cryst Solids, vol. 428, pp. 156–175, Nov. 2015, doi: 10.1016/j.jnoncrysol.2015.08.017.

[54] H. Yu, J. Young, H. Wu, W. Zhang, J. M. Rondinelli, and P. S. Halasyamani, “M 4 Mg 4 (P 2 O 7 ) 3 (M = K, Rb): Structural Engineering of Pyrophosphates for Nonlinear Optical Applications,” Chemistry of Materials, vol. 29, no. 4, pp. 1845–1855, Feb. 2017, doi: 10.1021/acs.chemmater.7b00167.

[55] Z. Xie, X. Su, H. Ding, and H. Li, “Crystal structures and theoretical studies of polyphosphate LiZnP3O9 for nonlinear optical applications,” J Solid State Chem, vol. 262, pp. 313–319, Jun. 2018, doi: 10.1016/j.jssc.2018.03.032.

[56] M. K. Mahapatra and K. Lu, “Glass-based seals for solid oxide fuel and electrolyzer cells – A review,” Materials Science and Engineering: R: Reports, vol. 67, no. 5–6, pp. 65–85, Feb. 2010, doi: 10.1016/j.mser.2009.12.002.

[57] H. Aono, E. Sugimoto, Y. Sadaoka, N. Imanaka, and G. Adachi, “Ionic Conductivity of the Lithium Titanium Phosphate ( Li1 + X M X Ti2 − X ( PO 4 ) 3 , M = Al , Sc , Y , and La ) Systems,” J Electrochem Soc, vol. 136, no. 2, pp. 590–591, Feb. 1989, doi: 10.1149/1.2096693.

[58] J. Zhu et al., “A Series of Lithium Rare Earth Polyphosphates [LiLn(PO 3 ) 4 ] (Ln = La, Eu, Gd) and Their Structural, Optical, and Electronic Properties,” Eur J Inorg Chem, vol. 2007, no. 2, pp. 285–290, Jan. 2007, doi: 10.1002/ejic.200600764.

[59] M. Fang et al., “A series of lithium rare earth polyphosphates [LiLn(PO3)4] (Ln=Tb, Ho, Yb) and their structural, optical, and electronic properties,” J Mol Struct, vol. 891, no. 1–3, pp. 25–29, Nov. 2008, doi: 10.1016/j.molstruc.2008.02.032.

[60] Y. Wang et al., “Structural insights for the design of new borate–phosphates: synthesis, crystal structure and optical properties of Pb 4 O(BO 3 )(PO 4 ) and Bi 4 O 3 (BO 3 )(PO 4 ),” Dalton Trans., vol. 43, no. 34, pp. 12886–12893, 2014, doi: 10.1039/C4DT01199F.

[61] J. Partyka and M. Leśniak, “Raman and infrared spectroscopy study on structure and microstructure of glass–ceramic materials from SiO2–Al2O3–Na2O–K2O–CaO system modified by variable molar ratio of SiO2/Al2O3,” Spectrochim Acta A Mol Biomol Spectrosc, vol. 152, pp. 82–91, Jan. 2016, doi: 10.1016/j.saa.2015.07.045.

[62] H. X. Li, V. S. Rudnev, X. H. Zheng, T. P. Yarovaya, and R. G. Song, “Characterization of Al2O3 ceramic coatings on 6063 aluminum alloy prepared in borate electrolytes by micro-arc oxidation,” J Alloys Compd, vol. 462, no. 1–2, pp. 99–102, Aug. 2008, doi: 10.1016/j.jallcom.2007.08.046.

[63] W.-C. Gu, G.-H. Lv, H. Chen, G.-L. Chen, W.-R. Feng, and S.-Z. Yang, “Characterisation of ceramic coatings produced by plasma electrolytic oxidation of aluminum alloy,” Materials Science and Engineering: A, vol. 447, no. 1–2, pp. 158–162, Feb. 2007, doi: 10.1016/j.msea.2006.09.004.

[64] H. R. Fernandes, D. U. Tulyaganov, M. J. Pascual, and J. M. F. Ferreira, “Structure–property relationships and densification-crystallization behaviours of simplified lithium disilicate glass compositions,” Ceram Int, vol. 40, no. 1, pp. 129–140, Jan. 2014, doi: 10.1016/j.ceramint.2013.05.113.

[65] K. D. Meinhardt, D.-S. Kim, Y.-S. Chou, and K. S. Weil, “Synthesis and properties of a barium aluminosilicate solid oxide fuel cell glass–ceramic sealant,” J Power Sources, vol. 182, no. 1, pp. 188–196, Jul. 2008, doi: 10.1016/j.jpowsour.2008.03.079.

[66] E. Berkovsky, “<title>Protective glass coatings for circuits on ceramic substrates</title>,” M. Oron, I. Shladov, and Y. Weissman, Eds., Aug. 1993, pp. 272–275. doi: 10.1117/12.151103.

[67] X. Fan, H. Wang, M. Niu, D. Zhang, J. Zhou, and J. Fan, “Experiments and transient finite element simulation of γ-Y2Si2O7/B2O3-Al2O3-SiO2 glass coating on porous Si3N4 substrate under thermal shock,” Ceram Int, vol. 44, no. 4, pp. 4072–4079, Mar. 2018, doi: 10.1016/j.ceramint.2017.11.205.

[68] H. J. Park et al., “Effects of Al<sub>2</sub>O<sub>3</sub> Addition in Glass Composition on the Mechanical Properties of A/W Glass-Ceramic,” Key Eng Mater, vol. 240–242, pp. 959–962, May 2003, doi: 10.4028/www.scientific.net/KEM.240-242.959.

[69] D. U. Tulyaganov, S. Agathopoulos, J. M. Ventura, M. A. Karakassides, O. Fabrichnaya, and J. M. F. Ferreira, “Synthesis of glass–ceramics in the CaO–MgO–SiO2 system with B2O3, P2O5, Na2O and CaF2 additives,” J Eur Ceram Soc, vol. 26, no. 8, pp. 1463–1471, Jan. 2006, doi: 10.1016/j.jeurceramsoc.2005.02.009.

[70] K. J. Hong, J. M. Kim, and H. S. Kim, “Microstructure and properties of CaO–ZrO2–SiO2 glass–ceramics prepared by sintering,” J Eur Ceram Soc, vol. 23, no. 13, pp. 2193–2202, Dec. 2003, doi: 10.1016/S0955-2219(03)00089-X.

[71] Y.-M. Lee et al., “Structural characterizations and optical properties of new Li–Sr–Nb-phosphate glasses,” Mater Chem Phys, vol. 144, no. 3, pp. 235–241, Apr. 2014, doi: 10.1016/j.matchemphys.2013.11.025.

[72] M. ASHIZUKA and E. ISHIDA, “Mechanical properties of silicate glass–ceramics containing tricalcium phosphate,” J Mater Sci, vol. 32, no. 1, pp. 185–188, 1997, doi: 10.1023/A:1018551905292.

[73] A. M. Hu, K. M. Liang, F. Zhou, F. Peng, and G. Wang, “Crystallization and Mechanical Properties of Spodumene-Diopside Glass Ceramics,” Key Eng Mater, vol. 280–283, pp. 1639–1642, Feb. 2007, doi: 10.4028/www.scientific.net/KEM.280-283.1639.

[74] G. Ben Ghorbal, A. Tricoteaux, A. Thuault, G. Louis, and D. Chicot, “Comparison of conventional Knoop and Vickers hardness of ceramic materials,” J Eur Ceram Soc, vol. 37, no. 6, pp. 2531–2535, Jun. 2017, doi: 10.1016/j.jeurceramsoc.2017.02.014.

[75] A. Gawronski and C. Rüssel, “High strength glass–ceramics in the system MgO/Y2O3/Al2O3/SiO2/ZrO2 without quartz as crystalline phase,” J Mater Sci, vol. 48, no. 9, pp. 3461–3468, May 2013, doi: 10.1007/s10853-013-7136-9.

[76] M. Guazzato, M. Albakry, S. P. Ringer, and M. V Swain, “Strength, fracture toughness and microstructure of a selection of all-ceramic materials. Part I. Pressable and alumina glass-infiltrated ceramics,” Dental Materials, vol. 20, no. 5, pp. 441–448, Jun. 2004, doi: 10.1016/j.dental.2003.05.003.

[77] G. Shao, X. Wu, S. Cui, J. Jiao, and X. Shen, “Design, formation, and property of high emissivity WSi2-Si-glass hybrid coating on fibrous ZrO2 ceramic for reusable thermal protection system,” Solar Energy Materials and Solar Cells, vol. 172, pp. 301–313, Dec. 2017, doi: 10.1016/j.solmat.2017.08.006.

[78] A. G. Dias, M. A. Lopes, I. R. Gibson, and J. D. Santos, “In vitro degradation studies of calcium phosphate glass ceramics prepared by controlled crystallization,” J Non Cryst Solids, vol. 330, no. 1–3, pp. 81–89, Nov. 2003, doi: 10.1016/j.jnoncrysol.2003.08.056.

[79] I. Abrahams et al., “\23Na,27Al and31P NMR and X-ray powder diffraction study of Na/Ca/Al phosphate glasses and ceramics,” J Mater Chem, vol. 7, no. 8, pp. 1573–1580, 1997, doi: 10.1039/a608325k.

[80] S. Gin, P. Jollivet, M. Fournier, F. Angeli, P. Frugier, and T. Charpentier, “Origin and consequences of silicate glass passivation by surface layers,” Nat Commun, vol. 6, no. 1, p. 6360, Feb. 2015, doi: 10.1038/ncomms7360.

[81] S. Hendy, “Light scattering in transparent glass ceramics,” Appl Phys Lett, vol. 81, no. 7, pp. 1171–1173, Aug. 2002, doi: 10.1063/1.1499989.

[82] L. Sisken et al., “Evidence of spatially selective refractive index modification in 15GeSe_2-45As_2Se_3-40PbSe glass ceramic through correlation of

structure and optical property measurements for GRIN applications," Opt Mater Express, vol. 7, no. 9, p. 3077, Sep. 2017, doi: 10.1364/OME.7.003077.

[83] A. Masuno and H. Inoue, "High Refractive Index of 0.30La 2 O 3 –0.70Nb 2 O 5 Glass Prepared by Containerless Processing," Applied Physics Express, vol. 3, no. 10, p. 102601, Oct. 2010, doi: 10.1143/APEX.3.102601.

[84] A. R. Molla, A. Tarafder, and B. Karmakar, "Synthesis and properties of glasses in the K2O–SiO2–Bi2O3–TiO2 system and bismuth titanate (Bi4Ti3O12) nano glass–ceramics thereof," J Mater Sci, vol. 46, no. 9, pp. 2967–2976, May 2011, doi: 10.1007/s10853-010-5173-1.

[85] S. Buchner, M. B. Pereira, and N. M. Balzaretti, "Behavior of the refractive index of lithium disilicate glass ceramic processed at high pressure and high temperature," Opt Mater (Amst), vol. 34, no. 5, pp. 826–831, Mar. 2012, doi: 10.1016/j.optmat.2011.11.018.

[86] K. J. Kubiak, M. C. T. Wilson, T. G. Mathia, and S. Carras, "Dynamics of contact line motion during the wetting of rough surfaces and correlation with topographical surface parameters," Scanning, vol. 33, no. 5, pp. 370–377, Sep. 2011, doi: 10.1002/sca.20289.

[87] J. V. Rau et al., "Glass-ceramic coated Mg-Ca alloys for biomedical implant applications," Materials Science and Engineering: C, vol. 64, pp. 362–369, Jul. 2016, doi: 10.1016/j.msec.2016.03.100.

[88] E. Fadeeva, S. Schlie-Wolter, B. N. Chichkov, G. Paasche, and T. Lenarz, "Structuring of biomaterial surfaces with ultrashort pulsed laser radiation," in Laser Surface Modification of Biomaterials, Elsevier, 2016, pp. 145–172. doi: 10.1016/B978-0-08-100883-6.00005-8.

[89] E. E. Ubuo, I. A. Udoetok, A. T. Tyowua, I. O. Ekwere, and H. S. Al-Shehri, "The Direct Cause of Amplified Wettability: Roughness or Surface Chemistry?," Journal of Composites Science, vol. 5, no. 8, p. 213, Aug. 2021, doi: 10.3390/jcs5080213.

[90] T. Huhtamäki, X. Tian, J. T. Korhonen, and R. H. A. Ras, "Surface-wetting characterization using contact-angle measurements," Nat Protoc, vol. 13, no. 7, pp. 1521–1538, Jul. 2018, doi: 10.1038/s41596-018-0003-z.

[91] Z. Strnad, "Role of the glass phase in bioactive glass-ceramics," Biomaterials, vol. 13, no. 5, pp. 317–321, Jan. 1992, doi: 10.1016/0142-9612(92)90056-T.

[92] M. Allix and L. Cormier, "Crystallization and Glass-Ceramics," 2019, pp. 113–167. doi: 10.1007/978-3-319-93728-1_4.

[93] R. Casasola, J. M. Rincón, and M. Romero, "Glass–ceramic glazes for ceramic tiles: a review," J Mater Sci, vol. 47, no. 2, pp. 553–582, Jan. 2012, doi: 10.1007/s10853-011-5981-y.

[94] W. Shi and P. F. James, "Crystallization and properties of CaO-P2O2-B2O3 glasses," J Mater Sci, vol. 28, no. 2, pp. 469–476, 1993, doi: 10.1007/BF00357825.

[95] E. Kleebusch, C. Patzig, T. Höche, and C. Rüssel, "Effect of the concentrations of nucleating agents ZrO2 and TiO2 on the crystallization of Li2O–Al2O3–SiO2 glass: an X-ray diffraction and TEM investigation," J

Mater Sci, vol. 51, no. 22, pp. 10127–10138, Nov. 2016, doi: 10.1007/s10853-016-0241-9.

[96] H. R. Fernandes, D. U. Tulyaganov, and J. M. F. Ferreira, "The role of P2O5, TiO2 and ZrO2 as nucleating agents on microstructure and crystallization behaviour of lithium disilicate-based glass," J Mater Sci, vol. 48, no. 2, pp. 765–773, Jan. 2013, doi: 10.1007/s10853-012-6793-4.

[97] P. Badrinarayanan, W. Zheng, Q. Li, and S. L. Simon, "The glass transition temperature versus the fictive temperature," J Non Cryst Solids, vol. 353, no. 26, pp. 2603–2612, Aug. 2007, doi: 10.1016/j.jnoncrysol.2007.04.025.

[98] S. W. Twiggs, R. D. Ringle, R. Morena, and C. W. Fairhurst, "Glass Transition Temperatures at Rapid Heating Rates," Journal of the American Ceramic Society, vol. 68, no. 2, Feb. 1985, doi: 10.1111/j.1151-2916.1985.tb15285.x.

[99] L. Han et al., "Crystallization, structure and properties of MgO-Al2O3-SiO2 highly crystalline transparent glass-ceramics nucleated by multiple nucleating agents," J Eur Ceram Soc, vol. 38, no. 13, pp. 4533–4542, Oct. 2018, doi: 10.1016/j.jeurceramsoc.2018.05.025.

[100] R. Cioffi, P. Pernice, A. Aronne, A. Marotta, and G. Quattroni, "Nucleation and crystal growth in a fly ash derived glass," J Mater Sci, vol. 28, no. 24, pp. 6591–6594, Dec. 1993, doi: 10.1007/BF00356400.

[101] A. Ramos and M. Gandais, "Earliest stages of crystal growth in a silicate glass containing titanium and zirconium as nucleating elements — HRTEM and XAS study," J Cryst Growth, vol. 100, no. 3, pp. 471–480, Mar. 1990, doi: 10.1016/0022-0248(90)90247-I.

[102] A. R. Cooper and A. H. Heuer, Eds., Mass Transport Phenomena in Ceramics. Boston, MA: Springer US, 1975. doi: 10.1007/978-1-4684-3150-6.

[103] M. L. F. Nascimento, V. M. Fokin, E. D. Zanotto, and A. S. Abyzov, "Dynamic processes in a silicate liquid from above melting to below the glass transition," J Chem Phys, vol. 135, no. 19, Nov. 2011, doi: 10.1063/1.3656696.

[104] S. Wen et al., "Pressureless Crystallization of Glass for Transparent Nanoceramics," Advanced Science, vol. 6, no. 17, Sep. 2019, doi: 10.1002/advs.201901096.

[105] J. Sułowska, I. Wacławska, M. Szumera, and Z. Olejniczak, "Characterization of thermally induced of crystalline phases in CuO-containing silicate–phosphate glasses," J Therm Anal Calorim, vol. 108, no. 2, pp. 657–663, May 2012, doi: 10.1007/s10973-011-1988-5.

[106] I. W. Donald, B. L. Metcalfe, and A. E. P. Morris, "Influence of transition metal oxide additions on the crystallization kinetics, microstructures and thermal expansion characteristics of a lithium zinc silicate glass," J Mater Sci, vol. 27, no. 11, pp. 2979–2999, 1992, doi: 10.1007/BF01154109.

[107] R. Raj, "Fundamental Research in Structural Ceramics for Service Near 2000°C," Journal of the American Ceramic Society, vol. 76, no. 9, pp. 2147–2174, Sep. 1993, doi: 10.1111/j.1151-2916.1993.tb07750.x.

[108] G. Lisachuk, K. Podchasova, L. Bilostotska, Y. Trusova, R. Krivibok, and L. Pavlova, “Effect of modified glass matrices on the strengthening of glass crystalline coatings,” Eastern-European Journal of Enterprise Technologies, vol. 4, no. 6(82), p. 44, Aug. 2016, doi: 10.15587/1729-4061.2016.74854.

[109] K. Maeda, K. Akatsuka, and A. Yasumori, “Practical strength of damage-resistant CaO–Al2O3–SiO2 glass-ceramic,” Ceram Int, vol. 47, no. 6, pp. 8728–8731, Mar. 2021, doi: 10.1016/j.ceramint.2020.11.236.

[110] G. Yan, M. Wang, T. Sun, X. Li, G. Wang, and W. Yin, “Anti-Corrosion Property of Glass Flake Reinforced Chemically Bonded Phosphate Ceramic Coatings,” Materials, vol. 12, no. 13, p. 2082, Jun. 2019, doi: 10.3390/ma12132082.

[111] S. Huang, J. Wang, X. Wei, Y. Zhou, L. Wang, and J. Zhang, “Microstructural characterization and film-forming mechanism of a phosphate chemical conversion ceramic coating prepared on the surface of 2A12 aluminum alloy,” RSC Adv, vol. 9, no. 33, pp. 18767–18775, 2019, doi: 10.1039/C9RA01173K.

[112] Q. Zhang, S. Gao, C. Liu, Y. Lu, X. Chen, and H. Yu, “Evaluation of Wear Resistance of Dental Chairside CAD/CAM Glass Ceramics Reinforced by Different Crystalline Phases,” J Tribol, vol. 141, no. 3, Mar. 2019, doi: 10.1115/1.4041536.

[113] L. Yang, M. Wen, X. Dai, G. Cheng, and K. Zhang, “Ultrafine Ceramic Grains Embedded in Metallic Glass Matrix: Achieving Superior Wear Resistance via Increase in Both Hardness and Toughness,” ACS Appl Mater Interfaces, vol. 10, no. 18, pp. 16124–16132, May 2018, doi: 10.1021/acsami.8b02338.

[114] R. J. Bratton, S. K. Lau, C. A. Andersson, and S. Y. Lee, “Ceramic Thermal Barrier Coatings for Gas Turbine Engines,” in Volume 5: Manufacturing Materials and Metallurgy; Ceramics; Structures and Dynamics; Controls, Diagnostics and Instrumentation; Education; Process Industries; Technology Resources; General, American Society of Mechanical Engineers, Apr. 1982. doi: 10.1115/82-GT-265.

[115] I. G. Wright and B. A. Pint, “Bond coating issues in thermal barrier coatings for industrial gas turbines,” Proceedings of the Institution of Mechanical Engineers, Part A: Journal of Power and Energy, vol. 219, no. 2, pp. 101–107, Mar. 2005, doi: 10.1243/095765005X6836.

[116] S. Dai, M. A. Rodriguez, and J. J. M. Griego, “Sealing Glass-Ceramics with Near Linear Thermal Strain, Part I: Process Development and Phase Identification,” Journal of the American Ceramic Society, vol. 99, no. 11, pp. 3719–3725, Nov. 2016, doi: 10.1111/jace.14364.

[117] P. Zhai, X. F. Duan, D. Q. Chen, and C. H. Wang, “Preparation and Characterization of β-Eucryptite Glass Ceramics,” Adv Mat Res, vol. 624, pp. 134–137, Dec. 2012, doi: 10.4028/www.scientific.net/AMR.624.134.

[118] J. Smith et al., “Thermal Barrier Coating Validation Testing for Industrial Gas Turbine Combustion Hardware,” J Eng Gas Turbine Power, vol. 138, no. 3, Mar. 2016, doi: 10.1115/1.4031448.

[119] H.-F. Chen et al., “Recent progress in thermal/environmental barrier coatings and their corrosion resistance,” Rare Metals, vol. 39, no. 5, pp. 498–512, May 2020, doi: 10.1007/s12598-019-01307-1.

[120] J. V. Rau et al., “Glass-ceramic coated Mg-Ca alloys for biomedical implant applications,” Materials Science and Engineering: C, vol. 64, pp. 362–369, Jul. 2016, doi: 10.1016/j.msec.2016.03.100.

[121] B. Ben-Nissan, “Nanoceramics in Biomedical Applications,” MRS Bull, vol. 29, no. 1, pp. 28–32, Jan. 2004, doi: 10.1557/mrs2004.13.

[122] F. Baino, “Quantifying the Adhesion of Silicate Glass–Ceramic Coatings onto Alumina for Biomedical Applications,” Materials, vol. 12, no. 11, p. 1754, May 2019, doi: 10.3390/ma12111754.

[123] G. Suárez, M. P. Albano, L. B. Garrido, and E. F. Aglietti, “Dispersion of concentrated aqueous yttria-stabilized zirconia with ammonium polyacrylate,” Ceram Int, vol. 33, no. 6, pp. 925–929, Aug. 2007, doi: 10.1016/j.ceramint.2006.02.003.

[124] M. Bengisu and E. Yilmaz, “Chemical Durability of Alumina and Selected Glasses in Simulated Body Fluid,” 2004, pp. 103–112. doi: 10.1007/978-0-306-48584-8_8.

[125] M. Montazerian and E. D. Zanotto, “Bioactive and inert dental glass-ceramics,” J Biomed Mater Res A, vol. 105, no. 2, pp. 619–639, Feb. 2017, doi: 10.1002/jbm.a.35923.

[126] T. Galstian, R. Vallée, and Y. Messaddeq, “Optical materials,” Advanced Optical Technologies, vol. 7, no. 4, pp. 205–207, Aug. 2018, doi: 10.1515/aot-2018-0036.

[127] T. Lohmueller, R. Brunner, and J. P., “Improved Properties of Optical Surfaces by Following the Example of the ‘Moth Eye,’” in Biomimetics Learning from Nature, InTech, 2010. doi: 10.5772/8782.

[128] A. Tarafder, A. R. Molla, and B. Karmakar, “Advanced Glass-Ceramic Nanocomposites for Structural, Photonic, and Optoelectronic Applications,” in Glass Nanocomposites, Elsevier, 2016, pp. 299–338. doi: 10.1016/B978-0-323-39309-6.00013-4.

[129] A. Sakamoto and S. Yamamoto, “Infrared Optical Properties of β-Spodumene Solid Solution Glass-Ceramic for Fiber-Optic Devices,” Jpn J Appl Phys, vol. 45, no. 9R, p. 6969, Sep. 2006, doi: 10.1143/JJAP.45.6969.

[130] I. W. Donald, B. L. Metcalfe, and A. E. P. Morris, “Influence of transition metal oxide additions on the crystallization kinetics, microstructures and thermal expansion characteristics of a lithium zinc silicate glass,” J Mater Sci, vol. 27, no. 11, pp. 2979–2999, 1992, doi: 10.1007/BF01154109.

[131] M. Goswami, G. P. Kothiyal, L. Montagne, and L. Delevoye, “MAS-NMR study of lithium zinc silicate glasses and glass-ceramics with various ZnO content,” J Solid State Chem, vol. 181, no. 2, pp. 269–275, Feb. 2008, doi: 10.1016/j.jssc.2007.11.023.

[132] M. Goswami, G. P. Kothiyal, L. Montagne, and L. Delevoye, “MAS-NMR study of lithium zinc silicate glasses and glass-ceramics with various ZnO

content," J Solid State Chem, vol. 181, no. 2, pp. 269–275, Feb. 2008, doi: 10.1016/j.jssc.2007.11.023.

[133] B. Chowdari, "XPS and ionic conductivity studies on Li2O–Al2O3–(TiO2 or GeO2)–P2O5 glass–ceramics," Solid State Ion, vol. 136–137, no. 1–2, pp. 1067–1075, Nov. 2000, doi: 10.1016/S0167-2738(00)00500-2.

[134] R. Dupree, D. Holland, and M. G. Mortuza, "Six-coordinated silicon in glasses," Nature, vol. 328, no. 6129, pp. 416–417, Jul. 1987, doi: 10.1038/328416a0.

[135] B. Łagowska, I. Wacławska, M. Sitarz, and M. Szumera, "Spectroscopic studies of structural interactions in silicate-borate-phosphate glass," J Mol Struct, vol. 1171, pp. 110–116, Nov. 2018, doi: 10.1016/j.molstruc.2018.05.085.

[136] X. Xu, Z. Wen, X. Wu, X. Yang, and Z. Gu, "Lithium Ion-Conducting Glass–Ceramics of Li 1.5 Al 0.5 Ge 1.5 (PO 4 ) 3 – x Li 2 O ( x =0.0–0.20) with Good Electrical and Electrochemical Properties," Journal of the American Ceramic Society, vol. 90, no. 9, pp. 2802–2806, Sep. 2007, doi: 10.1111/j.1551-2916.2007.01827.x.

[137] B. Chowdari, "XPS and ionic conductivity studies on Li2O–Al2O3–(TiO2 or GeO2)–P2O5 glass–ceramics," Solid State Ion, vol. 136–137, no. 1–2, pp. 1067–1075, Nov. 2000, doi: 10.1016/S0167-2738(00)00500-2.

[138] H. Masai, T. Ueno, Y. Takahashi, and T. Fujiwara, "Precipitation of ZnO in Al2O3-doped zinc borate glass ceramics," Opt Mater (Amst), vol. 33, no. 12, pp. 1980–1983, Oct. 2011, doi: 10.1016/j.optmat.2011.03.051.

[139] R. Ramteke, K. Kumari, S. Bhattacharya, and M. R. Rahman, "Synthesis and characterization of zinc oxide incorporated iron borate glass-ceramic," J Alloys Compd, vol. 811, p. 151876, Nov. 2019, doi: 10.1016/j.jallcom.2019.151876.

[140] H. R. Fernandes, D. U. Tulyaganov, and J. M. F. Ferreira, "The role of P2O5, TiO2 and ZrO2 as nucleating agents on microstructure and crystallization behaviour of lithium disilicate-based glass," J Mater Sci, vol. 48, no. 2, pp. 765–773, Jan. 2013, doi: 10.1007/s10853-012-6793-4.

[141] Y. B. Saddeek, E. R. Shaaban, K. A. Aly, and I. M. Sayed, "Crystallization kinetics of Li2O–PbO–V2O5 glasses," Physica B Condens Matter, vol. 404, no. 16, pp. 2412–2418, Aug. 2009, doi: 10.1016/j.physb.2009.04.051.

[142] S. Salman, S. Salama, and E. Mahdy, "Crystallization and thermo-mechanical properties of Li2O-ZnO-CaO-SiO2 glass-ceramics with In2O3 and Fe2O3 additives," Processing and Application of Ceramics, vol. 9, no. 4, pp. 215–223, 2015, doi: 10.2298/PAC1504215S.

[143] H. Masai, T. Ueno, Y. Takahashi, and T. Fujiwara, "Precipitation of ZnO in Al2O3-doped zinc borate glass ceramics," Opt Mater (Amst), vol. 33, no. 12, pp. 1980–1983, Oct. 2011, doi: 10.1016/j.optmat.2011.03.051.

[144] A. H. B. Teixeira, H. H. Venturelli, O. R. K. Montedo, and A. P. N. de Oliveira, "Strengthened surface crystallized 19.6Li2O·11.0ZrO2·69.4SiO2 and 20.0Li2O·6.7ZrO2·68.9SiO2·4.4Al2O3 glass-ceramics," Materials

Science and Engineering: A, vol. 751, pp. 62–69, Mar. 2019, doi: 10.1016/j.msea.2019.02.055.

[145] D. Perera, S. Ganeshalingam, N. Kuganathan, and A. Chroneos, "A Computational Study of Defects, Li-Ion Migration and Dopants in Li2ZnSiO4 Polymorphs," Crystals (Basel), vol. 9, no. 11, p. 563, Oct. 2019, doi: 10.3390/cryst9110563.

[146] Z. Shen, L. Zhu, Y. Zhang, Y. Chen, D. Yang, and X. Song, "Effect of CuO addition on crystallization and thermal expansion properties of Li 2 O–ZnO–SiO 2 glass-ceramics," Ceram Int, vol. 43, no. 9, pp. 7099–7105, Jun. 2017, doi: 10.1016/j.ceramint.2017.02.141.

[147] B. Zhai, X. L. Zhou, S. R. Zhai, and Z. Q. Wang, "Effect of BaO on Thermo-Physical Properties of Lithium Zinc Silicate Glass-Ceramics," Adv Mat Res, vol. 299–300, pp. 503–507, Jul. 2011, doi: 10.4028/www.scientific.net/AMR.299-300.503.

[148] B. Indrajit Sharma, M. Goswami, P. Sengupta, V. K. Shrikhande, G. B. Kale, and G. P. Kothiyal, "Study on some thermo-physical properties in Li2O–ZnO–SiO2 glass-ceramics," Mater Lett, vol. 58, no. 19, pp. 2423–2428, Jul. 2004, doi: 10.1016/j.matlet.2004.02.038.

[149] A. H. B. Teixeira, H. H. Venturelli, O. R. K. Montedo, and A. P. N. de Oliveira, "Strengthened surface crystallized 19.6Li2O·11.0ZrO2·69.4SiO2 and 20.0Li2O·6.7ZrO2·68.9SiO2·4.4Al2O3 glass-ceramics," Materials Science and Engineering: A, vol. 751, pp. 62–69, Mar. 2019, doi: 10.1016/j.msea.2019.02.055.

[150] X. Xu, Z. Wen, X. Wu, X. Yang, and Z. Gu, "Lithium Ion-Conducting Glass–Ceramics of Li 1.5 Al 0.5 Ge 1.5 (PO 4 ) 3 – x Li 2 O ( x =0.0–0.20) with Good Electrical and Electrochemical Properties," Journal of the American Ceramic Society, vol. 90, no. 9, pp. 2802–2806, Sep. 2007, doi: 10.1111/j.1551-2916.2007.01827.x.

[151] Y. Chen, W. Li, Y. Zhang, Z. Shen, D. Yang, and X. Song, "Crystallization and thermal expansion behavior of lithium zinc silicate sealing glass," Ceram Int, vol. 42, no. 10, pp. 11650–11653, Aug. 2016, doi: 10.1016/j.ceramint.2016.04.068.

[152] C. Chang and J. Jean, "Crystallization Kinetics and Mechanism of Low-Dielectric, Low-Temperature, Cofirable CaO-B 2 O 3 -SiO 2 Glass-Ceramics," Journal of the American Ceramic Society, vol. 82, no. 7, pp. 1725–1732, Jul. 1999, doi: 10.1111/j.1151-2916.1999.tb01992.x.

[153] S. M. Salman, S. N. Salama, and H. A. Abo-Mosallam, "Crystallization characteristics and physico-chemical properties of glass–ceramics based on Li 2 O–ZnO–SiO 2 system," Boletín de la Sociedad Española de Cerámica y Vidrio, vol. 56, no. 5, pp. 205–214, Sep. 2017, doi: 10.1016/j.bsecv.2017.02.002.

[154] H. Masai, T. Ueno, Y. Takahashi, and T. Fujiwara, "Precipitation of ZnO in Al2O3-doped zinc borate glass ceramics," Opt Mater (Amst), vol. 33, no. 12, pp. 1980–1983, Oct. 2011, doi: 10.1016/j.optmat.2011.03.051.

[155] R. Ramteke, K. Kumari, S. Bhattacharya, and M. R. Rahman, “Synthesis and characterization of zinc oxide incorporated iron borate glass-ceramic,” J Alloys Compd, vol. 811, p. 151876, Nov. 2019, doi: 10.1016/j.jallcom.2019.151876.

[156] L. Sisken et al., “Evidence of spatially selective refractive index modification in 15GeSe_2-45As_2Se_3-40PbSe glass ceramic through correlation of structure and optical property measurements for GRIN applications,” Opt Mater Express, vol. 7, no. 9, p. 3077, Sep. 2017, doi: 10.1364/OME.7.003077.

[157] I. A. Ashcroft and B. Derby, “Characterization of glass-ceramic to metal bonds,” J Mater Sci, vol. 29, no. 17, pp. 4436–4446, Sep. 1994, doi: 10.1007/BF00376266.

[158] J. N. Calata, G. Lu, and T. Chuang, “Constrained sintering of glass, glass–ceramic and ceramic coatings on metal substrates,” Surface and Interface Analysis, vol. 31, no. 7, pp. 673–681, Jul. 2001, doi: 10.1002/sia.1093.

[159] J. E. E. Baglin, “Adhesion at Metal-Ceramic Interfaces: Ion Beam Enhancement and the Role of Contaminants,” MRS Proceedings, vol. 47, p. 3, Feb. 1985, doi: 10.1557/PROC-47-3.

[160] W. G. Dorfeld, “Bonding thermosprayed silicon to glass-ceramic,” Thin Solid Films, vol. 47, no. 3, pp. 241–247, Dec. 1977, doi: 10.1016/0040-6090(77)90039-6.

[161] I. A. Ashcroft and B. Derby, “Characterization of glass-ceramic to metal bonds,” J Mater Sci, vol. 29, no. 17, pp. 4436–4446, Sep. 1994, doi: 10.1007/BF00376266.

[162] J. N. Calata, G. Lu, and T. Chuang, “Constrained sintering of glass, glass–ceramic and ceramic coatings on metal substrates,” Surface and Interface Analysis, vol. 31, no. 7, pp. 673–681, Jul. 2001, doi: 10.1002/sia.1093.

[163] J. V. Bellini, M. R. Morelli, and R. H. G. A. Kiminami, “Ceramic system based on ZnO–CuO–glass,” Mater Lett, vol. 62, no. 2, pp. 335–337, Jan. 2008, doi: 10.1016/j.matlet.2007.05.032.

[164] J. Wang et al., “Low-Temperature Sintering and Electric Properties of <scp> <scp>Pb</scp> </scp> 0.99 ( <scp> <scp>Zr</scp> </scp> 0.95 <scp> <scp>Ti</scp> </scp> 0.05 ) 0.98 <scp> <scp>Nb</scp> </scp> 0.02 <scp> <scp>O</scp> </scp> 3 Ferroelectric Ceramics with <scp> <scp>CuO</scp> </scp> Additive,” Journal of the American Ceramic Society, vol. 96, no. 8, pp. 2370–2373, Aug. 2013, doi: 10.1111/jace.12487.

[165] N. Neves et al., “Sintering Behavior of Nano- and Micro-Sized <scp> <scp>ZnO</scp> </scp> Powder Targets for rf Magnetron Sputtering Applications,” Journal of the American Ceramic Society, vol. 95, no. 1, pp. 204–210, Jan. 2012, doi: 10.1111/j.1551-2916.2011.04874.x.

[166] K.-C. Feng, C.-C. Chou, C.-S. Chen, L.-W. Chu, and H. Chen, “Phase evolution and electrical properties of copper-electroded BaTi4O9 materials with BaO–ZnO–B2O3–SiO2 glass system in reducing atmosphere,” Ceram Int, vol. 39, pp. S321–S324, May 2013, doi: 10.1016/j.ceramint.2012.10.086.

[167] A. Khaskhoussi, L. Calabrese, J. Bouaziz, and E. Proverbio, “Effect of TiO2 addition on microstructure of zirconia/alumina sintered ceramics,” Ceram Int,

vol. 43, no. 13, pp. 10392–10402, Sep. 2017, doi: 10.1016/j.ceramint.2017.05.074.

[168] A. Serrano et al., “Cold sintering process of ZnO ceramics: Effect of the nanoparticle/microparticle ratio,” J Eur Ceram Soc, vol. 40, no. 15, pp. 5535–5542, Dec. 2020, doi: 10.1016/j.jeurceramsoc.2020.05.059.

[169] Z. Shen, L. Zhu, Y. Zhang, Y. Chen, D. Yang, and X. Song, “Effect of CuO addition on crystallization and thermal expansion properties of Li 2 O–ZnO–SiO 2 glass-ceramics,” Ceram Int, vol. 43, no. 9, pp. 7099–7105, Jun. 2017, doi: 10.1016/j.ceramint.2017.02.141.

[170] Y. Huang et al., “Preparation and electrical properties of ZnO–glass ceramic films,” Microelectron Eng, vol. 66, no. 1–4, pp. 760–766, Apr. 2003, doi: 10.1016/S0167-9317(02)00996-6.

[171] T. Alizadeh and F. Soleimani, “Preparation of nano-glass ceramic in ZAS system without added nucleating agents,” J Non Cryst Solids, vol. 520, p. 119465, Sep. 2019, doi: 10.1016/j.jnoncrysol.2019.119465.

[172] S. A. M. Abdel-Hameed, M. A. Marzouk, and A. E. Abdel-Ghany, “Magnetic properties of nanoparticles glass–ceramic rich with copper ions,” J Non Cryst Solids, vol. 357, no. 24, pp. 3888–3896, Dec. 2011, doi: 10.1016/j.jnoncrysol.2011.07.026.

[173] H. Masai, T. Toda, Y. Takahashi, and T. Fujiwara, “Fabrication of Bi-free TiO2 nano-crystallized glass,” J Non Cryst Solids, vol. 356, no. 44–49, pp. 2674–2676, Oct. 2010, doi: 10.1016/j.jnoncrysol.2010.04.047.

[174] P. Loiko et al., “Structural transformations and optical properties of glass-ceramics based on ZnO, β- and α-Zn2SiO4 nanocrystals and doped with Er2O3 and Yb2O3: Part I. The role of heat-treatment,” J Lumin, vol. 202, pp. 47–56, Oct. 2018, doi: 10.1016/j.jlumin.2018.05.010.

[175] K. Sharma, A. Dixit, S. Bhattacharya, Jagannath, M. N. Deo, and G. P. Kothiyal, “Effect of ZnO on phase emergence, microstructure and surface modifications of calcium phosphosilicate glass/glass–ceramics having iron oxide,” Appl Surf Sci, vol. 256, no. 10, pp. 3107–3115, Mar. 2010, doi: 10.1016/j.apsusc.2009.11.082.

[176] X. Li, C. Fan, J. Li, S. Guo, J. Ren, and J. Wang, “Highly crystallized transparent luminescent glass ceramics containing dual-phase ZnGa2O4 spinel and α-Zn2SiO4 willemite nanocrystals,” J Eur Ceram Soc, vol. 41, no. 2, pp. 1550–1556, Feb. 2021, doi: 10.1016/j.jeurceramsoc.2020.09.066.

[177] S. Labib, H. S. Refai, and S. M. Ismail, “Effect of heat treatment on structure evolution and properties of nano zinc titanate ceramics,” Materwiss Werksttech, vol. 45, no. 3, pp. 169–176, Mar. 2014, doi: 10.1002/mawe.201400202.

[178] V. O. Soares, F. C. Serbena, G. dos S. Oliveira, C. da Cruz, R. F. Muniz, and E. D. Zanotto, “Highly translucent nanostructured glass-ceramic,” Ceram Int, vol. 47, no. 4, pp. 4707–4714, Feb. 2021, doi: 10.1016/j.ceramint.2020.10.039.

[179] V. Kumari, S. Yadav, J. Jindal, S. Sharma, K. Kumari, and N. Kumar, “Synthesis and characterization of heterogeneous ZnO/CuO hierarchical

nanostructures for photocatalytic degradation of organic pollutant," Advanced Powder Technology, vol. 31, no. 7, pp. 2658–2668, Jul. 2020, doi: 10.1016/j.apt.2020.04.033.

[180] L. Xiang-Qi et al., "Syntheses of ZnO Nano-Arrays and Spike-Shaped CuO/ZnO Heterostructure," Acta Physico-Chimica Sinica, vol. 31, no. 4, pp. 783–792, 2015, doi: 10.3866/PKU.WHXB201502062.

[181] F. H. Margha, M. I. Badawy, and T. A. Gad-Allah, "ZnO enriched transparent glass-ceramics for wastewater decontamination," Environ Prog Sustain Energy, vol. 36, no. 2, pp. 442–447, Mar. 2017, doi: 10.1002/ep.12482.

[182] X. L. Duan, Y. C. Wu, F. P. Yu, and D. R. Yuan, "Synthesis and photoluminescence of Eu3+-doped ZnO–Ga2O3–SiO2 nano-glass-ceramics," J Non Cryst Solids, vol. 354, no. 40–41, pp. 4695–4697, Oct. 2008, doi: 10.1016/j.jnoncrysol.2008.07.007.

[183] E. D. Zanotto, "The applicability of the general theory of phase transformations to glass crystallization," Thermochim Acta, vol. 280–281, pp. 73–82, Jul. 1996, doi: 10.1016/0040-6031(95)02636-3.

[184] M. C. Weinberg, "A few topics concerning nucleation and crystallization in glasses," J Non Cryst Solids, vol. 255, no. 1, pp. 1–14, Sep. 1999, doi: 10.1016/S0022-3093(99)00420-2.

[185] H. W. Choi, Y. H. Kim, Y. H. Rim, and Y. S. Yang, "Crystallization kinetics of lithium niobate glass: determination of the Johnson–Mehl–Avrami–Kolmogorov parameters," Physical Chemistry Chemical Physics, vol. 15, no. 24, p. 9940, 2013, doi: 10.1039/c3cp50909e.

[186] B. Rheingans and E. J. Mittemeijer, "Phase Transformation Kinetics: Advanced Modeling Strategies," JOM, vol. 65, no. 9, pp. 1145–1154, Sep. 2013, doi: 10.1007/s11837-013-0674-4.

[187] J. S. Blázquez, C. F. Conde, and A. Conde, "On the use of classical JMAK crystallization kinetic theory to describe simultaneous processes leading to the formation of different phases in metals," International Journal of Thermal Sciences, vol. 88, pp. 1–6, Feb. 2015, doi: 10.1016/j.ijthermalsci.2014.09.004.

[188] X. Lei, J. Huang, X. Jin, S. Chen, and X. Zhao, "Application of Johnson-Mehl-Avrami-Kolmogorov type equation in non-isothermal phase process: Re-discussion," Mater Lett, vol. 181, pp. 240–243, Oct. 2016, doi: 10.1016/j.matlet.2016.06.039.

[189] H. W. Choi, Y. H. Kim, Y. H. Rim, and Y. S. Yang, "Crystallization kinetics of lithium niobate glass: determination of the Johnson–Mehl–Avrami–Kolmogorov parameters," Physical Chemistry Chemical Physics, vol. 15, no. 24, p. 9940, 2013, doi: 10.1039/c3cp50909e.

[190] J. S. Blázquez, C. F. Conde, and A. Conde, "On the use of classical JMAK crystallization kinetic theory to describe simultaneous processes leading to the formation of different phases in metals," International Journal of Thermal Sciences, vol. 88, pp. 1–6, Feb. 2015, doi: 10.1016/j.ijthermalsci.2014.09.004.

[191] K. Dimitra and C. Konstantinos, “Nonisothermal Crystallization Kinetics: Studying the Validity of Different Johnson–Mehl–Avrami–Erofeev–Kolmogorov (JMAEK) Based Equations,” Thermochim Acta, vol. 704, p. 179030, Oct. 2021, doi: 10.1016/j.tca.2021.179030.

[192] A. F. Manchón-Gordón, J. S. Blázquez, C. F. Conde, and A. Conde, “Nanocrystallization kinetics understood as multiple microprocesses following the classical theory of crystallization,” J Alloys Compd, vol. 675, pp. 81–85, Aug. 2016, doi: 10.1016/j.jallcom.2016.03.087.

[193] M. C. Weinberg, D. P. Birnie, and V. A. Shneidman, “Crystallization kinetics and the JMAK equation,” J Non Cryst Solids, vol. 219, pp. 89–99, Oct. 1997, doi: 10.1016/S0022-3093(97)00261-5.

[194] N. Koga and J. Šesták, “Influence of Preliminary Nucleation on the Physicogeometric Kinetics of Glass Crystallization,” 2012, pp. 209–223. doi: 10.1007/978-90-481-3150-1_10.

[195] J. Shi, F. He, J. Xie, X. Liu, and H. Yang, “Kinetic analysis of crystallization in Li2O-Al2O3-SiO2-B2O3-BaO glass-ceramics,” J Non Cryst Solids, vol. 491, pp. 106–113, Jul. 2018, doi: 10.1016/j.jnoncrysol.2018.04.004.

[196] T. Ozawa, “Kinetics of non-isothermal crystallization,” Polymer (Guildf), vol. 12, no. 3, pp. 150–158, Mar. 1971, doi: 10.1016/0032-3861(71)90041-3.

[197] L. C. López and G. L. Wilkes, “Non-isothermal crystallization kinetics of poly(p-phenylene sulphide),” Polymer (Guildf), vol. 30, no. 5, pp. 882–887, May 1989, doi: 10.1016/0032-3861(89)90186-9.

[198] A. Riga and R. Collins, “Differential Scanning Calorimetry and Differential Thermal Analysis,” in Encyclopedia of Analytical Chemistry, Wiley, 2000. doi: 10.1002/9780470027318.a6602.

[199] E. B. Peixoto et al., “Study of the dynamic of crystallization of an amorphous Fe40Ni40P14B6 ribbon through Johnson-Mehl-Avrami model,” J Alloys Compd, vol. 731, pp. 1275–1279, Jan. 2018, doi: 10.1016/j.jallcom.2017.10.062.

[200] J. C. A. Martins, K. M. Novack, and A. S. Gomes, “Non-isothermal crystallization kinetics of thermotropic polyesters with flexible spacers in the main chain,” Polymer (Guildf), vol. 39, no. 26, pp. 6941–6944, Dec. 1998, doi: 10.1016/S0032-3861(98)00158-X.

[201] A. A. Joraid, S. N. Alamri, A. A. Abu-Sehly, and M. Benghanem, “Nonisothermal crystallisation kinetics of amorphous selenium prepared by high-energy ball milling: A comparison with the melt-quenching and thin-film techniques,” J Non Cryst Solids, vol. 358, no. 10, pp. 1268–1273, May 2012, doi: 10.1016/j.jnoncrysol.2012.02.029.

[202] M. L. Di Lorenzo and C. Silvestre, “Non-isothermal crystallization of polymers,” Prog Polym Sci, vol. 24, no. 6, pp. 917–950, Aug. 1999, doi: 10.1016/S0079-6700(99)00019-2.

[203] S. Haratian and M. Haddad-Sabzevar, “Thermal stability and non-isothermal crystallization kinetics of Ti41.5Cu42.5Ni7.5Zr2.5Hf5Si1 bulk metallic glass,” J Non Cryst Solids, vol. 429, pp. 164–170, Dec. 2015, doi: 10.1016/j.jnoncrysol.2015.09.009.

[204] Y. X. Zhuang, T. F. Duan, and H. Y. Shi, “Calorimetric study of non-isothermal crystallization kinetics of Zr60Cu20Al10Ni10 bulk metallic glass,” J Alloys Compd, vol. 509, no. 37, pp. 9019–9025, Sep. 2011, doi: 10.1016/j.jallcom.2011.06.112.

[205] A. Hammami and A. K. Mehrotra, “Non-isothermal crystallization kinetics of n-paraffins with chain lengths between thirty and fifty,” Thermochim Acta, vol. 211, pp. 137–153, Dec. 1992, doi: 10.1016/0040-6031(92)87014-2.

[206] J. A. Augis and J. E. Bennett, “Calculation of the Avrami parameters for heterogeneous solid state reactions using a modification of the Kissinger method,” Journal of Thermal Analysis, vol. 13, no. 2, pp. 283–292, Apr. 1978, doi: 10.1007/BF01912301.

[207] A. F. Kozmidis-Petrović, G. R. Štrbac, and D. D. Štrbac, “Kinetics of non-isothermal crystallization of chalcogenide glasses from the Sb32As5S48I15 system,” J Non Cryst Solids, vol. 353, no. 18–21, pp. 2014–2019, Jun. 2007, doi: 10.1016/j.jnoncrysol.2006.12.120.

[208] Y. X. Zhuang, T. F. Duan, and H. Y. Shi, “Calorimetric study of non-isothermal crystallization kinetics of Zr60Cu20Al10Ni10 bulk metallic glass,” J Alloys Compd, vol. 509, no. 37, pp. 9019–9025, Sep. 2011, doi: 10.1016/j.jallcom.2011.06.112.

[209] O. A. Lafi, M. M. A. Imran, M. K. Abdullah, and S. A. Al-Sakhel, “Thermal characterization of Se100−xSnx (x=4, 6 and 8) chalcogenide glasses using differential scanning calorimeter,” Thermochim Acta, vol. 560, pp. 71–75, May 2013, doi: 10.1016/j.tca.2013.03.024.

[210] N. Mehta, M. Zulfequar, and A. Kumar, “Kinetic parameters of crystallization in glassy Se 100– x Sb x alloys,” physica status solidi (a), vol. 203, no. 2, pp. 236–246, Feb. 2006, doi: 10.1002/pssa.200521185.

[211] H. E. Kissinger, “Variation of peak temperature with heating rate in differential thermal analysis,” J Res Natl Bur Stand (1934), vol. 57, no. 4, p. 217, Oct. 1956, doi: 10.6028/jres.057.026.

[212] H. E. Kissinger, “Reaction Kinetics in Differential Thermal Analysis,” Anal Chem, vol. 29, no. 11, pp. 1702–1706, Nov. 1957, doi: 10.1021/ac60131a045.

[213] S. Vyazovkin, “Kissinger Method in Kinetics of Materials: Things to Beware and Be Aware of,” Molecules, vol. 25, no. 12, p. 2813, Jun. 2020, doi: 10.3390/molecules25122813.

[214] D. Tranchida, D. Gloger, and M. Gahleitner, “A critical approach to the Kissinger analysis for studying non-isothermal crystallization of polymers,” J Therm Anal Calorim, vol. 129, no. 2, pp. 1057–1064, Aug. 2017, doi: 10.1007/s10973-017-6303-7.

[215] V. Erukhimovitch and J. Baram, “A model for non-isothermal crystallization kinetics,” J Non Cryst Solids, vol. 208, no. 3, pp. 288–293, Dec. 1996, doi: 10.1016/S0022-3093(96)00521-2.

[216] Y. X. Zhuang, T. F. Duan, and H. Y. Shi, “Calorimetric study of non-isothermal crystallization kinetics of Zr60Cu20Al10Ni10 bulk metallic glass,” J Alloys Compd, vol. 509, no. 37, pp. 9019–9025, Sep. 2011, doi: 10.1016/j.jallcom.2011.06.112.

[217] M. Venkatesh, P. Ravi, and S. P. Tewari, “Isoconversional Kinetic Analysis of Decomposition of Nitroimidazoles: Friedman method vs Flynn–Wall–Ozawa Method,” J Phys Chem A, vol. 117, no. 40, pp. 10162–10169, Oct. 2013, doi: 10.1021/jp407526r.

[218] B. S. Patial, N. Thakur, S. K. Tripathi, A. B. Garg, R. Mittal, and R. Mukhopadhyay, “Estimation of the Activation Energy for the Non-isothermal Crystallization in Amorphous Se[sub 70]Te[sub 15]In[sub 15] Alloy Using Iso-conversional Methods,” 2011, pp. 539–540. doi: 10.1063/1.3605971.

[219] K. Patidar, A. Singathia, M. Vashishtha, V. Kumar Sangal, and S. Upadhyaya, “Investigation of kinetic and thermodynamic parameters approaches to non-isothermal pyrolysis of mustard stalk using model-free and master plots methods,” Mater Sci Energy Technol, vol. 5, pp. 6–14, 2022, doi: 10.1016/j.mset.2021.11.001.

[220] A. A. Joraid and S. Y. Al-Raqa, “Kinetic and thermodynamic studies of phase transition from hexagonal to discotic liquid crystal in metal-free 1,4,8,11,15,18,22,25-octahexylphthalocyanine,” Liq Cryst, vol. 48, no. 12, pp. 1709–1722, Sep. 2021, doi: 10.1080/02678292.2021.1898054.

[221] M. Mohamed, A. Y. Abdel-Latief, M. A. Abdel-Rahim, N. M. A. Hadia, E. R. Shaaban, and M. N. Abd-el Salam, “Examination of the kinetic reaction mechanisms of amorphous As50Se50 chalcogenide glass,” Applied Physics A, vol. 124, no. 8, p. 562, Aug. 2018, doi: 10.1007/s00339-018-1976-8.

[222] B. S. Patial et al., “Iso-conversional Analysis of Amorphous-Crystalline Transformation of Se[sub 75]Te[sub 15]Sn[sub 10] Glassy Alloy,” 2011, pp. 95–96. doi: 10.1063/1.3653626.

[223] Z. P. Wu, Z. Q. Cheng, Z. B. Yang, W. Yi, and X. L. Xu, “Non-Isothermal Kinetics Analysis of <i>α→β</i> Transformation in Zirconium Alloy,” Materials Science Forum, vol. 993, pp. 344–350, May 2020, doi: 10.4028/www.scientific.net/MSF.993.344.

[224] M. I. Martín, F. A. López, F. J. Alguacil, and M. Romero, “Development of crystalline phases in sintered glass-ceramics from residual E-glass fibres,” Ceram Int, vol. 40, no. 2, pp. 2769–2776, Mar. 2014, doi: 10.1016/j.ceramint.2013.10.040.

[225] A. Chakrabarti, K. Biswas, and A. R. Molla, “Eu3+doped ferroelectric BaBi2Ta2O9 based glass-ceramic nanocomposites: Crystallization kinetics and energy storage properties,” J Alloys Compd, vol. 740, pp. 237–249, Apr. 2018, doi: 10.1016/j.jallcom.2018.01.038.

[226] A. Baranowska, M. Leśniak, M. Kochanowicz, J. Żmojda, P. Miluski, and D. Dorosz, “Crystallization Kinetics and Structural Properties of the 45S5 Bioactive Glass and Glass-Ceramic Fiber Doped with Eu3+,” Materials, vol. 13, no. 6, p. 1281, Mar. 2020, doi: 10.3390/ma13061281.

[227] H. Savabieh, P. Alizadeh, B. Nayebi, and F. J. Clemens, “Kinetics of crystallization in 13.2Li2O-67.6SiO2-14.49Al2O3-3.3TiO2-0.4BaO-0.97ZnO glass ceramic powder: Part I: A model-free vs. model-fitting approach,” Ceram Int, vol. 45, no. 7, pp. 8856–8865, May 2019, doi: 10.1016/j.ceramint.2019.01.214.

[228] T. Vlase, C. Păcurariu, R. I. Lazău, and I. Lazăn, "Kinetic studies of the crystallization process of glass-ceramics based on basalt," J Therm Anal Calorim, vol. 88, no. 3, pp. 625–629, Jun. 2007, doi: 10.1007/s10973-006-8016-1.

[229] J. Shi, F. He, J. Xie, X. Liu, and H. Yang, "Kinetic analysis of crystallization in Li2O-Al2O3-SiO2-B2O3-BaO glass-ceramics," J Non Cryst Solids, vol. 491, pp. 106–113, Jul. 2018, doi: 10.1016/j.jnoncrysol.2018.04.004.

[230] J. W. Graydon, S. J. Thorpe, and D. W. Kirk, "Determination of the Avrami exponent for solid state transformations from non-isothermal differential scanning calorimetry," J Non Cryst Solids, vol. 175, no. 1, pp. 31–43, Sep. 1994, doi: 10.1016/0022-3093(94)90312-3.

[231] M. Abu El-Oyoun, "Determination of the crystallization kinetic parameters of Ge22.5Te77.5 glass using model-free and model-fitting methods," J Alloys Compd, vol. 486, no. 1–2, pp. 1–8, Nov. 2009, doi: 10.1016/j.jallcom.2009.06.137.

[232] S. Panyata, S. Eitssayeam, T. Tunkasiri, A. Munpakdee, and K. Pengpat, "Crystallization kinetic of Er3+-doped BiO1.5-GeO2-BO1.5 glass-ceramic," Ceram Int, vol. 44, pp. S46–S49, Nov. 2018, doi: 10.1016/j.ceramint.2018.08.262.

[233] A. Chakrabarti, K. Biswas, and A. R. Molla, "Eu3+doped ferroelectric BaBi2Ta2O9 based glass-ceramic nanocomposites: Crystallization kinetics and energy storage properties," J Alloys Compd, vol. 740, pp. 237–249, Apr. 2018, doi: 10.1016/j.jallcom.2018.01.038.

[234] M. Abu El-Oyoun, "Effect of wide range of heating rate on the crystallization kinetic parameters of Se77Te20Sb3 glass," Thermochim Acta, vol. 494, no. 1–2, pp. 129–135, Oct. 2009, doi: 10.1016/j.tca.2009.05.006.

[235] N. Koga and J. Šesták, "Influence of Preliminary Nucleation on the Physicogeometric Kinetics of Glass Crystallization," 2012, pp. 209–223. doi: 10.1007/978-90-481-3150-1_10.

[236] T. E. L. Vila-Nova et al., "Effect of Adhesive Resin Application on the Durability of Adhesion to CAD/CAM Glass-Ceramics after either Hydrofluoric Acid Etching or Self-etch Primer Application.," J Adhes Dent, vol. 24, no. 1, pp. 279–289, Aug. 2022, doi: 10.3290/j.jad.b3240691.

[237] T. Karbowiak, F. Debeaufort, and A. Voilley, "Importance of Surface Tension Characterization for Food, Pharmaceutical and Packaging Products: A Review," Crit Rev Food Sci Nutr, vol. 46, no. 5, pp. 391–407, Jun. 2006, doi: 10.1080/10408390591000884.

[238] J. Chen, Z. Lin, S. J. Bull, C. L. Phillips, and P. D. Bristowe, "Experimental and modelling techniques for assessing the adhesion of very thin coatings on glass," J Phys D Appl Phys, vol. 42, no. 21, p. 214003, Nov. 2009, doi: 10.1088/0022-3727/42/21/214003.

[239] M. Rankl, S. Laib, and S. Seeger, "Surface tension properties of surface-coatings for application in biodiagnostics determined by contact angle measurements," Colloids Surf B Biointerfaces, vol. 30, no. 3, pp. 177–186, Jul. 2003, doi: 10.1016/S0927-7765(03)00085-7.

[240] C. Vladuta, L. Andronic, M. Visa, and A. Duta, “Ceramic interface properties evaluation based on contact angle measurement,” Surf Coat Technol, vol. 202, no. 11, pp. 2448–2452, Feb. 2008, doi: 10.1016/j.surfcoat.2007.08.033.

[241] P. Chen, D. Y. Kwok, R. M. Prokop, O. I. del Rio, S. S. Susnar, and A. W. Neumann, “Axisymmetric Drop Shape Analysis (ADSA) and its Applications,” 1998, pp. 61–138. doi: 10.1016/S1383-7303(98)80019-7.

[242] M. Aslannezhad et al., “A review of hydrogen/rock/brine interaction: Implications for Hydrogen Geo-storage,” Prog Energy Combust Sci, vol. 95, p. 101066, Mar. 2023, doi: 10.1016/j.pecs.2022.101066.

[243] M. de Meijer, S. Haemers, W. Cobben, and H. Militz, “Surface Energy Determinations of Wood: Comparison of Methods and Wood Species,” Langmuir, vol. 16, no. 24, pp. 9352–9359, Nov. 2000, doi: 10.1021/la001080n.

[244] R. S. Hebbar, A. M. Isloor, and A. F. Ismail, “Contact Angle Measurements,” in Membrane Characterization, Elsevier, 2017, pp. 219–255. doi: 10.1016/B978-0-444-63776-5.00012-7.

[245] C. D. Holcomb and J. A. Zollweg, “Improved calculation techniques for interfacial tensiometers,” J Colloid Interface Sci, vol. 134, no. 1, pp. 41–50, Jan. 1990, doi: 10.1016/0021-9797(90)90249-N.

[246] F. K. Hansen, “Surface Tension by Image Analysis: Fast and Automatic Measurements of Pendant and Sessile Drops and Bubbles,” J Colloid Interface Sci, vol. 160, no. 1, pp. 209–217, Oct. 1993, doi: 10.1006/jcis.1993.1386.

[247] Y. Zhang et al., “Spreading Dynamics of Molten Polymer Drops on Glass Substrates,” Langmuir, vol. 33, no. 34, pp. 8447–8454, Aug. 2017, doi: 10.1021/acs.langmuir.7b01500.

[248] G. Whyman, E. Bormashenko, and T. Stein, “The rigorous derivation of Young, Cassie–Baxter and Wenzel equations and the analysis of the contact angle hysteresis phenomenon,” Chem Phys Lett, vol. 450, no. 4–6, pp. 355–359, Jan. 2008, doi: 10.1016/j.cplett.2007.11.033.

[249] K. Seo, M. Kim, and D. H. Kim, “Re-derivation of Young’s Equation, Wenzel Equation, and Cassie-Baxter Equation Based on Energy Minimization,” in Surface Energy, InTech, 2015. doi: 10.5772/61066.

[250] Z. Yang, Y. Tian, and X. Liu, “The investigation of equilibrium contact state of liquid droplet on determined rough surfaces,” in 2017 IEEE International Conference on Manipulation, Manufacturing and Measurement on the Nanoscale (3M-NANO), IEEE, Aug. 2017, pp. 50–56. doi: 10.1109/3M-NANO.2017.8286314.

[251] J. Bachmann and G. McHale, “Superhydrophobic surfaces: a model approach to predict contact angle and surface energy of soil particles,” Eur J Soil Sci, vol. 60, no. 3, pp. 420–430, Jun. 2009, doi: 10.1111/j.1365-2389.2008.01118.x.

[252] I. Saira, “Fabrication and characterization of durable superhydrophobic and superoleophobic surfaces on stainless steel mesh substrates,” Mater Res

Express, vol. 11, no. 3, p. 036401, Mar. 2024, doi: 10.1088/2053-1591/ad2889.

[253] Sebastian Gropp, Michael Fischer, Lars Dittrich, Beate Capraro, Jens Müller, and Martin Hoffmann, "Wetting Behaviour of Glasses on Nanostructured Silicon Surfaces," J. of Electrical Engineering, vol. 3, no. 1, Mar. 2015, doi: 10.17265/2328-2223/2015.01.002.

[254] D. Li, X. Feng, J. He, B. Lian, and Y. Wang, "Research of surface wettability of plating on the ceramic shell," in 2014 Joint IEEE International Symposium on the Applications of Ferroelectric, International Workshop on Acoustic Transduction Materials and Devices & Workshop on Piezoresponse Force Microscopy, IEEE, May 2014, pp. 1208–1211. doi: 10.1109/ISAF.2014.6918069.

[255] K. Szymczyk and B. Jańczuk, "Wettability of a Glass Surface in the Presence of Two Nonionic Surfactant Mixtures," Langmuir, vol. 24, no. 15, pp. 7755–7760, Aug. 2008, doi: 10.1021/la8008078.

[256] J. V. Rau et al., "Glass-ceramic coated Mg-Ca alloys for biomedical implant applications," Materials Science and Engineering: C, vol. 64, pp. 362–369, Jul. 2016, doi: 10.1016/j.msec.2016.03.100.

[257] P. W. McMillan, G. Partridge, and F. R. Ward, "Glass-ceramics for use in silicon semiconductor applications," J Mater Sci, vol. 4, no. 7, pp. 634–640, Jul. 1969, doi: 10.1007/BF00550119.

[258] K. Huang et al., "Preparation and characterization of mesoporous 45S5 bioactive glass–ceramic coatings on magnesium alloy for corrosion protection," J Alloys Compd, vol. 580, pp. 290–297, Dec. 2013, doi: 10.1016/j.jallcom.2013.05.103.

[259] G. Wang, Z. Lu, X. Liu, X. Zhou, C. Ding, and H. Zreiqat, "Nanostructured glass–ceramic coatings for orthopaedic applications," J R Soc Interface, vol. 8, no. 61, pp. 1192–1203, Aug. 2011, doi: 10.1098/rsif.2010.0680.

[260] I. W. Donald, P. M. Mallinson, B. L. Metcalfe, L. A. Gerrard, and J. A. Fernie, "Recent developments in the preparation, characterization and applications of glass- and glass–ceramic-to-metal seals and coatings," J Mater Sci, vol. 46, no. 7, pp. 1975–2000, Apr. 2011, doi: 10.1007/s10853-010-5095-y.

[261] S. Sanyal, M. Shukla, N. Dandapat, and S. Ghosh, "In vitro evaluation of bioactive glass ceramic coating for application on Ti6Al4V based biomedical implants," J Non Cryst Solids, vol. 500, pp. 22–29, Nov. 2018, doi: 10.1016/j.jnoncrysol.2018.04.043.

[262] S. Sanyal, M. Shukla, N. Dandapat, and S. Ghosh, "In vitro evaluation of bioactive glass ceramic coating for application on Ti6Al4V based biomedical implants," J Non Cryst Solids, vol. 500, pp. 22–29, Nov. 2018, doi: 10.1016/j.jnoncrysol.2018.04.043.

[263] S.-M. Hsu et al., "Novel Coating to Minimize Corrosion of Glass-Ceramics for Dental Applications," Materials, vol. 13, no. 5, p. 1215, Mar. 2020, doi: 10.3390/ma13051215.

[264] X. Zhang, X.-W. Li, J.-G. Li, and X.-D. Sun, "Preparation and Characterizations of Bioglass Ceramic Cement/Ca–P Coating on Pure

Magnesium for Biomedical Applications," ACS Appl Mater Interfaces, vol. 6, no. 1, pp. 513–525, Jan. 2014, doi: 10.1021/am404574t.

[265] M. Xu et al., "A novel, efficient and cost-effective synthesis technique for the development of superhydrophobic glass surface," J Alloys Compd, vol. 781, pp. 1175–1181, Apr. 2019, doi: 10.1016/j.jallcom.2018.12.084.

[266] M. P. Ferraz, F. J. Monteiro, A. P. Serro, B. Saramago, I. R. Gibson, and J. D. Santos, "Effect of chemical composition on hydrophobicity and zeta potential of plasma sprayed HA/CaO–P2O5 glass coatings," Biomaterials, vol. 22, no. 23, pp. 3105–3112, Dec. 2001, doi: 10.1016/S0142-9612(01)00059-X.

[267] P. Xu, L. Pershin, J. Mostaghimi, and T. W. Coyle, "Efficient one-step fabrication of ceramic superhydrophobic coatings by solution precursor plasma spray," Mater Lett, vol. 211, pp. 24–27, Jan. 2018, doi: 10.1016/j.matlet.2017.09.077.

[268] J. H. Talal, D. B. Mohammed, and K. H. Jawad, "Fabrication of Hydrophobic Nanocomposites Coating Using Electrospinning Technique For Various Substrate," J Phys Conf Ser, vol. 1032, p. 012033, May 2018, doi: 10.1088/1742-6596/1032/1/012033.

[269] K. J. Kubiak, M. C. T. Wilson, T. G. Mathia, and Ph. Carval, "Wettability versus roughness of engineering surfaces," Wear, vol. 271, no. 3–4, pp. 523–528, Jun. 2011, doi: 10.1016/j.wear.2010.03.029.

[270] T. WATANABE, "Wettability of ceramic surfaces -A wide range control of surface wettability from super hydrophilicity to super hydrophobicity, from static wettability to dynamic wettability," Journal of the Ceramic Society of Japan, vol. 117, no. 1372, pp. 1285–1292, 2009, doi: 10.2109/jcersj2.117.1285.

[271] G. Aksoy, H. Polat, M. Polat, and G. Coskun, "Effect of various treatment and glazing (coating) techniques on the roughness and wettability of ceramic dental restorative surfaces," Colloids Surf B Biointerfaces, vol. 53, no. 2, pp. 254–259, Dec. 2006, doi: 10.1016/j.colsurfb.2006.09.016.

[272] J. H. Talal, D. B. Mohammed, and K. H. Jawad, "Fabrication of Hydrophobic Nanocomposites Coating Using Electrospinning Technique For Various Substrate," J Phys Conf Ser, vol. 1032, p. 012033, May 2018, doi: 10.1088/1742-6596/1032/1/012033.

[273] T. WATANABE, "Wettability of ceramic surfaces -A wide range control of surface wettability from super hydrophilicity to super hydrophobicity, from static wettability to dynamic wettability," Journal of the Ceramic Society of Japan, vol. 117, no. 1372, pp. 1285–1292, 2009, doi: 10.2109/jcersj2.117.1285.

[274] K. Choy, "Chemical vapour deposition of coatings," Prog Mater Sci, vol. 48, no. 2, pp. 57–170, 2003, doi: 10.1016/S0079-6425(01)00009-3.

[275] M. Psarski, G. Celichowski, E. Bystrzycka, D. Pawlak, J. Grobelny, and M. Cichomski, "Vapor phase deposition of fluoroalkyl trichlorosilanes on silicon and glass: Influence of deposition conditions and chain length on wettability

and adhesion forces," Mater Chem Phys, vol. 204, pp. 305–314, Jan. 2018, doi: 10.1016/j.matchemphys.2017.10.037.

[276] Q. Chen et al., "Recovery dynamics of acrylic coating surfaces under elevated relative humidity monitored by atomic force microscopy," Prog Org Coat, vol. 146, p. 105712, Sep. 2020, doi: 10.1016/j.porgcoat.2020.105712.

[277] D. Sola and J. I. Peña, "Foamy coating obtained by laser ablation of glass ceramic substrates at high temperature," Appl Surf Sci, vol. 255, no. 10, pp. 5322–5328, Mar. 2009, doi: 10.1016/j.apsusc.2008.09.028.

[278] A. Kumar, A. Gokhale, S. Ghosh, and S. Aravindan, "Effect of nano-sized sintering additives on microstructure and mechanical properties of Si3N4 ceramics," Materials Science and Engineering: A, vol. 750, pp. 132–140, Mar. 2019, doi: 10.1016/j.msea.2019.02.020.

[279] V. P. Maslov, Yu. M. Rodichev, and N. F. Tregubov, "Thermoresistant Nano-filled Glass-ceramics," Procedia Eng, vol. 10, pp. 1463–1466, 2011, doi: 10.1016/j.proeng.2011.04.243.

[280] Q. Xu, D. Zhan, D.-P. Huang, H.-X. Liu, W. Chen, and F. Zhang, "Effect of MgO–CaO–Al2O3–SiO2 glass additive on dielectric properties of Ba0.95Sr0.05Zr0.2Ti0.8O3 ceramics," J Alloys Compd, vol. 558, pp. 77–83, May 2013, doi: 10.1016/j.jallcom.2012.12.164.

[281] X. W. Wang et al., "Enhanced energy storage properties in Ba0.85Ca0.15Zr0.1Ti0.9O3 ceramics with glass additives," J Appl Phys, vol. 127, no. 7, Feb. 2020, doi: 10.1063/1.5138948.

[282] V. Marghussian, "Optical Properties of Nano-Glass Ceramics," in Nano-Glass Ceramics, Elsevier, 2015, pp. 63–123. doi: 10.1016/B978-0-323-35386-1.00002-5.

[283] F. Peng, K.-M. Liang, H. Shao, and A.-M. Hu, "Nano-crystal glass-ceramics obtained by crystallization of vitrified red mud," Chemosphere, vol. 59, no. 6, pp. 899–903, May 2005, doi: 10.1016/j.chemosphere.2004.11.002.

[284] W. Ming et al., "Progress in Transparent Nano-Ceramics and Their Potential Applications," Nanomaterials, vol. 12, no. 9, p. 1491, Apr. 2022, doi: 10.3390/nano12091491.

[285] A. Goel, A. A. Reddy, M. J. Pascual, L. Gremillard, A. Malchere, and J. M. F. Ferreira, "Sintering behavior of lanthanide-containing glass-ceramic sealants for solid oxide fuel cells," J Mater Chem, vol. 22, no. 19, p. 10042, 2012, doi: 10.1039/c2jm16300d.

[286] K. E. Easterling and A. R. Thölén, "A Study of Sintering Using Hot-Stage Electron Microscopy," Metal Science Journal, vol. 4, no. 1, pp. 130–135, Jan. 1970, doi: 10.1179/msc.1970.4.1.130.

[287] R. Aguiar, M. Godinho, E. Longo, and E. R. Leite, "In Situ Observation of Glass Particle Sintering," J Chem Educ, vol. 83, no. 3, p. 410, Mar. 2006, doi: 10.1021/ed083p410.

[288] M. I. Ojovan, "Ordering and structural changes at the glass–liquid transition," J Non Cryst Solids, vol. 382, pp. 79–86, Dec. 2013, doi: 10.1016/j.jnoncrysol.2013.10.016.

[289] N. Da, S. Krolikowski, K. H. Nielsen, J. Kaschta, and L. Wondraczek, "Viscosity and Softening Behavior of Alkali Zinc Sulfophosphate Glasses," Journal of the American Ceramic Society, vol. 93, no. 8, pp. 2171–2174, Aug. 2010, doi: 10.1111/j.1551-2916.2010.03707.x.

[290] H. Kato, A. Inoue, and H.-S. Chen, "On structural relaxation and viscous work heating during non-Newtonian viscous flow in a Zr55Al10Ni5Cu30 bulk metallic glass," Acta Mater, vol. 54, no. 4, pp. 891–898, Feb. 2006, doi: 10.1016/j.actamat.2005.10.024.

[291] K. Hosoi, S. Kawai, K. Yanagisawa, and N. Yamasaki, "Densification process for spherical glass powders with the same particle size by hydrothermal hot pressing," J Mater Sci, vol. 26, no. 23, pp. 6448–6452, Dec. 1991, doi: 10.1007/BF02387828.

[292] R. P. Miller and G. Sommer, "A hot stage microscope incorporating a differential thermal analysis unit," J Sci Instrum, vol. 43, no. 5, pp. 293–297, May 1966, doi: 10.1088/0950-7671/43/5/304.

[293] M. P. Shepilov, A. E. Kalmykov, and G. A. Sycheva, "Liquid–liquid phase separation in sodium borosilicate glass: Ordering phenomena in particle arrangement," J Non Cryst Solids, vol. 353, no. 24–25, pp. 2415–2430, Jul. 2007, doi: 10.1016/j.jnoncrysol.2007.03.019.

[294] M. Reading, "Thermal Analysis by Structural Characterization (TASC): Structural and Thermo-Rheological Information from Hot Stage Microscopy," Micros Today, vol. 25, no. 5, pp. 18–23, Sep. 2017, doi: 10.1017/S1551929517000815.

[295] J. L. Amorós, E. Blasco, A. Moreno, M. P. Gómez-Tena, and C. Feliu, "Non-isothermal sinter-crystallisation of satin glazes: A kinetic model," Ceram Int, vol. 44, no. 7, pp. 7780–7787, May 2018, doi: 10.1016/j.ceramint.2018.01.208.

[296] P. A. Tick, K. E. Lu, S. Mitachi, T. Kanamori, and S. Takahashi, "Hot stage optical microscopy studies of crystallization in fluoride glass melts," J Non Cryst Solids, vol. 140, pp. 275–280, Jan. 1992, doi: 10.1016/S0022-3093(05)80781-1.

[297] J. Liu, Y. Sun, W. Wang, and J. Chen, "Using the viscoelastic parameters to estimate the glass transition temperature of asphalt binders," Constr Build Mater, vol. 153, pp. 908–917, Oct. 2017, doi: 10.1016/j.conbuildmat.2017.07.120.

[298] V. N. Bliznyuk, H. E. Assender, and G. A. D. Briggs, "Surface Glass Transition Temperature of Amorphous Polymers. A New Insight with SFM," Macromolecules, vol. 35, no. 17, pp. 6613–6622, Aug. 2002, doi: 10.1021/ma011326a.

[299] M. A. Saied, O. C. Wilson, E. D. Rekow, and I. K. Lloyd, "Design of Join Glass Composition for Layered All-Ceramic Restorations," Journal of the American Ceramic Society, vol. 94, no. 8, pp. 2458–2463, Aug. 2011, doi: 10.1111/j.1551-2916.2011.04636.x.

[300] A. A. Omar, A. W. A. El-Shennawi, and A. R. El-Ghannam, "Thermal expansion of Li2O-ZnO-Al2O3-SiO2 glasses and corresponding glass-

ceramics," J Mater Sci, vol. 26, no. 22, pp. 6049–6056, 1991, doi: 10.1007/BF01113882.

[301] M. Goswami, A. Sarkar, B. I. Sharma, V. K. Shrikhande, and G. P. Kothiyal, "Effect of alumina concentration on thermal and structural properties of mas glass and glass-ceramics," J Therm Anal Calorim, vol. 78, no. 3, pp. 699–705, Jan. 2004, doi: 10.1007/s10973-005-0435-0.

[302] J. C. Mauro, Y. Yue, A. J. Ellison, P. K. Gupta, and D. C. Allan, "Viscosity of glass-forming liquids," Proceedings of the National Academy of Sciences, vol. 106, no. 47, pp. 19780–19784, Nov. 2009, doi: 10.1073/pnas.0911705106.

[303] M. Ikeda and M. Aniya, "Understanding the Vogel–Fulcher–Tammann law in terms of the bond strength–coordination number fluctuation model," J Non Cryst Solids, vol. 371–372, pp. 53–57, Jul. 2013, doi: 10.1016/j.jnoncrysol.2013.04.034.

[304] M. L. F. Nascimento and C. Aparicio, "Data classification with the Vogel–Fulcher–Tammann–Hesse viscosity equation using correspondence analysis," Physica B Condens Matter, vol. 398, no. 1, pp. 71–77, Aug. 2007, doi: 10.1016/j.physb.2007.04.074.

[305] M. Ikeda and M. Aniya, "Understanding the Vogel–Fulcher–Tammann law in terms of the bond strength–coordination number fluctuation model," J Non Cryst Solids, vol. 371–372, pp. 53–57, Jul. 2013, doi: 10.1016/j.jnoncrysol.2013.04.034.

[306] Q. Zheng and J. C. Mauro, "Viscosity of glass-forming systems," Journal of the American Ceramic Society, vol. 100, no. 1, pp. 6–25, Jan. 2017, doi: 10.1111/jace.14678.

[307] A. V. Granato, "A derivation of the Vogel–Fulcher–Tammann relation for supercooled liquids," J Non Cryst Solids, vol. 357, no. 2, pp. 334–338, Jan. 2011, doi: 10.1016/j.jnoncrysol.2010.08.012.

[308] K. Pathmanathan and G. P. Johari, "Temperature dependence of molecular relaxation rates and of viscosity of glass-forming liquids," Philosophical Magazine B, vol. 62, no. 2, pp. 225–228, Aug. 1990, doi: 10.1080/13642819008226988.

[309] O. Gedeon, "Origin of glass fragility and Vogel temperature emerging from Molecular dynamics simulations," J Non Cryst Solids, vol. 498, pp. 109–117, Oct. 2018, doi: 10.1016/j.jnoncrysol.2018.06.012.

[310] M. L. F. Nascimento and C. Aparicio, "Data classification with the Vogel–Fulcher–Tammann–Hesse viscosity equation using correspondence analysis," Physica B Condens Matter, vol. 398, no. 1, pp. 71–77, Aug. 2007, doi: 10.1016/j.physb.2007.04.074.

[311] C. Păcurariu, M. Liţă, I. Lazău, D. Tiţa, and G. Kovacs, "Kinetic study of the crystallization processes of some glass ceramics based on basalt, via thermal analysis," J Therm Anal Calorim, vol. 72, no. 3, pp. 811–821, 2003, doi: 10.1023/A:1025010013618.

[312] A. Arslan, H. Koralay, Ş. Çavdar, and A. Günen, "Crystallization kinetic studies on Bi1.75Pb0.25Sr2Ca2Cu3-xSnxOδ glass-ceramic by using non-

isothermal technique," J Non Cryst Solids, vol. 358, no. 9, pp. 1190–1195, May 2012, doi: 10.1016/j.jnoncrysol.2012.02.016.

[313] H. C. Park, S. H. Lee, B. K. Ryu, M. M. Son, H. S. Lee, and I. Yasui, "Nucleation and crystallization kinetics of CaO-Al2O3-2SiO2 in powdered anorthite glass," J Mater Sci, vol. 31, no. 16, pp. 4249–4253, Aug. 1996, doi: 10.1007/BF00356446.

[314] T. Vlase, C. Păcurariu, R. I. Lazău, and I. Lazăn, "Kinetic studies of the crystallization process of glass-ceramics based on basalt," J Therm Anal Calorim, vol. 88, no. 3, pp. 625–629, Jun. 2007, doi: 10.1007/s10973-006-8016-1.

[315] J. Deubener, M. Montazerian, S. Krüger, O. Peitl, and E. D. Zanotto, "Heating rate effects in time-dependent homogeneous nucleation in glasses," J Non Cryst Solids, vol. 474, pp. 1–8, Oct. 2017, doi: 10.1016/j.jnoncrysol.2017.07.019.

[316] T. Kokubu and M. Yamane, "Thermal and chemical properties of TiO2-SiO2 porous glass-ceramics," J Mater Sci, vol. 22, no. 7, pp. 2583–2588, Jul. 1987, doi: 10.1007/BF01082148.

[317] G. H. BEALL, B. R. KARSTETTER, and H. L. RITTLER, "Crystallization and Chemical Strengthening of Stuffed β-Quartz Glass-Ceramics," Journal of the American Ceramic Society, vol. 50, no. 4, pp. 181–190, Apr. 1967, doi: 10.1111/j.1151-2916.1967.tb15077.x.

[318] T. Srikumar et al., "Photostimulated optical effects and some related features of CuO mixed Li2O–Nb2O5–ZrO2–SiO2 glass ceramics," Ceram Int, vol. 37, no. 7, pp. 2763–2779, Sep. 2011, doi: 10.1016/j.ceramint.2011.04.031.

[319] M. Goswami, G. P. Kothiyal, L. Montagne, and L. Delevoye, "MAS-NMR study of lithium zinc silicate glasses and glass-ceramics with various ZnO content," J Solid State Chem, vol. 181, no. 2, pp. 269–275, Feb. 2008, doi: 10.1016/j.jssc.2007.11.023.

[320] I. W. Donald, B. L. Metcalfe, D. J. Wood, and J. R. Copley, "The preparation and properties of some lithium zinc silicate glass-ceramics," J Mater Sci, vol. 24, no. 11, pp. 3892–3903, Nov. 1989, doi: 10.1007/BF01168952.

[321] C. Bischoff, H. Eckert, E. Apel, V. M. Rheinberger, and W. Höland, "Phase evolution in lithium disilicate glass–ceramics based on non-stoichiometric compositions of a multi-component system: structural studies by 29Si single and double resonance solid state NMR," Physical Chemistry Chemical Physics, vol. 13, no. 10, p. 4540, 2011, doi: 10.1039/c0cp01440k.

[322] W. Höland, E. Apel, Ch. van 't Hoen, and V. Rheinberger, "Studies of crystal phase formations in high-strength lithium disilicate glass–ceramics," J Non Cryst Solids, vol. 352, no. 38–39, pp. 4041–4050, Oct. 2006, doi: 10.1016/j.jnoncrysol.2006.06.039.

[323] R. Hill and P. Gilbert, "High-Temperature Dynamic Mechanical Thermal Analysis of a Lithium Zinc Silicate Glass-Ceramic," Journal of the American Ceramic Society, vol. 76, no. 2, pp. 417–425, Feb. 1993, doi: 10.1111/j.1151-2916.1993.tb03800.x.

[324] Z. Xiao et al., “Crystallization behaviors, thermo-physical properties and seal application of Li 2 O–ZnO–MgO–SiO 2 glass-ceramics,” J Alloys Compd, vol. 657, pp. 231–236, Feb. 2016, doi: 10.1016/j.jallcom.2015.10.106.

[325] Y. Chen, W. Li, Y. Zhang, Z. Shen, D. Yang, and X. Song, “Crystallization and thermal expansion behavior of lithium zinc silicate sealing glass,” Ceram Int, vol. 42, no. 10, pp. 11650–11653, Aug. 2016, doi: 10.1016/j.ceramint.2016.04.068.

[326] M. Sander, P. Engelmann, P. Jacobs, and C. Roos, “Controlled surface crystallization of lithium-zinc-alumosilicate glass-ceramics using thermal poling,” Journal of the American Ceramic Society, vol. 105, no. 5, pp. 3279–3290, May 2022, doi: 10.1111/jace.18301.

[327] G. Han et al., “Extended Condensed Ultraphosphate Frameworks with Monovalent Ions Combine Lithium Mobility with High Computed Electrochemical Stability,” J Am Chem Soc, vol. 143, no. 43, pp. 18216–18232, Nov. 2021, doi: 10.1021/jacs.1c07874.

[328] B. Indrajit Sharma, M. Goswami, P. Sengupta, V. K. Shrikhande, G. B. Kale, and G. P. Kothiyal, “Study on some thermo-physical properties in Li2O–ZnO–SiO2 glass-ceramics,” Mater Lett, vol. 58, no. 19, pp. 2423–2428, Jul. 2004, doi: 10.1016/j.matlet.2004.02.038.

[329] E. C. Bucharsky, K. G. Schell, A. Hintennach, and M. J. Hoffmann, “Preparation and characterization of sol–gel derived high lithium ion conductive NZP-type ceramics Li1+x AlxTi2−x(PO4)3,” Solid State Ion, vol. 274, pp. 77–82, Jun. 2015, doi: 10.1016/j.ssi.2015.03.009.

[330] T. KATOH, Y. INDA, M. BABA, and R. YE, “Lithium-ion conductive glass-ceramics with composition ratio control and their electrochemical characteristics,” Journal of the Ceramic Society of Japan, vol. 118, no. 1384, pp. 1159–1162, 2010, doi: 10.2109/jcersj2.118.1159.

[331] X. Lu, L. Zhang, H. Talebinezhad, Y. Tong, and Z.-Y. Cheng, “Effects of CuO additive on the dielectric property and energy-storage performance of BaTiO3-SiO2 ceramic-glass composite,” Ceram Int, vol. 44, no. 14, pp. 16977–16983, Oct. 2018, doi: 10.1016/j.ceramint.2018.06.139.

[332] S. Arcaro et al., “Properties of LZS/nanoAl2O3 glass-ceramic composites,” J Alloys Compd, vol. 710, pp. 567–574, Jul. 2017, doi: 10.1016/j.jallcom.2017.03.299.

[333] I. W. Donald, B. L. Metcalfe, L. A. Gerrard, and S. K. Fong, “The influence of Ta2O5 additions on the thermal properties and crystallization kinetics of a lithium zinc silicate glass,” J Non Cryst Solids, vol. 354, no. 2–9, pp. 301–310, Jan. 2008, doi: 10.1016/j.jnoncrysol.2007.06.102.

[334] R. Kumar, A. Arvind, M. Goswami, S. Bhattacharya, V. K. Shrikhande, and G. P. Kothiyal, “The effect of NiO on the phase formation, thermo-physical properties and sealing behaviour of lithium zinc silicate glass–ceramics,” J Mater Sci, vol. 44, no. 13, pp. 3349–3355, Jul. 2009, doi: 10.1007/s10853-009-3408-9.

[335] Z. H. Xiao, L. G. Zhu, and S. L. Wang, “Preparation of High Thermal Expansion Coefficient Glass-Ceramics in Li<sub>2</sub>O-

ZnO-SiO<sub>2</sub> System," Adv Mat Res, vol. 412, pp. 348–351, Nov. 2011, doi: 10.4028/www.scientific.net/AMR.412.348.

[336] M. H. Misbah and H. Doweidar, "Transformation of Li4P4O12 rings into LiPO3 chains by CoO or CuO doping: Crystallization-induced reduction of photoluminescent Cu+ to plasmonic Cu° glass-ceramics," Ceram Int, vol. 47, no. 9, pp. 12695–12705, May 2021, doi: 10.1016/j.ceramint.2021.01.129.

[337] V. Yu. Solod and O. V. Nikulin, "APPROXIMATE INTEGRATION FOR DETERMINING THE SURFACE ROUGHNESS," Collection of scholarly papers of Dniprovsk State Technical University (Technical Sciences), vol. 1, no. 32, pp. 49–53, Sep. 2018, doi: 10.31319/2519-2884.32.2018.165.

[338] E. S. Gadelmawla, "Estimation of surface roughness for turning operations using image texture features," Proc Inst Mech Eng B J Eng Manuf, vol. 225, no. 8, pp. 1281–1292, Aug. 2011, doi: 10.1177/2041297510393643.

[339] V. I. Mironchenko, "On the Ratio of Surface Roughness Parameters," Measurement Techniques, vol. 48, no. 2, pp. 141–145, Feb. 2005, doi: 10.1007/s11018-005-0112-2.

[340] Q. Chen, Y. Wang, J. Zhou, Y. Wu, and H. Song, "Research on characterization of anisotropic and isotropic processing surfaces by characteristic roughness," J Mater Process Technol, vol. 275, p. 116277, Jan. 2020, doi: 10.1016/j.jmatprotec.2019.116277.

[341] G. Kumar and K. N. Prabhu, "Review of non-reactive and reactive wetting of liquids on surfaces," Adv Colloid Interface Sci, vol. 133, no. 2, pp. 61–89, Jun. 2007, doi: 10.1016/j.cis.2007.04.009.

[342] E. V. Gribanova, A. E. Kuchek, and M. I. Larionov, "Factors influencing the contact angle value. The contact angle, as a characteristic of the properties of solid surfaces," Russian Chemical Bulletin, vol. 65, no. 1, pp. 1–13, Jan. 2016, doi: 10.1007/s11172-016-1259-5.

[343] I. Malgarinos, N. Nikolopoulos, M. Marengo, C. Antonini, and M. Gavaises, "VOF simulations of the contact angle dynamics during the drop spreading: Standard models and a new wetting force model," Adv Colloid Interface Sci, vol. 212, pp. 1–20, Oct. 2014, doi: 10.1016/j.cis.2014.07.004.

[344] G. H. ten Brink, N. Foley, D. Zwaan, B. J. Kooi, and G. Palasantzas, "Roughness controlled superhydrophobicity on single nanometer length scale with metal nanoparticles," RSC Adv, vol. 5, no. 36, pp. 28696–28702, 2015, doi: 10.1039/C5RA02348C.

[345] D. Murakami, H. Jinnai, and A. Takahara, "Wetting Transition from the Cassie–Baxter State to the Wenzel State on Textured Polymer Surfaces," Langmuir, vol. 30, no. 8, pp. 2061–2067, Mar. 2014, doi: 10.1021/la4049067.

[346] Y. Wang, M. Muhler, and Ch. Wöll, "Spectroscopic evidence for the partial dissociation of H2O on ZnO(10$\bar{1}$0)," Physical Chemistry Chemical Physics, vol. 8, no. 13, p. 1521, 2006, doi: 10.1039/b515489h.

[347] R. Yang and Y. Du, "Adsorption and dissociation of a single water molecule on graphene-like ZnO monolayer with oxygen vacancies: a first-principles study," Phys Scr, vol. 98, no. 3, p. 035826, Mar. 2023, doi: 10.1088/1402-4896/acba59.

[348] T. Kano, T. Isobe, S. Matsushita, and A. Nakajima, “Hydrophobicity and Leidenfrost point of ZnO nanorod array combined with nanoscale roughness on the topmost surface,” Mater Chem Phys, vol. 217, pp. 192–198, Sep. 2018, doi: 10.1016/j.matchemphys.2018.06.075.

[349] V. Khranovskyy, T. Ekblad, R. Yakimova, and L. Hultman, “Surface morphology effects on the light-controlled wettability of ZnO nanostructures,” Appl Surf Sci, vol. 258, no. 20, pp. 8146–8152, Aug. 2012, doi: 10.1016/j.apsusc.2012.05.011.

[350] J. Schroers, A. Masuhr, W. L. Johnson, and R. Busch, “Pronounced asymmetry in the crystallization behavior during constant heating and cooling of a bulk metallic glass-forming liquid,” Phys Rev B, vol. 60, no. 17, pp. 11855–11858, Nov. 1999, doi: 10.1103/PhysRevB.60.11855.

[351] K. Nakayama, K. Kojima, I. Tamaru, Y. Masaki, A. Kitagawa, and M. Suzuki, “Heating rate dependence of phase transition temperature in Se7Te3 glasses,” J Non Cryst Solids, vol. 198–200, pp. 758–761, May 1996, doi: 10.1016/0022-3093(96)00123-8.

[352] P. M. Anderson and A. E. Lord, “Exact values for crystallization temperatures at different heating rates from isothermal transformation times,” Materials Science and Engineering, vol. 43, no. 1, pp. 93–96, Mar. 1980, doi: 10.1016/0025-5416(80)90212-8.

[353] Y. X. Zhuang, P. F. Xing, H. Y. Shi, J. Chen, P. W. Wang, and J. C. He, “On the heating rate dependence of crystallization temperatures of metallic glasses,” J Appl Phys, vol. 108, no. 3, Aug. 2010, doi: 10.1063/1.3457336.

[354] L. Soifer and E. Korin, “Effect of Heating Rate on Crystallization Kinetics of Amorphous Al91La5Ni4 Alloys by DSC,” J Therm Anal Calorim, vol. 56, no. 1, pp. 437–446, 1999, doi: 10.1023/A:1010131508113.

[355] L. Lilensten, Q. Fu, B. R. Wheaton, A. J. Credle, R. L. Stewart, and J. T. Kohli, “Kinetic study on lithium-aluminosilicate (LAS) glass-ceramics containing MgO and ZnO,” Ceram Int, vol. 40, no. 8, pp. 11657–11661, Sep. 2014, doi: 10.1016/j.ceramint.2014.03.171.

[356] H. Li, L. Wu, X. Wang, D. Xu, Y. Teng, and Y. Li, “Crystallization behavior and microstructure of barium borosilicate glass–ceramics,” Ceram Int, vol. 41, no. 10, pp. 15202–15207, Dec. 2015, doi: 10.1016/j.ceramint.2015.08.095.

[357] B. Karmakar, P. Kundu, S. Jana, and R. N. Dwivedi, “Crystallization Kinetics and Mechanism of Low-Expansion Lithium Aluminosilicate Glass-Ceramics by Dilatometry,” Journal of the American Ceramic Society, vol. 85, no. 10, pp. 2572–2574, Oct. 2002, doi: 10.1111/j.1151-2916.2002.tb00498.x.

[358] T. S. Sasikala, C. Pavithran, and M. T. Sebastian, “Effect of lithium magnesium zinc borosilicate glass addition on densification temperature and dielectric properties of Mg2SiO4 ceramics,” Journal of Materials Science: Materials in Electronics, vol. 21, no. 2, pp. 141–144, Feb. 2010, doi: 10.1007/s10854-009-9882-7.

[359] M. Goswami et al., “Crystallization behaviour of Li2OZnOSiO2 glass–ceramics system,” Ceram Int, vol. 33, no. 5, pp. 863–867, Jul. 2007, doi: 10.1016/j.ceramint.2006.01.013.

[360] Z. H. Xiao, L. G. Zhu, and S. L. Wang, “Preparation of High Thermal Expansion Coefficient Glass-Ceramics in Li<sub>2</sub>O-ZnO-SiO<sub>2</sub> System,” Adv Mat Res, vol. 412, pp. 348–351, Nov. 2011, doi: 10.4028/www.scientific.net/AMR.412.348.

[361] Z. Shen, L. Zhu, Y. Zhang, Y. Chen, D. Yang, and X. Song, “Effect of CuO addition on crystallization and thermal expansion properties of Li 2 O–ZnO–SiO 2 glass-ceramics,” Ceram Int, vol. 43, no. 9, pp. 7099–7105, Jun. 2017, doi: 10.1016/j.ceramint.2017.02.141.

[362] O. C. Mocioiu, M. Zaharescu, G. Jitianu, and P. Budrugeac, “Kinetic parameters determination in non-isothermal conditions for the crystallisation of a silica-soda-lead glass,” J Therm Anal Calorim, vol. 86, no. 2, pp. 429–436, Nov. 2006, doi: 10.1007/s10973-005-7273-8.

[363] L. Lilensten, Q. Fu, B. R. Wheaton, A. J. Credle, R. L. Stewart, and J. T. Kohli, “Kinetic study on lithium-aluminosilicate (LAS) glass-ceramics containing MgO and ZnO,” Ceram Int, vol. 40, no. 8, pp. 11657–11661, Sep. 2014, doi: 10.1016/j.ceramint.2014.03.171.

[364] B. Karmakar, P. Kundu, S. Jana, and R. N. Dwivedi, “Crystallization Kinetics and Mechanism of Low-Expansion Lithium Aluminosilicate Glass-Ceramics by Dilatometry,” Journal of the American Ceramic Society, vol. 85, no. 10, pp. 2572–2574, Oct. 2002, doi: 10.1111/j.1151-2916.2002.tb00498.x.

[365] D. Trache, A. Abdelaziz, and B. Siouani, “A simple and linear isoconversional method to determine the pre-exponential factors and the mathematical reaction mechanism functions,” J Therm Anal Calorim, vol. 128, no. 1, pp. 335–348, Apr. 2017, doi: 10.1007/s10973-016-5962-0.

[366] E. G. Colgan and F. M. d’Heurle, “Kinetics of silicide formation measured by in situ ramped resistance measurements,” J Appl Phys, vol. 79, no. 8, pp. 4087–4095, Apr. 1996, doi: 10.1063/1.361771.

[367] S. Vyazovkin, “Kissinger Method in Kinetics of Materials: Things to Beware and Be Aware of,” Molecules, vol. 25, no. 12, p. 2813, Jun. 2020, doi: 10.3390/molecules25122813.

[368] Z. F. Yao, J. C. Qiao, C. Zhang, J. M. Pelletier, and Y. Yao, “Non-isothermal crystallization transformation kinetics analysis and isothermal crystallization kinetics in super-cooled liquid region (SLR) of (Ce0.72Cu0.28)90−xAl10Fex (x=0, 5 or 10) bulk metallic glasses,” J Non Cryst Solids, vol. 415, pp. 42–50, May 2015, doi: 10.1016/j.jnoncrysol.2015.02.017.

[369] V. R. V. Ramanan and G. E. Fish, “Crystallization kinetics in Fe−B−Si metallic glasses,” J Appl Phys, vol. 53, no. 3, pp. 2273–2275, Mar. 1982, doi: 10.1063/1.330797.

[370] J. J. Suñol and J. Bonastre, “Crystallization kinetics of metallic glasses,” J Therm Anal Calorim, vol. 102, no. 2, pp. 447–450, Nov. 2010, doi: 10.1007/s10973-010-0955-x.

[371] M. Hua, P. Shu-Jie, L. Ran, and Z. Tao, “Crystallization Kinetics of Co 48 Cr 15 Mo 14 C 15 B 6 Er 2 Bulk Metallic Glass with High Thermal Stability,” Chinese Physics Letters, vol. 23, no. 2, pp. 417–419, Feb. 2006, doi: 10.1088/0256-307X/23/2/039.

[372] B. A. Legg, J. Schroers, and R. Busch, “Thermodynamics, kinetics, and crystallization of Pt57.3Cu14.6Ni5.3P22.8 bulk metallic glass,” Acta Mater, vol. 55, no. 3, pp. 1109–1116, Feb. 2007, doi: 10.1016/j.actamat.2006.09.024.

[373] C. Ohtsuki, H. Inada, M. Tanihara, M. Kamitakahara, and T. Miyazaki, “Fabrication of Bioactive Glass-Ceramics Containing Zinc Oxide,” Key Eng Mater, vol. 254–256, pp. 59–62, Dec. 2003, doi: 10.4028/www.scientific.net/KEM.254-256.59.

[374] I. P. Alekseeva, O. S. Dymshits, A. A. Zhilin, S. S. Zapalova, and D. V. Shemchuk, “Transparent glass–ceramics based on ZnO and ZnO:Co^2+ nanocrystals,” Journal of Optical Technology, vol. 81, no. 12, p. 723, Dec. 2014, doi: 10.1364/JOT.81.000723.

[375] B. Mirhadi, B. Mehdikhani, and N. Askari, “Effect of zinc oxide on microhardness and sintering behavior of MgO–Al2O3–SiO2 glass–ceramic system,” Solid State Sci, vol. 14, no. 4, pp. 430–434, Apr. 2012, doi: 10.1016/j.solidstatesciences.2012.01.010.

[376] A. T. G. Kullberg, A. A. S. Lopes, J. P. B. Veiga, M. M. R. A. Lima, and R. C. C. Monteiro, “Formation and crystallization of zinc borosilicate glasses: Influence of the ZnO/B2O3 ratio,” J Non Cryst Solids, vol. 441, pp. 79–85, Jun. 2016, doi: 10.1016/j.jnoncrysol.2016.03.022.

[377] M. Duan, J. Wang, C. Liu, J. Xie, and J. Han, “Effects of SnO doping on the optical properties of ZnO in glass,” J Non Cryst Solids, vol. 459, pp. 32–35, Mar. 2017, doi: 10.1016/j.jnoncrysol.2016.12.024.

[378] M. Eskandari, A. Shanaghi, M. Kamani, and M. A. Niari, “Effect of nano-metal oxides (ZnO, Al2O3, CuO, and TiO2) on the corrosion behavior of a nano-metal oxide/epoxy coating applied on the copper substrate in the acidic environment,” Appl Nanosci, vol. 11, no. 5, pp. 1605–1615, May 2021, doi: 10.1007/s13204-021-01806-7.

[379] C. Han et al., “Heterostructured CuO@ZnO@Ag biomimetic setaria as wettability-switchable difunctional SERS substrate for trace pesticide and DNA detections,” Nanophotonics, vol. 10, no. 10, pp. 2671–2682, Aug. 2021, doi: 10.1515/nanoph-2021-0179.

[380] X. Feng, L. Feng, M. Jin, J. Zhai, L. Jiang, and D. Zhu, “Reversible Super-hydrophobicity to Super-hydrophilicity Transition of Aligned ZnO Nanorod Films,” J Am Chem Soc, vol. 126, no. 1, pp. 62–63, Jan. 2004, doi: 10.1021/ja038636o.

[381] P. Senthil Kumar, M. Selvakumar, S. Ganesh Babu, S. Induja, and S. Karuthapandian, “CuO/ZnO nanorods: An affordable efficient p-n heterojunction and morphology dependent photocatalytic activity against organic contaminants,” J Alloys Compd, vol. 701, pp. 562–573, Apr. 2017, doi: 10.1016/j.jallcom.2017.01.126.

[382] C. Shu, Z. Wenjuan, G. Xu, Z. Wei, J. Wei, and W. Dongmei, “Dissolution behavior and bioactivity study of glass ceramic scaffolds in the system of CaO–P2O5–Na2O–ZnO prepared by sol–gel technique,” Materials Science and Engineering: C, vol. 30, no. 1, pp. 105–111, Jan. 2010, doi: 10.1016/j.msec.2009.09.006.

# PUBLICATIONS FROM THE THESIS

**Conference Papers**

**1**. N. Çöpoğlu and Buğra Çiçek, “Nano-Copper Oxide-Induced Surface Improvements In $(Na,Li)_2O$-ZnO-$P_2O_5$-$B_2O_3$-$SiO_2$ Glass-Ceramic Coatings” 15th ECerS Conference for Young Scientists in Ceramics, CYSC-2023 Novi Sad, Serbia, October 11-14, 2023, pp. 126.

**2**. N. Çöpoğlu, A. Soylu and B. Çiçek, “Crystallization Kinetics and Thermal Behavior Of Lithium Zinc Borosilicate Glass-Ceramic Coatings” 3rd International Congress on Engineering And Sciences, Istanbul, Turkiye, May 10-11, pp. 304.

**Papers**

**1**. N. Çöpoğlu, S. Daloğlu, O. Karaahmet, and B. Çiçek, “Influence of nano-CuO modification on crystallization behavior and surface characteristics of P2O5 containing Li2O-ZnO-B2O3-SiO2 glass-ceramics,” *Surface & coatings technology*, pp. 130942–130942, doi: 10.1016/j.surfcoat.2024.130942.